NUREG/CR–6235
BMI–2179

Assessment of Short Through-Wall Circumferential Cracks in Pipes

Experiments and Analysis

March 1990 – December 1994

Prepared by
F. W. Brust, P. Scott, S. Rahman, N. Ghadiali, T. Kilinski, B. Francini,
C. W. Marschall, N. Miura, P. Krishnaswamy, G. M. Wilkowski

Battelle

Prepared for
U.S. Nuclear Regulatory Commission

AVAILABILITY NOTICE

Availability of Reference Materials Cited in NRC Publications

Most documents cited in NRC publications will be available from one of the following sources:

1. The NRC Public Document Room, 2120 L Street, NW., Lower Level, Washington, DC 20555-0001

2. The Superintendent of Documents, U.S. Government Printing Office, P. O. Box 37082, Washington, DC 20402-9328

3. The National Technical Information Service, Springfield, VA 22161-0002

Although the listing that follows represents the majority of documents cited in NRC publications, it is not intended to be exhaustive.

Referenced documents available for inspection and copying for a fee from the NRC Public Document Room include NRC correspondence and internal NRC memoranda; NRC bulletins, circulars, information notices, inspection and investigation notices; licensee event reports; vendor reports and correspondence; Commission papers; and applicant and licensee documents and correspondence.

The following documents in the NUREG series are available for purchase from the Government Printing Office: formal NRC staff and contractor reports, NRC-sponsored conference proceedings, international agreement reports, grantee reports, and NRC booklets and brochures. Also available are regulatory guides, NRC regulations in the *Code of Federal Regulations*, and *Nuclear Regulatory Commission Issuances*.

Documents available from the National Technical Information Service include NUREG-series reports and technical reports prepared by other Federal agencies and reports prepared by the Atomic Energy Commission, forerunner agency to the Nuclear Regulatory Commission.

Documents available from public and special technical libraries include all open literature items, such as books, journal articles, and transactions. *Federal Register* notices, Federal and State legislation, and congressional reports can usually be obtained from these libraries.

Documents such as theses, dissertations, foreign reports and translations, and non-NRC conference proceedings are available for purchase from the organization sponsoring the publication cited.

Single copies of NRC draft reports are available free, to the extent of supply, upon written request to the Office of Administration, Distribution and Mail Services Section, U.S. Nuclear Regulatory Commission, Washington, DC 20555-0001.

Copies of industry codes and standards used in a substantive manner in the NRC regulatory process are maintained at the NRC Library, Two White Flint North, 11545 Rockville Pike, Rockville, MD 20852-2738, for use by the public. Codes and standards are usually copyrighted and may be purchased from the originating organization or, if they are American National Standards, from the American National Standards Institute, 1430 Broadway, New York, NY 10018-3308.

DISCLAIMER NOTICE

NUREG/CR-6235
BMI-2179

Assessment of Short Through-Wall Circumferential Cracks in Pipes

Experiments and Analysis

March 1990 – December 1994

Manuscript Completed: March 1995
Date Published: April 1995

Prepared by
F. W. Brust, P. Scott, S. Rahman, N. Ghadiali, T. Kilinski, B. Francini,
C. W. Marschall, N. Miura*, P. Krishnaswamy, G. M. Wilkowski

Battelle
505 King Avenue
Columbus, OH 43201

Prepared for
Division of Engineering Technology
Office of Nuclear Regulatory Research
U.S. Nuclear Regulatory Commission
Washington, DC 20555-0001
NRC Job Code B5702

*Central Research Institute of Electric Power Industry
Komae Research Laboratory
Tokyo 201 Japan

ABSTRACT

This topical report summarizes the work performed for the Nuclear Regulatory Commission's (NRC) research program entitled "Short Cracks in Piping and Piping Welds" that specifically focuses on pipes with short through-wall cracks. Previous NRC efforts, conducted under the Degraded Piping Program, focused on understanding the fracture behavior of larger cracks in piping and fundamental fracture mechanics developments necessary for this technology.

This report gives details on: (i) material property determinations, (ii) pipe fracture experiments, and (iii) development, modification, and validation of fracture analysis methods.

The material property data required to analyze the experimental results are included. These data were also implemented into the NRC's PIFRAC database.

Three pipe experiments with short through-wall cracks were conducted on large diameter pipe. Also, experiments were conducted on a large-diameter uncracked pipe and a pipe with a moderate-size through-wall crack.

The analysis results reported here focus on simple predictive methods based on the J-Tearing theory as well as limit-load and ASME Section XI analyses. Some of these methods were improved for short-crack-length predictions. The accuracy of the various methods was determined by comparisons with experimental results from this and other programs.

CONTENTS

CONTENTS

CONTENTS

CONTENTS

LIST OF FIGURES Page

CONTENTS

CONTENTS

CONTENTS

CONTENTS

CONTENTS

LIST OF TABLES

CONTENTS

EXECUTIVE SUMMARY

This topical report summarizes the work performed for the Nuclear Regulatory Commission's (NRC) research program entitled "Short Cracks in Piping and Piping Welds", which specifically focused on pipes with short through-wall cracks. The Short Cracks program was five years long and began in March 1990. The overall research program objective was to verify and improve fracture analyses for circumferentially cracked large-diameter nuclear piping with crack sizes typically used in leak-before-break (LBB) analysis or in-service flaw evaluations (referred to as "short cracks"). The length of a typical crack is about 6 percent of the circumference for large diameter pipes in LBB evaluations, which is much less than the 20- to 40-percent crack ratios investigated in many of the past pipe fracture programs. The program was based on synergistic interactions of material characterization, full-scale pipe fracture experiments, and analysis. Only quasi-static loading rates were considered here since the NRC's International Piping Integrity Research Group (IPIRG) program focused on seismic loading rates on cracked piping systems.

There are three technical evaluations required to gain an understanding of, and to predict the fracture behavior of, through-wall-cracked pipe. These are material characterization, pipe experiments, and analysis methods. The material characterization data were used as input to the analysis methods to enable pipe fracture predictions and LBB to be predicted. The pipe experiments were used to benchmark, document, and improve the predictive methods by determining how well the methods predict the full-scale pipe fracture behavior. This report summarizes the results for these three technical evaluations.

Material Characterizations

Four different pipe materials were characterized as part of this effort:

- one A106 Grade B carbon steel pipe left over from a past Battelle/AEC program,
- one A515 Grade 60 carbon steel pipe obtained from a canceled Tennessee Valley Authority plant,
- one TP316 stainless steel pipe obtained from the excess pipe inventory of the Nine Mile Point Nuclear plant, and
- one TP316L stainless steel obtained from Electricité de France.

In addition, property data were obtained from the submerged-arc welds from the carbon and stainless steel pipes evaluated. These welds were fabricated using procedures obtained from Babcock and Wilcox (B&W) and General Electric.

Chemical composition, tensile, Charpy V-notch, and compact tension, C(T), tests were conducted for each of these materials. The C(T) tests were used to determine the fracture resistance of each material. All testing was done at quasi-static loading rates. These data were also input into the NRC's PIFRAC database.

Important points from the material characterization results are given below.

- The high Mn-Mo carbon steel pipe submerged-arc weld evaluated in this program was produced using a weld procedure employed in 90-percent of the B&W piping welds. Data on welds made by this weld procedure were not previously available. The B&W Mn-Mo-Ni weld procedure, which was used to make the welds assessed in the Degraded Piping Program, was used in the other 10-percent of their carbon steel piping welds, as well as for some of their pressure vessel welds. For the C(T) specimen tests at 22 C (72 F) for the high Mn-Mo weld evaluated in this program, only a small amount of stable crack growth occurred prior to the specimens undergoing an unstable, cleavage fracture. At 288 C (550 F), these two weld procedures had virtually identical fracture resistance (J-R curves).

- The French TP316L pipe material had an unusually low elastic modulus of 152 GPa (22,000,000 psi) at room temperature. This was verified by tests by several organizations in France.

- The stainless steel SAW evaluated in this program was created using the same General Electric weld procedure used in the Degraded Piping and the IPIRG-1 Programs. There were significant differences in the weld metal yield strengths between the three welds, but the J-R curves of the three different welds were not significantly different. The stainless steel welds had a lower toughness than the B&W high Mn-Mo carbon steel pipe weld.

- Crack instabilities occurred in the side-grooved C(T) specimens for the material evaluated from the 28-inch nominal diameter A515 Grade 60 carbon steel pipe experiment, but not in the non-side-grooved specimens. In the pipe experiment, crack instabilities occurred. These crack instabilities are attributed to dynamic strain aging effects. This pipe material was also included in the study on dynamic strain aging in NUREG/CR-6226, "Effect of Dynamic Strain Aging on the Strength and Toughness of Nuclear Ferritic Piping at LWR Temperatures".

Pipe Fracture Experiments

During the Degraded Piping Program, six large diameter and eight smaller diameter through-wall-cracked pipe experiments were conducted. In each case, the crack length was about 37 percent of the circumference. In addition, there have been about 25 other tests performed in the U.S., again with relatively large cracks. This void in the test database for pipes with short through-wall cracks was the motivation for this work.

Pipe experiments reported on were for:

- two A515 Grade 60 carbon steel base metal experiments both at 288 C (550 F), one with a 6.25-percent circumferential crack and one with no crack,
- one TP316 stainless steel pipe experiment at 288 C (550 F) with the crack in the submerged arc weld and a crack length to pipe circumference ratio of 6.25 percent,
- one A106 Grade B carbon steel pipe experiment at 288 C (550 F) with the crack in a submerged-arc weld and a crack length to pipe circumference ratio of 7.9 percent, and
- one experiment performed at room temperature on a French TP316L stainless steel pipe with a crack 24.4-percent of the circumference in the base metal.

These data increased the database for large diameter pipes with short through-wall cracks significantly. These pipe test data were added to the CIRCUMCK.WK1 pipe fracture database developed as part of the Short Cracks in Piping and Piping Welds Program.

For each experiment, the applied loads, displacements, crack-growth history, crack-mouth-opening displacement, pipe rotation, ovalization, and temperature were recorded. These data were then used for comparison with the results predicted using the J-estimation methods in order to document the accuracy of the predictive methods. Key aspects from these tests are given below.

- The French TP316L pipe experiment was a repeat of an Electricité de France (EDF) pipe experiment. This experiment was conducted to assess the reproducibility of pipe test data between laboratories. The Battelle and EDF maximum loads agreed within 3 percent of each other. This was within the 5-percent repeatability of pipe experiments observed in identical pipe tests conducted at Battelle, and replicated pipe tests between Battelle and David Taylor Research Center during the Degraded Piping Program. The confirmation of this test was important for the following reason.

  For several U.S. TP304 stainless steel pipe experiments tested in the past at Battelle, finite element analyses (FEA) by several organizations underpredicted the loads at crack initiation by 20 to 30 percent. However, for the French stainless steel pipe experiment, the results from several different FEA agreed well with the experimental results. The FEAs agreed well with each other for each experiment, so those analyses were consistent. One concern that was raised was the possibility of experimental error between the French and Battelle results. The test results for this experiment showed that there was no significant experimental error. After exhaustive review of the experimental data and analyses, it is believed that the only explanation of the FEA underprediction of the U.S. TP304 stainless steel pipe tests is due to differences in the constitutive behavior.

  Interestingly, the French TP316L stainless steel showed significant anisotropy as is indicated by the elliptical fracture surface in the longitudinal tensile test specimen. The U.S. TP304 steel showed no signs of anisotropy. The French steel also had an unusually

low elastic modulus, as noted earlier. Therefore, precise fracture analyses of stainless steel base metals may require more attention to the constitutive behavior of the material. The FEA underprediction for the U.S. stainless steel may be the reason the GE/EPRI (FEA based) method underpredicts the experimental failure loads the most of all the J-estimation schemes.

- Three pipe experiments were conducted on the same 28-inch nominal diameter A515 Grade 60 pipe. These were an uncracked pipe experiment (from this program), a pipe experiment with a 6.25-percent circumferential through-wall crack (from this program), and a pipe experiment with a 37-percent circumferential through-wall crack (from the Degraded Piping Program). Surprisingly, the 6.25-percent-cracked-pipe maximum load was only 65 percent of the uncracked pipe maximum load. From the Net-Section-Collapse analysis, it was expected that the loads would be within 5 percent between the uncracked-pipe and short-cracked-pipe experiments. Hence, the failure was an elastic-plastic fracture even though it had such a short crack length.

- Ovalization measurements from all the pipe experiments showed that the through-wall-cracked-pipe experiments ovalized in the opposite plane as uncracked pipe, but the magnitude of the ovalization was small.

- During the stainless steel welded-pipe experiment, the crack grew two-thirds more on one side than on the other side. The crack followed the fusion line of the weld on the side with the longer crack growth, even though the initial through-wall crack was in the center of the weld. On the short-crack-growth side, the crack grew from the center of the weld to the fusion line and then turned into the base metal. In another report from the Short Cracks in Piping and Piping Welds Program ("Stainless Steel Submerged Arc Weld Fusion-Line Toughness," NUREG/CR-6251), it was found that the J-R curve from a stainless steel submerged-arc-weld fusion line was much lower than the J-R curves for the base metal and the weld metal after small amounts of crack growth. This explains why the crack grew from the center of the weld to the fusion line. It is not known why the crack grew from the fusion line into the base metal on one side, since the base metal toughness is so much higher. However, the fact that it did grow into the base metal on this side explains why that crack was shorter than the crack on the other side which followed the fusion line.

Pipe Fracture Analyses

The results of the material characterizations served as input to the J-estimation schemes. Predictions from the J-estimation schemes were then compared with experimental pipe test data to document the accuracy of the predictive methods.

The analysis results reported here focussed on simple predictive methods based on J-Tearing theory. The J-estimation methods evaluated were the GE/EPRI, Paris/Tada, LBB.NRC, LBB.ENG2, LBB.ENG3, and the R-6 Option 1 analyses. In addition, new GE/EPRI solutions were developed for short cracks, along with a new methodology to predict the fracture behavior of cracks in pipe welds

(LBB.ENG3). Improvements were also made to the methods to increase the accuracy of fracture predictions for pipe with short through-wall cracks. In summary, all predictive methods attempted to estimate the crack-driving force as measured with the J-integral either by using a matrix of numerical solutions (GE/EPRI) or by estimating the load-displacement record and predicting J using mathematical principles (all other methods). Often numerical solutions were also used to verify the accuracy of the J-estimation schemes. The theory is discussed in detail for the GE/EPRI methods, the LBB.ENG2, and the LBB.ENG3 method, while all other methods are briefly summarized.

Predictions of all pipe fracture experiments were then made and compared with the corresponding experimental results. Crack initiation loads, maximum loads, crack growth response, and load-point displacements were compared between experiment and analysis. (Crack-opening-displacement analyses and comparisons with experimental data are covered in a separate report, NUREG/CR-6300 - "Refinement and Evaluation of Crack-Opening Analyses for Short Circumferential Through-Wall Cracks in Pipes"). The key findings from the current report are given below.

- The newly developed GE/EPRI functions showed significant improvement in the displacement predictions, but small improvements for the load predictions.

- The combined tension and bending GE/EPRI functions for pipes at PWR pressures were developed. If used for BWR pipe analyses, these functions will underpredict the actual cracked-pipe loads but overpredict the displacements.

  The new GE/EPRI functions, which were developed and implemented into the NRCPIPE code, were for tension plus bending without hoop stress considerations. Subsequently, it was also found that the hoop stress significantly affected the GE/EPRI crack-opening and pipe-displacement functions under combined loading.

- Ovalization effects were found to be small and hence were not specifically included in the J-estimation schemes except for the GE/EPRI method, which is based on finite element analysis and hence inherently incorporates ovalization effects.

- A modification to the LBB.ENG2 analysis (called LBB.ENG3) was developed to include the strength of the weld and base metals in the J-estimation scheme. This was the first and only J-estimation scheme that accounts for the weld and base metal strengths. Better predictions were made in some cases and little difference occurred in others.

- Various pipe fracture analyses were compared with the experimental data from this program and pressure-plus-bend data from other programs. The comparisons showed the following.

  - There was better agreement between analyses and experiments for long cracks than for short cracks.

  - The analyses that gave the most accurate predictions were the LBB.NRC, LBB.ENG2, and LBB.GE methods.

- The GE/EPRI analyses consistently underpredicted the experimental loads the most of all the J-estimation schemes. It did not matter if the plastic zone was included in the elastic term or not, nor if the old or new h_1 functions were used.

- The Paris/Tada and Net-Section-Collapse analyses were erratic, sometimes underpredicting and sometimes overpredicting the loads significantly.

- The ASME Section XI IWB-3640 or IWB-3650 pipe fracture analyses (without safety factors) generally underpredicted the experimental loads the most of all analyses; however, in one stainless steel base-metal-cracked pipe experiment, the IWB-3640 source equations overpredicted the experimental maximum load. In this experiment, the strength of the pipe was very close to the Code values at temperature, perhaps indicating that the choice of $3S_m$ for flow stress is slightly too high for a material that just meets the Code strength values.

- There was less accuracy in the prediction of the pipe experiments under pressure plus bending than for pure bending, but the relative accuracy of the estimation schemes under either bending or pressure plus bending was the same.

- The R6, Revision 3, Option 1 method was always found to underpredict loads when compared with experimental data, but for one experiment the predicted loads were 3 percent below the experimental loads. This method is a failure avoidance criteria with inherent (not applied) safety factors. Although this 3-percent margin may be of concern, using conservative material properties (as would be done in practice) rather than actual properties would further increase the inherent margin in the analysis for this experiment.

- Each of the analyses previously discussed was conducted using the Ramberg-Osgood fit of the engineering stress-strain curve over a strain range of 0.1-percent strain to the strain corresponding to 80-percent of the ultimate strength. C(T) specimen J-R curves were extrapolated using the C(T) specimen data for crack growth up to 30 percent of the initial specimen ligament and a power-law equation for extrapolating the J-R curve for larger amounts of crack growth. In general, it was found that the standard C(T) specimen J-R curve was lower than the quasi-static pipe test J-R curve. However, work in other programs showed that when the pipe is loaded dynamically or under cyclic tearing (as in a seismic event), the J-R curve from the pipe test can be lower than the J-R curves developed using the standard ASTM, quasi-static, monotonically loaded, C(T) specimen testing procedures.

- An η-factor analysis procedure for calculating the J-R curve from pipe experiments with short through-wall cracks was developed and compared with finite element results. The results showed that accounting for the uncracked pipe or remote plasticity that occurs with short cracks can be done in a bounding manner. For determining the J-R curve from a short-through-wall-cracked pipe, it would be better to develop an η-factor analysis that uses the load versus center-crack-opening displacement data to eliminate the concern

of the plasticity from the uncracked pipe. This new η-factor function could be developed using the new GE/EPRI functions from this program.

For pipes under combined pressure plus bending loads, an η-factor analysis method was developed and used to analyze several past pipe experiments with long through-wall cracks. For two different pipes there were both pure-bending and pressure-plus-bending experiments. The J-R curve from the pure-bending pipe experiment was slightly higher than the J-R curve from the pressure-plus-bending experiment for each pipe. However, the differences were not significant and C(T) specimen J-R curves were lower than the pressure plus bending pipe J-R curves.

ACKNOWLEDGMENT

This work was supported by the U.S. Nuclear Regulatory Commission through the Electrical, Materials and Mechanical Engineering Branch of the Office of Nuclear Regulatory Research under Contract No. NRC-04-90-069. Mr. A. Hiser and Mr. M. Mayfield were the NRC Program Managers for this program.

Mr. Naoki Miura of CRIEPI, Japan, performed some of the pipe test analyses reported here while he was a visiting scientist at Battelle. We thank him for his diligent efforts.

We would also like to thank others at Battelle who have helped in these efforts. Those who contributed to the experimental efforts were: Dr. A. Rosenfield, Mr. R. Gertler, Mr. P. Held, Mr. P. Mincer, Mr. D. Rider, Mr. J. Ryan, Mr. D. Shoemaker, and Mr. J. Woods. We thank Mrs. V. Kreachbaum, Ms. C. Pepper, and Ms. A. Armitage for typing this report, and Mr. D. Hayes and Ms. Judy Ward for drafting assistance.

NOMENCLATURE

1. SYMBOLS

A	Crack area
A_1, A_2	Constants in R-6 Analyses
$\bar{A}_1$, $\bar{A}_2$, $\bar{A}_3$	Parameters used in LBB.ENG3 method
A_b	Constants to define stress intensity factor due to bending
A_t	Constants to define stress intensity factor due to tension
a	Half the crack length
a_e	Effective half crack length (plastic-zone corrected)
a_o	Initial half crack length
a^*	Half crack length at maximum load
$\hat{a}$	Reduced thickness length in LBB.ENG analyses
B_b	Constants to define stress intensity factor due to bending
B_t	Constants to define stress intensity factor due to tension
C_1, C_2, C_3, C_4, C_5, C_6	Integration constants
C'	Coefficient used to fit J-resistance curve
C_b	Constants to define stress intensity factor due to bending
C_t	Constants to define stress intensity factor due to tension
c	Half the mean circumferential crack length
$\bar{C}$	Constant defined in LBB.ENG2 and LBB.ENG3 method
D_m	Mean pipe diameter
D_o	Outside diameter
$\hat{D}$	Proportional constant in LBB.ENG3

E, E_1, E_2, E_i	Young's modulus, generic, for material 1, for material 2, and for material i
F	Function used in elastic stress intensity factor definition in GE/EPRI Method
F_B	Geometric factor for K_I due to bending loads
F_T	Geometric factor for K_I due to tension loads
f_1, f_2, f_3, f_4	Elastic functions tabulated in GE/EPRI method
$G_k(\theta)$	Function used in deriving the LBB.ERG3 method
$G_k'(\theta)$	First derivative of $G_k(\theta)$ with respect to θ
g_1, g_2	Functions for maximum load predictions
H_B	Factor used in LBB.ENG2 method
h	Factor used in η-factor approach
h_1,h_2,h_3,h_4	Functions tabulated in GE/EPRI method
h_1^b, h_2^b, h_3^b, h_4^b	Functions tabulated in GE/EPRI method for bending
h_1^T, h_2^T, h_3^T, h_4^T	Functions tabulated in GE/EPRI method for tension
I	Moment of inertia
I_B, I_{B1}, I_{B2}, I_{B3}	Compliance (function of θ)
J	J-integral fracture parameter
J_{ABAQUS}	Total J from ABAQUS
J_B	J from bending
J_B^e	Elastic J due to bending
J_B^p	Plastic J due to bending
J_D	Deformation J
J_e	Elastic component of J-integral

J_i	J-integral at crack initiation but not necessarily a valid J_{Ic} by ASTM E813-81
J_{Ic}	J at crack initiation under Mode I loading
J_M	Modified value of J integral
J_p	Plastic component of J-integral
J_R, J-R	J-integral resistance (curve)
J_T	J from tension
J_T^e	Elastic J for tension
J_T^p	Plastic J for tension
K_I	Mode I stress intensity factor
K_{Ic}	Linear elastic fracture toughness
K_{IB}	Stress intensity factor; bending
K_{IT}	Stress intensity factory; tension
K_i	Factor to estimate J via LBB.ENG2 method
K_r	Toughness ratio in R-6 method
$\hat{K}$, $\hat{K}_i$	Function in LBB.ENG method, for material i
k	Constant used in defining $G_k(\theta)$
L	Half pipe length
L_B	Length factor used in LBB.ENG2 method
L_B^d	Length factor for weld in LBB.ENG3
L_R	Load ratio in R6 analysis
L_r	Strength ratio in R-6 Analysis
L_w	Length of weld in LBB.ENG3 analysis

M	Moment
M_L^c	Limit moment due to the crack
M_{nsc}	Net-Section-Collapse Moment
M_0	Reference moment for a pipe
M_{01}, M_{02}	Reference moments used by LBB.ENG3 method
M_{RP}	Rigid-plastic limit moment
M_l^d	Limit moment at reduced cross section in LBB.ENG3
M_1, M_2, M_i	Uncracked pipe elastic bending moment for σ_{01}, σ_{02}, σ_{0i}
m	Exponent used to fit J-resistance curve
n, n_1, n_2, n_i	Ramberg-Osgood strain-hardening exponent, for material 1, for material 2, for material i
P	Tension load due to internal pressure
P_i	Crack initiation load
P_{max}	Maximum load
P_o	Axial force at limit load
p	Pressure
R_i	Inside radius
R_m	Mean pipe radius
R_o	Outside radius
r	A normalizing constant used in fitting the J-R curve
r_y	Plastic-zone radius
S_m	ASME design stress
t	Thickness of pipe wall

t_e	Effective thickness of pipe
U	d-c electric potential; also, internal strain energy
U^c	Internal strain energy due to crack
U^{nc}	Internal strain energy without crack
U^T	Total internal strain energy ($U^c + U^{nc}$)
U_o	Electric potential at crack initiation
$V(\theta)$	Ovalization function
V_1, V_2, V_3	Displacement functions in GE/EPRI analysis
V_1^B, V_2^B, V_3^B	Displacement functions in GE/EPRI analysis for bending
V_1^T, V_2^T, V_3^T	Displacement functions in GE/EPRI analysis for tension
W	Compact tension specimen width
Z	A stress multiplier in the ASME Section XI IWB-3640 and -3650 analyses
z	Distance from crack plane
α	Ramberg-Osgood parameter
β	Fully plastic neutral axis angle; also, factor used in η-factor approach
Δ	Pipe displacement at the load point
Δ^c	Pipe displacement at load point due to the crack
Δ^{nc}	Pipe load-line displacement without the crack
Δ^c_{ABAQUS}	Pipe load-line displacement due to the crack from ABAQUS
Δ^c_B	Pipe load-line displacement due to the crack due to bending
Δ_{pl}	Plastic load-line displacement; total
Δ^c_{pl}	Plastic load-line displacement; due to crack
Δ^{nc}_{pl}	Plastic load-line displacement; uncracked pipe

Δ_T^c	Pipe load-line displacement due to the crack due to tension
Δa	Increment of crack growth
δ	Total crack-opening displacement
δ_{ABAQUS}	Total δ from ABAQUS
δ_B	Total crack-opening displacement due to bending
δ_B^e	Total elastic crack-opening displacement due to bending
δ_e	Total elastic crack-opening displacement
δ_p	Plastic component of total crack-opening displacement
δ_p^c	Plastic component of total crack-opening displacement due to the crack
δ_T	Total crack-opening displacement due to tension
ϵ	Strain
ϵ_0, ϵ_{0i}	Reference strain (σ_0/E), for material i
γ	Factor used in η-factor analysis
ϕ	Half rotation of pipe
ϕ^c	Half rotation of pipe due to crack
ϕ_{ABAQUS}^c	Half rotation of pipe due to the crack from ABAQUS
ϕ_B^c	Half rotation of pipe in bending due to the crack
$\phi_B^c \mid_{elastic}$	Half of pipe elastic rotation of pipe at bending due to crack
ϕ_e^d	Elastic half pipe rotation at material's discontinuity in LBB.ENG2
ϕ_e^c	Elastic pipe rotation due to crack
ϕ_e^{nc}	Elastic half rotation of uncracked pipe

ϕ_p^c	Plastic pipe rotation due to crack
ϕ_P^{nc}	Plastic half rotation of uncracked pipe
ϕ_p^d	Plastic half pipe rotation at material's discontinuity in LBB.ENG2
ϕ_T^c	Half rotation of pipe in tension due to the crack
ϕ_{Tot}^c	$\phi_e^c + \phi_P^c$
ϕ_o	Half rotation of pipe at crack initiation
η	Geometric factor used in J-integral analysis
θ	Half-crack angle
λ	Ratio of tension to bending stress
σ	Stress
σ_B	Bending stress
σ_f	Flow stress
σ_{limit}	Stress at limit moment
σ_{nsc}	Net-section-collapse analysis predicted failure stress
σ_T	Tension stress
σ_u	Ultimate stress
σ_y	Yield stress
σ_0, σ_{01}, σ_{02}, σ_{0i}	Reference stresses, generic, for material 1, for material 2, and for material i

2. ACRONYMS AND INITIALISMS

A/D	Analogue to digital

ASME	American Society of Mechanical Engineers
ASTM	American Society for Testing and Materials
B&W	Babcock and Wilcox
BWR	Boiling Water Reactor
CEGB	Central Electricity Generating Board (U.K.)
CMOD	Crack-mouth-opening displacement
COD	Crack-opening displacement
COV	Coefficient of variation
C(T)	Compact (tension) specimen
DAS	Data acquisition systems
d-c EP	Direct-current electric potential
DP^3II	Degraded Piping Program - Phase II
DSA	Dynamic strain aging
DTRC	David Taylor Research Center (U.S.)
EDF	Electricite de France
EPFM	Elastic-plastic fracture mechanics
EPRI	Electric Power Research Institute (U.S.)
FAC	Failure assessment curve
FAD	Failure assessment diagram
FEM	Finite element method
GE	General Electric
GTAW	Gas tungsten arc weld
HAZ	Heat-affected zone

IBM	International Business Machine (computer)
IPIRG	International Piping Integrity Research Group
LBB	Leak-before-break
L-C	Longitudinal-circumferential orientation (direction of through-wall-crack growth around pipe circumference)
LLD	Load-line displacement
LVDT	Linear variable displacement transducer
MTS	MTS Systems Company (materials testing machine manufacturer)
NRC	Nuclear Regulatory Commission (U.S.)
NSC	Net-section collapse
NUREG/CR	Nuclear Regulatory Commission contractor report
PC	Personal computer
PWR	Pressurized water reactor
SAW	Submerged-arc weld
SMAW	Shielded metal arc weld
SMiRT	Structural Mechanics in Reactor Technology
TIG	Tungsten inert gas (weld)
TVA	Tennessee Valley Authority
TWC	Through-wall crack, through-wall-cracked
UK	United Kingdom
USNRC	United States Nuclear Regulatory Commission

PREVIOUS REPORTS IN SERIES

Reports from this Program

"Short Cracks in Piping and Piping Welds," First Semiannual Report, NUREG/CR-4599, Vol. 1, No. 1, March 1991.

"Short Cracks in Piping and Piping Welds," Second Semiannual Report, NUREG/CR-4599, Vol. 1, No. 2, April 1992.

"Short Cracks in Piping and Piping Welds," Third Semiannual Report, NUREG/CR-4599, Vol. 2, No. 1, September 1992.

"Short Cracks in Piping and Piping Welds," Fourth Semiannual Report, NUREG/CR-4599, Vol. 2, No. 2, February 1993.

"Short Cracks in Piping and Piping Welds," Fifth Semiannual Report, NUREG/CR-4599, Vol. 3, No. 1, October 1993.

"Short Cracks in Piping and Piping Welds," Sixth Semiannual Report, NUREG/CR-4599, Vol. 3, No. 2, March 1994.

"Short Cracks in Piping and Piping Welds," Seventh Program Report, NUREG/CR-4599, BMI-2173, Vol. 4, No. 1, April 1995.

"Fracture Evaluations of Fusion-Line Cracks in Nuclear Pipe Bimetallic Welds," NUREG/CR-6297, April 1995.

"Effect of Dynamic Strain Aging on the Strength and Toughness of Nuclear Ferritic Piping at LWR Temperatures," NUREG/CR-6226, October 1994.

"Effects of Toughness Anisotropy and Combined Tension, Torsion, and Bending Load on Fracture Behavior of Ferritic Nuclear Pipe," NUREG/CR-6299, April 1995.

"Refinement and Evaluation of Crack-Opening Analyses for Short Circumferential Through-Wall Cracks in Pipes," NUREG/CR-6300, April 1995.

"Probabilistic Pipe Fracture Evaluations for Leak-Rate Detection Applications," NUREG/CR-6004, April 1995.

"Stainless Steel Submerged Arc Weld Fusion Line Toughness," NUREG/CR-6251, April 1995.

"Validity Limits in J-Resistance Curve Determination--Volume 1: An Assessment of the J_M Parameter," NUREG/CR-6264, Volume 1, February 1995.

"Validity Limits in J-Resistance Curve Determinations--Volume 2: A Computational Approach to Ductile Crack Growth Under Large-Scale Yielding Condition," NUREG/CR-6264, Volume 2, February 1995.

Previous Related Documents from NRC's Degraded Piping Program

"Degraded Piping Program - Phase II," Semiannual Report, NUREG/CR-4082, Vol. 1, Oct. 1984.

"Degraded Piping Program - Phase II," Semiannual Report, NUREG/CR-4082, Vol. 2, June 1985.

"Degraded Piping Program - Phase II," Semiannual Report, NUREG/CR-4082, Vol. 3, March 1986.

"Degraded Piping Program - Phase II," Semiannual Report, NUREG/CR-4082, Vol. 4, July 1986.

"Degraded Piping Program - Phase II," Semiannual Report, NUREG/CR-4082, Vol. 5, Dec. 1986.

"Degraded Piping Program - Phase II," Semiannual Report, NUREG/CR-4082, Vol. 6, April 1988.

"Degraded Piping Program - Phase II," Semiannual Report, NUREG/CR-4082, Vol. 7, March 1989.

"Degraded Piping Program - Phase II," Semiannual Report, NUREG/CR-4082, Vol. 8, March 1989.

"NRC Leak-Before-Break (LBB.NRC) Analysis Method for Circumferentially Through-Wall Cracked Pipes Under Axial Plus Bending Loads," Topical Report, NUREG/CR-4572, March 1986.

"Elastic-Plastic Finite Element Analysis of Crack Growth in Large Compact Tension and Circumferentially Through-Wall-Cracked Pipe Specimen--Results of the First Battelle/NRC Analysis Round Robin," Topical Report, NUREG/CR-4573, September 1986.

"An Experimental and Analytical Assessment of Circumferential Through-Wall Cracked Pipes Under Pure Bending," Topical Report, NUREG/CR-4574, June 1986.

"Predictions of J-R Curves With Large Crack Growth From Small Specimen Data," Topical Report, NUREG/CR-4687, September 1986.

"An Assessment of Circumferentially Complex-Cracked Pipe Subjected to Bending," Topical Report, NUREG/CR-4687, September 1986.

"Analysis of Cracks in Stainless Steel TIG Welds," Topical Report, NUREG/CR-4806, November 1986.

"Approximate Methods for Fracture Analyses of Through-Wall Cracked Pipes," Topical Report, NUREG/CR-4853, January 1987.

"Assessment of Design Basis for Load-Carrying Capacity of Weld-Overlay Repair," Topical Report, NUREG/CR-4877, February 1987.

"Analysis of Experiments on Stainless Steel Flux Welds," Topical Report, NUREG/CR-4878, February 1987.

"Experimental and Analytical Assessment of Circumferentially Surface-Cracked Pipes Under Bending," Topical Report, NUREG/CR-4872, April 1987.

Previous Related Documents from NRC's International Piping Integrity Research Group (IPIRG) Program

"Evaluation and Refinement of Leak-Rate Estimation Models," NUREG/CR-5128, Revision 1.

"Loading Rate Effects on Strength and Fracture Toughness of Pipe Steels Used in Task 1 of the IPIRG Program," Topical Report, NUREG/CR-6098, October 1993.

"Stability of Cracked Pipe Under Inertial Stresses," NUREG/CR-6233, Volume 1, August 1994.

Other Related Program Reports

"Validation of Analysis Methods for Assessing Flawed Piping Subjected to Dynamic Loading," NUREG/CR-6234, August 1994.

1. INTRODUCTION

This report presents the results of a combined experimental/analytical study of crack growth and instability behavior of circumferential through-wall-cracked (TWC) pipes. In a number of previous programs funded by the United States Nuclear Regulatory Commission (NRC), pipes with large TWCs were investigated. For large diameter pipe in leak-before-break (LBB) analyses, most cracks of concern are small (of the order of 6 to 12 percent of the pipe circumference); hence, it was important to investigate short crack behavior. This is because most of the predictive methods were developed, and verified, by comparing predictions based on J-tearing theory with pipe test experimental data developed using large through-wall cracks. Short circumferential through-wall cracks in both base metal and weld metal were considered in this study.

This report is organized as follows. Section 2.0, Material Characterization, summarizes the material property data for the pipes tested in this program. These data include stress-strain behavior and J-resistance curves developed from compact tension specimens machined from the pipe. Section 3.0, Pipe Experiments, provides the results from all of the short TWC tests conducted during the course of the program. The data presented include initiation and maximum loads, crack growth response, load-point displacements (for the four-point bend tests), pipe rotations, and pipe ovalization behavior. Section 4.0, Short Through-Wall-Cracked Pipe Analysis, provides details of analysis methods and predictive results. This section provides a short overview of analysis methods and procedures, the presentation of several new analysis methods (including a new method to predict fracture of cracked pipe welds), and comparisons of predictions with experimental data from this program as well as data from other programs using these methods.

2. MATERIAL CHARACTERIZATIONS

In this section, the results of the material characterization efforts for the materials specifically characterized for the pipe experiments are discussed. The discussion begins with a description of the materials selected for use as test specimens. Next the results of the chemical composition analyses, tensile tests, Charpy tests, and fracture toughness tests for the test specimen materials are presented. Some of these results were developed during the course of this program, while other data were available from the Degraded Piping Program previously conducted at Battelle.

2.1 Material Selection

2.1.1 Test Specimen Materials

Four different materials were evaluated for the one uncracked and four cracked-pipe experiments conducted as part of this effort, see Table 2.1. The four pipe materials chosen for the cracked-pipe experiments were a 711-mm (28-inch) diameter A155-KC60 Class 1 carbon steel pipe (made from A515 Grade 60 steel), a 711-mm (28-inch) diameter TP316L stainless steel pipe, a 610-mm (24-inch) diameter SA333 Grade 6 carbon steel pipe, and a 101.6-mm (4-inch) diameter Z3 CND 18-12 stainless steel pipe. The designation Z3 CND 18-12 is a French pipe designation, which is similar to the U.S. pipe designation TP316L. Note, however, that chemical analyses indicated that nitrogen was deliberately added to the melt (the nitrogen content was 0.194 percent by weight), and microstructural examination indicated the presence of titanium carbonitride. Both of these findings suggest that the pipe may have been more like TP316LN, rather than TP316L, as previously suspected. Cracks were located in the center of shop fabricated submerged-arc welds (SAW) in the 711-mm (28-inch) diameter TP316L pipe and the 610-mm (24-inch) diameter SA333 Grade 6 pipe. The test material for the uncracked pipe experiment (Expériment 1.1.1.25) was a section of A155-KC60 Class 1 carbon steel pipe, i.e., the same material used in the cracked-pipe Experiment 1.1.1.21.

The first three pipes listed in Table 2.1 were all relatively large diameter, low toughness pipes for which the failure should be governed by elastic-plastic fracture mechanics (EPFM) conditions. The fourth pipe material was a small diameter, high toughness material for which the failure should be governed by limit-load conditions. This 101.6-mm (4-inch) diameter stainless steel pipe sample was donated to this program by Électricité de France (EDF). This pipe material was left over from EDF pipe Experiment Number 24. The specific objective of this experiment (1.1.1.26) was to compare results from the Battelle experimental pipe facility with results generated by EDF using their pipe testing facility in France.

The large diameter carbon and stainless steel pipes were nuclear grade materials obtained from nuclear plants. The carbon steel pipe material used in Experiments 1.1.1.21 and 1.1.1.25 (DP2-F26) carried the pipe designation A155-KC60-CL1. The plate material used in the fabrication of this longitudinally seam-welded pipe was A515 Grade 60 plate. The carbon steel material used in Experiment 1.1.1.24 (DP2-F4) was SA333 Grade 6 pipe and was obtained from a cancelled Tennessee Valley Authority (TVA) nuclear plant. The stainless steel pipe material used in

Table 2.1 List of pipe materials and welds evaluated as part of Task 1 of the Short Cracks in Piping and Piping Welds Program

Material	Nominal Pipe Diameter, mm (inch)	Nominal Wall Thickness, mm (inch)	Battelle Pipe Material Identification Number	Battelle Weld Identification Number for Material Property Tests	Applicable Pipe Experiment Number
A515 Grade 60 Carbon Steel	711 (28)	22.2 (0.875)	DP2-F26	NA[a]	1.1.1.21 1.1.1.25
TP316L Stainless Steel SAW	711 (28)	30.2 (1.19)	DP2-A51	DP2-A45W1 DP2-A45W2 DP2-A8W4	1.1.1.23
SA333 Grade 6 Carbon Steel SAW	610 (24)	31.0 (1.219)	DP2-F4	DP2-F49W	1.1.1.24
Z3 CND 18-12 Stainless Steel (TP316L)	102 (4)	8.56 (0.337)	IP-A2	NA[a]	1.1.1.26

(a) NA = not applicable

Experiment 1.1.1.23 (DP2-A51) was TP316L stainless steel. This section of pipe was obtained from the excess pipe inventory of the Nine Mile Point nuclear plant.

The weld procedures used in fabricating both the stainless steel and carbon steel welds were submerged-arc welding (SAW) procedures obtained from vendors in the United States. The stainless steel weld procedure, which was obtained from the General Electric Company (GE), had a toughness value close to the lower bound toughness value used in Section XI IWB-3640 for submerged-arc welds. This stainless steel weld was a single-Vee weld having a 1.6-mm (0.063-inch) land and a 2.4-mm (0.094-inch) gap. The first two root passes employed the gas tungsten arc process (GTAW), the next two passes used the shielded-metal arc process (SMAW), and the remaining passes used the submerged-arc process (SAW). The filler metal met Specification SFA-5.9 (Class ER-308) for GTAW and SAW and SFA-5.4 (Class ER-308) for SMAW. The flux was ER-308/ST-100 (Lincolnweld). The carbon steel weld procedure was obtained from Babcock & Wilcox (B&W) as being typical of the weld procedure used in piping girth welds in the Midland plant and about 90 percent of the carbon steel pipe welds in other B&W plants. It also had a very low fracture toughness. This carbon steel weld procedure was automatic submerged-arc, using a high manganese, high molybdenum wire carrying the designations EA3 and SFA 5.23. The flux was Linde 80.

2.2 Chemical Composition

Table 2.2 shows the results of the chemical composition analyses for the pipe materials and weld metals evaluated as part of this effort.

Table 2.2 Chemical composition, percent by weight, of pipe materials and weld metals evaluated as part of Task 1 of the Short Cracks in Piping and Piping Welds Program

Experiment Number	1.1.1.21 1.1.1.25	1.1.1.23		1.1.1.24		1.1.1.26
Material Material Identification	A515 Gr. 60 F26	TP316L A51	SAW A45W2	A333 Gr. 6 F4	SAW F49W	Z3 CND 18-12 IP-A2
C	0.13	0.021	0.03	ND	0.084	0.02
Mn	0.80	1.8	2.26	ND	1.55	1.68
P	0.009	0.031	0.032	ND	0.016	0.024
S	0.027	0.018	0.010	ND	0.013	0.009
Si	0.25	0.55	0.89	ND	0.44	0.48
Cu	0.12	0.2	0.26	ND	0.055	0.13
Sn	0.007	0.008	0.010	ND	0.003	0.008
Ni	0.13	9.8	9.6	ND	0.013	12.9
Cr	0.13	17.3	19.7	ND	0.024	17.0
Mo	0.40	2.1	0.10	ND	0.47	2.5
Al	0.003	0.01	0.015	ND	0.005	0.015
V	0.000	0.08	0.070	ND	0.001	0.059
Nb	0.000	0.013	0.012	ND	0.000	0.008
Zr	0.000	0.001	0.015	ND	0.001	0.000
Ti	0.000	0.004	0.006	ND	0.001	0.014
B	0.000	0.0002	0.0008	ND	0.0003	0.0012
Ca	ND	0.0024	0.0008	ND	0.0006	0.0009
Co	0.06	0.12	0.13	ND	0.002	0.076
W	0.00	0.0	0.0	ND	ND	0.0
Se	ND	0.00	0.00	ND	ND	0.00
Pb	0.00	ND	ND	ND	0.00	ND
N	ND	0.076	ND	ND	ND	0.164

ND = not determined

2.3 Tensile Test Results

Summary graphs and tables of longitudinal tensile test results are presented in this section. All specimens were machined longitudinal to the pipe axis. All tests were conducted at quasi-static loading rates. For the weld metal experiments (1.1.1.23 and 1.1.1.24), both the base metal and weld metal tensile properties are shown.

2.3.1 A155-KC60 Class 1 (A515 Grade 60) Carbon Steel

Round-bar tensile specimens were machined from a section of the A155-KC60 Class 1 (A515 Grade 60) carbon steel pipe material (DP2-F26) and were used to conduct quasi-static tensile tests at room temperature, 149 C (300 F), and 288 C (550 F). These data were developed during the Degraded Piping Program--Phase II (Ref. 2.1). The tensile tests were conducted using a Baldwin hydraulic testing machine at a cross-head speed selected to produce fracture within 10 to 20 minutes, corresponding to the approximate times to achieve crack initiation in the pipe fracture experiments. The results of those tests are summarized in Table 2.3.

Table 2.3 Longitudinal tensile properties of Pipe DP2-F26

Specimen Identification Number	Temperature, C (F)	0.2% Offset Yield Strength, MPa (ksi)	Ultimate Tensile Strength, MPa (ksi)	Elongation, percent in 25.4 mm (1 inch)	Area Reduction, percent
F26-1	22 (72)	276.5 (40.1)	440.6 (63.9)	31.2	69.0
F26-2	22 (72)	262.0 (38.0)	436.4 (63.3)	37.2	70.0
Average		269.3 (39.1)	438.5 (63.6)	34.3	69.5
F26-3	149 (300)	270.3 (39.2)	524.7 (76.1)	22.5	53.1
F26-4	149 (300)	266.1 (38.6)	527.4 (76.5)	23.0	50.1
Average		268.2 (38.9)	526.1 (76.3)	22.8	51.6
F26-5	288 (550)	231.0 (33.5)	541.9 (78.6)	30.5	54.1
F26-6	288 (550)	230.3 (33.4)	545.4 (79.1)	29.0	53.1
Average		230.7 (33.5)	543.6 (78.9)	29.8	53.6

Figure 2.1 shows engineering stress-strain curves from tensile tests for this carbon steel at 288 C (550 F). This steel did not exhibit the pronounced serrations on the stress-strain curves at this temperature/strain rate condition as has been observed for other carbon steel materials. These serrations are typically attributed to dynamic strain aging effects. The absence of serrations in Figure 2.1 indicates that this material may not be susceptible to dynamic strain aging at these temperature/strain rate conditions. However, as will be discussed later, the 288 C (550 F), quasi-static fracture toughness tests for this material did exhibit distinct periods of unstable crack growth, which were attributed to dynamic strain aging effects. One possible explanation for this apparent discrepancy is that the strain rate at the crack tip for the nominal quasi-static fracture toughness tests may have been sufficiently higher than the nominal strain rate for the quasi-static tensile test such that the material at the crack tip in the fracture toughness tests may have been transitioning into a region of the temperature/strain rate regime for which the material was more susceptible to dynamic strain aging effects (Ref. 2.2).

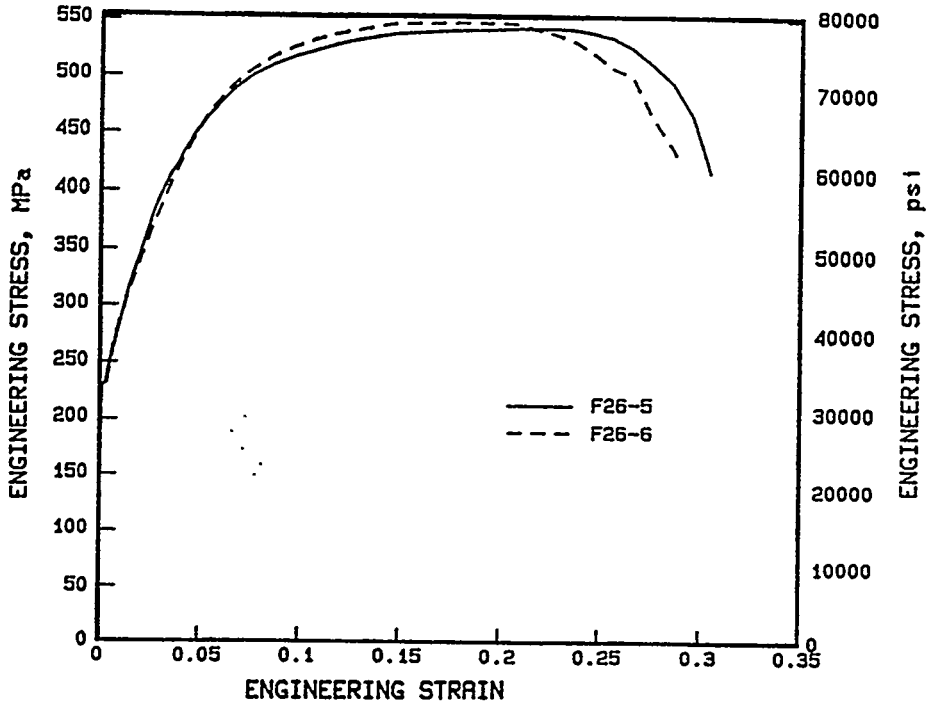

Figure 2.1 Engineering stress-strain curves for longitudinal tensile specimens machined from Pipe DP2-F26 at 288 C (550 F) (from Ref. 2.1)

2.3.2 TP316L Stainless Steel and Associated Submerged-Arc Weld

Round-bar tensile specimens were machined from a section of the TP316L stainless steel pipe material (DP2-A51) and subjected to quasi-static tensile tests at room temperature and 288 C (550 F). These data were developed during this program. Tensile properties for this stainless steel base metal material (DP2-A51) are summarized in Table 2.4. Figure 2.2 shows the engineering stress-strain curves for this material at room temperature and 288 C (550 F) and demonstrates the effect of test temperature on tensile properties. As evident in Table 2.4 and Figure 2.2, the higher test temperature caused a dramatic decrease in both the strength (yield and ultimate) and ductility (fracture elongation and reduction in area) for this stainless steel material. Strength decreases are the expected result of increased test temperature. However, the reason for the decrease in fracture elongation and reduction in area as temperature was raised is unknown. The reduction in both is too large to be attributed to experimental scatter.

Round-bar tensile specimens were machined from sections of stainless steel submerged-arc welds and used for quasi-static tensile tests at room temperature and 288 C (550 F). Some of these data were developed in this program, while additional data were developed in other programs as noted later. Tensile specimens were machined and tested from three different welds, made at three different times. The weld procedures for each weld were nominally the same as used in the pipe experiments. Two of the welds (Ref. 2.3) were fabricated in flat plates (DP2-A45W1 and DP2-A45W2), and one (Ref.2.4) was fabricated in a section of 406.4-mm (16-inch) nominal diameter, Schedule 100, TP304 stainless steel pipe (DP2-A8W4).

Table 2.4 Longitudinal tensile properties of Pipe DP2-A51 (wrought TP316L stainless steel)

Specimen Number	Test Temperature, C (F)	0.2% Offset Yield Strength, MPa (ksi)	Ultimate Tensile Strength, MPa (ksi)	Elongation, pct. in 25.4 mm (1.0 inch)	Area Reduction, percent
A51-1	20 (68)	254 (36.9)	ND (ND)	79.0	82.8
A51-2	20 (68)	263 (38.1)	597 (86.6)	79.0	83.9
A51-4	288 (550)	143 (20.8)	427 (62.0)	38.4	70.8

ND = Not Determined

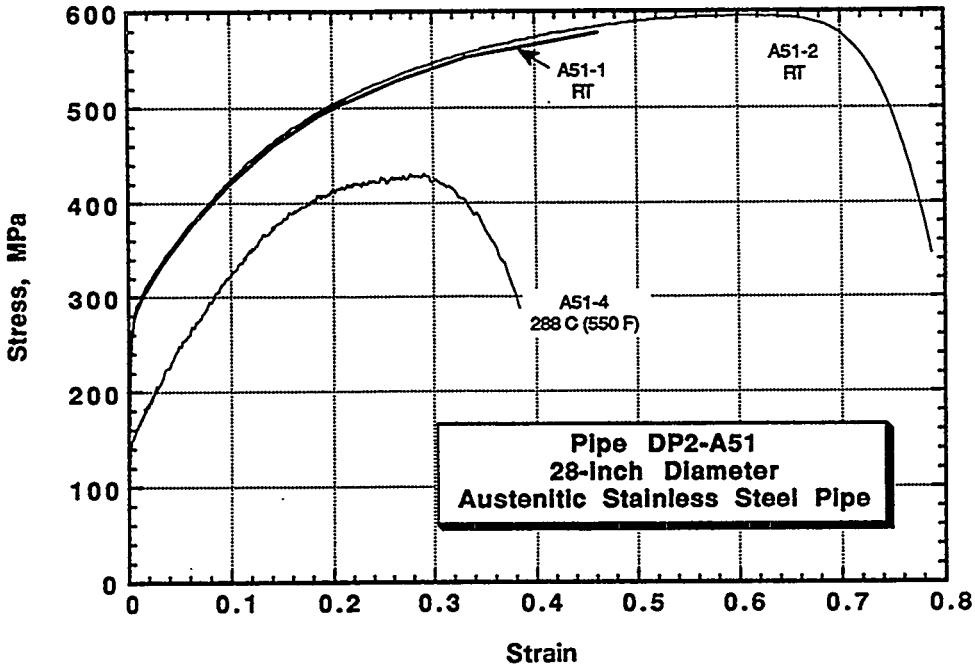

Figure 2.2 Engineering stress-strain curves for longitudinal tensile specimens machined from Pipe DP2-A51, wrought TP316L

Tensile properties for these stainless steel welds are summarized in Table 2.5. Figure 2.3 shows the engineering stress-strain curves for this material at room temperature and 288 C (550 F) and demonstrates the effect of test temperature on tensile properties for the Weld DP2-A45W2. (Note, only 288 C (550 F) tensile data were generated for Welds DP2-A45W1 and DP2-A8W4.) As can be seen in Table 2.5 and Figure 2.3 there was a decrease in strength (especially ultimate strength) and elongation with increasing test temperature. Of further note from Table 2.5 is the fact that there was significant scatter in the 288 C (550 F) tensile data from one weld to another. Of particular note is the fact that the yield strength of Weld DP2-A8W4 was 42 percent less than the yield strength for Weld DP2-A45W2.

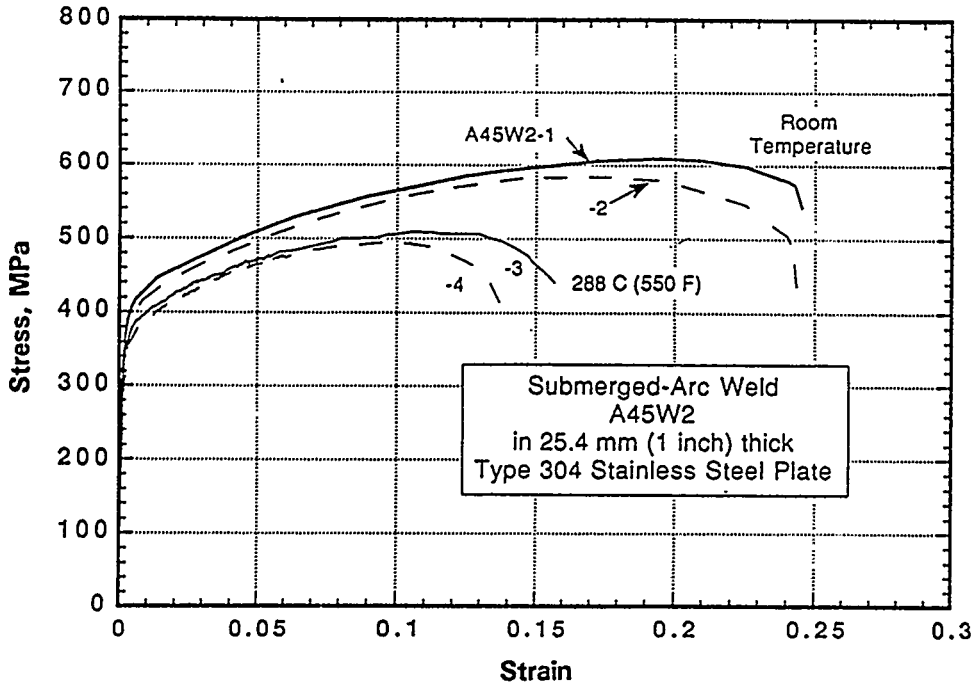

Figure 2.3 Engineering stress-strain curves for a submerged-arc weld (DP2-A45W2) in TP304 stainless steel plate (from Ref. 2.3)

Table 2.5 Summary table showing the average yield and ultimate strength values for quasi-static testing rates for Welds DP2-A45W1, DP2-A45W2, and DP2-A8W4

Weld Identification	Plate or Pipe Weld	Program which Developed Data	0.2% Offset Yield Strength, MPa (ksi)	Ultimate Tensile Strength, MPa (ksi)
A45W1	Plate	Degraded Piping (Ref. 2.3)	325 (47.1[a])	466 (67.6[a])
A45W2	Plate	Short Cracks	366 (53.1[a]) 390[b] (56.5[b])	503 (72.9[a]) 596[b] (86.4[b])
A8W4	Pipe	IPIRG-1 (Ref. 2.4)	258 (37.4[c])	469 (68.0[c])
Average			316 (45.9)	479 (69.5)

(a) Round bar tensile specimen with 19-mm (0.75-inch) gage section, which was made entirely of weld metal.
(b) Room temperature data; all other data obtained at 288 C (550 F).
(c) Flat, pin-loaded tensile specimens with a 20.3-mm (0.8-inch) gage section, which was made entirely of weld metal.

2.3.3 SA333 Grade 6 Carbon Steel and Associated Submerged-Arc Weld

Round-bar longitudinal tensile specimens were machined from a section of the SA333 Grade 6 carbon steel pipe material (DP2-F4) and used to conduct quasi-static tensile tests at 288 C (550 F). These data were developed during the course of this program.

Tensile properties for this carbon steel base metal material (DP2-F4) are summarized in Table 2.6. Figure 2.4 shows the engineering stress-strain curves for the tensile tests for this carbon steel material at 288 C (550 F). As was the case for the A515 Grade 60 carbon steel material evaluated in Experiments 1.1.1.21 and 1.1.1.25 (DP2-F26), this material did not exhibit the pronounced serrations on the stress-strain curves at this temperature/strain rate condition, which typically are indicative of dynamic strain aging.

Table 2.6 Longitudinal tensile properties of Pipe DP2-F4 (SA333 Grade 6) at 288 C (550 F)

Specimen Number	0.2% Offset Yield Strength, MPa (ksi)	Ultimate Tensile Strength, MPa (ksi)	Elongation pct. in 25.4 mm (1 inch)	Area Reduction, pct.
F4-1	234 (33.9)	521 (75.6)	28.2	66.1
F4-2	224 (32.5)	530 (76.8)	30.5	65.0
Average	229 (33.2)	525 (76.2)	29.4	65.6

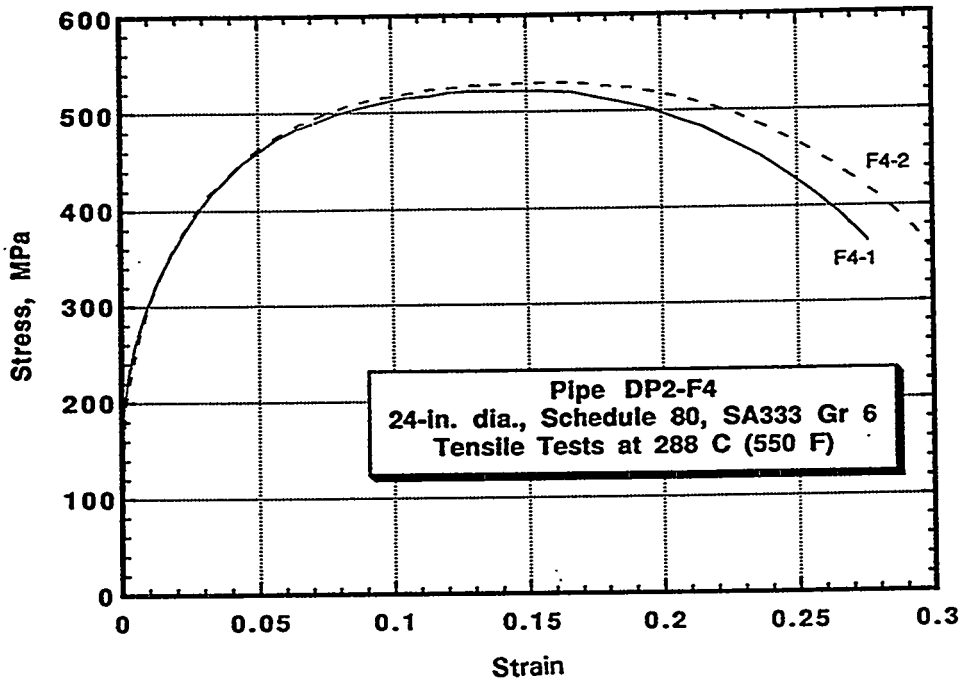

Figure 2.4 Engineering stress-strain curves for longitudinal tensile specimens machined from Pipe DP2-F4

Round-bar tensile specimens were machined from a section of a carbon steel submerged-arc weld and used for quasi-static tensile tests at room temperature and 288 C (550 F). The weld from which these tensile specimens were machined was fabricated in a 31.8-mm (1.25-inch) thick A516 Grade 70 flat plate (DP2-F49W) at the same time as the weld that was used in the pipe experiment was fabricated.

Tensile properties for this carbon steel weld are summarized in Table 2.7. Figure 2.5 shows the engineering and true stress-strain curves for this material at room temperature and 288 C (550 F) and shows the effect of test temperature on tensile properties. Note from Table 2.7 that the yield strength and fracture elongation were decreased slightly by increasing the test temperature while the ultimate strength increased slightly with increasing test temperature. This indicates the weld was susceptible to dynamic strain aging.

2.3.4 Z3 CND 18-12 Stainless Steel

Round-bar longitudinal tensile specimens were machined from a section of the Z3 CND 18-12 stainless steel pipe material (IP-A2) and subjected to quasi-static tensile tests at room temperature. The results of these longitudinal tensile tests are summarized in Table 2.8. Figure 2.6 shows the engineering stress-strain curves at room temperature from the longitudinal tensile tests for this stainless steel. These data were developed in this program.

Table 2.7 Tensile properties of submerged-arc weld metal (DP2-F49W) in 31.8-mm (1.25-inch)-thick A516 Grade 70 plate (transverse to weld)

Specimen Identification	Test Temperature, C (F)	Strain Rate, s^{-1}	0.2% Offset Yield Strength, MPa (ksi)	Ultimate Tensile Strength, MPa (ksi)	Elongation, percent in 25.4 mm (1 inch)	Area Reduction, percent
F49W-1	22 (72)	4.2×10^{-4}	447 (64.8)	554 (80.4)	20.8	62.1
F49W-2	22 (72)	4.2×10^{-4}	445 (64.5)	554 (80.3)	21.2	62.8
Average			446 (64.7)	554 (80.4)	21.0	62.5
F49W-3	288 (550)	4.0×10^{-4}	412 (59.8)	574 (83.3)	19.9	54.1
F49W-4	288 (550)	3.9×10^{-4}	417 (60.5)	576 (83.5)	17.1	48.8
Average			415 (60.2)	575 (83.4)	18.5	51.5

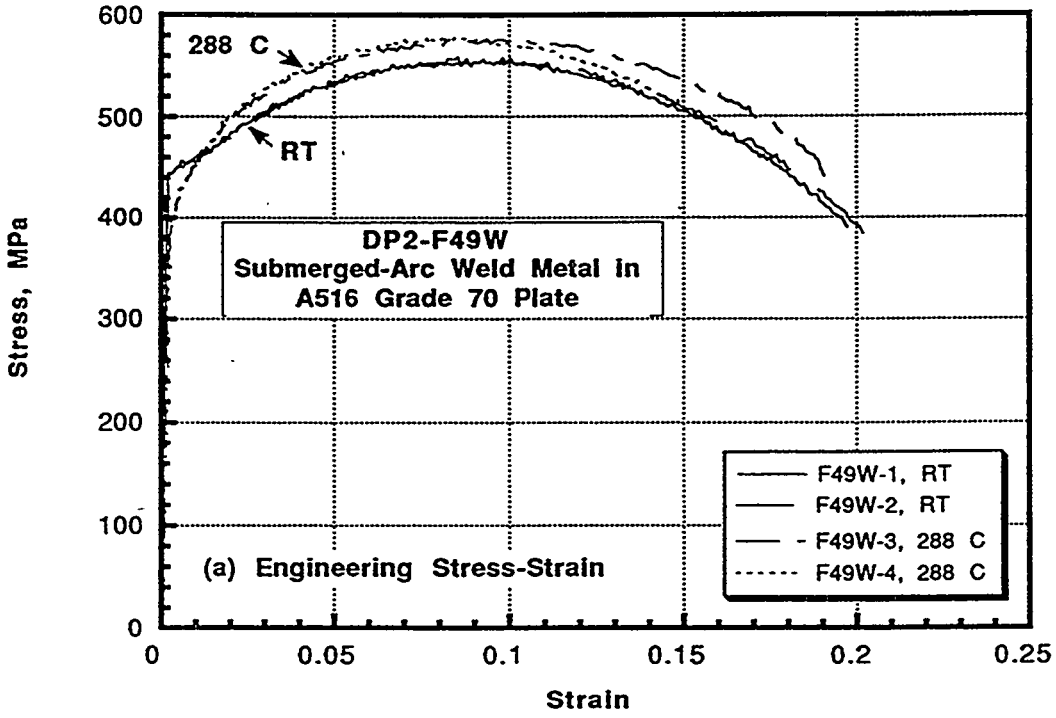

(a) Engineering stress-strain curve

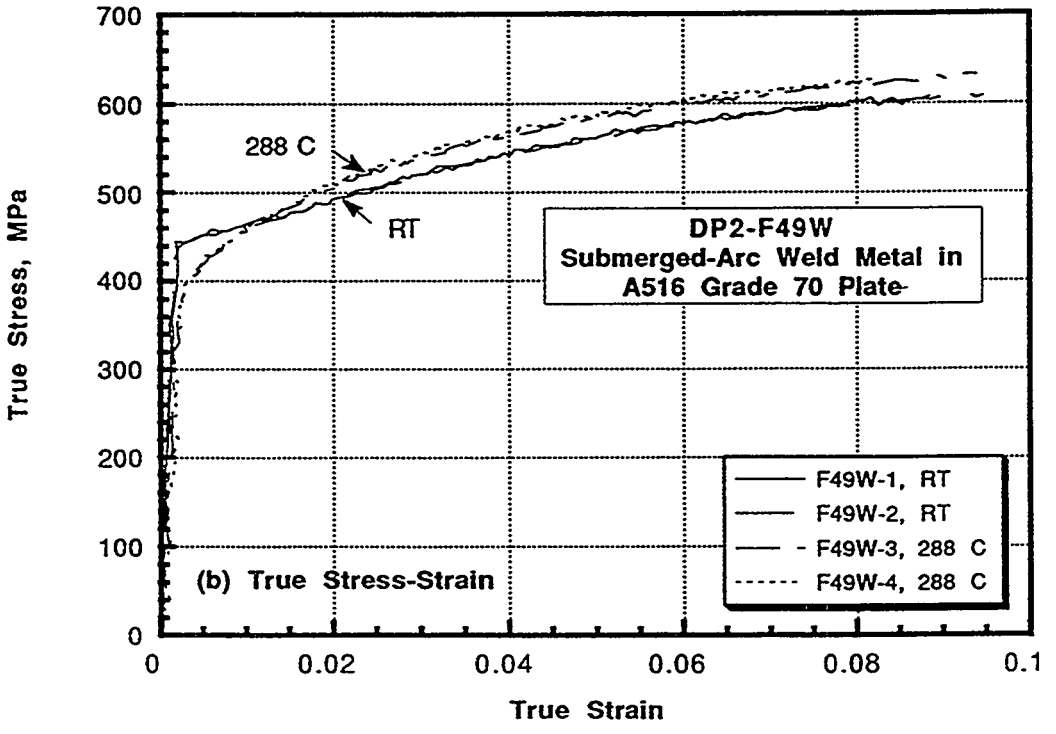

(b) True stress-strain curve

Figure 2.5 Tensile properties for carbon steel submerged-arc weld DP2-F49W

Table 2.8 Longitudinal tensile properties of Pipe IP-A2 at room temperature[a]

Specimen Identification Number	Strain Rate, s^{-1}	0.2% Offset Yield Strength, MPa (ksi)	Ultimate Tensile Strength, MPa (ksi)	Elongation, percent in 25.4 mm (1 inch)	Area Reduction, percent
IP-A2-1	1.6×10^{-3}	250 (36.2)	536 (77.7)	55	~84[b]
IP-A2-2	3.1×10^{-4}	258 (37.4)	527 (76.5)	58	~83[b]

(a) The modulus of elasticity in the direction of the pipe axis was found to be 157.5 GPa (22.84×10^6 psi) on the basis of a resonant frequency experiment. French tests confirmed this low elastic modulus.
(b) The final cross section was elliptical; the ratio of the ellipse minor axis to the ellipse major axis was approximately 0.58. The average of the two values was used in the calculation of the reduction of area.

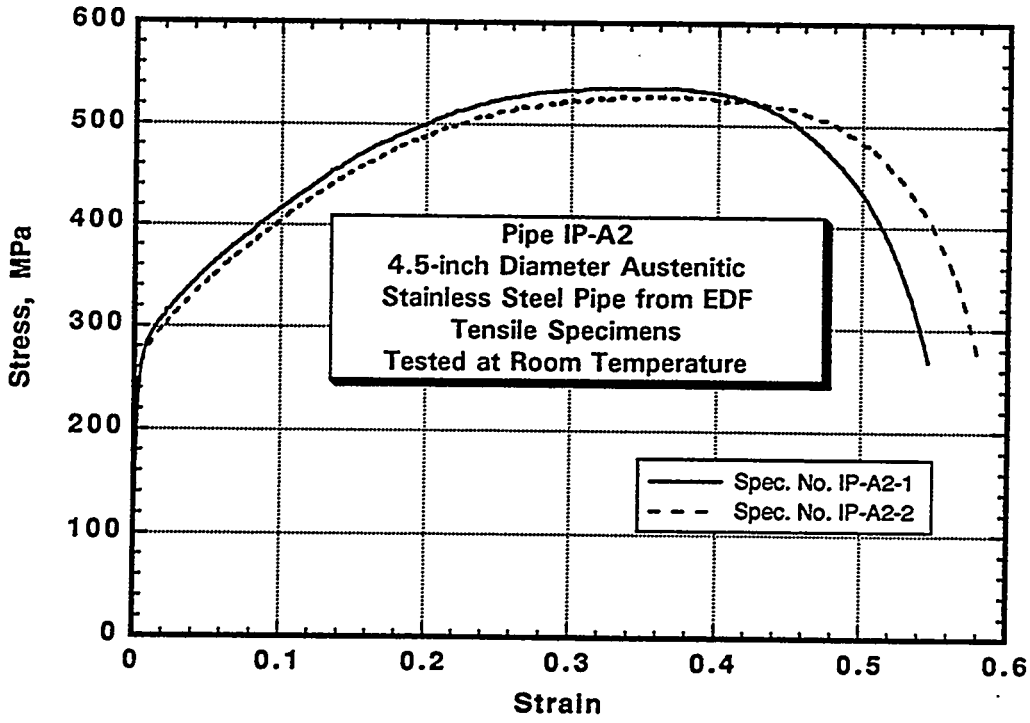

Figure 2.6 Engineering stress-strain curves for longitudinal tensile specimens machined from Pipe IP-A2

2.4 Charpy Test Results

In this section of the report, the results from a series of Charpy test on the carbon steel pipe material evaluated in Experiments 1.1.1.21 and 1.1.1.25 and the stainless and carbon steel welds evaluated in Experiments 1.1.1.23 and 1.1.1.24, respectively, are presented.

2.4.1 A155-KC60-CL1 (A515 Grade 60)

As part of a previous program (Ref. 2.1), full-size Charpy V-notch specimens were machined from Pipe DP2-F26 such that the fracture extended in the circumferential direction normal to the pipe axis (L-C orientation). Test temperatures were selected to encompass the ductile/brittle transition region. Test results are summarized in Table 2.9.

Figures 2.7 and 2.8 are plots of the above data, i.e., Charpy energy and shear area, respectively, as a function of temperature for pipe material DP2-F26.

2.4.2 Stainless Steel Submerged-Arc Weld

As part of this program, standard Charpy V-notch impact specimens were machined from the welded plate such that the crack would grow in the middle of the weld along the welding direction. Tests were conducted in duplicate at room temperature and at 288 C (550 F).

The results, shown in Table 2.10, indicated that the toughness was similar at the two temperatures but, on average, was slightly greater at 288 C (550 F) than at room temperature. This finding for an impact-loaded notched bend specimen differs from that for a quasi-statically loaded precracked compact specimen (see next section of this report). In the latter case, toughness values at 288 C (550 F) are significantly below those at room temperature.

2.4.3 Carbon Steel Submerged-Arc Weld

As part of this program, six Charpy V-notch impact specimens were machined from the weldment such that the notch was located in the center of the weld and the crack grew in the direction of the weld. Three were tested at room temperature and three at 288 C (550 F) to determine energy absorption values and the percentage of the fracture surface that exhibited shear. The results are presented in Table 2.11. On average, the specimens were tougher at 288 C than at 22 C -- 106 Joules (77.8 ft-lb) versus 77.1 Joules (56.8 ft-lb) and 100 percent shear versus 77 percent shear, respectively.

Table 2.9 Charpy V-notch impact properties for Pipe DP2-F26 (Ref. 2.1)

Temperature, C (F)	Energy, J (ft-lb)	Lateral Expansion, mm (inch)	Shear Area, percent
26 (-15)	6.8 (5)	0.183 (0.0072)	2
-9 (15)	11 (8)	0.310 (0.0122)	10
0 (32)	43 (32)	0.533 (0.0210)	20
0 (32)	95 (70)	1.75 (0.0688)	40
12 (54)	103 (76)	1.93 (0.0758)	40
13 (55)	122 (90)	2.13 (0.0838)	55
24 (75)	136 (100)	2.27 (0.0892)	60
46 (115)	157 (116)	2.38 (0.0936)	85
66 (150)	172 (127)	2.34 (0.0920)	100
100 (212)	171 (126)	2.35 (0.0926)	100

Table 2.10 Charpy V-notch impact tests on submerged-arc weld (DP2-A45W2) in TP304 stainless steel plate

Test Temperature, C (F)	Absorbed Energy, J (ft-lb)
22 (72)	56 (41)
22 (72)	62 (46)
288 (550)	64 (47)
288 (550)	67 (49.5)

Table 2.11 Charpy V-notch results for submerged-arc weld metal (DP2-F49W) in 31.8-mm (1.25-inch)-thick A516 Grade 70 plate

Test Temperature, C (F)		Absorbed Energy, J (ft-lb)		Shear Area, Percent
21 (70)		76.6 (56.5)		75
21 (70)		84.1 (62.0)		80
21 (70)		70.5 (52.0)		75
	Average	77.1 (56.8)	Average	77
288 (550)		104 (76.5)		100
288 (550)		110 (81.0)		100
288 (550)		103 (76.0)		100
	Average	106 (77.8)	Average	100

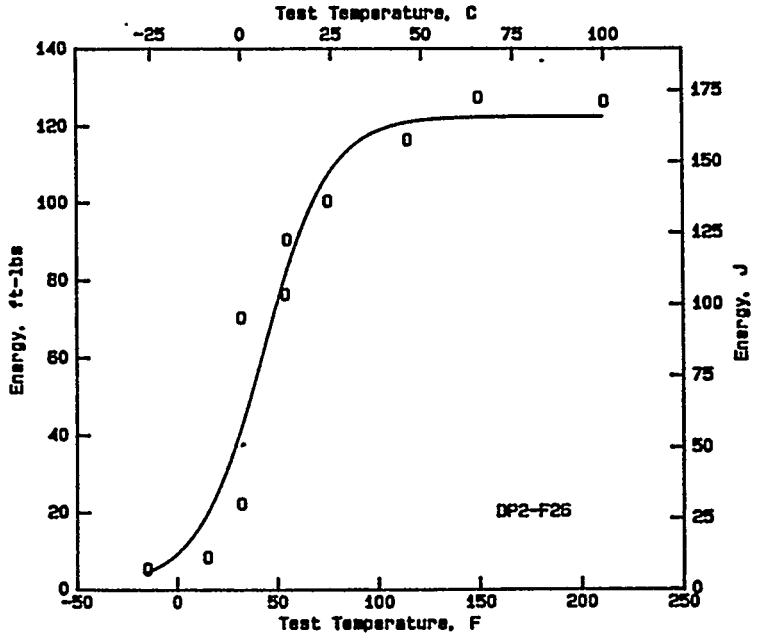

Figure 2.7 Charpy impact energy versus test temperature for Pipe Material DP2-F26 (Ref. 2.1)

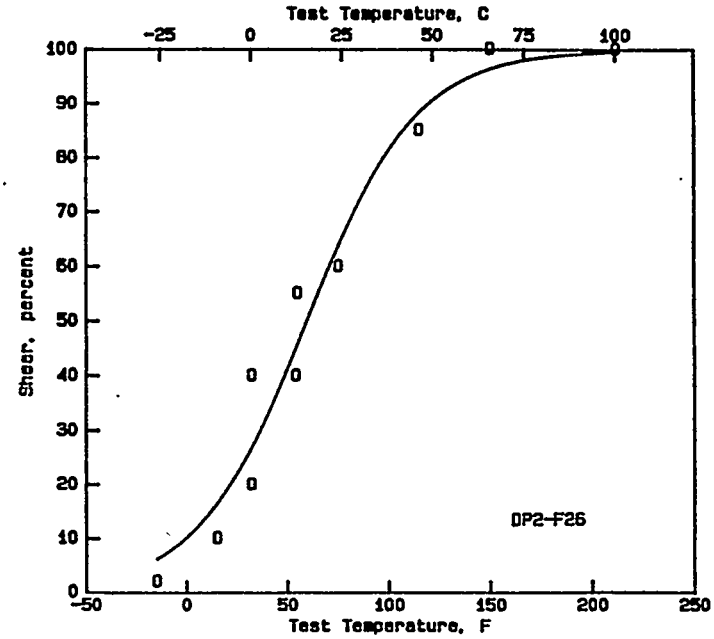

Figure 2.8 Shear area versus test temperature for Pipe Material DP2-F26 (Ref. 2.1)

2.5 J-R Curve Test Results

Summary graphs and tables of quasi-static J-R curve tests are presented in this section. All specimens were machined in the L-C orientation, which simulates growth of a circumferential through-wall crack.

Data obtained during each of these fracture toughness tests were load, P, load-line displacement, LLD, and d-c electric potential, U. The point of crack initiation, U_0, was estimated from the electric potential data. To achieve this estimate, graphs of electric potential versus load-line displacement and load versus electric potential were examined for points of slope change prior to maximum load. Engineering judgement was then applied to estimate U_0, the value of U at crack initiation. Crack growth beyond crack initiation was then calculated from the ratio U/U_0 using the Johnson expression (Ref. 2.5). Note that the term for the spacing between the voltage probes in the Johnson expression was allowed to increase in proportion to the LLD as the test progressed, because experience has shown that this procedure provides a more accurate estimate of the crack growth in highly ductile materials (Ref. 2.6).

2.5.1 A155 KC60-Class 1 (A515 Grade 60) Carbon Steel

Compact (tension) fracture toughness specimens, 1T-planform size, were machined from this carbon steel pipe material and tested at 288 C (550 F). These tests were conducted during the Degraded Piping Program--Phase II (Ref. 2.1). Specimen thicknesses were the maximum achievable from the 22.2 mm (0.875 inch) nominal wall thickness of the pipe and ranged from 19.1 to 21.1 mm (0.75 to 0.83 inch). Two different types of starting notches were employed: (a) a fatigue precrack, and (b) a sharp machined notch having a radius of about 0.13 mm (0.005 inch), introduced with a 0.20-mm (0.008-inch)-thick saw blade. The latter notch type is the same as that used in the pipe fracture experiments for this material. The initial crack (or notch) depth was such that a/W was about 0.5.

Because the initial tests at 288 C (550 F) on the fatigue-cracked and machined-notch nonside-grooved specimens produced crack growth at an angle to the intended fracture plane, duplicate specimens were side-grooved 10-percent per side prior to testing to achieve crack growth in the intended plane.

The specimens were tested at 288 C (550 F) at a displacement rate designed to cause crack initiation in about 5 to 15 minutes, similar to that required for the pipe fracture tests. The tests were terminated once the crack had extended by an amount equal to 40-60 percent of the original ligament.

In the two specimens that contained side grooves, stable crack growth was interrupted several times by small bursts of rapid ductile fracture. These were indicated by distinct steps in the load versus displacement and electric-potential versus displacement records, see Figure 2.9. The compact specimens without side grooves, on the other hand, displayed only stable crack growth. In those compact specimens that displayed bursts of rapid fracture, the fracture surface provided no obvious indications of a change in fracture mechanism when stable fracture changed to unstable fracture and back again.

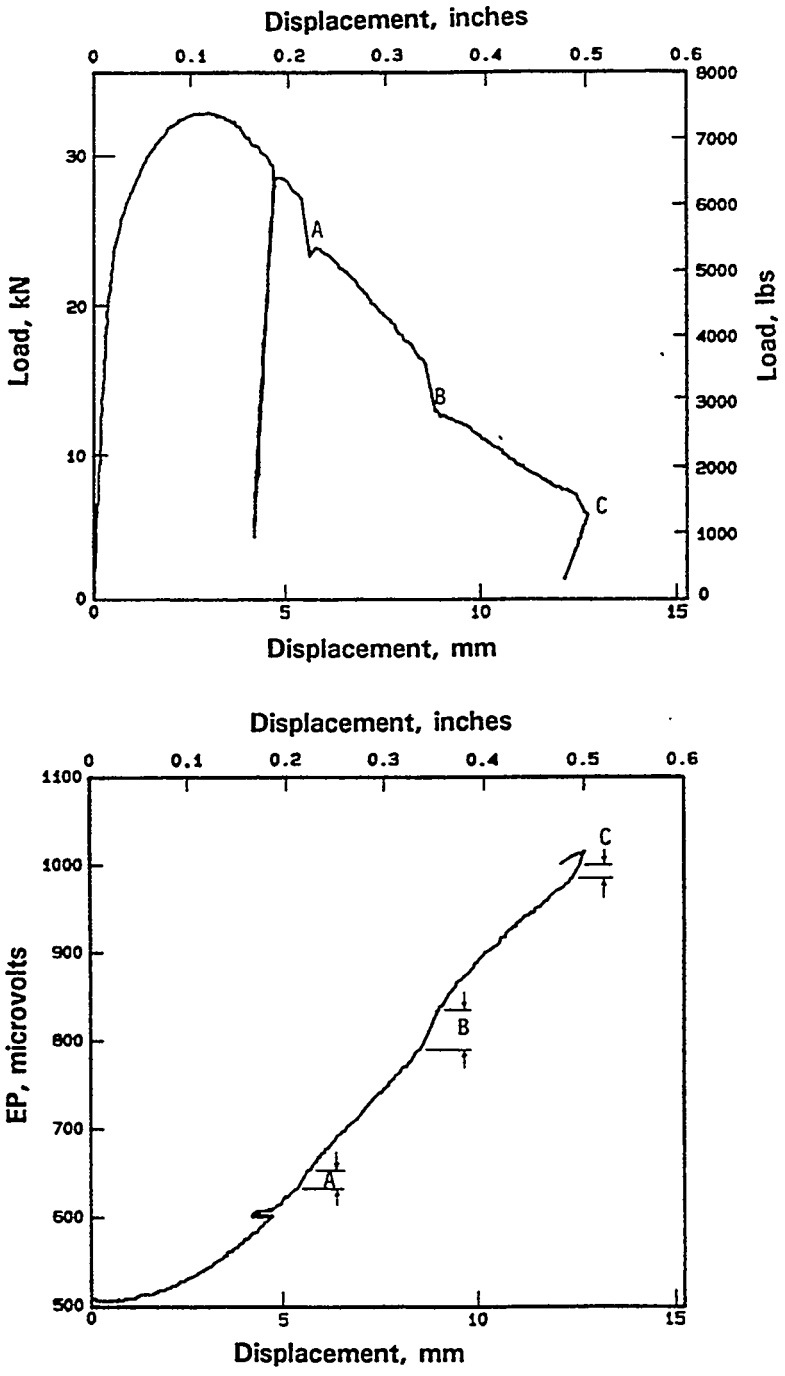

Figure 2.9 Test records for pre-cracked and side-grooved compact specimen from material DP2-F26 tested at 288 C (550 F) (Ref. 2.1)
(A, B, and C indicate points at which stable crack growth was interrupted by a crack jump. Displacement shown is at 0.25W from the load line)

Deformation J, J_D, and Modified J, J_M, were calculated for each specimen. J_D was calculated in the manner specified in ASTM E813-81 following a method developed by Ernst and Paris that takes into account crack growth, Ref. 2.7. J_M was calculated in the manner developed by Ernst, Paris, and Landes (Ref. 2.8). J-resistance curves for this material are shown in Figure 2.10 and values of J_i and dJ/da are summarized in Table 2.12. The J-R curves were terminated at the point of the first significant crack jump because there is no standard method for calculating J during and after a crack instability.

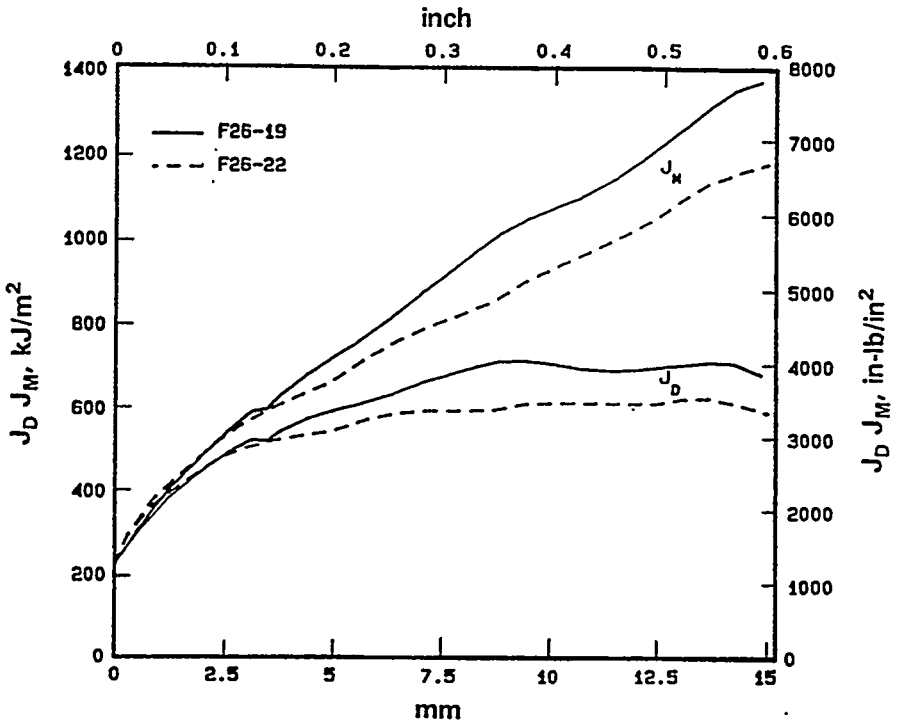

Figure 2.10 J_M-R and J_D-R curves for Pipe DP2-F26 at 288 C (550 F) (Ref. 2.1)

Table 2.12 Summary of J_i and dJ/da values for Pipe DP2-F26 at 288 C (550 F)

Specimen Number	J at Initiation, kJ/m^2 (in-lb/in^2)	dJ/da[(a)], MJ/m^3 (in-lb/in^3)
F26-17[(b)]	180.4 (1,030)	--
F26-19[(c)]	217.2 (1,240)	135 (19,500)
F26-21[(b)]	259.7 (1,483)	--
F26-22[(c)]	206.5 (1,180)	126 (18,200)
Average	216.0 (1,233)	130 (18,850)

(a) Initial slope just after crack initiation
(b) Nonside-grooved specimens
(c) Side-grooved specimens

2.5.2 Stainless Steel Submerged-Arc Weld

Compact (tension) fracture toughness specimens were machined from sections of stainless steel submerged-arc welds and tested at room temperature and 288 C (550 F). Specimens were machined and tested from three different welds made at three different times. The weld procedures for each weld were the same as used in the pipe experiment, Experiment 1.1.1.23. Two of the welds were fabricated in flat plates (DP2-A45W1 and DP2-A45W2) and one was fabricated in a section of 406.4-mm (16-inch) nominal diameter, Schedule 100, stainless steel pipe (DP2-A8W4). The A45W2 data were developed in this program, while the A45W1 data were developed in the Degraded Piping Program--Phase II (Ref. 2.3) and the A8W4 data were developed during the IPIRG-1 program (Ref. 2.4).

Compact type specimens, 1T, 3T, and 9.5T-planform size, 25.4-mm (1-inch) thick, were machined from the submerged-arc weld DP2-A45W1 and 1T-planform size specimens were machined from the other two welds. In each case the specimens were oriented such that crack growth would be along the weld centerline. Specimen thicknesses were the full thickness of the plates or the maximum achievable from the 26.1-mm (1.031-inch) nominal wall thickness of the pipe. The weld crown was left intact for the 3T and 9.5T specimens, but was ground off for the 1T specimens. The 3T and 9.5T data are given in Reference 2.9.

Two different types of starting notches were employed: (a) a fatigue precrack, and (b) a sharp machined notch having a radius of approximately 0.13 mm (0.005 inch). The fatigue cracking was carried out under the guidelines of ASTM E813-81, and the crack was grown at least 2.5 percent of the specimen width. The sharp machine notch was introduced by electric-discharge machining the slot with a 0.020-mm (0.008-inch) diameter wire. This sharp machine notch is the same notch radius as used in the pipe tests. The initial crack (or notch) depths were such that the a/W values were between 0.5 and 0.55.

The specimens were tested at a displacement rate designed to cause crack initiation in about 5 to 20 minutes, similar to that required for crack initiation in the quasi-static pipe fracture tests.

The crack path in the 1T compact specimens was typically along the weld centerline and was accompanied by a modest amount of thickness reduction at the crack plane. The crack front on the root side (TIG weld-region) lagged behind that on the crown side (SAW).

Deformation J, J_D, and Modified J, J_M were calculated for each specimen. J_D was calculated in the manner specified in ASTM E813-81 following a method developed by Ernst and Paris that takes into account crack growth (Ref. 2.7). J_M was calculated in the manner developed by Ernst, Paris, and Landes (Ref. 2.8). In calculating both J_D and J_M, no account was taken of the thinning of the specimen ahead of the crack or of the thickening at the back edge. J-resistance curves for each of the three stainless steel submerged-arc welds tested are shown in Figures 2.11 through 2.13. Values of J_i and dJ/da for each weld are summarized in Table 2.13. Both Figure 2.12 (Weld DP2-A45W2) and Table 2.13 show the marked effect of test temperature on the fracture resistance of the weld metal, with or without side grooves present. At 288 C (550 F), both J_i and dJ/da were approximately only half of their values at room temperature. Differences between side-grooved and nonside-grooved specimens were relatively small.

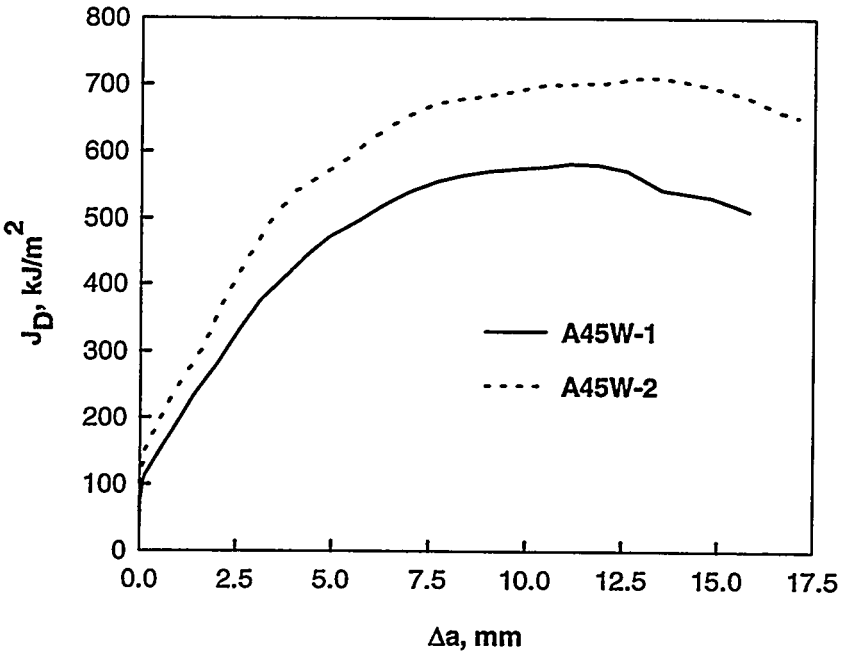

(a) Fatigue-precracked compact specimens

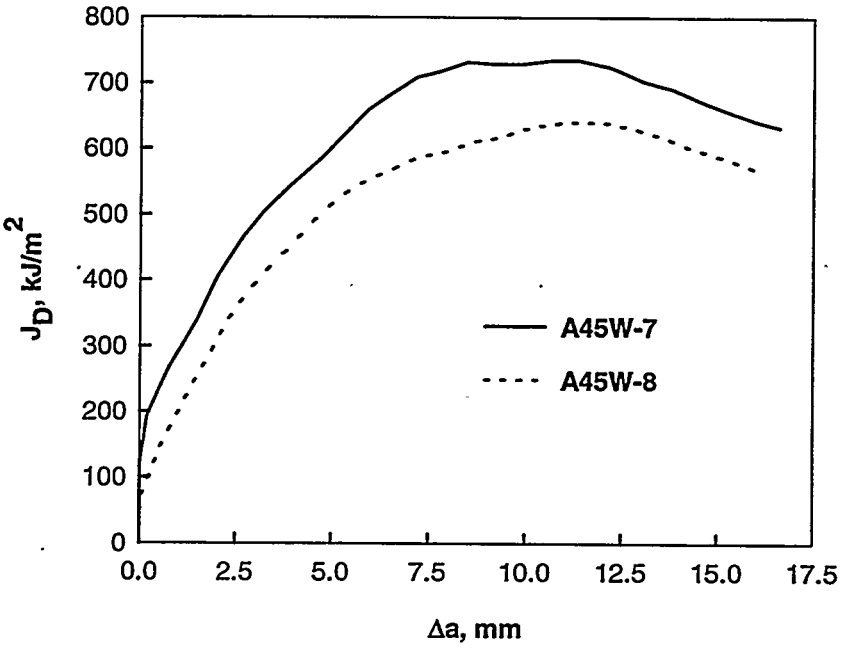

(b) Sharp-notched compact specimens

Figure 2.11 J_D-resistance curves for stainless steel SAW (DP2-A45W1) 1T specimens tested at 288 C (550 F)

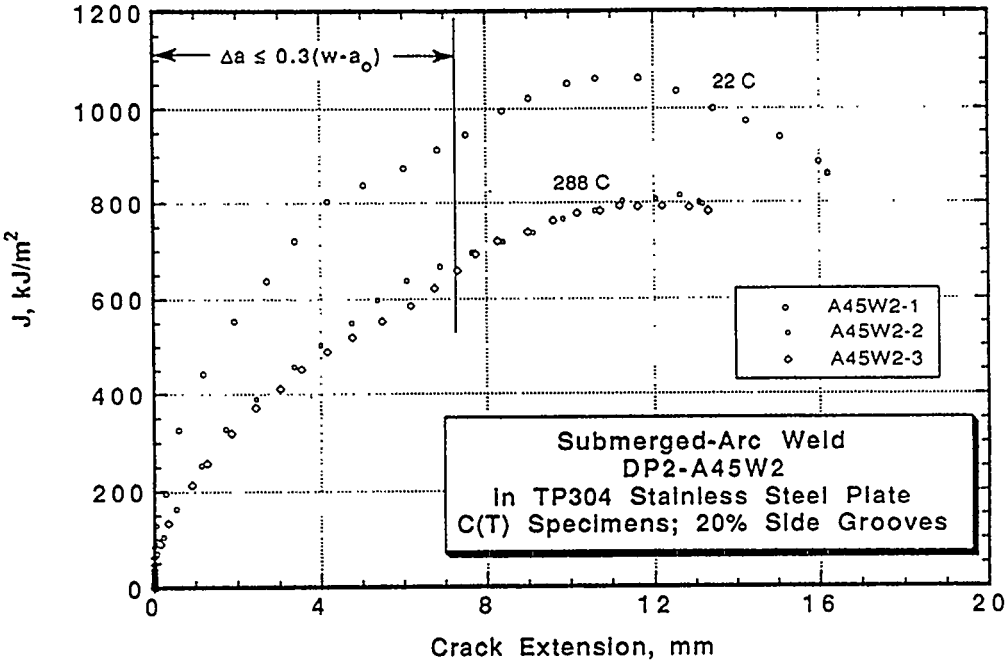

(a) 20-percent-side-groove compact specimens

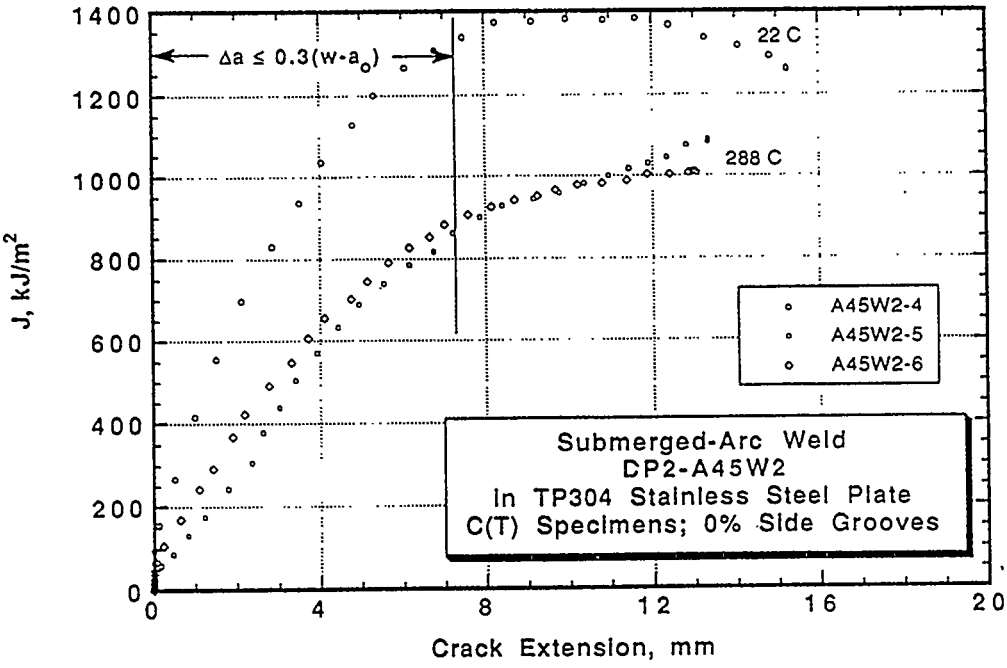

(b) Non-side-grooved compact specimens

Figure 2.12 J_D-resistance curves for submerged-arc weld (DP2-A45W2)

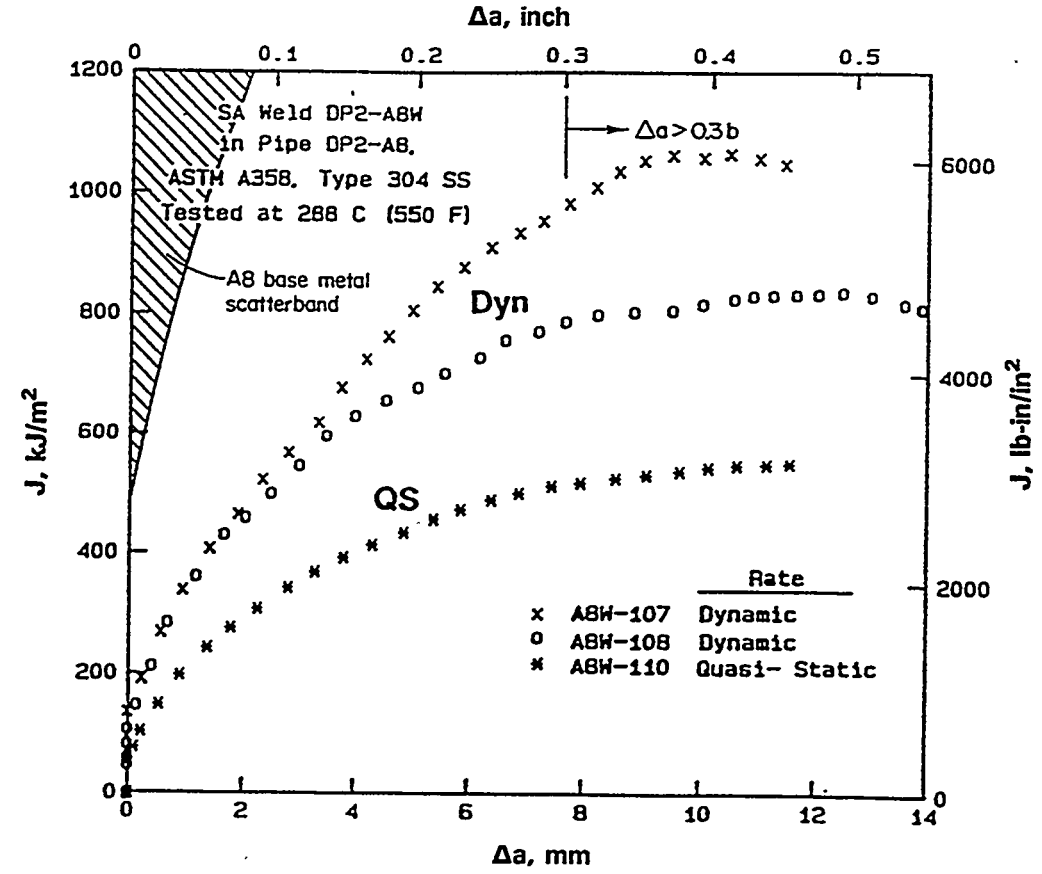

Figure 2.13 J_D-resistance curves at 288 C (550 F) for compact specimens from a submerged-arc weld (DP2-A8W4) in a 406.4-mm (16-inch) diameter TP304 stainless steel pipe

2.5.3 Carbon Steel Submerged-Arc Weld

Six 1.25T-planform-size compact (tension) fracture toughness specimens were machined from this carbon steel submerged-arc weld (DP2-F49W). Four were side grooved to a depth of 10-percent per side, two of which were tested at 22 C (72 F) and two at 288 C (550 F). The remaining two specimens were tested without side grooves at 288 C (550 F). Specimens were oriented such that crack growth would be along the weld centerline in the direction of the weld. The weld from which these compact (tension) specimens were machined was fabricated in a flat plate at the same time as the weld used in the pipe experiment was fabricated.

The specimens were fatigue precracked according to the specifications in ASTM E1152-87, Standard Test Method for Determining J-R Curves, to produce an initial average crack length of about 0.53W.

Table 2.13 Summary tables showing the average J_i and dJ/da values for quasi-static rates for Welds DP2-A45W1, DP2-A45W2, and DP2-A8W4

Weld Identification	Plate or Pipe Weld	Program which Developed Data	J_i, kJ/m^2 (in-lb/in^2)	dJ/da,[a] MJ/m^3 (in-lb/in^3)
A45W1	Plate	Degraded Piping (Ref. 2.3)	108[b] (616[b])	109 (15,800)
A45W2	Plate	Short Cracks	59.7[c] (341[c]) 47.3[d] (270[d]) 114[c,e] (649[c,e]) 106[d,e] (605[d,e])	160 (23,250) 147 (21,350) 334 (48,400) 289 (41,900)
A8W4	Pipe	IPIRG-1 (Ref. 2.4)	55.2[c] (315)[c]	135 (19,550)
		Average of 288 C data	67.5 (385)	139 (19,990)

(a) Using data from initial portion of J-R curve from 0.15-mm (0.006-inch) $< \Delta a <$ 1.5-mm (0.060-inch).
(b) Data from fatigue precracked nonside-grooved 1T C(T) specimens. (Note this value is an average value of two specimens. There were also 3T and 9.5T specimens tested with the same thickness. See NUREG/CR-4575, Table 3.1).
(c) Data from fatigue precracked 20-percent side-grooved specimens.
(d) Data from fatigue precracked nonside-grooved specimens.
(e) Room temperature data; all other data obtained at 288 C (550 F).

The specimens were tested in displacement control. The crosshead speed was 0.635 mm/min (0.025 inch/min) to cause crack initiation in approximately 4 to 7 minutes. Each high temperature test was terminated when the crack had extended by an amount equal to 40 to 55 percent of the original ligament. In the tests conducted at room temperature, the C(T) specimens showed only a small amount of stable crack growth before undergoing rapid, unstable cleavage fracture. Unstable fracture in these room temperature tests occurred at the maximum load.

The procedures used to calculate J values from each compact-specimen test were those specified in ASTM E1152-87, Standard Test Method of Determining J-R Curves. In addition, values of Modified J (J_M) were calculated, following the procedures outlined by Ernst, Ref. 2.8. J-resistance curves from these six compact-specimen tests are shown in Figure 2.14 and values of J_i and dJ/da are summarized in Table 2.14.

2.5.4 French Z3 CND 18-12 (TP316L) Stainless Steel

Three 0.5T-planform-size compact type specimens (10.2-mm [0.4-inch] thick) were machined from this stainless steel pipe (Battelle Pipe Number IP-A2) for the purpose of conducting J-resistance tests at room temperature. Specimen thicknesses were the maximum achievable from the wall thickness of the pipe. No side grooves were employed in these tests. These data were developed in this program.

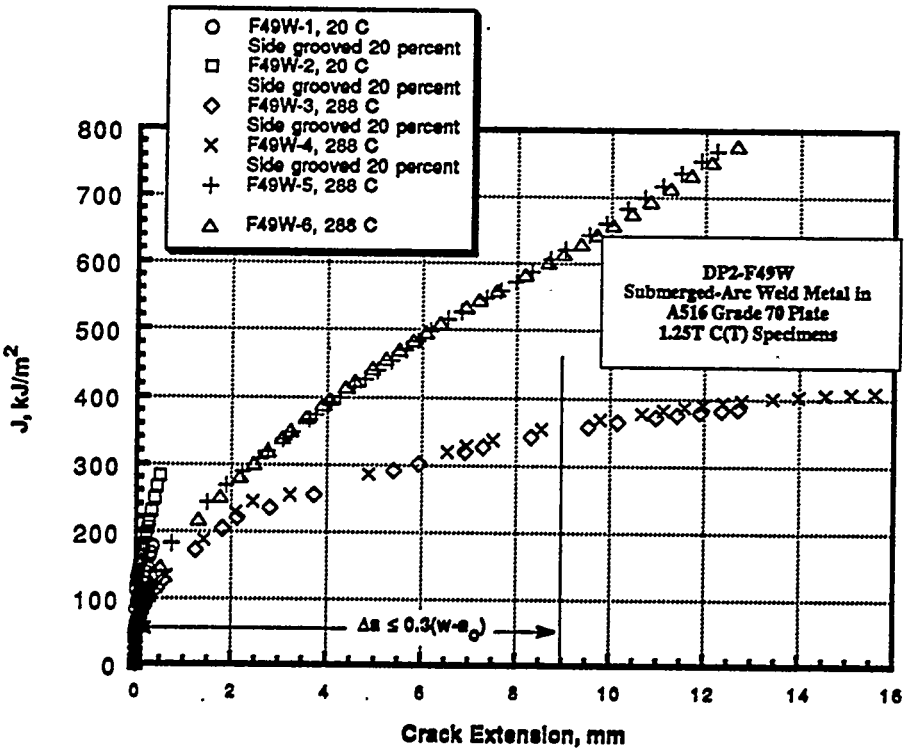

Figure 2.14 Composite plot of J_D-resistance curves for Series DP2-F49W tests (20 C [68 F] tests failed in cleavage after ductile crack growth)

Table 2.14 Summary of J_i and dJ/da values obtained from compact specimens machined from Weld DP2-F49W

Specimen Identification Number	Test Temperature, C (F)	J_i, kJ/m^2 (in-lb/in^2)	dJ/da[(a)], MJ/m^3 (in-lb/in^3)
F49W-1	22 (72)	84 (479)	256[(b)] (37,125)
F49W-2	22 (72)	117 (665)	316[(b)] (45,830)
Average		101 (572)	286 (41,480)
F49W-4	288 (550)	53 (303)	65 (9,430)
F49W-4	288 (550)	59 (336)	65 (9,430)
Average		56 (320)	65 (9,430)
F49W-5[(c)]	288 (550)	55 (315)	93 (13,490)
F49W-6[(c)]	288 (550)	62 (356)	93 (13,490)
Average		59 (336)	93 (13,490)

(a) Linear fit of J-R curve for crack growth of 0.15-mm (0.006-inch) to 1.5-mm (0.060-inch).
(b) Stable crack growth less than 1.5-mm (0.06-inch).
(c) Nonside-grooved; other specimens were side grooved 20 percent.

The specimens were fatigue precracked according to the specifications in ASTM E1152-87 to produce an initial average crack length of approximately 14.02 mm (0.55 inch). Specimens were tested at room temperature in displacement control at a crosshead speed of 1.25 mm/min (0.05 inch/min). The tests were terminated when the crack had extended by an amount equal to 60 to 65 percent of the original ligament.

Each of the three specimens exhibited very extensive crack tip blunting and thickness reduction (necking) prior to the extension of the fatigue crack. A photograph of one of the tested specimens is shown in Figure 2.15. Thickness reductions were approximately 50 to 55 percent of the original specimen thickness.

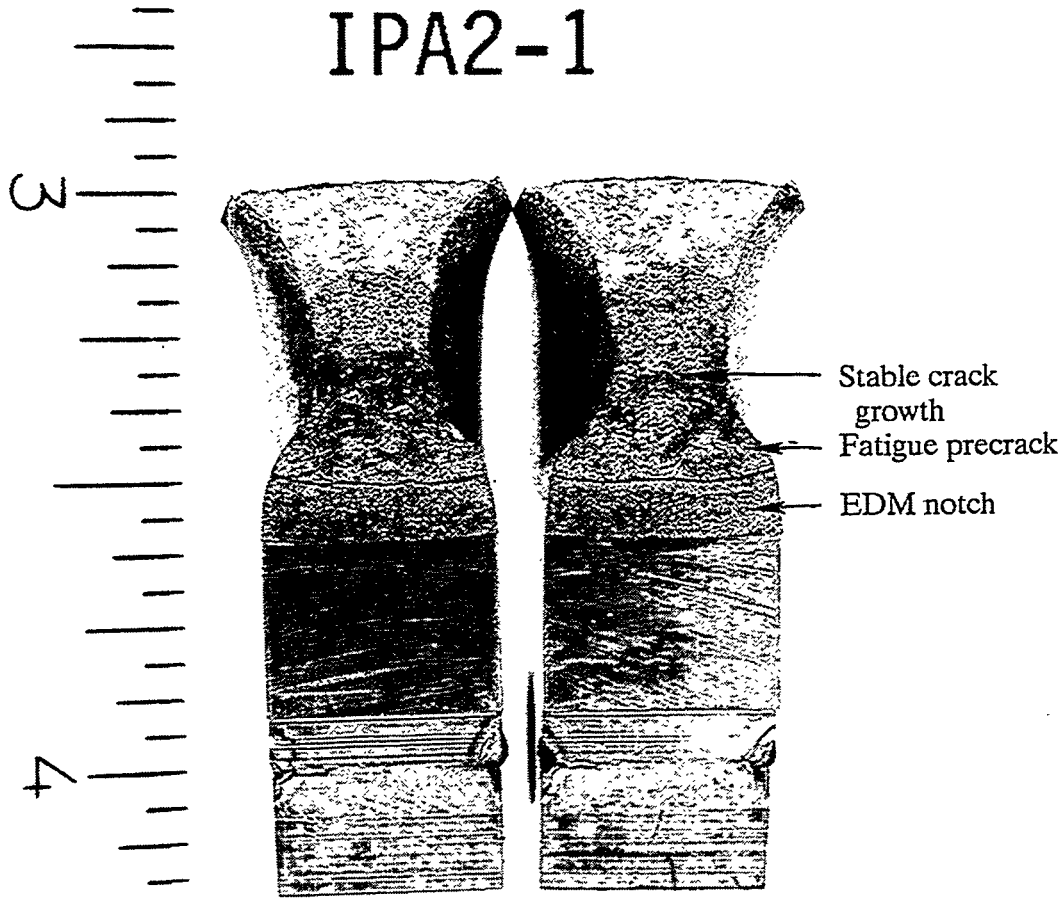

Figure 2.15 Fracture surfaces of C(T) Specimen IPA2-1, illustrating extensive thickness reduction during stable crack growth (scale in inches)

The procedures used to calculate J values from each compact-specimen test were those specified in ASTM E1152-87, Standard Test Method for Determining J-R Curves. In addition, values of Modified J, J_M, were calculated following the procedures outlined by Ernst, Ref. 2.8. J-resistance curves from these three compact-specimen tests are shown in Figure 2.16 and values of J_i and dJ/da are summarized in Table 2.15.

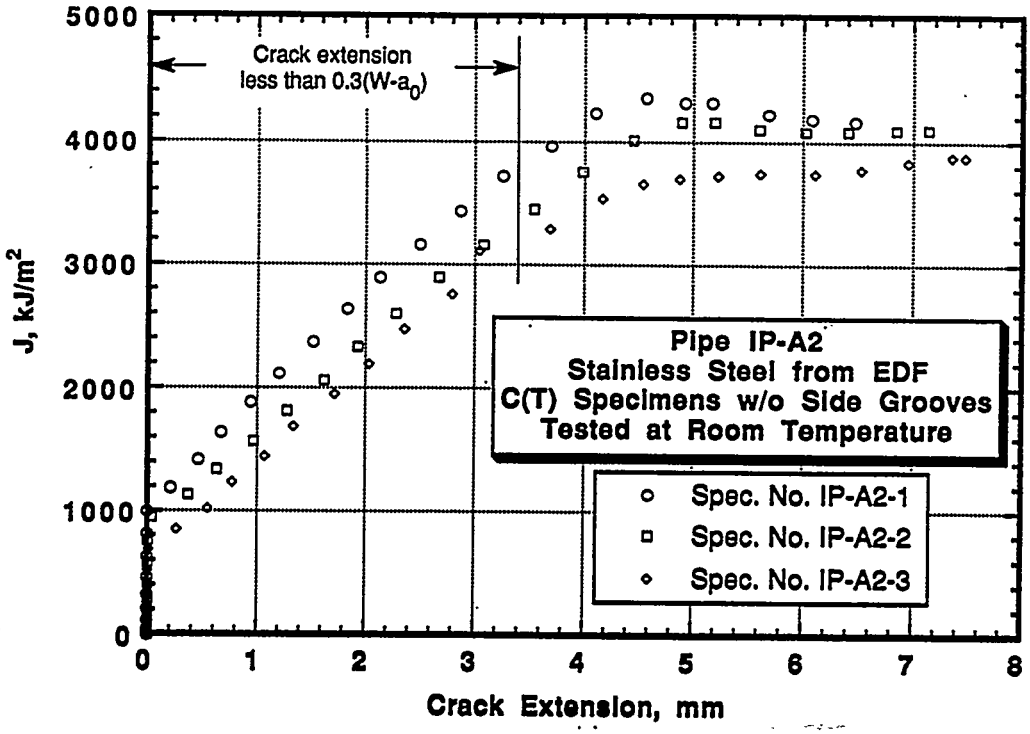

Figure 2.16 J_D-resistance curves for compact specimens machined from French TP316L stainless steel pipe (Pipe IP-A2) in the L-C orientation (w/o = without)

Table 2.15 Summary of J_i and dJ/da values for Pipe IP-A2 obtained from compact specimens tested at room temperature

L-C orientation; no side grooves		
Specimen Identification Number	J at Initiation, kJ/m^2 (in-lb/in^2)	dJ/da[(a)], MJ/m^3 (in-lb/in^3)
IP-A2-1	1,050 (6,000)	903 (131,000)
IP-A2-2	910 (5,195)	703 (102,000)
IP-A2-3	680 (3,865)	758 (110,000)
Average	880 (5,020)	788 (114,300)

(a) From initial slope of J-R curve after crack initiation.

2.6 References

2.1 Wilkowski, G. M., and others, "Degraded Piping Program - Phase II," Summary of Technical Results and Their Significance to Leak-Before-Break and In-Service Flaw Acceptance Criteria, March 1984-January 1989, by Battelle Columbus Division, NUREG/CR-4082, Vol. 8, March 1989.

2.2 Marschall, C. W., Mohan, R., Krishnaswamy, P., and Wilkowski, G. M., "Effect of Dynamic Strain Aging on the Strength and Toughness of Nuclear Ferritic Piping at LWR Temperatures," NUREG/CR-6226, October 1994.

2.3 Wilkowski, G. M., and others, "Analysis of Experiments on Stainless Steel Flux Welds," NUREG/CR-4878, April 1987.

2.4 Marschall, C. W., Landow, M. P. and Wilkowski, G. M., "Loading Rate Effects on Strength and Fracture Toughness of Pipe Steels Used in Task 1 of the IPIRG Program," NUREG/CR-6098, October 1993.

2.5 Schwalbe, K. and Hellmann, D., "Application of the Electric Potential Method to Crack Length Measurements Using Johnson's Formula," *Journal of Testing and Evaluation*, Vol. 9, No. 3, pp. 218-221, May 1981.

2.6 Marschall, C. W., Held, P. R., Landow, M. P., and Mincer, P. N., "Use of the Direct-Current Electric Potential Method to Monitor Large Amounts of Crack Growth in Highly Ductile Metals," *Fracture Mechanics: Twenty-First Symposium, ASTM STP 1074*, J. P. Gudas, J. A. Joyce, and E. M. Hackett, Eds., American Society for Testing and Materials, Philadelphia, pp. 581-593, 1990.

2.7 Ernst, H. A. and Paris, P. C., "Techniques of Analysis of Load-Displacement Records by J-Integral Method," U.S. Nuclear Regulatory Commission, Report NUREG/CR-1122, January 1980.

2.8 Ernst, H. A., Paris, P. C., and Landes, J. D., "Estimation of the J-Integral and Tearing Modulus T from Single Specimen Test Record," *Fracture Mechanics - 13th Conference, ASTM STP 743*, R. Roberts, ed., American Society for Testing and Materials, pp. 476-502, 1981.

2.9 Papaspyropoulos, V., Marschall, C., and Landow, M., "Predicting of J-R Curves With Large Crack Growth From Small Specimen Data," NUREG/CR-4575, September 1986.

3. PIPE EXPERIMENTS

During the Degraded Piping Program - Phase II (Ref. 3.1), six large-diameter [greater than 711-mm (28-inch diameter)] through-wall-cracked pipe experiments were conducted, see Table 3.1. There were also eight relatively small diameter (406.4-mm [16-inch] diameter and smaller) through-wall-cracked pipe experiments conducted as part of that program. In each case, the through-wall-crack length was relatively long, approximately 37 percent of the pipe circumference. In addition to these Degraded Piping Program data, there were over 25 small diameter relatively long through-wall-cracked pipe experiments conducted as part of an EPRI program at Battelle (Ref. 3.2) and two USNRC programs conducted at David Taylor Research Center (DTRC) (Refs. 3.3 and 3.4). Test conditions, experimental results, and material property data for each of these long through-wall crack experiments are included in the circumferentially cracked pipe fracture database, CIRCUMCK.WK1, compiled as part of Task 8 of this program (Ref. 3.5.) What is lacking in this database is through-wall-cracked large-diameter-pipe fracture data for shorter crack lengths. There was a single small diameter, stainless steel, short through-wall-cracked pipe experiment conducted as part of the Battelle/EPRI program (Ref. 3.2). However, for this small diameter, high toughness pipe experiment (Experiment 4T), limit-load conditions would undoubtedly prevail. Consequently, prior to this program there was a definite void in the pipe fracture database for short through-wall-cracked pipe experiments for which elastic-plastic conditions would exist. The test matrix for this program was designed to address this need.

Table 3.1 Large diameter long-through-wall-cracked pipe experiments conducted as part of the Degraded Piping Program (Ref. 3.1)

Experiment Number	Outside Pipe Diameter, mm (inch)	Wall Thickness, mm (inch)	Material	Crack Length, % circumference	Test Temperature, C (F)
4111-2	711 (28.0)	22.8 (0.930)	A515 Gr. 60	37.0	288 (550)
4111-3	1,067 (42.0)	7.11 (0.280)	TP304	37.0	7 (45)
4111-4	1,067 (42.0)	15.9 (0.625)	API-5LX65	37.0	-7 (20)
4111-5	720 (28.33)	30.2 (1.89)	TP316 SMAW	37.0	288 (550)
4111-6	910 (35.83)	72.8 (2.868)	A516 Gr. 70	37.0	288 (550)
4141-7	933 (36.73)	86.6 (3.410)	A516 Gr. 70 SAW	37.0	288 (550)

3.1 Test Matrix

The test matrix of short through-wall-cracked pipe experiments for this program is shown in Table 3.2. The test matrix contains five experiments. The first three experiments listed in Table 3.2 (Experiments 1.1.1.21, 1.1.1.23, and 1.1.1.24) were large-diameter short-through-wall-cracked pipe experiments. The mean pipe radius-to-thickness ratio, R_m/t, for these experiments ranged from 9 to

15. The initial through-wall-crack length for the two 711-mm (28-inch) diameter experiments was 140 mm (5.5 inches). This corresponds to a normalized crack length of 6.25 percent of the pipe circumference. The initial crack length for the 610-mm (24-inch) diameter experiment was 152 mm (6.0 inches). This corresponds to a normalized crack length of 7.9 percent of the pipe circumference. These crack lengths are typical of those used in large-diameter pipe leak-before-break (LBB) analyses. The pipe materials were chosen so that elastic-plastic conditions would prevail. The materials used for these experiments were a carbon steel base metal (1.1.1.21), a stainless steel submerged-arc weld (1.1.1.23), and a carbon steel submerged-arc weld (1.1.1.24). Consequently, since the pipe diameters were relatively large and the material toughnesses were relatively low, elastic-plastic conditions should prevail. The test temperature for each experiment was 288 C (550 F). Each test specimen was unpressurized.

Table 3.2 Test matrix of pipe experiments from Task 1 of the Short Cracks in Piping and Piping Welds Program

Expt. Number	Battelle Pipe Identification Number	Nominal Pipe Diameter, mm (inch)	Wall Thickness, mm (inch)	Material	Crack Length, % Circumference	Test Temperature, C (F)
1.1.1.21	DP2-F26	711 (28)	22.7 (0.893)	A515 Gr. 60	6.25	288 (550)
1.1.1.23	DP2-A51	711 (28)	30.2 (1.19)	TP316L SAW	6.25	288 (550)
1.1.1.24	DP2-F4	610 (24)	31.3 (1.239)	SA333 Gr. 6 SAW	7.9	288 (550)
1.1.1.25	DP2-F26	711 (28)	24.0 (0.945)	A515 Gr. 60	0.0	288 (550)
1.1.1.26	IP-A2	102 (4)	8.3 (0.327)	Z3 CND18-12 (TP 316L)	24.4	20 (70)

The fourth experiment listed in Table 3.2 was a 711-mm (28-inch) diameter carbon steel base metal uncracked-pipe experiment (Experiment 1.1.1.25). The objective of this experiment was to provide experimental data for the validation of an elastic-plastic uncracked-pipe analysis that was used to calculate the uncracked-pipe moment-rotation response for the rest of the test specimens used in the Short Cracks pipe experiments. The uncracked-pipe moment-rotation response for these experiments was needed so that the uncracked-pipe moment-rotation response could be separated from the overall moment-rotation response for the cracked pipe to get the moment-rotation response due solely to the crack. In the long through-wall-cracked pipe experiments conducted previously, all of the plasticity was localized at the crack section. However, in the case of the short cracks of interest to this program, the applied loads required to cause the through-wall cracks to initiate and grow were high enough to cause plastic deformations in the pipe away from the crack section. This plasticity significantly complicated the uncracked-pipe analysis. The data from Experiment 1.1.1.25 were used to validate this uncracked-pipe analysis method. The test temperature for this uncracked-pipe experiment was 288 C (550 F). The test specimen was unpressurized.

The fifth experiment listed in Table 3.2 was a small diameter stainless steel through-wall-cracked pipe experiment (Experiment 1.1.1.26). This experiment was not included in the original test matrix. The specific objective of this experiment was to compare results from one of Battelle's experimental pipe

test facilities with those from a pipe test facility in France. Électricité de France (EDF) conducted a series of stainless steel through-wall-cracked pipe experiments on 101.6-mm (4-inch) nominal diameter pipe. Two experiments of specific interest to this effort were EDF Experiment Numbers 5 and 24.

The reason for conducting this experiment was to clarify discrepancies observed between FEM analyses and experimental data. In the IPIRG-1 program, it was found that there was excellent agreement between finite element predictions and experimental results for EDF Experiment Number 5 (Ref. 3.6). However, for another stainless steel through-wall-cracked experiment conducted during the IPIRG-1 program at Battelle, the finite element results underpredicted the experimental initiation load by 30 percent. For both the EDF and IPIRG-1 experiments, several finite element analyses were conducted by different organizations. The finite element results were in good agreement with each other, but not necessarily with the experimental results (Ref. 3.7). Hence, it was decided to conduct a replicate experiment to one of the EDF experiments to see if experimental differences could be the cause of the disagreement with finite element results. Unfortunately, there was no extra material from the pipe used in EDF Experiment Number 5 that could be used for this comparison experiment. However, there was extra material left over from EDF Experiment Number 24. Consequently, it was decided to use a section of pipe from the ends of the moment arms for EDF Experiment Number 24 and test it in the same pipe bend facility as used in the IPIRG experiment.

The test conditions for Experiment 1.1.1.26 were chosen to match those for EDF Experiment Number 24 as closely as possible. The test specimen was machined to match the diameter and wall thickness used in the EDF experiment. The initial through-wall-crack length was about 25 percent of the pipe circumference for both experiments. The test temperature for both experiments was 22 C (72 F). Neither test specimen was pressurized.

3.2 Test Specimen Materials

Four different materials were evaluated in the five pipe experiments. The Battelle material identification numbers for each of these materials is included in the test matrix in Table 3.2. The chemical composition, tensile properties, and fracture toughness values for these pipe materials were reported in Section 2 of this report.

3.2.1 DP2-F26

DP2-F26 is a seam-welded 711-mm (28-inch) diameter by 22.2-mm (0.875-inch) nominal wall thickness A155-KC60 Class 1 carbon steel pipe. The pipe was fabricated from A515 Grade 60 plate. The pipe was obtained from the excess pipe inventory from a nuclear power plant. The pipe would have been used as part of the main steam-line piping system in the plant. The specific heat number for this section of pipe is 60719. For Experiment 1.1.1.21 the crack was located in the base metal. There was no crack in Experiment 1.1.1.25. A long through-wall-cracked pipe experiment (Experiment 4111-2) was conducted using this same pipe material as part of the Degraded Piping Program--Phase II (Ref. 3.1).

3.2.2 DP2-A51

Pipe DP2-A51 is a longitudinally seam welded 711-mm (28-inch) nominal diameter by 30.2-mm (1.19-inch) wall thickness SA-240 TP316L stainless steel pipe. The pipe was obtained from the excess pipe inventory from the Nine Mile Point Nuclear Power Plant. The pipe would have been used as part of the main recirculation line piping system in this plant. The crack was located in a shop-fabricated submerged-arc weld (SAW). The same weld procedure was used to fabricate a number of similar stainless steel submerged-arc welds as part of the Degraded Piping and IPIRG programs. Note, as part of the Degraded Piping Program a long through-wall-crack pipe experiment was conducted on a section of 711-mm (28-inch) diameter by 30.2-mm (1.19-inch) wall thickness SA-240 TP316 stainless steel pipe (Experiment 4111-5). The crack in that experiment was located in a shielded-metal-arc weld (SMAW) in a section of the recirculation line which had been removed from service from the Nine Mile Point Plant.

3.2.3 DP2-F24

Pipe DP2-F24 is a longitudinally seam-welded 610-mm (24-inch) nominal diameter Schedule 80 SA-333 Grade 6 carbon steel pipe. The pipe was obtained from the excess pipe inventory of a nuclear power plant. The crack was located in the center of a shop fabricated submerged-arc weld. The weld wire was a high-manganese, high-molybdenum wire carrying the designations EA3 and SFA 5.23. The flux was Linde 80. The procedure was obtained from Babcock and Wilcox (B&W) as being typical of the procedures used by B&W in the construction of the Midland nuclear power plant and 90 percent of welds in their other plants.

3.2.4 IP-A2

Pipe IP-A2 is a seamless 101.6-mm (4-inch) nominal diameter, Schedule 160 stainless steel pipe, with a French designation of Z3 CND 18-12. This is equivalent to TP316L stainless steel. Note, however, that the presence of nitrogen and particles that appear to be titanium carbonitride suggest that the pipe material may be TP316LN, rather than TP316L stainless steel. The length of pipe was obtained from EDF in France from the Pipe Specimen Number 24.

3.3 Experimental Facilities

Battelle's large pipe bend facility at West Jefferson, Ohio, was used for the three large diameter short through-wall-cracked pipe experiments and the uncracked-pipe experiment, see Figure 3.1. The strongback for this facility is a large welded double-web beam 15.25 m (50 feet) long, 2.75 meters (9 feet) wide, and 2.0 meters (6.5 feet) high. The strongback is equipped with two hydraulic rams, each with a load capacity of 2.0 MN (450,000 lbs) at 20.7 MPa (3,000 psi) pressure, and a stroke capacity of 1.22 meters (48 inches). The spacing between the hydraulic rams (i.e., the inner span) is 3.35 meters (11 feet). The test pipes were held down at the ends by a series of wire ropes. The spacing between the wire ropes (i.e., outer span) was 11.6 meters (38 feet). A series of rollers on top of the rams allowed the test pipes to rotate and translate as they were being loaded in bending.

Battelle's 580 kN (130 kip) MTS servo-hydraulic load frame in Battelle's fatigue laboratory was the test frame used for the 101.6-mm (4-inch) diameter stainless steel through-wall-cracked pipe experiment, see Figure 3.2. The roller assemblies shown in Figure 3.2 allowed the pipe to rotate and translate as it was being loaded in bending. The inner and outer spans for this facility were 610 mm (24 inches) and 1,524 mm (60 inches), respectively.

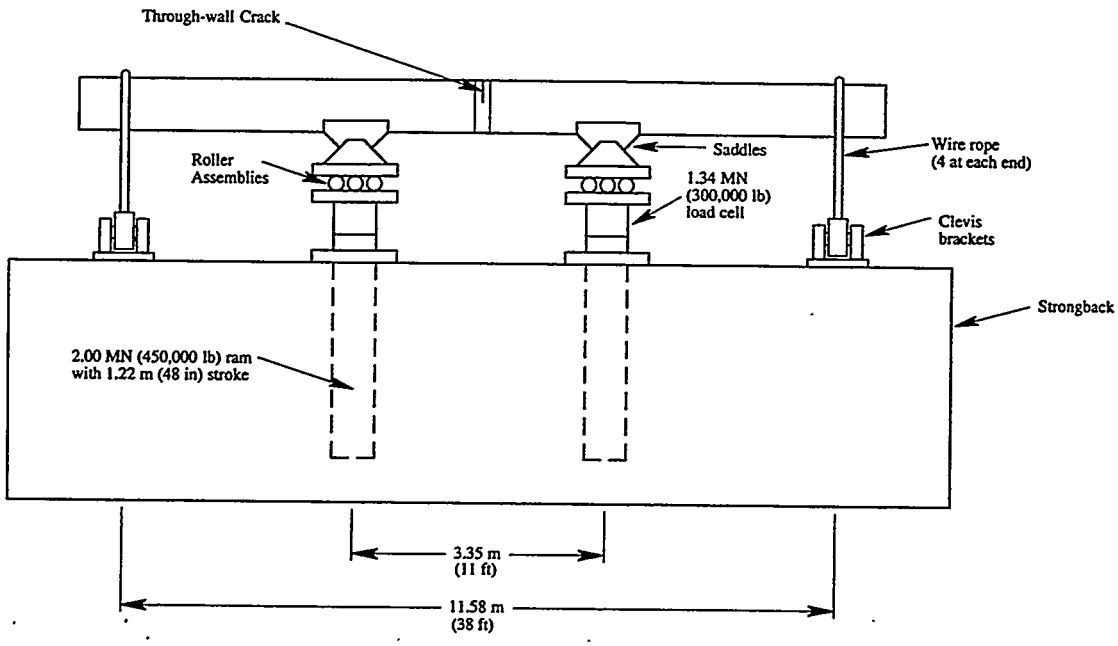

Figure 3.1 Schematic of pipe in large pipe bend facility

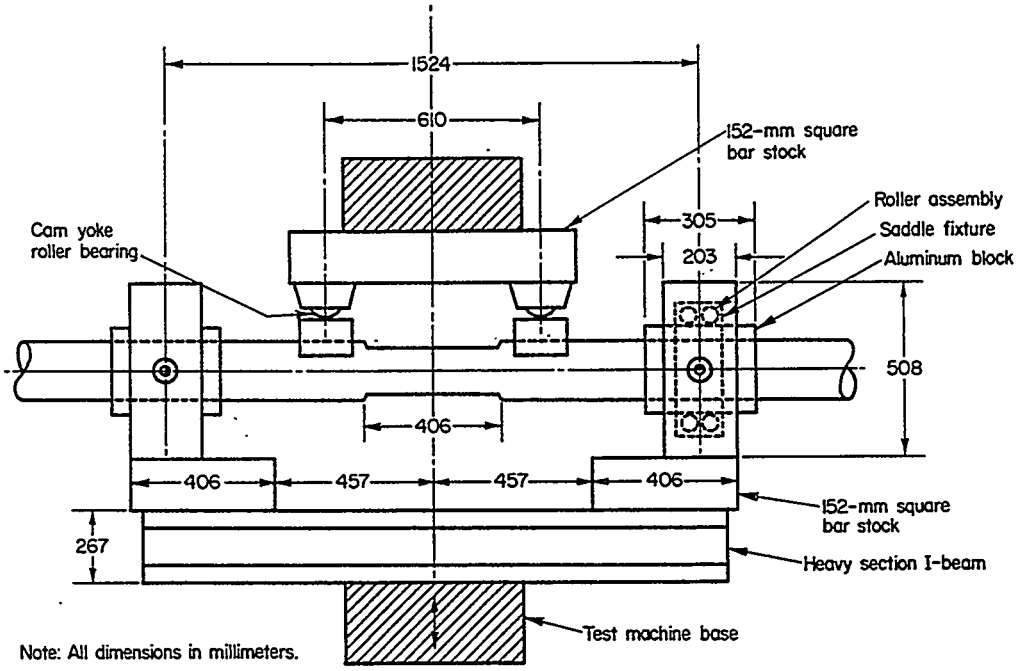

Figure 3.2 Schematic of test apparatus used in Experiment 1.1.1.26

3.4 Instrumentation and Data Acquisition

The instrumentation scheme for the three large diameter through-wall-cracked pipe experiments was very similar. The data collected during each of these experiments consisted of:

- The applied load at each actuator using Lebeau 1,335 kN (300 kip) compression only load cells in series with each load train.
- The displacement of each actuator using Temposonics displacement transducers.
- The direct-current electric potential (d-c EP) at the center of the crack, at each crack tip, and a reference base metal potential reading.
- The crack-mouth-opening displacement (CMOD) at the crack centerline, at each crack tip, and at a location halfway between the center of the crack and one of the crack tips. The CMOD data were obtained using clip gages.
- The rotation of the pipe on either side of the crack plane using inclinometers.

- The vertical displacements of the pipe relative to the outer load points at the crack plane, 0.61 meters (24 inches) on either side of the crack plane, and 1.68 meters (66 inches) on either side of the crack plane. These displacement measurements were made using a series of string potentiometers. From these displacements, the rotation of the pipe could be determined at these locations along the length of the pipe.

- The ovalization at the crack plane. Note, for Experiments 1.1.1.21 and 1.1.1.23, ovalization data were also collected at a location 336 mm (14 inches) east of the crack plane. These ovalization measurements were made using a series of string potentiometers.

- The pipe temperature at several locations on the pipe surface.

For the uncracked-pipe experiment the crack-mouth-opening displacement and electric-potential data were obviously not collected; however, strains at the top and bottom of the pipe on both the inside and outside surfaces and the strain in the pipe at the neutral axis on the outside surface were recorded. Both longitudinal and circumferential strains were recorded at the top and bottom of the pipe. Only longitudinal strains were recorded at the neutral axis.

For the 101.6-mm (4-inch) diameter stainless steel comparison experiment, the data collected were very similar to those collected for the three large diameter short through-wall-cracked pipe experiments. The major difference being that in some cases different instrumentation schemes were used to collect the data. For example, the rotation data were acquired using an LVDT based device instead of inclinometers. In addition, no crack-mouth-opening displacement data halfway between the crack centerline and one crack tip, no relative pipe displacements, and no ovalization data were acquired.

For all five experiments the data were acquired with an IBM-PC compatible computer with Metrabyte® DAS-8, 8-channel, high speed A/D converters and Metrabyte® EXP-16 expansion multiplexer/conditioners. The computer collected data at 12-bit resolution using LabTech Notebook data acquisition and control software.

3.5 Experimental Procedures

Once the test pipe was placed in the loading fixture, and the final instrumentation calibration checks completed, it was heated to 288 C (550 F). The pipe was brought to temperature using a series of flexible heater tapes wound helically along the length of the pipe. The pipe was covered in fiberglass insulation prior to testing to reduce heat loss. Figure 3.3 shows a pre-test photograph of Experiment 1.1.1.21 in the load frame.

After the pipe temperature had stabilized at the test temperature for at least 60 minutes, bending loads were applied to the pipe at quasi-static loading rates. The loading rates for the large-diameter experiments conducted in the large pipe bend facility at West Jefferson were in the range of 1 to 15 mm/second (0.04 to 0.6 inches/second). The loading rate for the 101.6-mm (4-inch) diameter pipe experiment conducted in the 580-kN (130-kip) fatigue machine was 0.05 mm/second (0.002 inch/second). The machined notches were fatigue precracked only in Experiment 1.1.1.26.

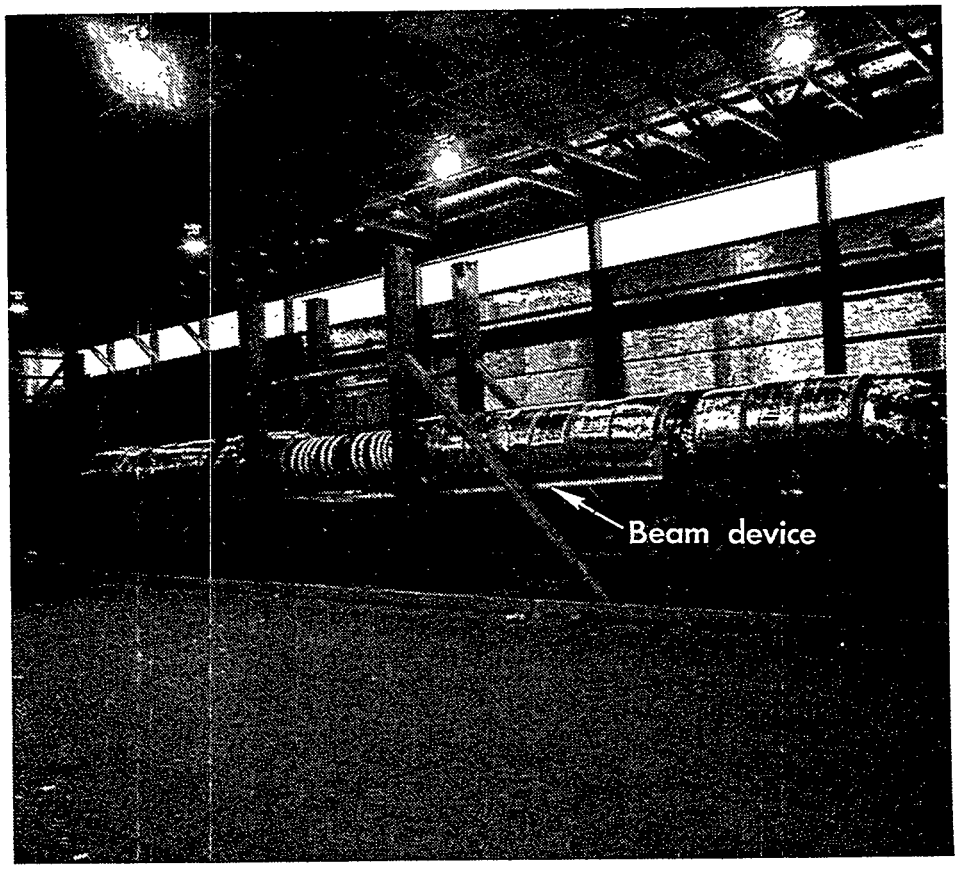

Figure 3.3 A pre-test photograph of Experiment 1.1.1.21 showing the beam device attached to the pipe which is used to calculate rotations

3.6 Experimental Results

Table 3.3 presents the key results from the five pipe experiments conducted as part of this effort. Table 3.3 includes the pertinent pipe and crack dimensions, material data, and applied moments at crack initiation and maximum load.

3.6.1 Moment-Rotation Response

Figures 3.4 through 3.6 are graphs of the applied crack section moment as a function of crack rotation for the three large-diameter through-wall-cracked pipe experiments, i.e., Experiments 1.1.1.21, 1.1.1.23, and 1.1.1.24. Of note from Figure 3.4 is the presence of 22 small drops in moment in the moment-rotation curve for Experiment 1.1.1.21. These drops in moment are associated with small crack instabilities that occurred during the course of the experiment. Crack instabilities similar to these also occurred in the companion, long through-wall-cracked pipe experiment conducted as part of the Degraded Piping Program (Experiment 4111-2) and are attributed to the dynamic strain aging sensitivity of the carbon steel pipe. The length of the crack jumps were comparable in both experiments, i.e., less than 50 mm (2 inches).

Table 3.3 Key results from pipe experiments from Task 1 of the Short Cracks in Piping and Piping Welds Program

Experiment Number	Outside Diameter, mm (inch)	Wall Thickness, mm (inch)	R_m/t	Material	$2c/\pi D$	Yield Strength, MPa (ksi)	Ultimate Strength, MPa(ksi)	J_i, kJ/m^2 (in-lb/in^2)	Moment at Crack Initiation, kN-m (in-kips)	Maximum Moment, kN-m (in-kips)
1.1.1.21	711 (28.0)	22.7 (0.893)	15.2	A515 Gr. 60	0.0625	231 (33.5)	544 (78.9)	216 (1,233)	2,565 (22,700)	3,015 (26,690)
1.1.1.23	711 (28.0)	30.2 (1.19)	11.3	TP316L SAW	0.0625	143 (20.8) 366 (53.1)	427 (62.0) 503 (72.9)	— 59.5 (341)	2,620 (23,190)	3,062 (27,100)
1.1.1.24	612 (24.1)	31.3 (1.23)	9.3	SA-333 Gr. 6 SAW	0.079	229 (33.2) 415 (60.2)	525 (76.2) 575 (83.4)	— 56.0 (320)	2,284 (20,210)	3,416 (30,230)
1.1.1.25	711 (28.0)	24.0 (0.945)	14.3	A515 Gr. 60	0.0	231 (33.5)	544 (78.9)	216 (1,233)	—	4,632 (40,990)
1.1.1.26	106 (4.183)	8.3 (0.327)	5.9	Z3 CND 18-12	0.244	254 (36.8)	532 (77.1)	880 (5,020)	16.57 (146.7)	17.11 (151.4)

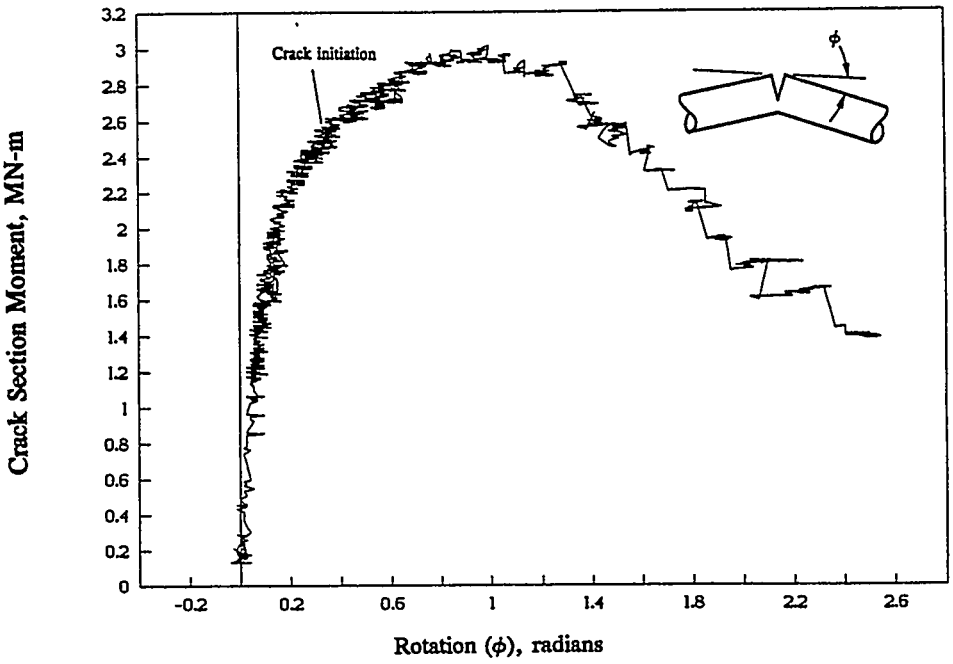

Figure 3.4 Moment versus half rotation based on the inclinometers for Experiment 1.1.1.21

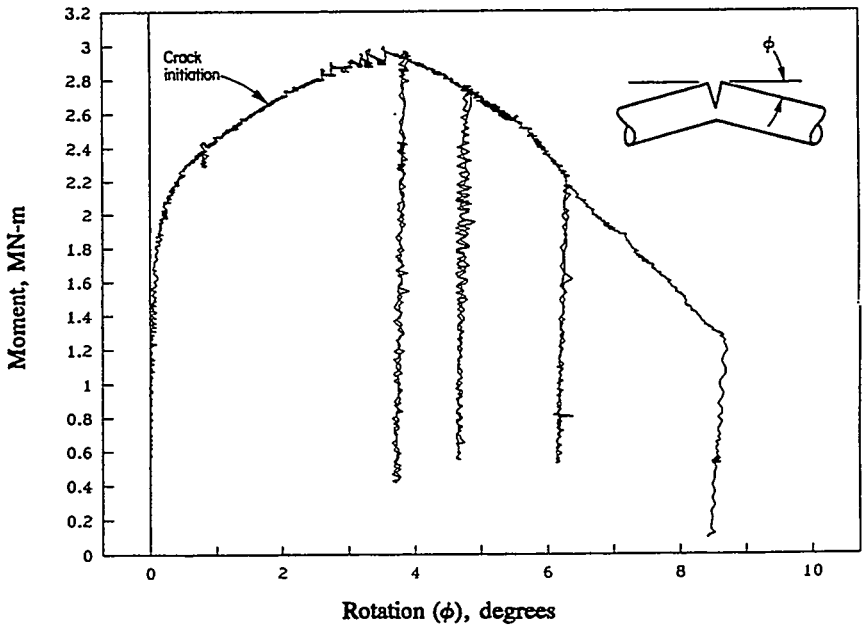

Figure 3.5 Moment versus half rotation based on the inclinometers for Experiment 1.1.1.23

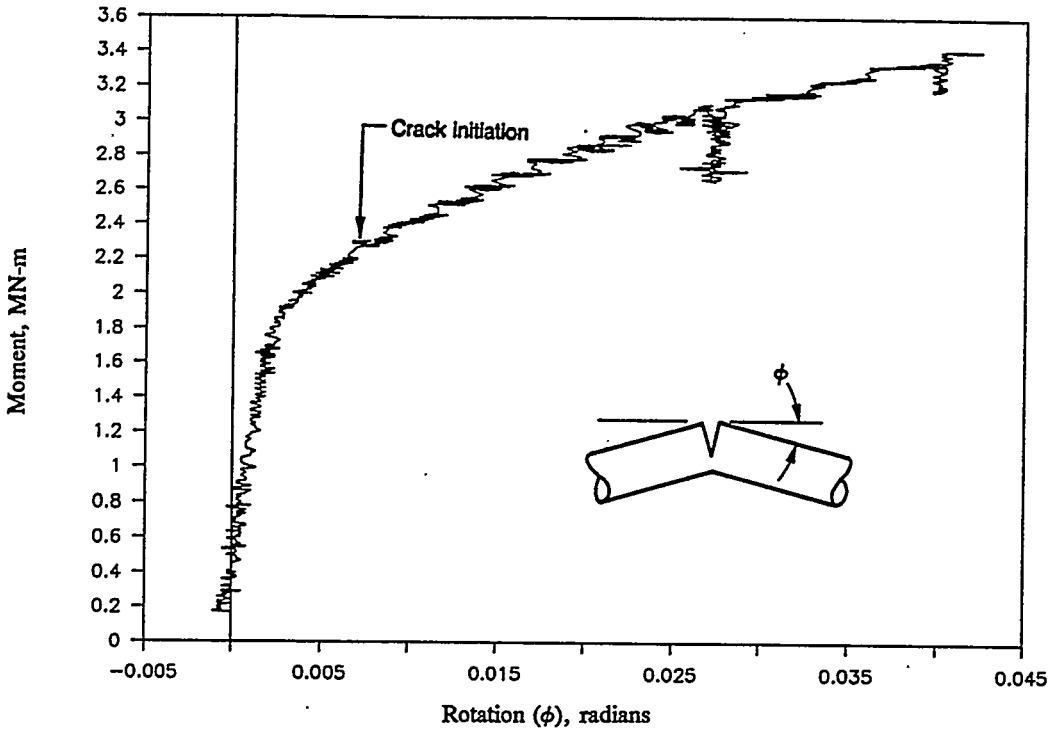

Figure 3.6 Crack section moment versus crack section half rotation (ϕ) for Experiment 1.1.1.24

Figure 3.7 is a plot of the applied crack section moment as a function of the crack section rotation for the 711-mm (28-inch) diameter uncracked pipe experiment. Included on Figure 3.7 are the moment-rotation responses from Experiments 1.1.1.21 and 4111-2 (i.e., the long through-wall-cracked pipe experiment from the Degraded Piping Program, Ref. 3.1). As noted previously, the test specimens for each of these experiments came from the same length of pipe. As can be seen in Figure 3.7, the presence of a through-wall crack 6.25 percent of the pipe circumference in length had a very significant effect on the load-carrying capacity of this pipe. The maximum moment for this short through-wall-cracked pipe experiment was only 65 percent of the maximum moment from the uncracked-pipe experiment. The rotations at maximum load were also reduced significantly. The rotation at maximum load for the uncracked-pipe experiment was 5.3 degrees while the rotation at maximum load for the short through-wall-cracked pipe experiment was only 1.0 degree. Part of this difference is due to the fact that the wall thickness at the crack plane for the cracked-pipe experiment was slightly less than that for the uncracked pipe experiment, 22.7 mm (0.893 inch) versus 24.0 mm (0.945 inch). However, as will be shown in Section 4 of this report, the maximum moment from this uncracked-pipe experiment approached the maximum moment one would expect to obtain based on a limit-load analysis; whereas the maximum moment from the short-cracked-pipe experiment was significantly below what one would expect based on a limit-load analysis, i.e., the short-cracked-pipe specimen failed in the elastic-plastic regime.

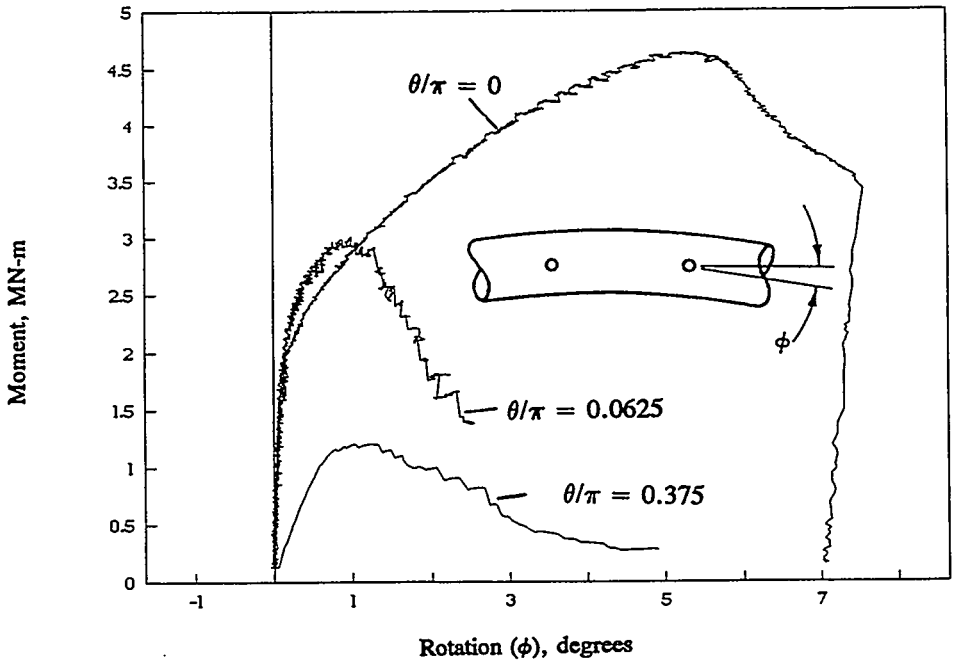

Figure 3.7 Moment versus half rotation (ϕ) for Experiments 1.1.1.25 (θ/π=0), 1.1.1.21 (θ/π=0.0625), and 4111-2 (θ/π=0.375)

From Figure 3.7 one can also see the effect of crack length on the moment-carrying capacity of this section of pipe. The maximum moment for the long-cracked-pipe experiment (4111-2) was only 40 percent of the maximum moment for the short-cracked-pipe experiment (1.1.1.21). In Section 4 of this report the effect of crack length will be discussed further.

Figure 3.8 is a plot of the moment-rotation response for the 101.6-mm (4-inch) nominal diameter stainless steel pipe experiment. Included in Figure 3.8 is a line showing the maximum moment from EDF Experiment Number 24. As can be seen, the maximum moments for the two experiments are comparable. Furthermore, when one takes into consideration the small differences in pipe and crack dimensions by normalizing the results to the Net-Section-Collapse analysis predictions, the agreement between maximum loads of the two experiments is within 3.6 percent. This difference is within the $\pm$5 percent repeatability of identical pipe experiments previously conducted at Battelle.

3.6.2 Pipe Ovalization Data

Figures 3.9 through 3.13 are plots of the pipe ovalization at the crack section as a function of the pipe displacement at the actuator for the five experiments. For each of the through-wall-cracked pipe

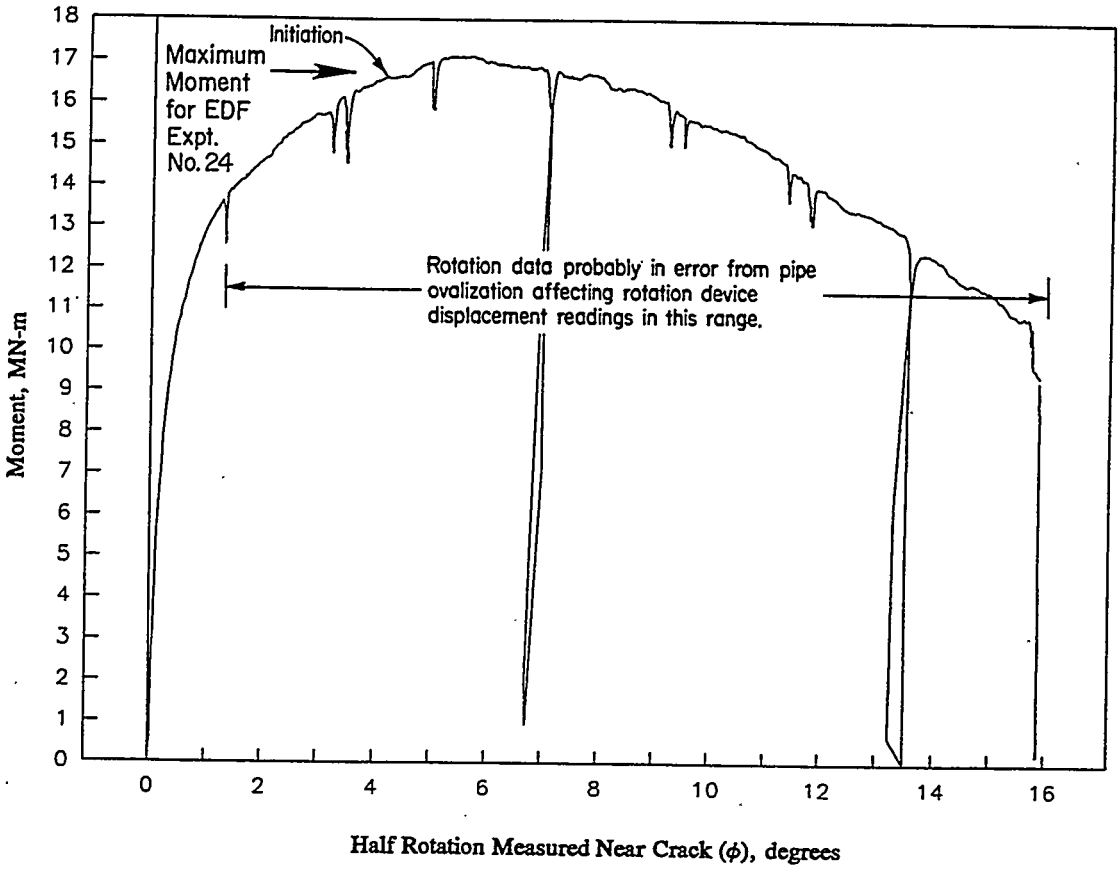

Figure 3.8 Moment versus half rotation for Experiment 1.1.1.26

experiments, the pipe diameter increased in the vertical plane and decreased in the horizontal plane due to the applied loads. This is consistent with observations from the Degraded Piping Program for long through-wall cracks. (Note, Figures 3.9 and 3.10 also include the ovalization data for the companion long through-wall-cracked pipe experiments from the Degraded Piping Program.) Conversely, for the uncracked-pipe experiment the pipe diameter decreased in the vertical plane and increased in the horizontal plane. Furthermore, the extent of pipe ovalization was significantly greater for the uncracked-pipe experiment. Comparing Figures 3.9 and 3.12, the ovalization data for the two 711-mm (28-inch) diameter carbon steel base metal experiments (one cracked and one uncracked), one sees that the extent of pipe ovalization at maximum load for the cracked-pipe case was approximately 3.5 percent while the extent of ovalization at maximum load for the uncracked case was over 7 percent. (Note, for this uncracked-pipe experiment, the pipe section buckled at two cross sections in the center section at a load level near the maximum load for the experiment. Buckling occurred in the base pipe away from any of the girth welds or load points. Figure 3.14 is a photograph of the buckled pipe.)

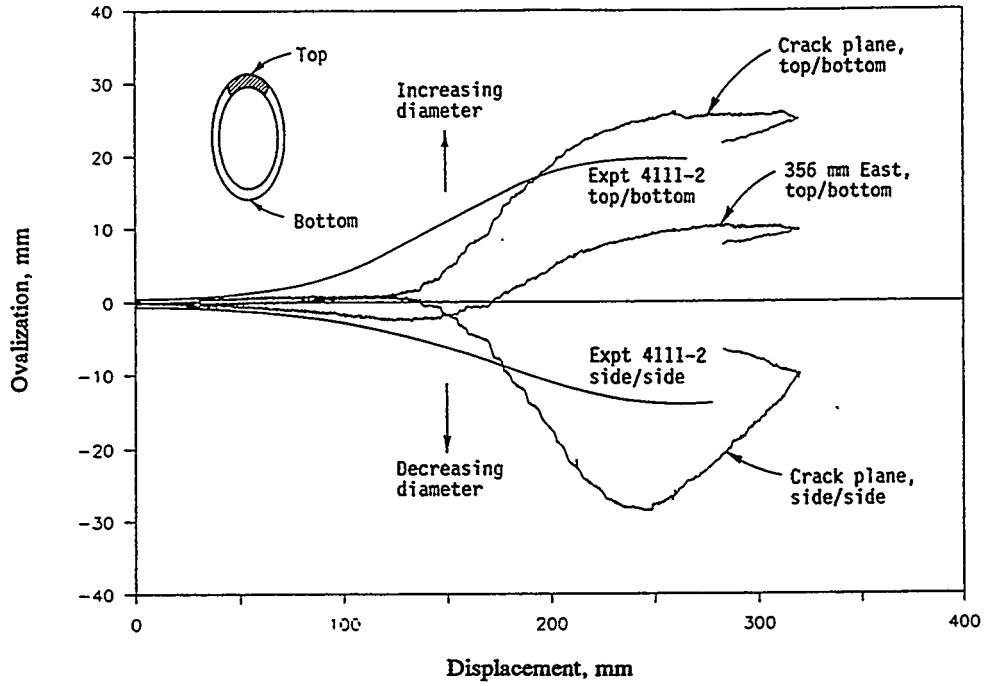

Figure 3.9 Ovalization at the crack plane and 356 mm (14 inches) from the crack plane versus pipe displacement at the actuator for Experiments 1.1.1.21 and 4111-2 (maximum load occurred at 169 mm of displacement for Experiment 1.1.1.21)

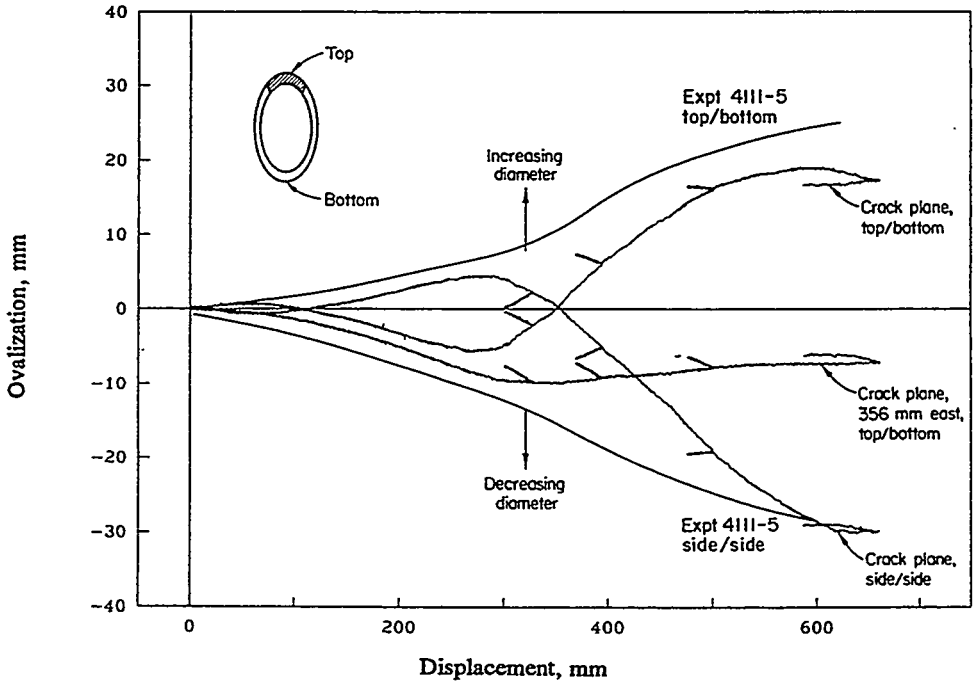

Figure 3.10 Ovalization at the crack plane and 356 mm (14 inches) from the crack plane versus pipe displacement at the actuator for Experiments 1.1.1.23 and 4111-5 (maximum load occurred at 417 mm of displacement for Experiment 1.1.1.23)

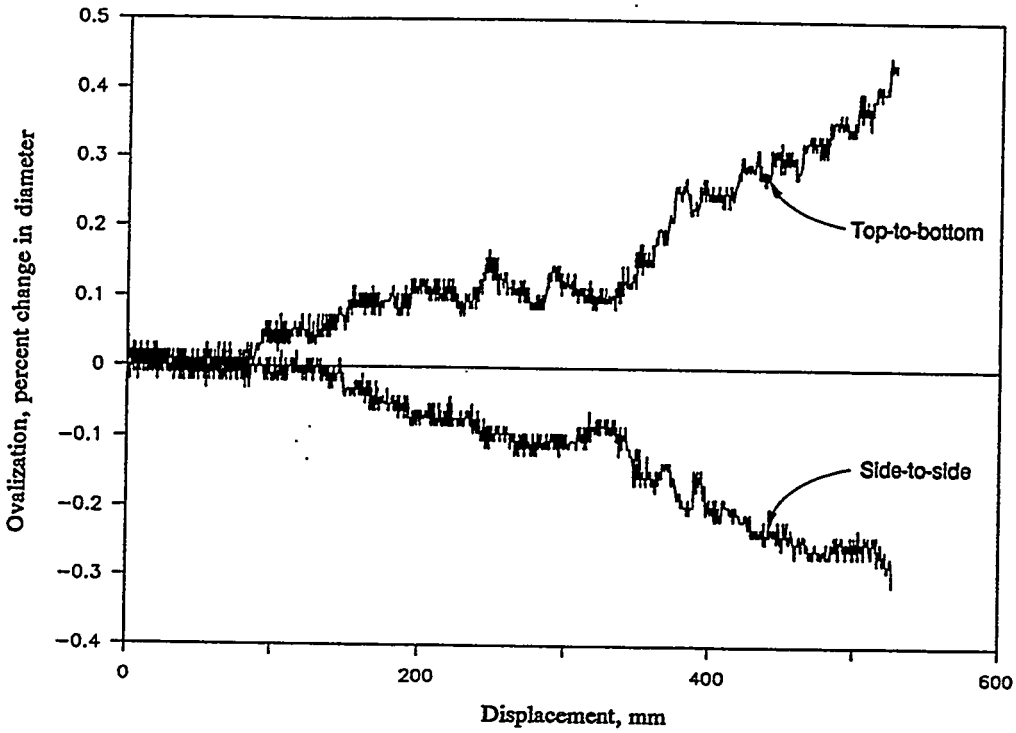

Figure 3.11 Ovalization (percent change in outside diameter) versus pipe displacement at the actuator for Experiment 1.1.1.24 (maximum load occurred at 516 mm of displacement)

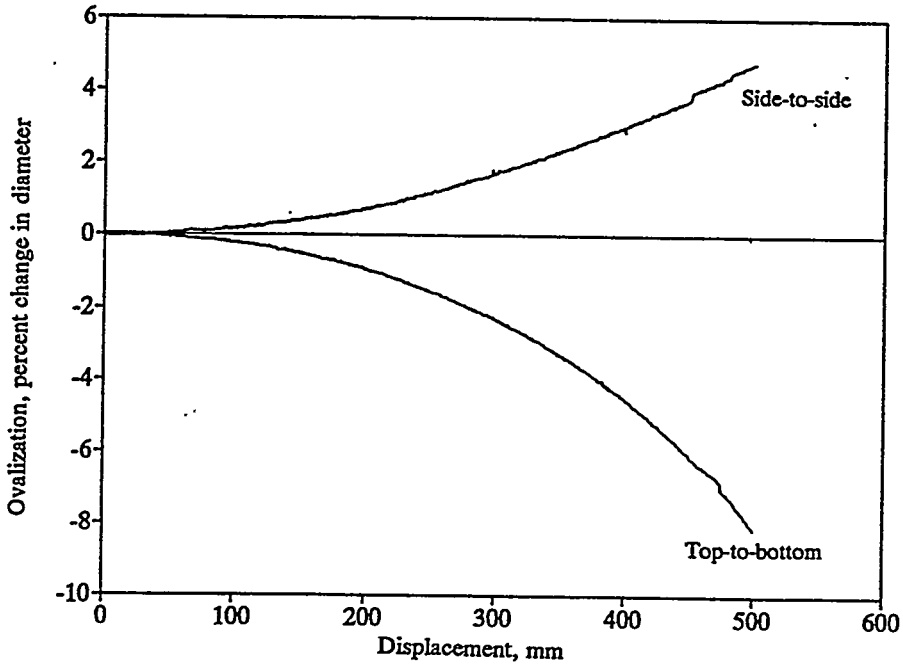

Figure 3.12 Ovalization versus pipe displacement at the actuator for Experiment 1.1.1.25 (maximum load occurred at 480 mm of displacement)

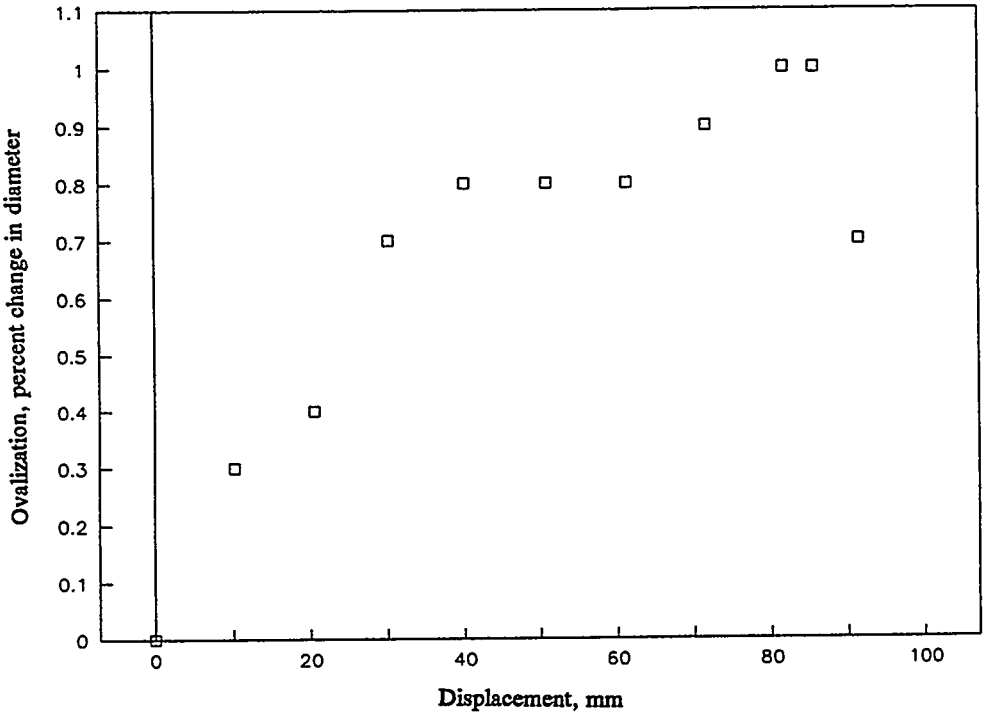

Figure 3.13 Top-to-bottom ovalization versus pipe displacement at the actuator for Experiment 1.1.1.26, manual not digital measurements (maximum load occurred at 31.7 mm of displacement)

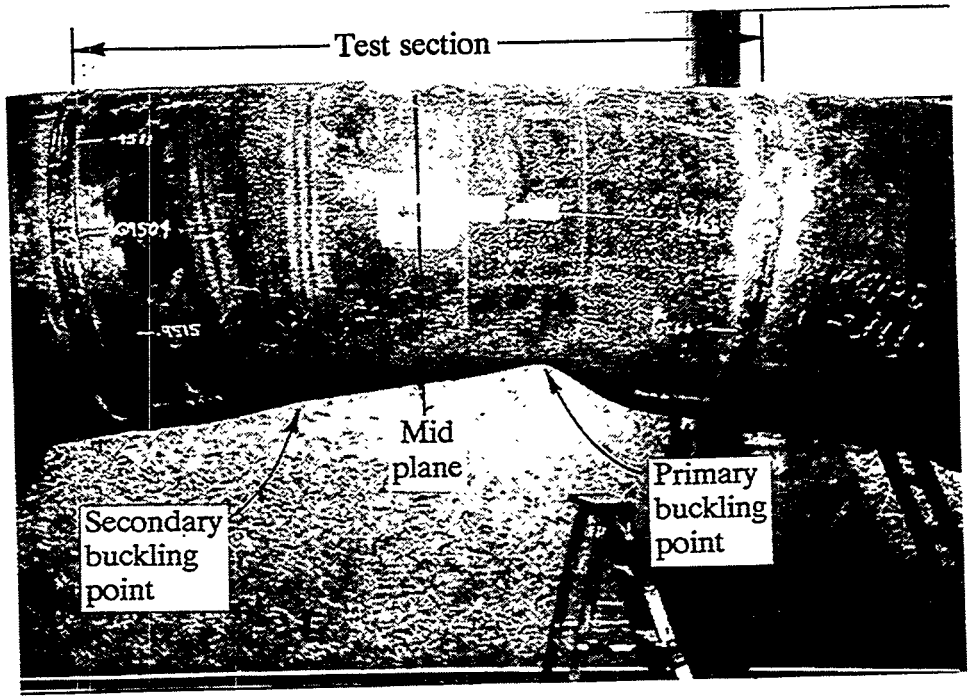

Figure 3.14 Post-test photo showing buckled section of pipe for Experiment 1.1.1.25

3.6.3 Crack Growth Data

Figures 3.15 through 3.18 are plots of through-wall-crack growth from one crack tip as a function of pipe displacement at the actuator for the four cracked-pipe experiments. Of special interest from these figures is the fact that the crack in the stainless steel submerged-arc weld experiment (1.1.1.23), see Figure 3.16, grew almost twice as much at one crack tip as it did at the other. The crack at Side A, the side which grew less, was reported to have initiated at a later time than the crack at Side B. In addition, the crack at Side A grew completely out of the weld zone and into the base metal after 100 to 125 mm (4 to 5 inches) of crack extension, whereas the crack at Side B tended to remain, at least partially, in the weld metal. It was also reported that several jeweler's saw blades were required to cut the final slot in Side A, while only a single blade was needed for Side B. Hence, there may have been a difference in the hardness at the two crack tips.

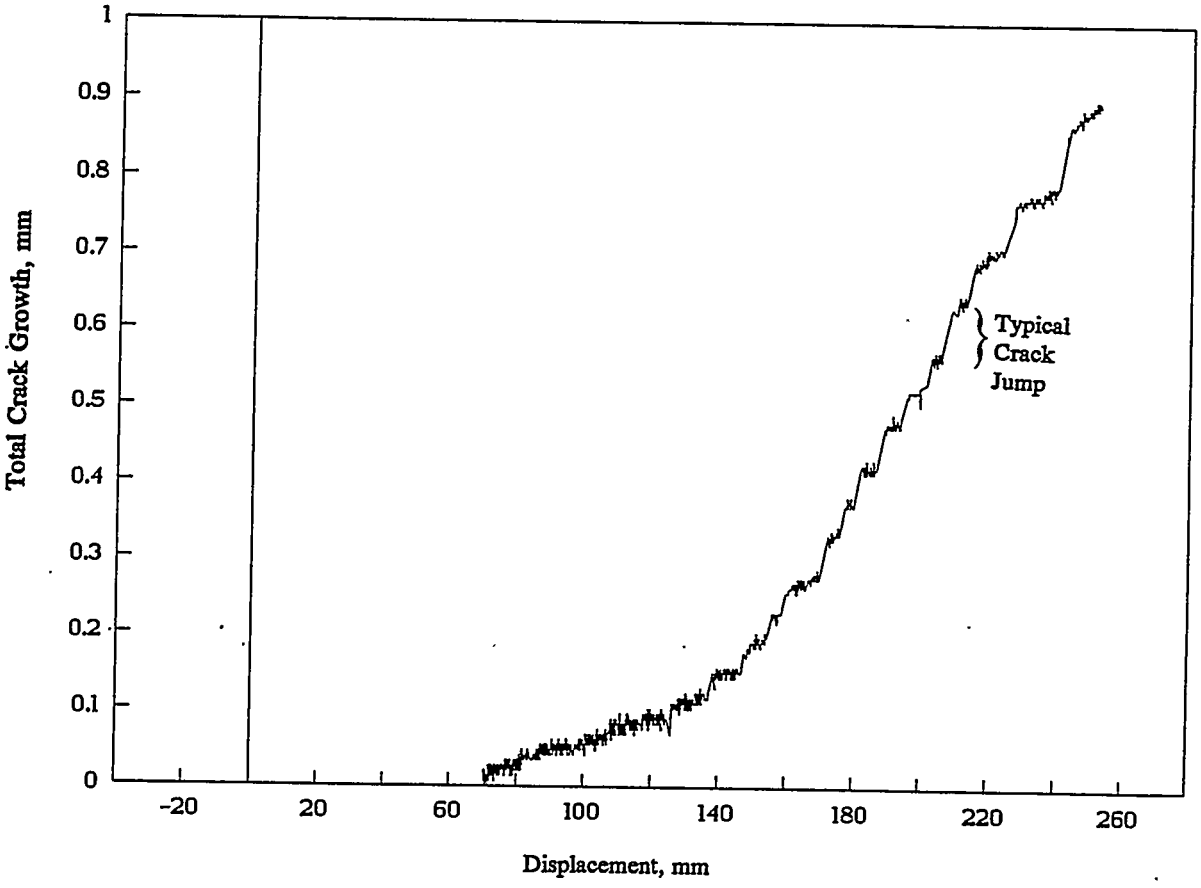

Figure 3.15 Total crack growth (both crack tips) versus pipe displacement at the actuator for Experiment 1.1.1.21

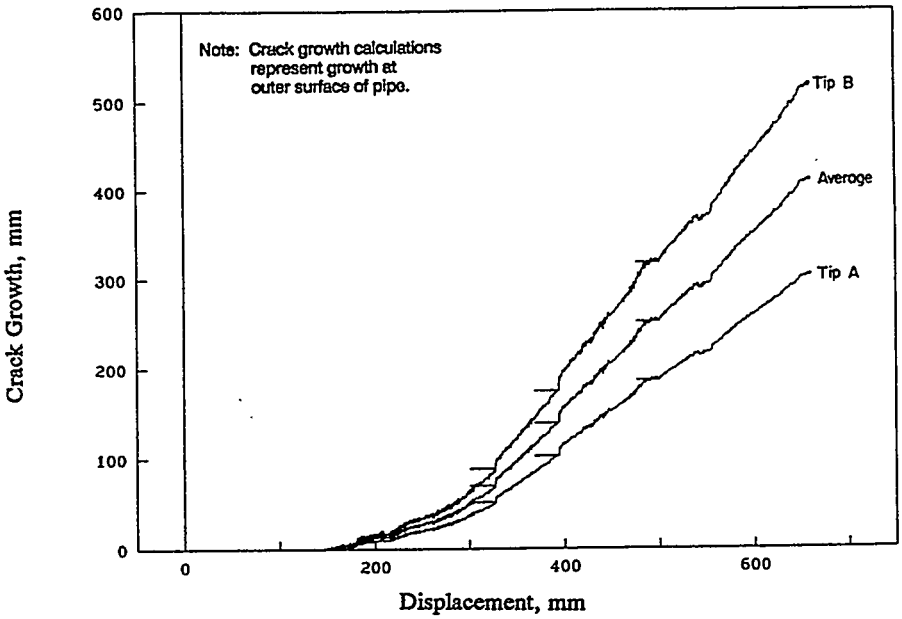

Figure 3.16 Tip A, Tip B, and the average of Tip A and B crack growth versus pipe displacement at the actuator for Experiment 1.1.1.23

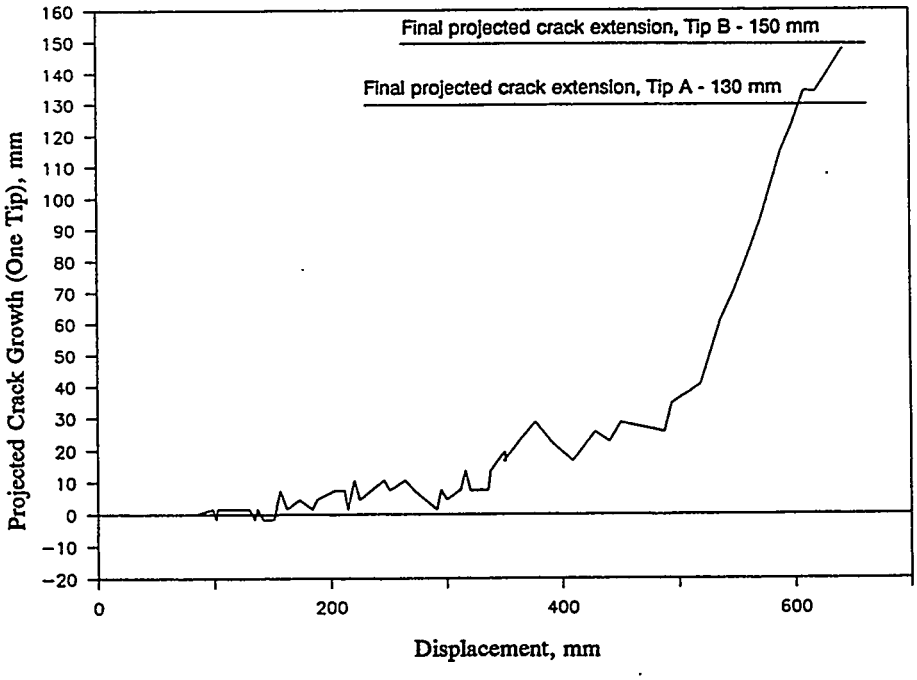

Figure 3.17 Projected crack growth (projected back into circumferential plane) at one crack tip (average growth for Tips A and B) as a function of pipe displacement at the actuator for Experiment 1.1.1.24

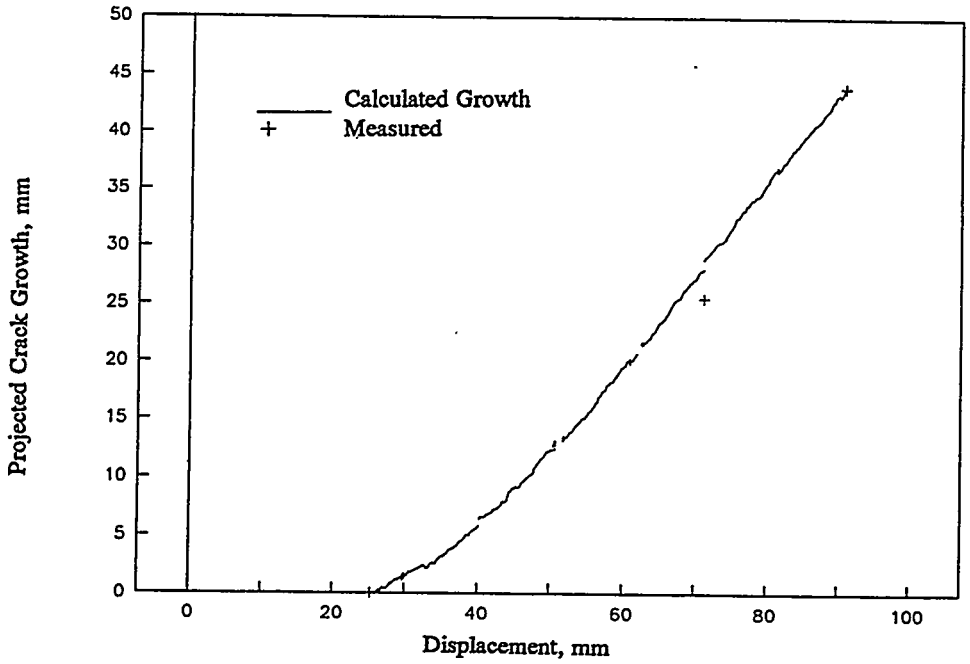

Figure 3.18 Crack growth from one crack tip versus pipe displacement at the actuator for Experiment 1.1.1.26

A sketch of the fracture path for Experiment 1.1.1.23 is shown in Figure 3.19. During the early stages of crack growth, the Side B fracture appeared to be less tilted than the Side A fracture. The fracture surfaces permitted three additional observations: (1) the tilt of the Side A and Side B fracture surfaces during the early stages of growth were in opposite directions, (2) the Side A fracture surface exhibited a bifurcation in the crack at the end of the saw-cut notch, and (3) the length of the crack front in the early stages of growth was larger on Side A than Side B due to the greater tilt angle.

Sections were taken from each side of the crack for metallographic examination. Sections A1 and B1 (see Figure 3.19) contained the jewelers-saw-cut portion of the through-wall flaw; Sections A2 and B2 were located approximately 25 mm (1 inch) from the original flaw tips. The arrows in Figure 3.19 indicate the viewing direction of each cross section. Each section was ground through 600 grit paper and etched to reveal the location of the weld. Figure 3.20 shows that the saw-cut starter notch was located very near the center of the root pass of the weld zone at each end of the flaw. Figure 3.21 shows the crack location relative to the weld zone at Sections A2 and B2. Most of the fracture surfaces on both sides of the crack appear to be along, or very close to, the weld fusion line. The presence of the weld metal in Section A2 and the near absence of weld metal in Section B2 indicates that the crack on Side A extended along one fusion line and the crack from Side B extended along the other fusion line. Notice also that the tilt angle through the thickness in Section B2 is substantially less than in Section A2.

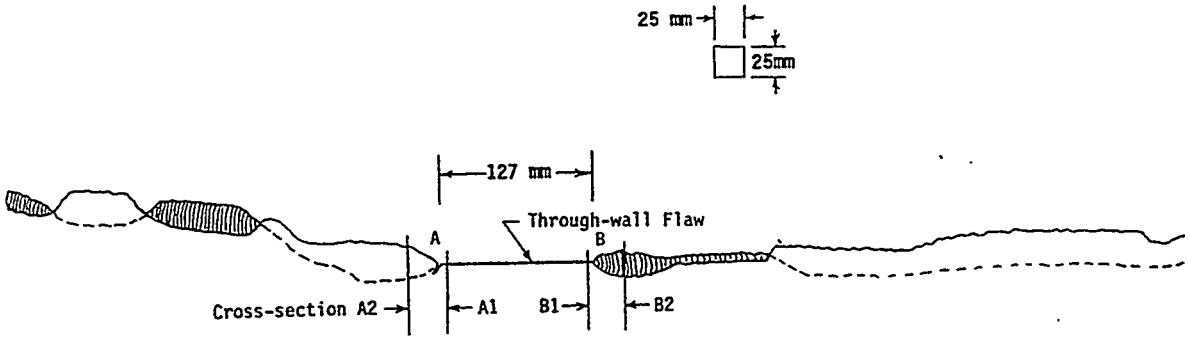

Figure 3.19 Sketch of fracture path in Pipe Test 1.1.1.23
(The view is from the outside of the pipe and assumes the pipe to be flattened. The shaded areas indicate fracture surfaces tilted toward the viewer)

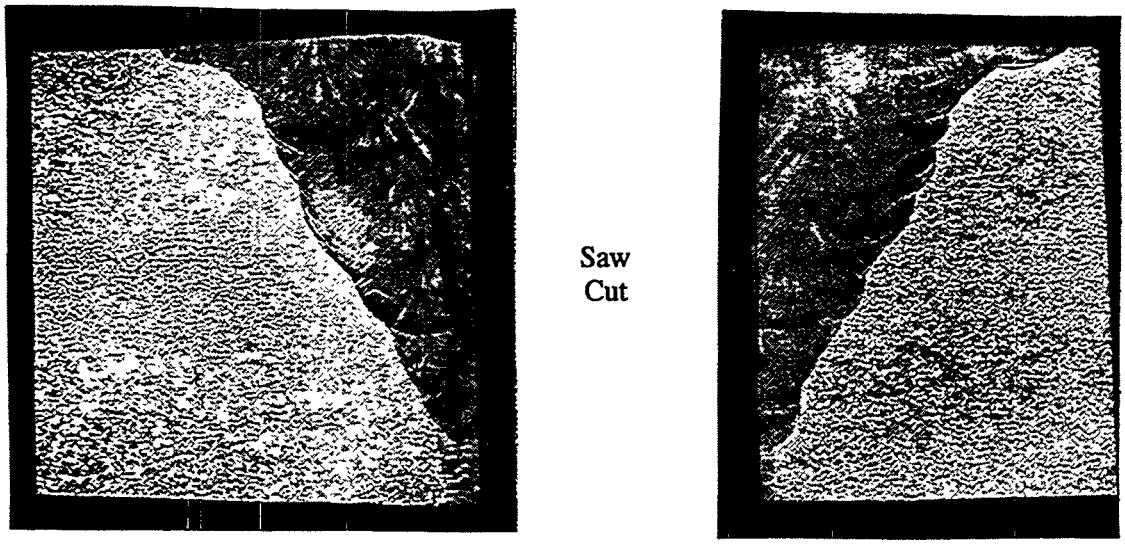

2X Section A1 at Tip A 50228

2X Section B1 at Tip B 50230

Figure 3.20 Cross sections showing the location of the saw cut notch in the weld for Experiment 1.1.1.23

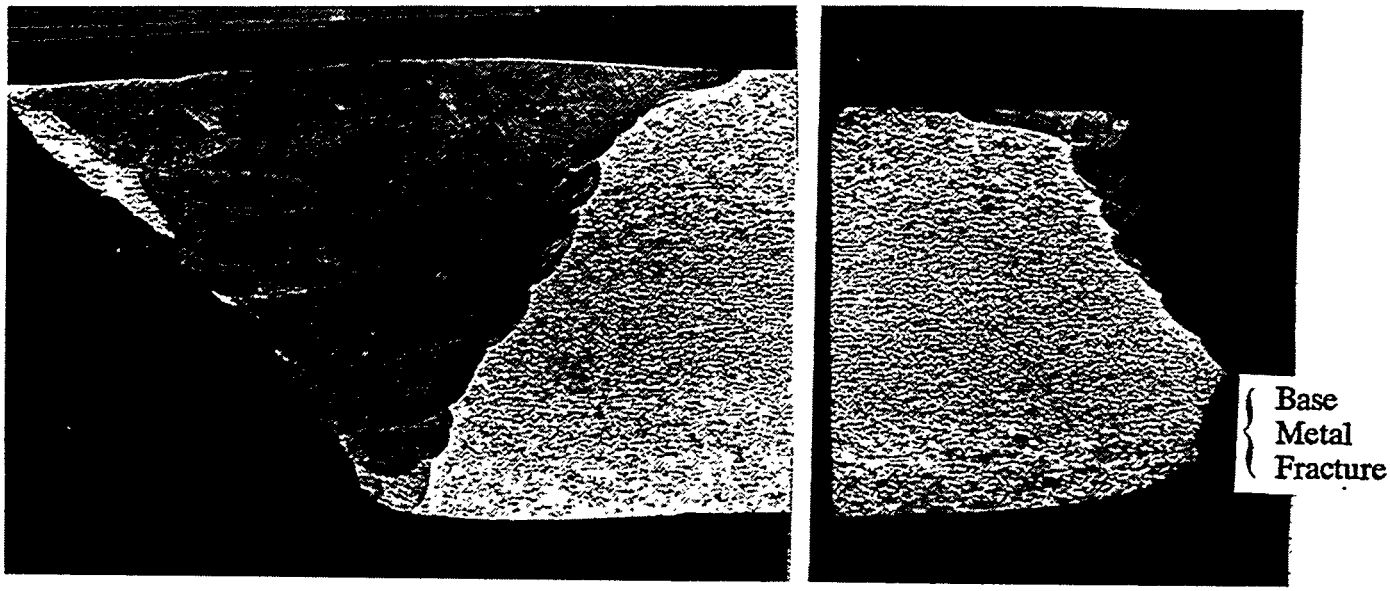

2X Section A2 (close to Tip A) 50229 2X Section B2 (close to Tip B) 50231

Figure 3.21 Cross sections showing the location of the crack with respect to the weld after 25 mm (1 inch) of crack growth

Knoop microhardness and Rockwell B hardness profiles were determined in the weld in Sections A1 and B1. Figure 3.22 shows the approximate locations at which the hardness measurements were made and lists the corresponding hardness numbers. The results show very little difference between the two sides of the weld. The hardness of the weld varied from 85 to 97 Rockwell B (143 to 232 Knoop hardness number) on Side A and from 89 to 96 Rockwell B (190 to 263 Knoop) on Side B. The average Rockwell B hardness was 91.4 for Side A and 92.8 for Side B. The Knoop hardness numbers showed a higher variation than the Rockwell B numbers, which is typical for microhardness test results in weld metals. They also showed that on average, Side B was slightly harder than Side A. Thus, the observation that cutting the final slot in Side A required more jewelers-saw blades than in Side B cannot be explained by greater average hardness at Side A. Rather, it is likely that the problem of excessive saw-blade wear at Side A may have been caused by small particles of entrapped slag from the welding process.

The precise reasons for the differences in crack extension between the two sides of this weld remains unknown. However, the crack bifurcation on Side A of the crack tends to be associated with higher energy for crack initiation. In addition, each crack extended along a different fusion line, each with an unknown J-R curve. Each of these observations might help to explain the later onset and smaller amount of crack growth at Side A relative to Side B. However, they do not explain why the crack at Side A veered away from the weld after 100 to 125 mm (4 to 5 inches) of crack growth, and, thereafter, grew in the base metal. The phenomenon of angled crack growth is being investigated in a separate study and will be reported in NUREG/CR-6299, "Effect of Toughness Anisotropy and Combined Loading on Fracture Behavior of Ferritic Nuclear Pipe".

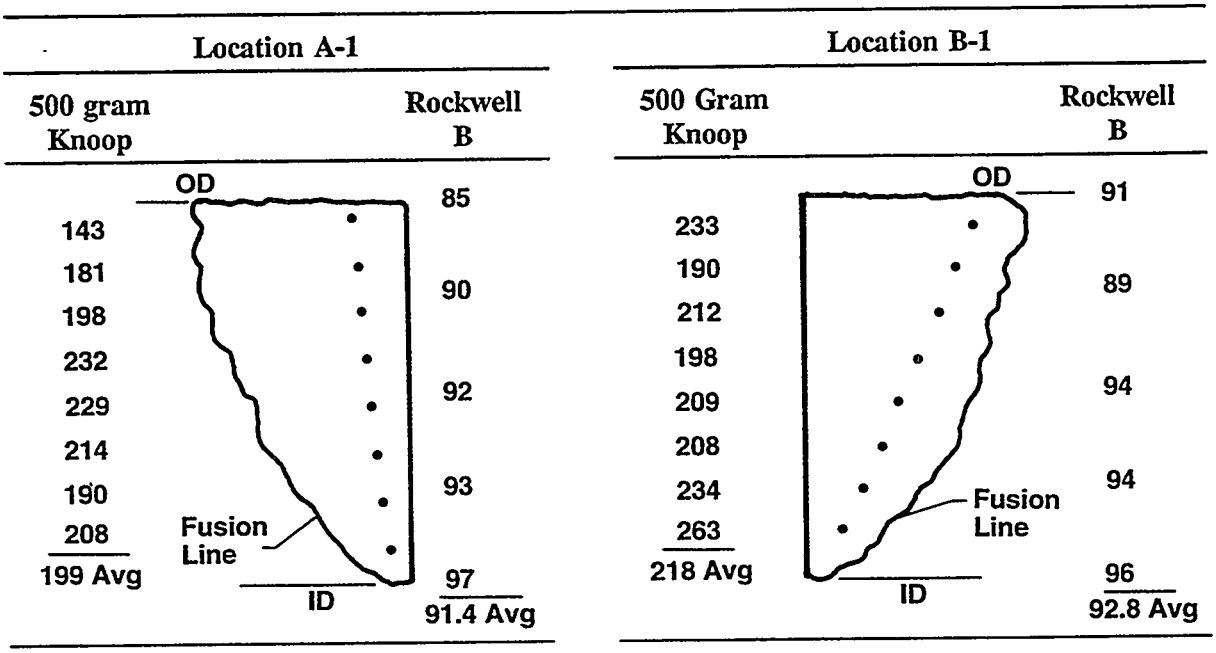

Figure 3.22 Locations and results of the hardness tests for weld region in Experiment 1.1.1.23. (See photograph in Figure 3.20.)

The most striking observation in this examination was the strong tendency for the crack to extend along or very close to the fusion line of the weld. Similar findings were reported in the Degraded Piping Program (Ref. 3.8) for submerged-arc welds in austenitic stainless steels, lending further credence to the suspicion that the fusion-line region in the austenitic welds may possess lower toughness than the SAW or base metal. A separate topical report on stainless steel weld fusion line toughness is in the process of being published. It will be NUREG/CR-6226. This report showed that the fusion-line J-R curve reached a steady-state value whereas the weld metal J-R curve was increasing. This may be the reason why cracks frequently turn and follow the fusion line in pipe weld crack experiments.

Photographs of the fracture surfaces for this stainless steel weld through-wall-cracked pipe experiment as well as photographs of the fracture surfaces for the other three through-wall-cracked pipe experiments conducted as part of this effort are shown in Figures 3.23 through 3.25.

3.6.4 Crack-Mouth-Opening Displacement Data

Figures 3.26 through 3.29 are plots of the crack-mouth-opening displacement (CMOD) data as a function of pipe displacement at the actuator for the four cracked-pipe experiments. These data can be used to verify crack-opening-area analyses for leak-rate analyses.

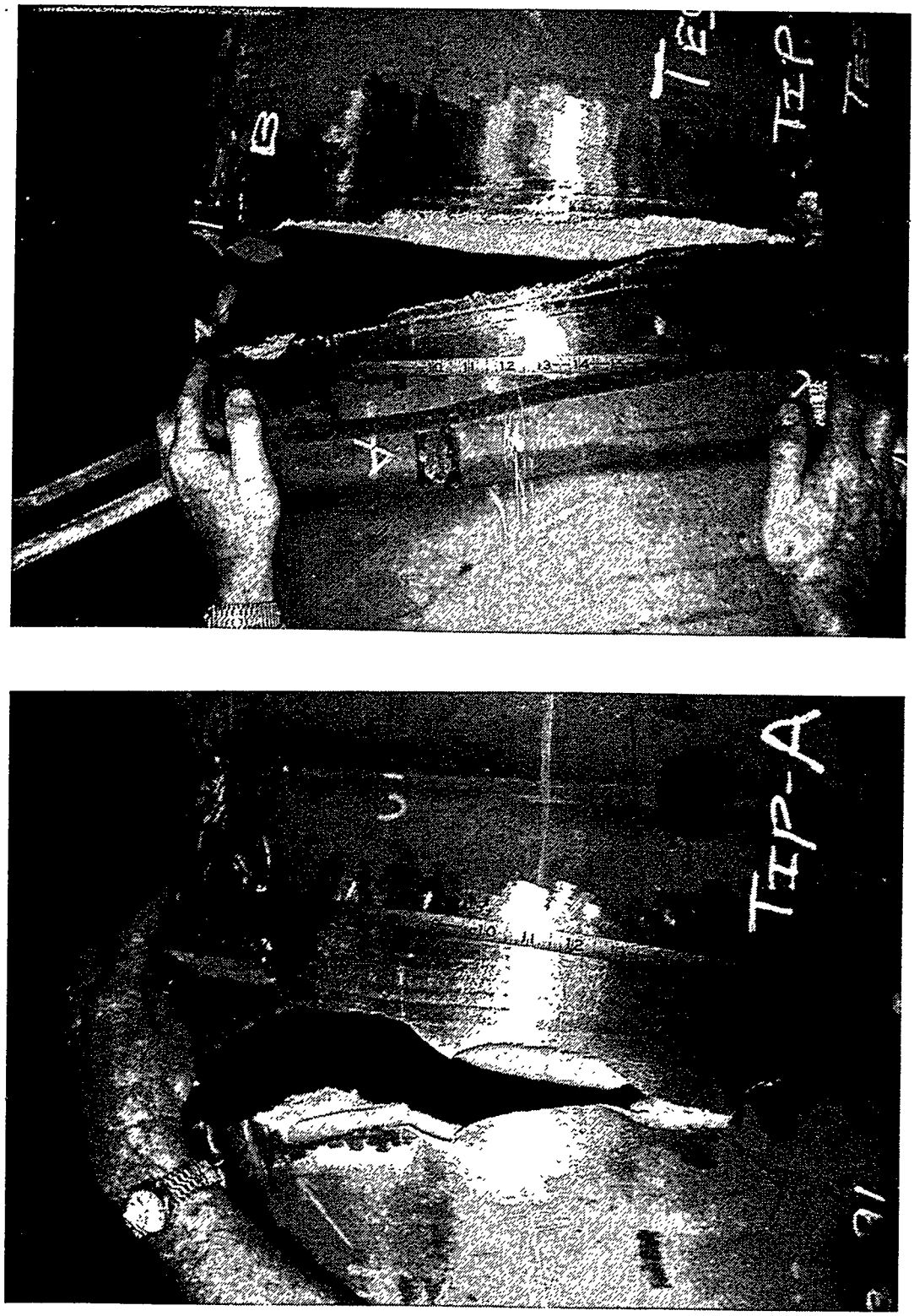

(a) Tip A (b) Tip B

Figure 3.23 Post-test photographs showing crack growth behavior for Experiment 1.1.1.23 (scale is in inches)

(a) Tip A

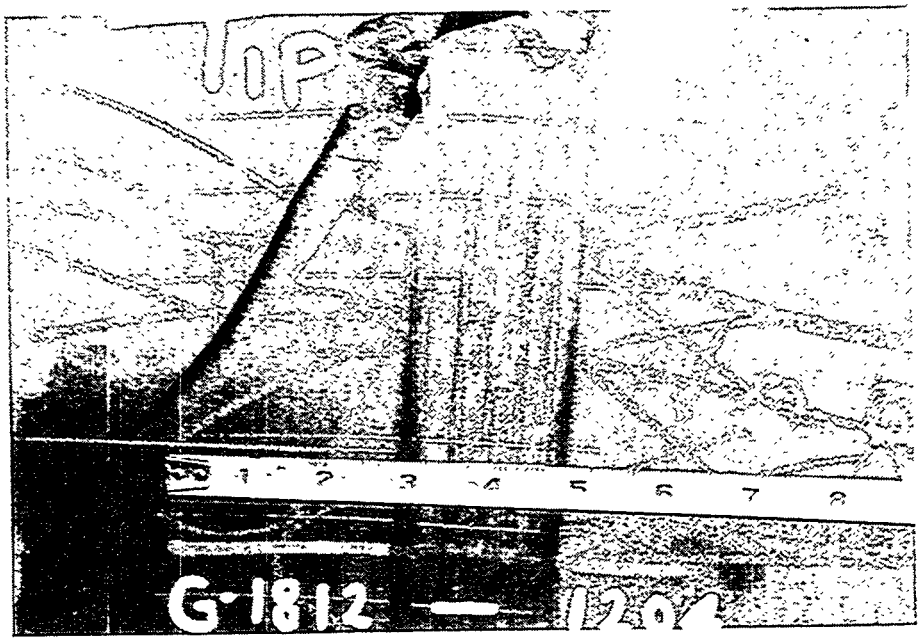

(b) Tip B

Figure 3.24 Post-test photographs of the crack growth at Crack Tips A and B for Experiment 1.1.1.24 (scale is in inches)

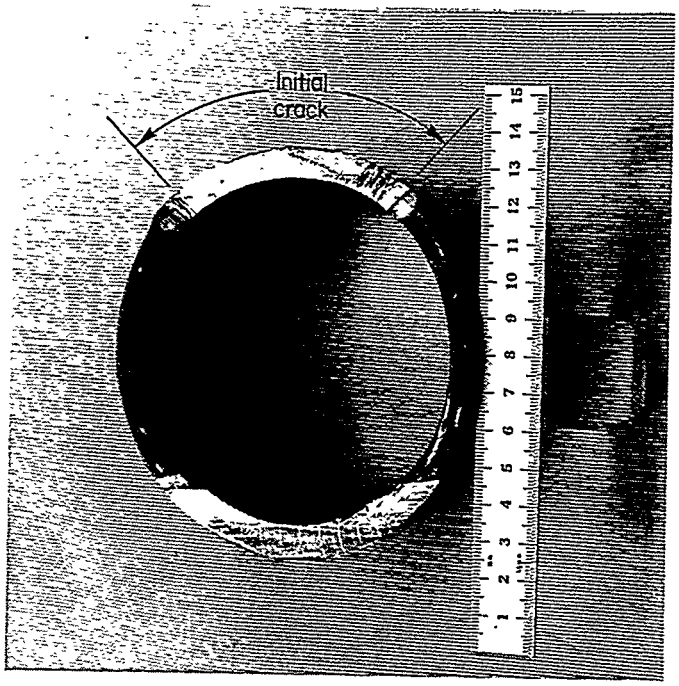

Figure 3.25 A post-test photograph of the fracture surface from Experiment 1.1.1.26 (scale is in mm)

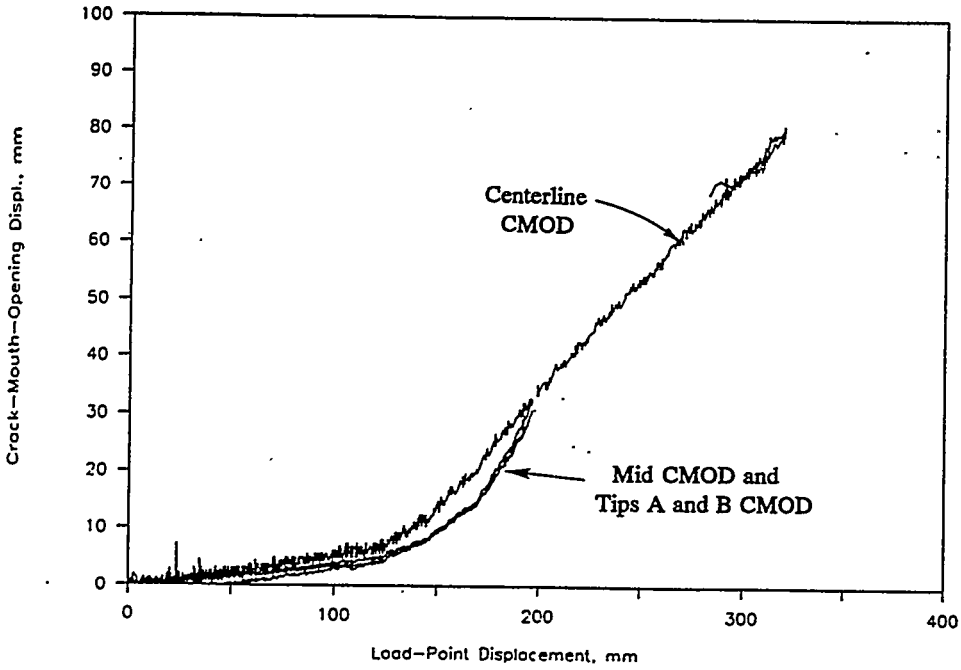

Figure 3.26 Crack-mouth-opening displacement at the crack centerline, Tip A, Tip B, and at a point between Tip A and crack centerline versus pipe displacement at the actuator for Experiment 1.1.1.21

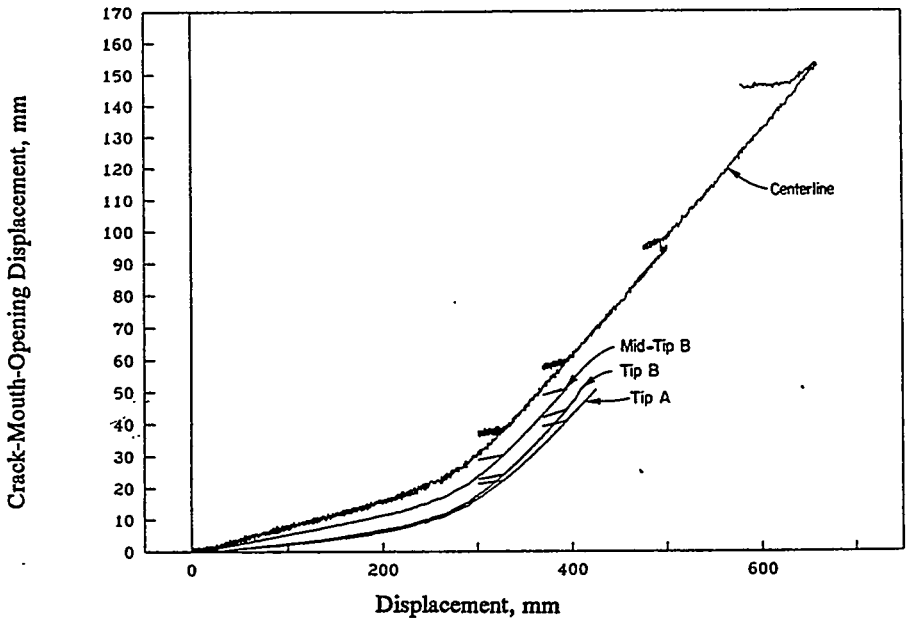

Figure 3.27 Crack-mouth-opening displacement at the crack centerline, Tip A, Tip B, and at a point halfway between Tip B and crack centerline versus pipe displacement at the actuator for Experiment 1.1.1.23

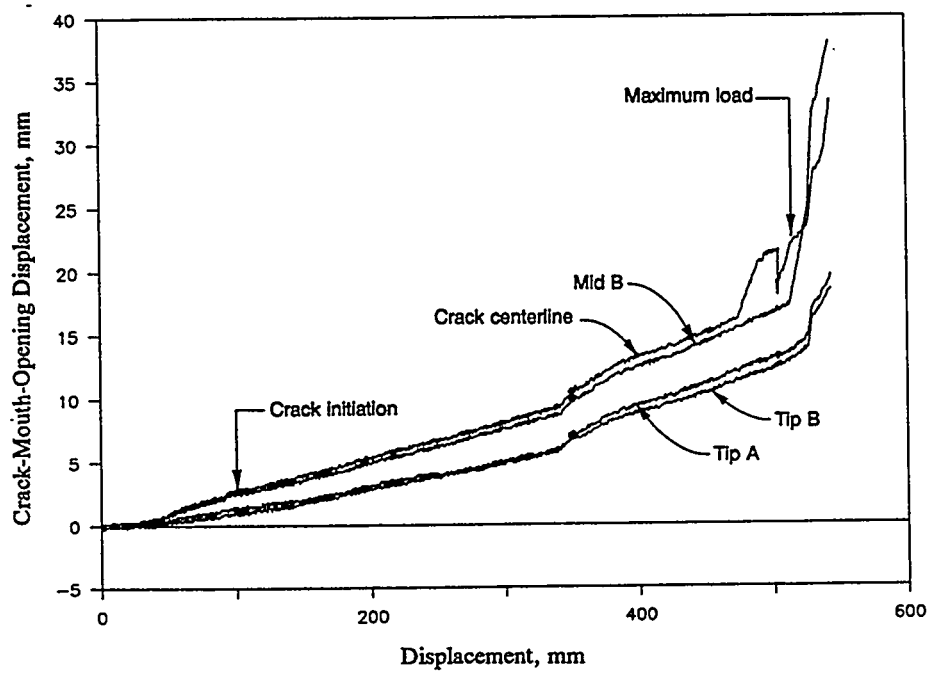

Figure 3.28 Crack-mouth-opening displacements at the crack centerline, midway between the crack centerline and Tip B, and at Crack Tips A and B as a function of pipe displacement at the actuator for Experiment 1.1.1.24

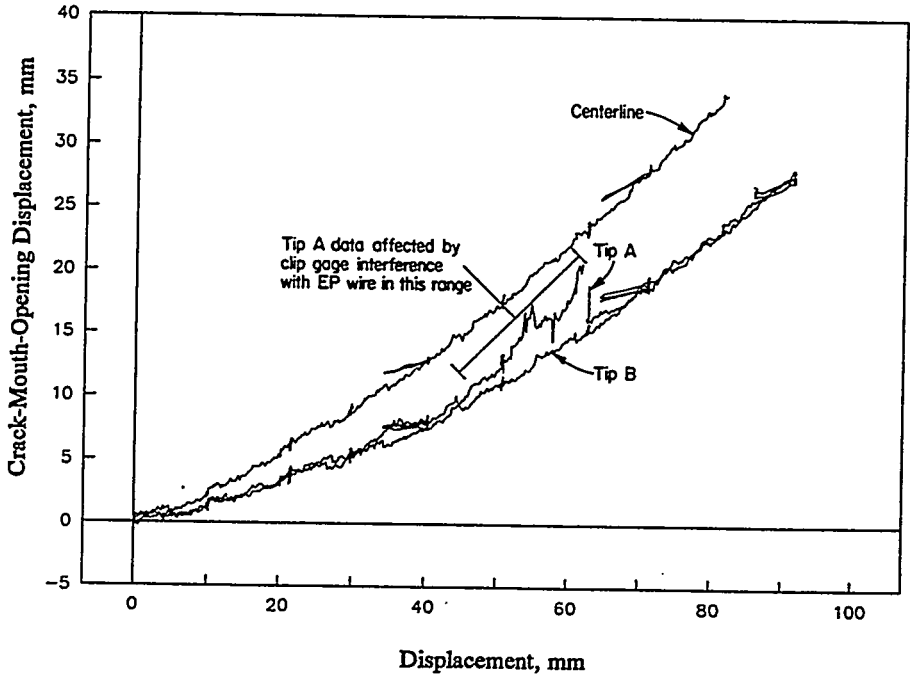

Figure 3.29 Crack-mouth-opening displacement versus pipe displacement at the actuator for Experiment 1.1.1.26

3.7 References

3.1 Wilkowski, G. M., and others, "Degraded Piping Program - Phase II," Summary of Technical Results and Their Significance to Leak-Before-Break and In-Service Flaw Acceptance Criteria, March 1984-January 1989, by Battelle Columbus Division, NUREG/CR-4082, Vol. 8, March 1989.

3.2 Kanninen, M. F., and others, "Instability Predictions for Circumferentially Cracked TP304 Stainless Steel Pipes Under Dynamic Loadings," Final Report on EPRI Project T118-2, by Battelle Columbus Laboratories, EPRI Report Number NP-2347, April 1982.

3.3 Vassilaros, M. G., Hays, R. A., Gudas, J. P., and Joyce, J. A., "J-Integral Testing Instability Analysis for 8-Inch ASTM A106 Steel Pipe," NUREG/CR-2347, April 1984.

3.4 Hays, R. A., and others, "Fracture Analysis of Welded TP304 Stainless Steel Pipe," NUREG/CR-4538, Vol. 1, May 1986.

3.5 Wilkowski, G. M., and others, "Short Cracks in Piping and Piping Welds," Semiannual Report, April 1992 - September 1992, NUREG/CR-4599, Vol. 3, No. 1, September 1993.

3.6 R. A. Schmidt, G. M. Wilkowski, and M. Mayfield, "The International Piping Integrity Research Group (IPIRG) Program--An Overview," SMiRT-11 Proceedings, Paper G23/1, August 1991.

3.7 Brust, et al., "Comparison Between Finite Element Analysis Predictions and Pipe Fracture Experiments," *Nuclear Engineering and Design*, 143, pp 201-215, 1993.

3.8 Wilkowski, G. M., and others, "Analysis of Experiments on Stainless Steel Flux Welds," NUREG/CR-4878, April 1987.

4. ANALYSIS OF PIPE WITH SHORT THROUGH-WALL CRACKS

4.1 Analysis Overview

The objective of this program was to determine if the fracture behavior of short through-wall-cracked (TWC) pipes is similar to that observed for pipes with larger cracks. Earlier studies were concerned for the most part with larger cracks (greater than 30 percent of the pipe circumference) where the nominal failure stresses were below the yield stresses. This section concerns itself with how well the TWC predictive methods perform for the short crack problem. A short crack is considered to be the crack length for LBB analyses in large diameter pipe. This length is typically 6 to 8 percent of the circumference. In addition, the predictive ability of small TWCs in welded pipe are assessed.

Section 4 is separated into three main subsections:

4.1 Review of Analysis Methods,

4.2 Improvements to Analysis, and

4.3 Comparison with Experimental Data.

Section 4.1 reviews the analysis procedures that have been developed to date to predict the fracture behavior of through-wall-cracked pipe. Section 4.2 discusses improvements that have been made to some of the methods to provide better predictions for short cracks and to better predict the behavior of welded pipe. Finally, Section 4.3 shows comparisons between predictions made using these analysis methods and the pipe experiments discussed in Section 3.0 as well as pipe experiments from other programs, particularly for the case of TWC pipes under pressure and bending loads. The analysis comparisons involve load, J, pipe load-line displacements, and pipe rotations. Crack-opening displacement accuracy and related factors are desribed in a separate report "Refinement and Evaluation of Crack-Opening Analyses for Short Circumferential Through-Wall Cracks in Pipes" (NUREG/CR-6300). The effects of angled crack growth that occurs in ferritic pipes and combined tension, bending and torsion loading are the subject of a separate report, NUREG/CR-6299, "Effect of Toughness Anisotropy and Combined Tension, Torsion, and Bending Loads on Fracture Behavior of Ferritic Nuclear Pipe".

4.1.1 Review of Analysis Methods

The objective of this section is to review analysis methods for fracture of circumferential TWC pipes under pure bending. The general analysis methodology based on classical J-Tearing theory is also reviewed. Five different J-estimation methods are evaluated: (1) GE/EPRI method (Refs. 4.1-4.2, 4.3), (2) Paris/Tada method (Ref. 4.4), (3) LBB.NRC method (Ref. 4.5), (4) LBB.ENG2 method (Refs. 4.6-4.8), and (5) LBB.ENG3 method (Refs. 4.9-4.11). In addition, some analyses also involve using the EPRI NP-192 Net-Section-Collapse (NSC) method (Ref. 4.12) and the ASME Section XI IWB-3640 and IWB-3650 pipe flaw evaluation criteria (Refs. 4.13 and 4.14) to compute the maximum loads. All of these methods are briefly reviewed below. The R6, Revision 3 Option 1 method is discussed later in this section.

4.1.1.1 J-estimation Analyses

In general, the estimation schemes may be classified as either predictive or generative. Predictive schemes require knowledge of the crack-growth resistance (e.g., J-resistance or J-R curve) and plastic-flow (e.g., stress-strain curve) behavior of the material. This information is used to predict the load-displacement behavior of the structure including loads and displacements at crack initiation and at crack-growth instability. Results of the analyses, presented in Section 4.3, are based on predictive J-estimation methods. Generative schemes, on the other hand, require apriori knowledge of the experimentally derived load-displacement record and are frequently used to calculate J-resistance curves as a function of crack extension. This type of analysis is referred to as η-factor analysis. An η-factor analysis can be valuable to evaluate fracture toughness data from small specimen geometry such as compact tension [C(T)] specimens, or cracked pipe, but it cannot be used to predict loads or displacements of a cracked pipe by itself; hence for licensing applications its main value is to show similitude between pipe and specimen J-R curves. However, in some predictive analyses (i.e., LBB.NRC, LBB.ENG, LBB.GE, and Paris/Tada) η-factor analyses are inherent in the pipe fracture predictions, as will be shown later.

4.1.1.2 Idealizations of Material Properties

In conducting numerical calculations, several analytical idealizations were considered. For example, it was assumed that the constitutive law characterizing the material's stress-strain response can be represented by the Ramberg-Osgood model

$$\frac{\epsilon}{\epsilon_0} = \frac{\sigma}{\sigma_0} + \alpha \left[\frac{\sigma}{\sigma_0}\right]^n \tag{4-1}$$

in which σ_0 is a reference stress usually assumed to be the yield stress, $\epsilon_0 = \sigma_0/E$ is the associated reference strain, E is the modulus of elasticity, and α and n are strain-hardening parameters usually chosen from the best fit of laboratory data. This representation of the stress-strain curve is necessary, since the J-integral in most estimation schemes is formulated based on power-law idealizations.

In characterizing the fracture toughness of materials, the ASTM Deformation J-resistance curve (J_D-R curve) was used and the curve was extrapolated using a power-law form for crack-growth beyond 30 percent of the uncracked ligament in the C(T) specimens. Thus, the J_D-R curve was deemed to be adequately characterized by a power-law equation of the form

$$J_R(\Delta a) = J_{Ic} + C_1 \left[\frac{\Delta a}{r}\right]^m \tag{4-2}$$

in which Δa is the crack length extension during crack growth, J_{Ic} is the toughness at crack initiation, and C_1 and m are power-law parameters from a best fit of experimental data. In Equation 4-2, r is a convenient normalizing parameter with a value of unity and the same units as Δa. For example, if J and Δa are expressed in kJ/m^2 and mm, respectively, the dimension of C_1 also becomes kJ/m^2 if r = 1 mm. Because C(T) specimens that are cut from pipe are small, large extrapolation of the data was required in order to predict crack growth in a pipe. Note that "Δa" here is the physical crack

extension, i.e., without blunting. This is because blunting is automatically accounted for in the pipe estimation schemes.

4.1.2 Estimation Methods

Consider a TWC pipe with mean radius R_m, wall thickness t, and a through-wall-crack angle 2θ. The pipe is subjected to a remote moment, M, via a four-point bend test typically used in a pipe fracture experiment (Ref. 4.6). In a typical J-estimation scheme it is generally assumed that the load-point rotation due to the presence of crack, ϕ^c, and the relevant crack driving force, such as J-integral, admit additive decomposition of elastic and plastic components given by (Ref. 4.6)

$$J = J_e + J_p \tag{4-3}$$

$$\phi^c = \phi_e^c + \phi_p^c \tag{4-4}$$

where the subscripts "e" and "p" refer to elastic and plastic contributions. In the elastic range, ϕ_e^c and M are uniquely related. In addition, if the deformation theory of plasticity holds, a unique relationship also exists between ϕ_p^c and M. Once these relationships are determined, the elastic component, J_e, and the plastic component, J_p, of the total energy release rate J can be readily obtained.

In this study, five J-estimation schemes are considered. The following sections provide a brief discussion of the methods. Improvements and/or modifications to the methods are discussed in Section 4.2, while comparisons of predictions with experimental pipe fracture data are provided in Section 4.3.

4.1.2.1 GE/EPRI Method

The GE/EPRI method is based on a compilation of finite-element solutions for TWC pipes using deformation theory of plasticity. These solutions are catalogued in References 4.1 to 4.3 for various geometric and material parameters. For pure bending in pipes containing through-wall cracks, the J-integral is calculated by Equation 4-3 in which J_e and J_p are given by (Refs. 4.1-4.3)

$$J_e = f_1(\theta/\pi, R_m/t)\, M^2/E \tag{4-5}$$

$$J_p = \alpha\, \sigma_0\, \epsilon_0\, R_m \theta\, (1-\theta/\pi)\, h_1(\theta/\pi, R_m/t, n)\, (M/M_0)^{n+1} \tag{4-6}$$

where $f_1(\theta/\pi, R_m/t)$ and $h_1(\theta/\pi, R_m/t, n)$ are influence functions calculated from finite element results and tabulated in References 4.1 to 4.3. M_0 is the limit-moment of a through-wall-cracked pipe under pure bending. In using the GE/EPRI method, no plastic-zone correction was made in the elastic solution since plasticity is explicitly accounted for in the plastic part of J-integral. These solutions were recompiled during this program. The results are listed in Section 4.2.

4.1.2.2 Paris/Tada Method

In the Paris/Tada method (Ref. 4.4), J is obtained by an η-factor method using the moment versus pipe rotation solution from an interpolation between the linear-elastic and fully-plastic limit-load solutions. In effect, the procedure uses the techniques developed in References 4.15 and 4.16 for a planar fracture specimen appropriately adapted for a through-wall-cracked pipe. Thus, J calculated by this method depends only on the cracked-pipe geometry and flow stress and does not explicitly account for hardening behavior of the material.

For linear-elastic and rigid-plastic conditions in through-wall-cracked pipes, the moment-rotation and J-rotation relationships are well-established (Ref. 4.4). The Paris/Tada method interpolates between these two solutions by artificially increasing the crack size using a plastic-zone size correction and substituting this artificially increased crack size into the elastic solution to obtain the moment-rotation relationship in the elastic-plastic regime. The procedure is based on the Irwin estimate of the size of the plastic zone. Hence, it is not theoretically rigorous and should be treated merely as an engineering tool.

From linear-elastic fracture mechanics, it can be shown that the moment and elastic rotation are related via (Refs. 4.4, 4.6, and 4.9 to 4.11)

$$M = \frac{E\pi R_m^2 t}{I_B}\phi_e^c \tag{4-7}$$

where I_B is a compliance function defined in Reference 4.6 and listed in Appendix A. Using the effective crack size, θ_e, (i.e., applying plastic-zone correction) and total rotation, ϕ^c, in place of θ and ϕ_e^c in Equation 4-7 and the expression for rigid-plastic moment, the final equations for J_e and J_p by Paris/Tada method are (Refs. 4.4 and 4.6)

$$J_e = \frac{K_I^2}{E} \tag{4-8}$$

where

$$K_I = \frac{M}{\pi R_m^2 t} F_B \sqrt{\pi R_m \theta} \tag{4-9}$$

and

$$J_p = \frac{\sigma_f R_m [\sin(\theta/2) + \cos\theta]}{M_{RP}} \int_0^{\phi_p^c} M d\phi_p^c \qquad (4\text{-}10)$$

where σ_f is the flow stress and M_{RP} is the rigid-plastic moment from a limit-load analysis (Ref. 4.4). F_B in Equation 4-9 represents an appropriate geometry function with the explicit functional forms of F_B and I_B listed in Appendix A. Equation 4-10 is the η-factor solution where the constants outside the integral are the η-factor. (Note: during crack growth calculations, this term should be inside the integral since θ changes with increasing ϕ.)

4.1.2.3 LBB.NRC Method

The LBB.NRC method (Ref. 4.5) for through-wall-cracked pipes subjected to bending is similar to the Paris/Tada method, which was described earlier. However, the plastic component of rotation due to a crack is written as

$$\phi_p^c = \alpha \left[\frac{\sigma}{\sigma_f}\right]^{n-1} \phi_e^c \qquad (4\text{-}11)$$

with $\phi_e^c = \phi_e^c(\theta_e)$ from the Paris/Tada solution. Hence, the elastic component of rotation is increased by the Irwin plastic-zone correction and the plastic component of rotation is increased or decreased depending on the current applied stress level. In this method, the effects of strain-hardening are incorporated in the evaluation of the J-integral.

4.1.2.4 LBB.ENG2 Method

The LBB.ENG2 method was originally developed by Brust and Gilles during the Degraded Piping Program (Refs. 4.6 to 4.8) to compute energy release rates for through-wall-cracked pipes under pure bending. It involves an equivalence criterion incorporating reduced thickness analogy for simulating system compliance due to the presence of a crack in pipe.. Detailed derivations of both elastic and plastic components of J-integral in this method are available in the references cited below. Only the final expressions are presented here.

The elastic component, J_e, by LBB.ENG2 method, is identical to that by the Paris/Tada method and hence is also given by Equation 4-8. The plastic component, J_p, is given by

$$J_p = \frac{\alpha}{E\sigma_0^{n-1}} \frac{\pi R_m}{2(n+1)} H_B(n,\theta) L_B(n,\theta) I_B \left[\frac{M}{\pi R_m^2 t}\right]^{n+1} \qquad (4\text{-}12)$$

where $H_B(n,\theta)$ and $L_B(n,\theta)$ are conveniently defined elementary functions with explicit forms available in References 4.6 to 4.8. The development of the LBB.ENG2 method is discussed in more detail in Section 4.2, which deals with method improvements.

4.1.2.5 LBB.ENG3 Method

The LBB.ENG3 method was developed by Rahman and Brust (Refs. 4.9 to 4.11) as part of this program to improve the computation of the J-integral for TWC pipe welds by incorporating weld-metal strength properties. The method is similar to the LBB.ENG2 method and is also based on an equivalence criterion incorporating a reduced thickness analogy for simulating system compliance due to the presence of a crack in the pipe. The elastic solution by this method is identical to that of the LBB.ENG2 or Paris/Tada method and is given by Equation 4-8. The plastic solution is given by

$$J_p = \frac{\alpha_1}{E_1 \sigma_{01}^{n_1-1}} \frac{\pi R_m}{2(n_1+1)} H_B(n_1, n_2, \theta) L_B(n_1, n_2, \theta) I_B \left[\frac{M}{\pi R_m^2 t}\right]^{n_1+1} \quad (4\text{-}13)$$

in which the additional subscripts "1" and "2" on the variables E, σ_0, α, and n are needed to represent base and weld metal properties, respectively. In Equation 4-13, $H_B(n_1,n_2,\theta)$ and $L_B(n_1,n_2,\theta)$ are algebraic functions and are more complex than their counterparts in Equation 4-12 due to the inclusion of both base and weld metal properties.

Note that Equation 4-13 has similar characteristics to those of Equation 4-12, required to calculate J_p for a base metal crack (LBB.ENG2 method). However, from Equation 4-13 it can be seen that the tensile strength properties of both base and weld metals are accounted for in calculating the J-integral. Equation 4-13 is strongly dependent on base metal properties, but the weld metal properties are also considered via the L_B- and H_B-functions. When differences in the base metal and weld metal properties vanish, it can be shown that Equation 4-13 degenerates to Equation 4-12, as one would expect. This method is further discussed in Section 4.2 and corresponding predictions are compared with experimental data in Section 4.3.

4.1.2.6 Net-Section-Collapse Analysis

The Net-Section-Collapse analysis (Ref. 4.12) for cracked structures is a simple strength of materials limit-load analysis that assumes that the material is tough enough to reach fully plastic conditions before failing. Both fracture toughness and crack growth are neglected. It is used to predict maximum load only and cannot predict crack initiation load. Therefore, it is necessary that there be very little crack growth from crack initiation to the maximum load in order for a Net-Section-Collapse analysis to be accurate. Under pure flexure, the bending moment predicted by this method is (Ref. 4.12)

$$M_{nsc} = 4 \sigma_f R_m^2 t \left[\cos\frac{\theta}{2} - \frac{1}{2}\sin\theta\right] \quad (4\text{-}14)$$

where M_{nsc} is the Net-Section-Collapse or limit moment. In this report, the value of flow stress, σ_f, is assumed to be the average of the yield stress and the ultimate stress. Numerous other modifications to the original Net-Section-Collapse analysis from Reference 4.12 have been proposed, but are not included in this report.

4.1.2.7 ASME Section XI IWB-3640 Analysis

The Net-Section-Collapse analysis was slightly modified and used as the technical basis for the ASME Section XI Article IWB-3640 and Appendix C analyses of flaws in austenitic piping (Ref. 4.13). This method, however, accounts for low-toughness flux welds in an indirect way. For pure bending, there are three differences between Net-Section-Collapse analysis and the IWB-3640 analysis.

The first difference is the definition of flow stress. The IWB-3640 analysis uses a definition of $3S_m$ for austenitic steels where S_m is defined as the material design stress intensity and is tabulated as a function of temperature for a wide variety of material grades and types. The second difference is that Article IWB-3640 is applicable only for Class 1 piping for which Section III requires that the bending stress be calculated at the outer fiber with the exact expression for the moment of inertia of an uncracked pipe. In the original Net-Section-Collapse analysis, the bending stress is defined using thin-wall shell equations and is similar to the ASME Code for Class 2 piping stress analysis.

The third and most important difference is that the IWB-3640 analysis requires that a correction factor, known as the Z-factor, be used in reducing the predicted maximum allowable stress by 1/Z. The Z-factor is introduced to account for lower toughness of flux welds. From circumferential through-wall-cracked pipe analyses using the original GE/EPRI estimation scheme, it was proposed that (Ref. 4.13)

$$\begin{aligned} Z &= 1.15\left[1 + 0.013\,(D - 4)\right] \text{ for austenitic SMAW cracks} \\ Z &= 1.30\left[1 + 0.010\,(D - 4)\right] \text{ for austenitic SAW cracks} \end{aligned} \qquad (4\text{-}15)$$

where the unit of the nominal diameter, D, is in inches. When the diameter of the pipe is less than 610 mm (24 inch), the Code says to use D = 24 to account for uncertainties in the thermal expansion stresses in small-diameter pipes. Further details on this method can be found in Reference 4.13.

4.1.2.8 ASME Section XI IWB-3650 and Appendix H Analyses

The procedures embodied in Article IWB-3650, and Appendix H of Section XI, for evaluating flaws in ferritic piping are fundamentally similar to those embodied in Article IWB-3640 and Appendix C for austenitic piping. Both sets of procedures incorporate a limit-load analysis based on the Net-Section-Collapse analysis for evaluating flaws in high toughness materials. Both also incorporate an elastic-plastic analysis, using a stress multiplier (i.e., a Z-factor), for evaluating flaws in lower toughness materials, such as welds. However, only the ferritic pipe criteria include a linear-elastic analysis for evaluating flaws in very low toughness materials.

The procedures in Appendix H for the ferritic pipe criteria include a screening criterion for assessing which type of analysis procedure, i.e., limit-load, elastic-plastic, or linear-elastic, is most appropriate. If the screening criterion parameter, which is the ratio of the stress intensity factor normalized by the material toughness (K_r) to the sum of the primary bending and expansion stresses normalized by the bending stress at limit-load (S_r), is less than 0.2 then the limit-load analysis should be used. For all intents and purposes the limit-load analysis in Appendix H for ferritic piping is the same as the limit-load analysis in Appendix C with the exception that the flow stress in Appendix C is defined as $3S_m$ while the flow stress in Appendix H is defined as the average of the material's yield and ultimate

strengths, if those values are known. If the yield and ultimate strengths are unknown, then the flow stress is defined as $2.4S_m$.

If the screening criterion parameter is greater than or equal to 0.2 but less than 1.8, then the elastic-plastic analysis should be used. The elastic-plastic analysis in Appendix H for ferritic piping is the same as the elastic-plastic analysis in Appendix C (for austenitic piping) except for the differences in the flow stress definition as discussed above. Different formulations for the elastic-plastic stress and load multiplier, Z, are used in the two appendices. The Z-factor formulations for the ferritic piping cases are as follows.

$$Z = 1.2[1 + 0.021A(NPS-4)] \tag{4-16}$$

for Material Category 1; seamless or shielded metal arc welded wrought carbon steel pipe and pipe fittings that have a specified minimum yield strength not greater than 275 MPa (40 ksi) and welds made with E7015, E7016, or E7018 electrodes in the as-welded or postweld heat treated condition. Z is defined by

$$Z = 1.35[1 + 0.184A(NPS-4)] \tag{4-17}$$

for Material Category 2; all other ferritic shielded-metal-arc and submerged-arc welds with specified minimum tensile strengths not greater than 550 MPa (80 ksi) in the as-welded or postweld heat treat condition.

The "A" in these Z-factor expressions is a function of the pipe R_m/t ratio and is given by

$$A = [0.125(R_m/t) - 0.25]^{0.25} \text{ for } 5 \leq R_m/t \leq 10 \tag{4-18a}$$

or

$$A = [0.4(R_m/t) - 3.0]^{0.25} \text{ for } 10 < R_m/t \leq 20 \tag{4-18b}$$

The term NPS in the above expressions is the nominal pipe size, in inches, and the terms "R_m" and "t" denote the mean pipe radius and pipe wall thickness, respectively.

Finally, if the screening criterion parameter is greater than or equal to 1.8 then linear-elastic fracture mechanics analysis must be used. This analysis stipulates that the applied stress intensity factor, K_I, must be less than the plane stress fracture toughness of the material. The plane stress fracture toughness is expressed in terms of the parameter J_{Ic} and the elastic modulus, E, using the expression

$$K_{Ic} = \{J_{Ic}E/(1-\nu^2)\}^{0.5} \tag{4-19}$$

For this analysis it is assumed that ductile crack extension does not occur prior to fracture. Further details of these analyses can be found in Reference 4.14. Although both ASME criteria are used for surface-cracked pipe flaw evaluations, they were originally developed from through-wall-cracked pipe J-estimation schemes. Hence, their accuracy is worth reviewing in this report. They are also reviewed in detail in the short surface-cracked pipe report from this program, NUREG/CR-6298, "Fracture Behavior of Short Circumferentially Surface-Cracked Pipe".

4.1.3 Pipe Fracture Evaluation

In order to evaluate structural integrity, the load-carrying capacity of a piping system needs to be determined. In a typical J-estimation scheme, there are several means by which this can be estimated. They are based on various definitions of failure criteria such as initiation of crack growth and unstable crack growth in elastic-plastic fracture mechanics. Failure loads based on these criteria are defined below.

4.1.3.1 Initiation Load

The initiation load, P_i, is defined as the load that corresponds to initiation of crack growth in a pipe. If J is a relevant crack driving force, P_i can be estimated by solving the following nonlinear equation

$$J(P_i, a_o) - J_{Ic} = 0 \tag{4-20}$$

in which $J(P_i,a_o)$ is the energy release rate for the initial crack size, a_o, and load, P_i, and J_{Ic} is the fracture toughness at crack initiation. Standard numerical techniques, such as the bisection method, Newton-Raphson method or others, can be applied to solve Equation 4-20.

4.1.3.2 Maximum Load

In applications of nonlinear fracture mechanics, particularly for nuclear power plants, J-tearing theory is a very prominent concept for calculating the maximum load-carrying capacity of a pipe. It is based on the fact that fracture instability can occur after some amount of stable crack growth in tough and ductile materials with an attendant higher applied load level at fracture. Let J and J_R denote the crack-driving force and toughness of a ductile piping material as a function of load and crack size. The limit state characterizing fracture instability based on J-tearing theory is given by

$$J(P_{max}, a^*) = J_R(a^* - a) \tag{4-21}$$

$$\frac{\partial J}{\partial a}(P_{max}, a^*) = \frac{dJ_R}{da}(a^* - a) \tag{4-22}$$

here P_{max} and a^* represent the values of load and crack size when crack growth becomes unstable under load-controlled conditions. Equations 4-21 and 4-22 are two nonlinear simultaneous equations with the independent variables P_{max} and a^*. They can be solved by standard methods such as the Newton-Raphson method.

4.1.3.3 Load-Displacement Relationship

Another desirable feature of any J-estimation scheme is its ability to predict load-displacement or moment-rotation behavior not only up to, but preferably beyond, maximum load. This ability is important for several reasons. First, some estimation methods, such as the Paris/Tada, LBB.NRC, LBB.ENG2, and LBB.ENG3 methods, calculate the applied crack driving force (i.e., J-integral) by estimating the moment-rotation relationship and integrating that relationship to determine the applied J by an η-factor solution. Consequently, the J values depend on how well the experimental load-displacement record is predicted.

The second reason for evaluating the load-displacement predictions involves the evaluation of leak-before-break if significant thermal expansion (displacement-controlled) stresses exist. The instability predictions for such compliant loading, especially if snubbers were to be removed for more flexible designs, depend on the accuracy of the predicted load-displacement behavior.

The third reason for requiring accurate load-displacement predictions is for evaluating cracked piping when earthquake conditions prevail. For such a cyclic and dynamic load calculation, the stiffness response of the cracked pipe section for calibration of a cracked-pipe element in finite element analysis is often determined from the estimation methods (Ref. 4.17).

4.2 Improvements to Analyses

Improvements to some of the analysis methods discussed above are described in the following sections. For the most part, they were made to improve handling the short crack problem and accommodating the weld fracture problem.

4.2.1 Introduction

This section provides a discussion of a number of improvements that were made to several of the through-wall-cracked analysis methods. First, in Section 4.2.2, we provide improvements to the GE/EPRI solutions (Refs. 4.1 and 4.2) for short and long through-wall-cracked pipe subjected to bending. Next, solutions for small TWC pipes subjected to combined pressure (tension) and bending are provided. The solutions were developed using the finite element method and are tabulated in "h-function" tables completely analogous to the original GE/EPRI method. These new functions were necessary because anomalies have been observed in some of the original GE/EPRI solutions. For instance, negative rotations due to the crack were obtained in the previous solutions. Also, solutions for some values of material parameters were unavailable due to numerical problems.

Next, in Section 4.2.3, the LBB.ENG2 method is discussed in detail, with improvements made to the original method of Reference 4.6. These improvements have greatly simplified the application of the method since all equations are written in closed form rather than requiring numerical integration. Section 4.2.4 discusses a modification of the LBB.ENG2 method (referred to as the LBB.ENG3 method) to enable better predictions of crack growth in a welded pipe. Currently, to predict crack growth in a welded pipe, the Ramberg-Osgood properties of the base metal along with the fracture resistance (J-R) curve from the weld metal are used to make a fracture assessment. The method

discussed here accounts for the tensile behavior of both base and weld metal. Finally, Section 4.2.5 provides a discussion of ovalization effects on predicting crack growth in TWC pipe.

4.2.2 Improvements to GE/EPRI Method

Analytical methods for predicting the elastic or elastic-plastic behavior of large circumferential through-wall cracks in cylinders subjected to bending, tension, or combined bending and tension are well developed. Five such methods and a number of comparisons of analytically predicted results with experimental data are described in References 4.6 and 4.7. These techniques consist of developing a method for estimating the value of the J-integral. Classical J-tearing theory is used for the analyses.

Unfortunately, the ability of these J-estimation techniques to predict the crack growth behavior for short cracks ($\leq$ 12 percent of the circumference) has not been established even though such short cracks are often the concern in practical LBB analyses. Indeed, the finite element solutions compiled in the GE/EPRI handbook (Ref. 4.2) appear quite inadequate for short cracks. This section of the report presents the results of a series of finite element solutions for cracks tabulated in the spirit of the GE/EPRI handbook (Ref. 4.2).

Specifically, the solutions compiled to improve the F-, V-, and h-functions were done for Ramberg-Osgood coefficients n = 1, 2, 3, 5, 7, 10 and for several crack angles (2θ) for the following three cases:

1. Short through-wall cracks under bending (θ/π = 1/16, 1/8),
2. Long through-wall cracks under bending (θ/π = 1/4, 1/2), and
3. Short through-wall cracks under combined tension and bending (θ/π = 1/16, 1/8).

The effect of combined hoop stress, tension, and bending was examined for one case.

4.2.2.1 The Sanders' Elastic F-Function

The Sanders' F-function (Ref. 4.18) is known to be applicable for relatively long crack lengths, which are longer than the lengths used in LBB analyses for large-diameter pipe. Figure 4.1 shows that the Sanders' solution approaches zero as the crack length approaches zero. Typically, such F-functions for other geometries approach values of 1.0 to 1.3 as the crack length approaches 0 (Ref. 4.19). It was assumed by Paris and Tada in Reference 4.4, and subsequently by Brust in Reference 4.6, that Sanders' solution should approach a value of 1 as the crack length approaches zero (Ref. 4.19). Assessment of this assumption was one of the objectives of this activity. The results showed that these assumptions, which have been used for years in many of the estimation schemes, are quite adequate. Explicit forms for Sanders' functions may be found in Appendix A.

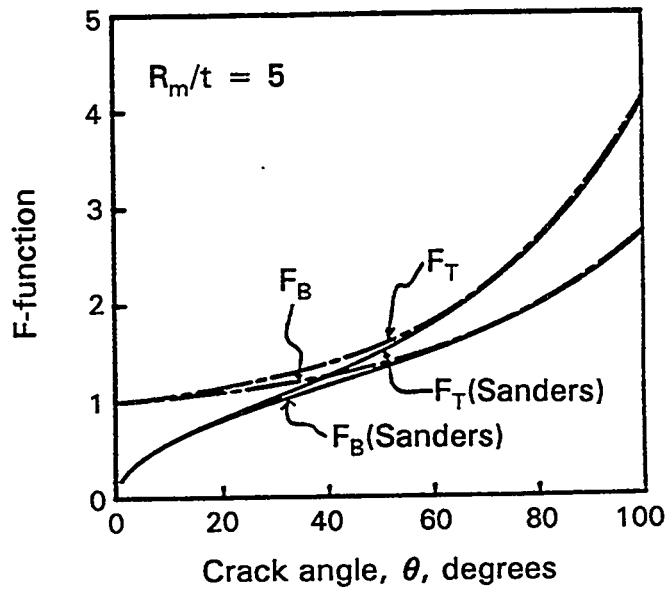

Figure 4.1 Comparison of Sanders' F-functions for $R_m/t = 5$ and a polynomial fit assuming F = 1 as the crack angle approaches zero (The solutions from Table 4.3, which represent new functions, fall on the extrapolated F_B curve)

4.2.2.2 The GE/EPRI Estimation Scheme for Bending

The GE/EPRI method takes advantage of the scaling properties in linear and nonlinear elasticity to interpolate over the range from small-scale yielding to large-scale yielding and to normalize fracture parameters such as J, crack-opening displacement (COD), pipe rotation, and load-point displacements. The elastic-plastic solution is obtained by superposition of a small-scale yielding solution and the fully plastic solution. The stress-strain law is defined by a Ramberg-Osgood relationship:

$$\frac{\epsilon}{\epsilon_0} = \frac{\sigma}{\sigma_0} + \alpha \left[\frac{\sigma}{\sigma_0} \right]^n \tag{4-23}$$

where σ_0 is an arbitrary reference stress, but is usually defined as the yield stress, n is the strain-hardening exponent, α is a curve fitting parameter, $\epsilon_0 = \sigma_0/E$, and E is the elastic modulus.

This normalization reduces the fracture parameter determination to the computation of coefficients that depend, for given types of geometry and loading, only on the strain-hardening coefficient, n, and a few geometrical parameters. Tabulated values of these coefficients were computed using the finite element technique. J, for a through-wall-cracked pipe in bending, is written in the following form:

$$J = J_e + J_p = f_1 \frac{M^2}{E} + \alpha \sigma_0 \epsilon_0 a (1 - \theta/\pi) h_1 (M/M_0)^{n+1} \quad (4\text{-}24a)$$

In Equation 4-24a, θ is the half-crack angle, a is the half crack length ($a = R_m\theta$), R_m is the mean pipe radius, and M_0 is the limit moment. Also, M is the applied moment (see Figure 4.2). The functions f_1 and h_1 are:

$$f_1 = f_1 (a_e, R_m/t) \quad (4\text{-}24b)$$

$$h_1 = h_1(\theta/\pi, R_m/t, n) \quad (4\text{-}24c)$$

and are tabulated for subsequent calculations (t is the pipe wall thickness). The effective crack size, a_e, is based on an Irwin plastic-zone correction and is written as:

$$a_e = a + \frac{r_y}{1 + (M/M_0)^2} \quad (4\text{-}25a)$$

where

$$M_0 = 4\sigma_0 R_m^2 t \left[\cos\frac{\theta}{2} - \frac{1}{2}\sin\theta\right] \quad (4\text{-}25b)$$

and

$$r_y = \frac{1}{2\pi}\left[\frac{n-1}{n+1}\right]\left[\frac{K_I}{\sigma_o}\right]^2 \quad (4\text{-}25c)$$

where K_I, the stress intensity factor, is a function of a and not of a_e. Other parameters such as crack-opening displacement and load-point rotations were also evaluated in Reference 4.2.

The GE/EPRI method, as developed for a TWC pipe, appears to underpredict loads more than desired; i.e., the compiled values of h_1 and, hence, J, are too large. In fact, for the smaller crack sizes, the results appear quite inadequate. The pipe rotations due to the crack are negative for θ/π = 1/16, as compiled in Reference 4.2 for both elastic and plastic solutions. Furthermore, Reference 4.2 shows that the V_3 (pipe elastic-crack rotation function) and the fully plastic crack-rotation function (h_4) are negative for the shorter crack lengths. It is physically impossible for the pipe to have less rotation with a crack than without a crack. The V_3 solutions were determined at the same time as the Sanders' elastic F-function was verified.

During the course of this work, it was also found that the solutions for larger cracks can be improved. Hence, Section 4.2.2.5 recompiles the GE/EPRI solutions for large cracks in bending for completeness.

As discussed in Reference 4.6, this problem may have occurred as a result of using nine noded shell elements in the computation in Reference 4.1. These elements are overly stiff and may have led to the errors discussed above. Here we recomputed the solutions of Kumar, et al., (Ref. 4.2) for θ/π = 1/8 and θ/π = 1/16 using 20-noded, isoparametric, 3D-brick elements in ABAQUS. In this fashion, more reliable predictions of crack instability for the smaller crack sizes using the GE/EPRI scheme were expected.

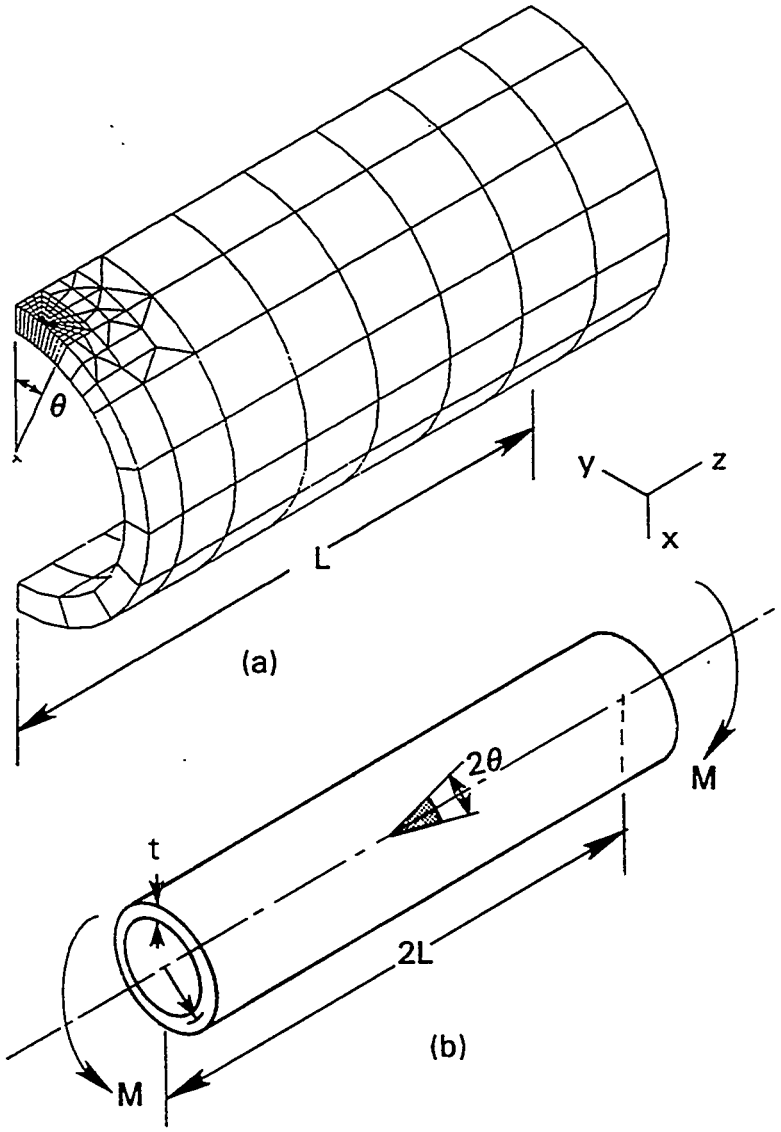

Figure 4.2 Typical finite element mesh used for (a) analysis (1/4 model) and (b) circumferential-cracked-pipe geometry

Comments on the Plastic-Zone Size Correction

In References 4.20 and 4.21, it was said that the linear elastic solution underestimates the actual J value when M/M_0 exceeds 0.5 when the J_p component is too small, i.e., for large n values. This is the apparent reason why Kumar, et al., (Ref. 4.1) extended the plastic-zone size formula established by Rice (Ref. 4.22) for the antiplane shear problem. This extended formula (Equation 4-22a) has been developed in order to increase J_e when M becomes closer to M_0. We see no justification for the choice of the $1/(1 + M/M_0)^2$ function except for ensuring continuity of the partial derivatives of J with respect to the applied load at $M = M_0$. The adequacy of applying a plastic-zone correction in the GE/EPRI method is evaluated later in this report.

4.2.2.3 Short Through-Wall Cracks (Bending)

Finite Element Model and Analysis Matrix

Six finite element meshes were developed, one for each case listed in Table 4.1. A typical finite element mesh and geometric definitions are illustrated in Figure 4.2. A quarter model was used by taking advantage of symmetry. Twenty node isoparametric brick elements were used with focused elements at the crack tip. Only one element through the pipe wall was used, and, as such, the tabulated results should be considered as average values through the pipe wall.

The elastic solutions were developed using linear elastic properties. A deformation theory plasticity algorithm in the ABAQUS finite element code was used to generate the plastic solution. Because a through-wall-cracked pipe subjected to bending is a plane stress problem, the special (hybrid) elements in the ABAQUS library, which adequately handle plastic incompressibility, are not necessary. A reduced (2 x 2) Gaussian quadrature integration rule was used.

Table 4.1 Matrix of finite element calculations for short through-wall cracks under bending (total of 30 analyses)

Model No.	Model Name	R_m/t	n[(a)]	θ/π	Remarks	Loading
1	CASE1A3DM	5	1,2,3,5,7,10	0.0625	5 Runs	Bending
2	CASE2A3DM	10	1,2,3,5,7,10	0.0625	5 Runs	Bending
3	CASE3A3DM	20	1,2,3,5,7,10	0.0625	5 Runs	Bending
4	CASE1B3DM	5	1,2,3,5,7,10	0.1250	5 Runs	Bending
5	CASE2B3DM	10	1,2,3,5,7,10	0.1250	5 Runs	Bending
6	CASE3B3DM	20	1,2,3,5,7,10	0.1250	5 Runs	Bending

(a) n = 1 is elastic

The GE/EPRI handbook (Ref. 4.2) contains compiled tables whereby J, the crack-mouth-opening displacement (at the center of the crack), δ, and the load-point rotation, ϕ, are tabulated for specific geometric and material parameters. The parameters include R_m/t, θ, and the Ramberg-Osgood power law exponent, n. For a uniaxial tensile bar, the Ramberg-Osgood relationship is as written in Equation 4-23.

Here we follow the nomenclature of the handbook, (Ref. 4.2), and compile the GE/EPRI functions for J (see Equation 4-21a), the crack-opening displacement (δ), and the additional pipe rotation due to the presence of the crack (ϕ^c):

$$\delta = \delta_e + \delta_p = f_2 M/E + \alpha\epsilon_0 a h_2 (M/M_0)^n \tag{4-26a}$$

$$\phi^c_{Tot} = \phi^c_e + \phi^c_p = f_4 M/E + \alpha\epsilon_0 h_4 (M/M_0)^n \tag{4-26b}$$

where δ_e, δ_p, and ϕ^c_e, ϕ^c_p are elastic and plastic contributions, respectively. ϕ^c_{Tot} is the total (elastic plus plastic) rotation due to the crack.

For the elastic contribution, using the GE/EPRI nomenclature (Equation 4-24), we define:

$$f_1(\theta/\pi, R_m/t) = \pi a (R_m/I)^2 F^2(\theta/\pi, R_m/t) \tag{4-27}$$

$$f_2(\theta/\pi, R_m/t) = 4a (R_m/I) V_1(\theta/\pi, R_m/t) \tag{4-28}$$

$$f_4(\theta/\pi, R_m/t) = 4(R_m/I) V_3(\theta/\pi, R_m/t) \tag{4-29}$$

In Equations 4-27 to 4-29, I is the moment of inertia of the uncracked pipe section, which for large R_m/t is written as:

$$I = \pi R_m^3 t \tag{4-30}$$

and F, V_1, and V_3 are compiled from the finite element solutions. Note that F is the function conventionally defined in the stress intensity factor definition as:

$$K_I = \sigma\sqrt{\pi a}\, F(\theta/\pi, R_m/t) \tag{4-31}$$

The plastic functions h_1, h_2, and h_4 are also compiled.

The ABAQUS deformation theory routine uses a constitutive law that includes the elastic term (Equation 4-1), i.e., it is not truly a fully plastic solution. The analyses were performed to a load level in which plastic strains greatly dominate elastic strains everywhere in the body, which effectively results in a nearly fully plastic solution. However, for completeness, we obtained the fully plastic solution by subtracting the elastic results, which had been separately calculated. Hence, from Equations 4-24 and 4-26, h_1, h_2, and h_4 were evaluated using*:

$$h_1 = \frac{J - J_e}{\alpha \sigma_0 \epsilon_0 a(1 - \theta/\pi)(M/M_0)^{n+1}} \tag{4-32}$$

$$h_2 = \frac{\delta - \delta_e}{\alpha \epsilon_0 a(M/M_0)^n} \tag{4-33}$$

$$h_4 = \frac{(\phi - \phi_e^c - \phi_e^{nc} - \phi_p^{nc})}{\alpha \epsilon_0 (M/M_0)^n} \tag{4-34}$$

In Equations 4-32 to 4-34, J, δ, and ϕ are obtained from the ABAQUS finite element solution. Also, in Equation 4-34, the "nc" superscript refers to "no crack". These are well known and are listed in Kumar, et al., (Ref. 4.2). The dimensionless elastic functions are compiled first (F, V_1, V_3) to determine J_e, δ_e, and ϕ_c^e. Then the results of the ABAQUS solution provide J, δ, and ϕ, which are elastic plus plastic values. From these, Equations 4-32 to 4-34 provide the h_1, h_2, and h_4 values.

4.2.2.4 Results for Short Cracks

Table 4.1 showed the matrix of finite element calculations that were performed. A complete set of analyses was performed using ABAQUS for (n = 1, 2, 3, 5, 7, 10). Both elastic and fully plastic (deformation theory) computations were made for bending loads.

Since the original GE/EPRI functions for J-integral were found to be more accurate for large crack sizes, a comparison for the case of $R_m/t=10$ was made to verify the accuracy of our approach. For this case, $\theta/\pi = 0.5$ and n = 3 were chosen. Table 4.2 lists the results. The comparison for the value of the J-integral (h_1) is excellent. Further verification may be found in Reference 4.23. The h_2- and h_4-functions that were computed by ABAQUS appear to be smaller than the original functions. Additional calculations for large TWC pipe are provided in Section 4.2.2.5.

* Note that Reference 4.3 also compiles f_3 and h_3, which are the axial stretch due to the crack. However, for a bending only load, this displacement is not relevant.

Table 4.2 Check Case for $R_m/t = 10$, $\theta/\pi = 1/2$, and n = 3

Function	GE/EPRI (Ref. 4.2)	3D-Solid ABAQUS (This report)
h_1	2.105	2.008
h_2	3.331	3.015
h_4	3.232	2.756

Tables 4.3 through 4.6 provide the solutions compiled for all of the cases listed in Table 4.1. Table 4.3 is the elastic solution, while Tables 4.4 to 4.6 provide plastic solutions for $R_m/t = 5$, 10, and 20, respectively. Note that the GE/EPRI handbook did not provide solutions for n = 10 and some of the n = 7 cases due to numerical difficulties.

Table 4.3 F, V_1, and V_3 for bending ($R_m/t = 5$, 10, and 20) (ABAQUS - 3D solid element solution); this represents the n=1 case of Table 4.1

		$R_m/t = 5$	$R_m/t = 10$	$R_m/t = 20$
$\theta/\pi = 1/16$	F	1.022	1.049	1.097
	V_1	1.234	1.206	1.111
	V_3	0.028	0.035	0.098
$\theta/\pi = 1/8$	F	1.103	1.208	1.418
	V_1	1.388	1.480	1.482
	V_3	0.126	0.160	0.231

Table 4.4 h-functions for through-wall cracks in bending ($R_m/t = 5$) (ABAQUS - 3D solid element solution)

		n = 2	n = 3	n = 5	n = 7	n = 10
$\theta/\pi = 1/16$	h_1	5.202	5.451	5.766	5.681	5.263
	h_2	6.686	6.896	7.003	6.715	6.087
	h_4	0.553	0.826	1.452	1.879	2.371
$\theta/\pi = 1/8$	h_1	4.575	4.484	3.976	3.372	2.464
	h_2	5.972	5.820	4.999	4.164	2.959
	h_4	0.958	1.194	1.454	1.461	1.291

Table 4.5 h-functions for through-wall cracks in bending ($R_m/t = 10$) (ABAQUS - 3D solid element solution)

		n = 2	n = 3	n = 5	n = 7	n = 10
$\theta/\pi = 1/16$	h_1	5.588	6.225	6.761	6.784	6.749
	h_2	6.701	7.422	7.739	7.632	7.527
	h_4	0.745	1.156	1.802	2.220	2.826
$\theta/\pi = 1/8$	h_1	5.694	5.791	5.512	4.790	3.823
	h_2	6.619	6.654	6.319	5.329	4.221
	h_4	1.234	1.550	1.886	1.864	1.713

Table 4.6 h-functions for through-wall cracks in bending ($R_m/t = 20$) (ABAQUS - 3D solid element solution)

		n = 2	n = 3	n = 5	n = 7	n = 10
$\theta/\pi = 1/16$	h_1	6.272	7.044	8.022	8.756	8.815
	h_2	7.155	7.073	8.050	8.787	8.812
	h_4	0.979	1.505	2.348	3.087	3.770
$\theta/\pi = 1/8$	h_1	8.019	8.448	8.281	7.748	6.524
	h_2	7.934	7.498	7.491	7.160	5.890
	h_4	1.730	2.216	2.738	2.963	2.728

In order to obtain the h-functions, the ABAQUS calculations involved elastic and plastic analyses (deformation theory) for a series of bending moment loads until a fully plastic criterion was met. One check on the accuracy of the fully plastic h-functions listed in Tables 4.4 through 4.6 was to calculate these functions at all load levels and verify that the h-functions do not vary once a load level where plasticity dominates is reached. A typical plot of the h_1 function and bending moment, shown in Figure 4.3, indicates that the h_1 function levels off after some load value. This criterion was used to produce all of the h-functions. Note that this plotting procedure is performed in order to obtain the h-functions only because ABAQUS includes both elastic and plastic strains in the solution.

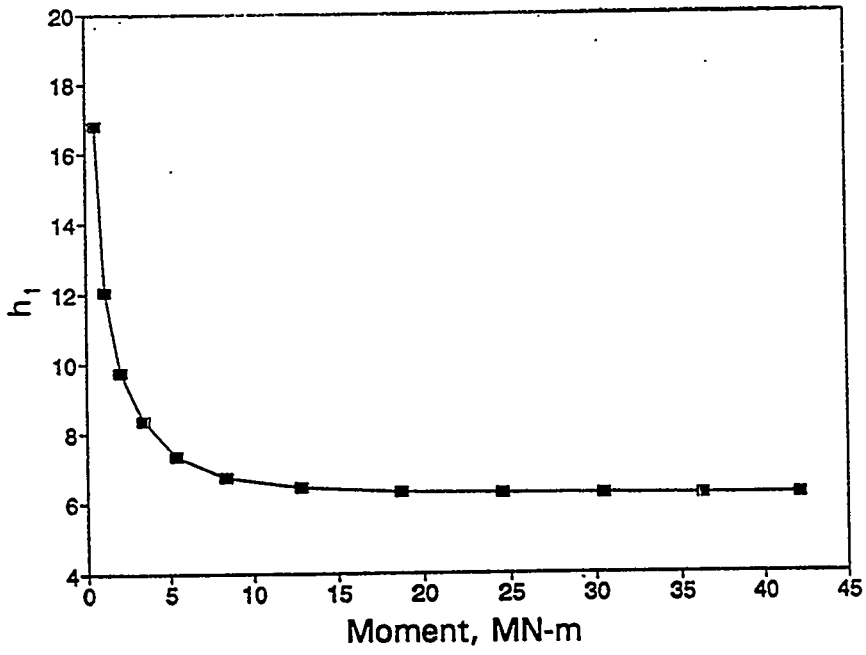

Figure 4.3 Plasticity function h_1 (ABAQUS - Solid Element Results) for pipe under bending with $R_m/t = 10$, $n = 3$, and $\theta/\pi = 0.0625$

Discussion of Results

The differences between the previously developed solutions (Ref. 4.2) and the present results appear to be most important for small crack sizes (θ/π = 1/16 and 1/8). The present solutions were developed using the 3-dimensional solid elements (20-node brick) and the deformation theory algorithm of ABAQUS. The solutions presented here are believed to be the more accurate of the two solutions because full three-dimensional elements were used instead of relying on shell elements. However, the results of Reference 4.2 will underpredict loads. The analyses presented in Reference 4.2 appeared to produce results that are too stiff, and, indeed, solutions for large n were not possible as convergence problems occurred. Here, no convergence problems were experienced. The problems with the short-crack solutions of Reference 4.2 are discussed in much more detail in References 4.6 and 4.7.

A plot of the F-function results (Equation 4-31) computed in this work and the GE/EPRI solution is seen in Figure 4.4a as a function of R_m/t for θ/π = a/b = 1/16, where a is the crack length and b is the uncracked ligament. The differences are about three percent. Figure 4.4b shows comparison of V_1 (Equation 4-28), which is related to the crack-opening displacement. The differences are about 20 percent for R_m/t = 5. Comparisons of h_1 (J-integral) and h_2 (crack-opening displacement) values are presented in Figures 4.5 and 4.6, respectively. The maximum difference between h_1 and h_2 values for the two solutions is less than 25 percent.

Finally, comparisons of J as a function of moment are made in Figures 4.7, for θ/π = 1/8, R_m/t = 5, and n = 3, 7, and in Figure 4.8, for θ/π = 1/16, R_m/t = 20, and n = 3, 7. As seen, the differences between the original and modified solutions are not so significant for load predictions.

No comparisons are made with the h_4 functions. As discussed earlier, the original GE/EPRI h_4 functions are negative for most small-crack cases that were developed in Reference 4.2 and were obviously in error in these cases.

4.2.2.5 Long Through-Wall Cracks (Bending) (θ/π = 1/2, θ/π = 1/4)

In order to be consistent with the functions developed for short through-wall cracks using ABAQUS 3D-solid elements, additional calculations were performed for longer cracks. The methodology and technical discussions are identical to those described for short cracks. This section describes only the models used and results obtained. Again, a comparison is made with the functions reported in Reference 4.2.

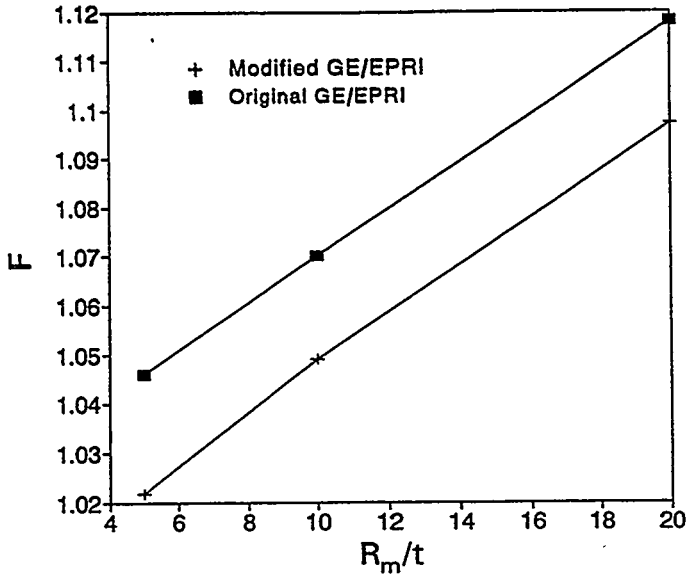

(a) F-function comparison, $\theta/\pi = 1/16$ (F relates elastic stress intensity factor to stress)

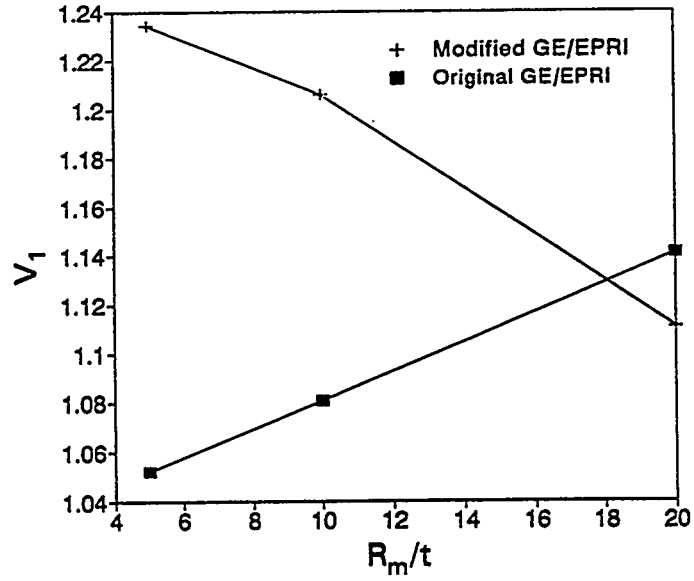

(b) Comparison of V_1-function values for $\theta/\pi = 1/16$ (V_1 relates elastic center-crack-mouth-opening displacement to moment)

Figure 4.4 Comparison of ABAQUS FEM results with past GE/EPRI solutions for elastic functions

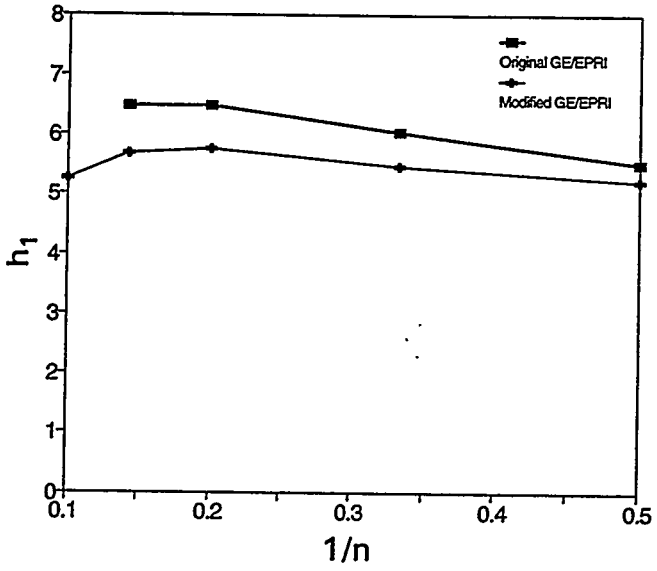

(a) $R_m/t = 5$, $\theta/\pi = 1/16$

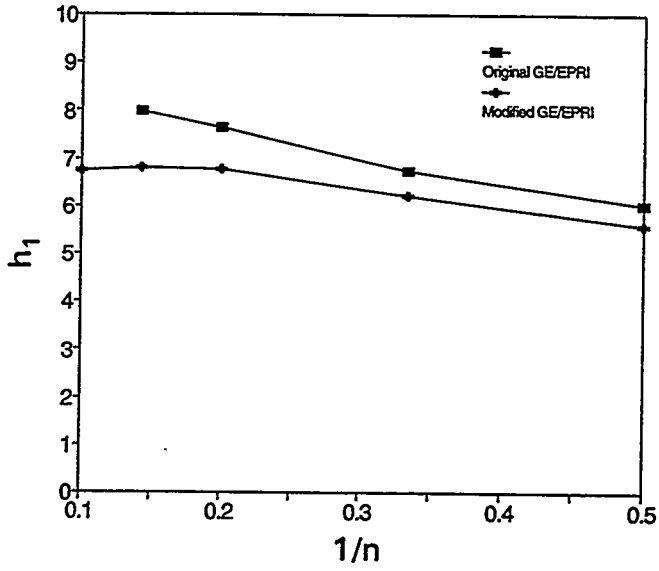

(b) $R_m/t = 10$, $\theta/\pi = 1/16$

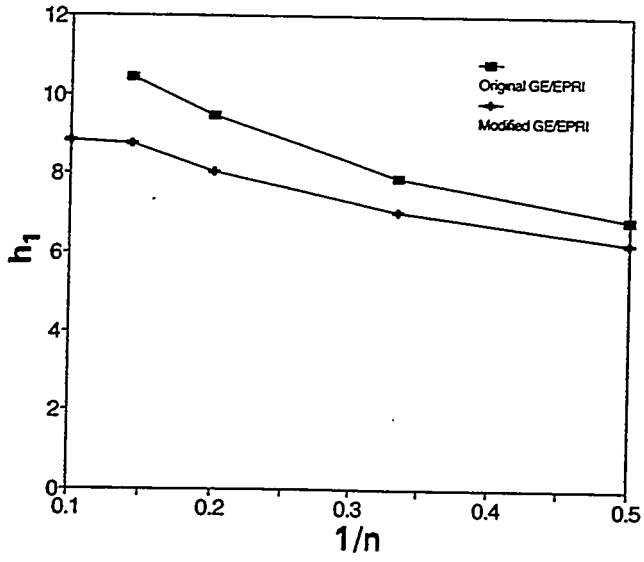

(c) $R_m/t = 20$, $\theta/\pi = 1/16$

Figure 4.5 Comparison of ABAQUS FEM results with past GE/EPRI solutions for h_1 fully plastic functions (h_1 relates fully plastic J to moment)

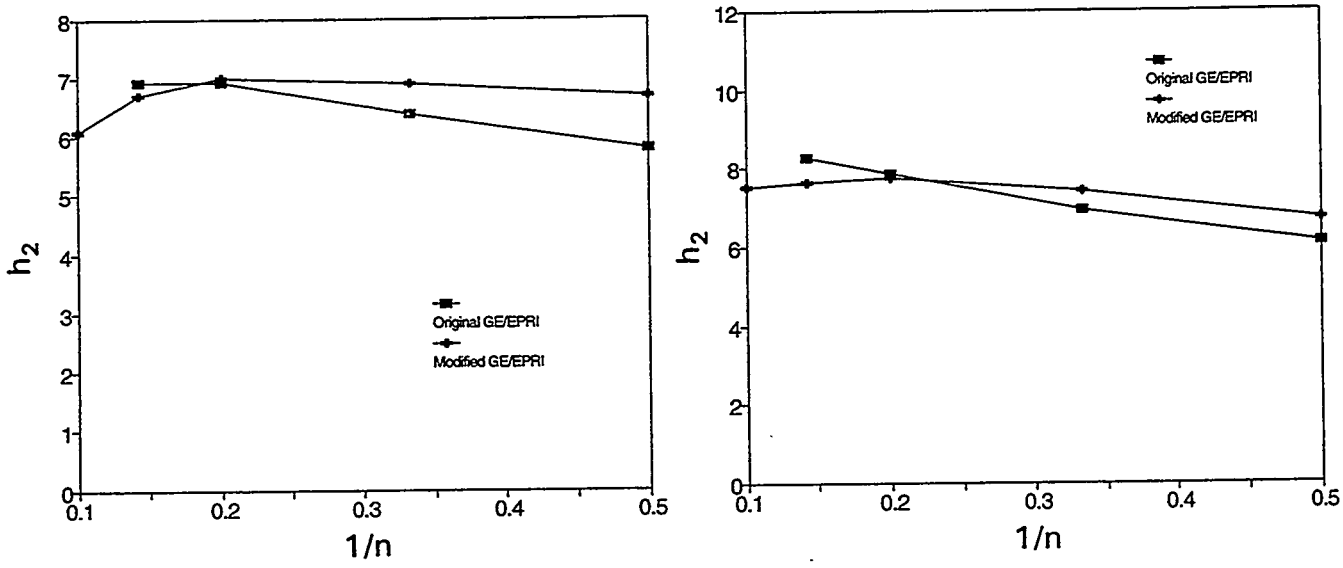

(a) $R_m/t = 5$, $\theta/\pi = 1/16$

(b) $R_m/t = 10$, $\theta/\pi = 1/16$

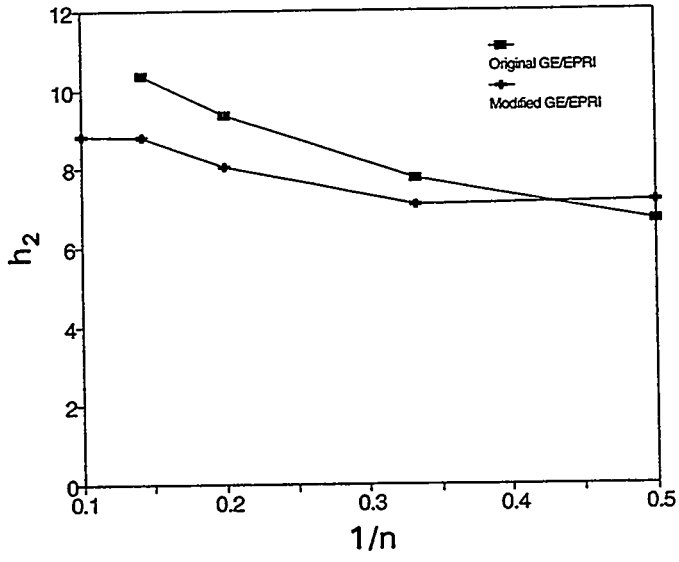

(c) $R_m/t = 20$, $\theta/\pi = 1/16$

Figure 4.6 Comparison of ABAQUS FEM results with past GE/EPRI solutions for h_2 fully plastic functions (h_2 relates fully plastic center-crack-opening displacement to moment)

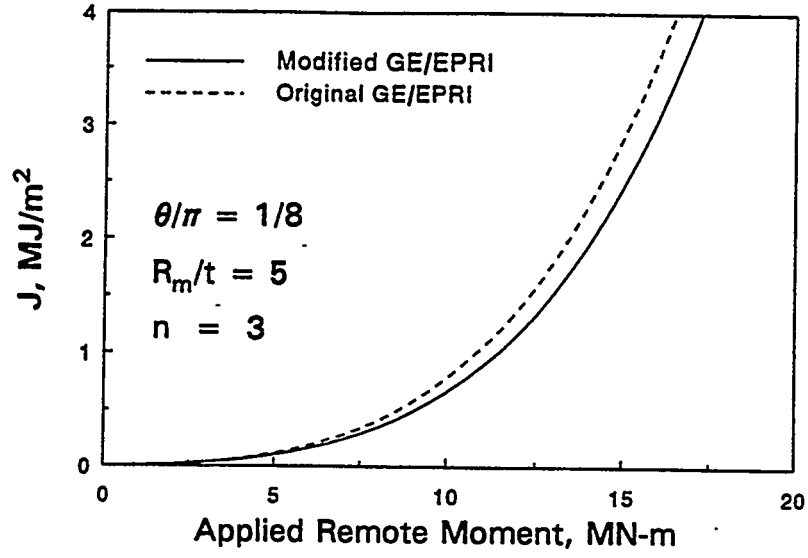

(a) n = 3

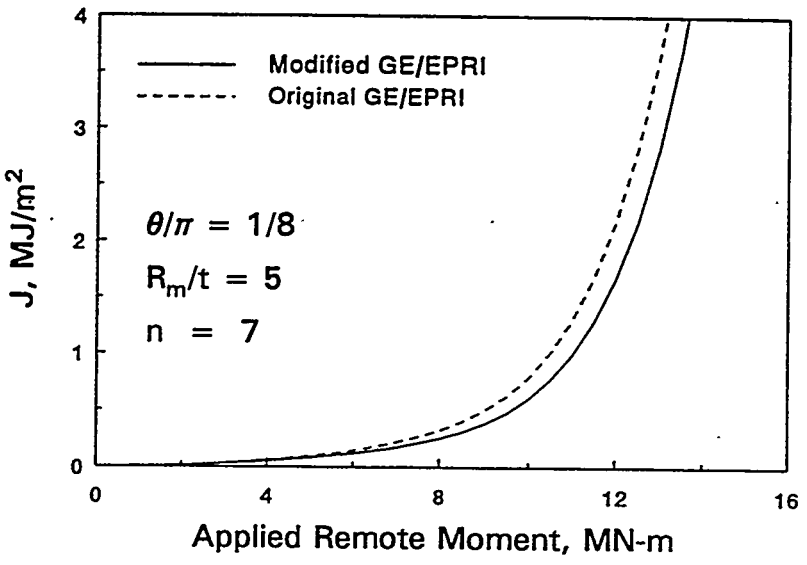

(b) n = 7

Figure 4.7 Comparison of J versus moment for $R_m/t = 5$, $\theta/\pi = 1/8$

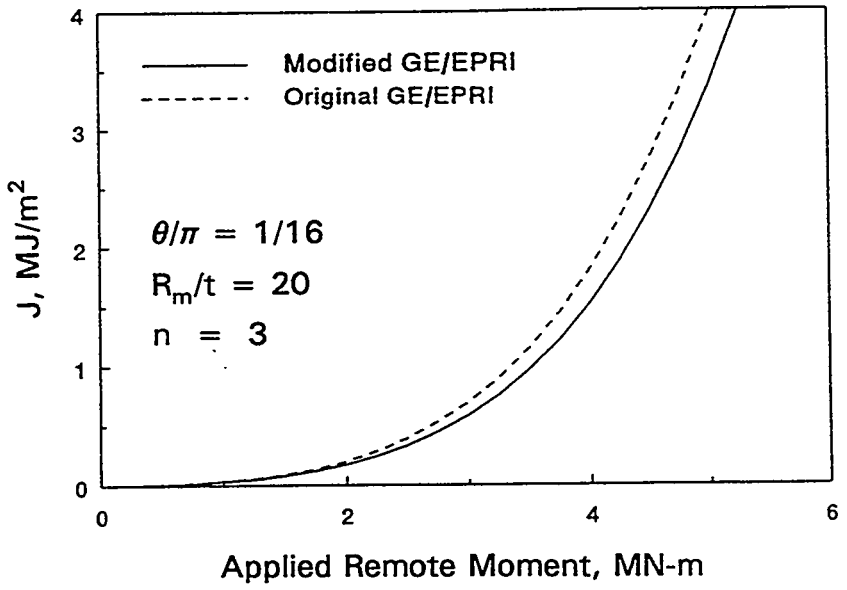

(a) n = 3

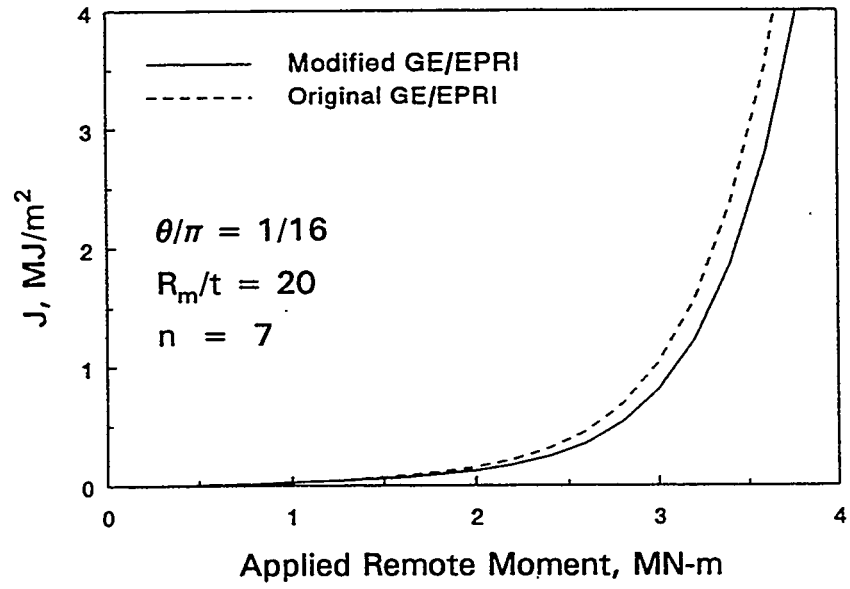

(b) n = 7

Figure 4.8 Comparison of J versus moment for $R_m/t = 20$, $\theta/\pi = 1/16$

Finite Element Model and Analysis Matrix

Six finite element meshes were developed, one for each case listed in Table 4.7. The details of the mesh, solution techniques, etc., are described above.

Table 4.7 Matrix of finite element calculations for long through-wall cracks under bending (total of 30 analyses)

Model No.	Model Name	R_m/t	n[(a)]	θ/π	Remarks	Loading
1	CASE4A3DM	5	1,2,3,5,7,10	0.5000	5 runs	Bending
2	CASE4B3DM	10	1,2,3,5,7,10	0.5000	5 runs	Bending
3	CASE4C3DM	20	1,2,3,5,7,10	0.5000	5 runs	Bending
4	CASE5A3DM	5	1,2,3,5,7,10	0.2500	5 runs	Bending
5	CASE5B3DM	10	1,2,3,5,7,10	0.2500	5 runs	Bending
6	CASE5C3DM	20	1,2,3,5,7,10	0.2500	5 runs	Bending

(a) n = 1 is the elastic case.

Results

Tables 4.8 through 4.11 provide the solutions compiled for all the cases listed in Table 4.7. Table 4.8 is the elastic solution, while Tables 4.9 to 4.11 provide solutions for $R_m/t = 5$, 10 and 20, respectively.

Table 4.8 F, V_1, V_2, and V_3 for bending with $R_m/t = 5$, 10, and 20

	Function	$R_m/t = 5$	$R_m/t = 10$	$R_m/t = 20$
$\theta/\pi = 1/4$	F	1.434	1.697	2.120
	V_1	2.008	2.379	3.079
	V_3	0.327	0.439	0.637
$\theta/\pi = 1/2$	F	2.552	3.031	3.902
	V_1	5.331	7.165	11.585
	V_3	3.792	5.228	8.567

Table 4.9 h-functions for through-wall cracks in bending for $R_m/t = 5$ (ABAQUS - 3D solid solution)

	Function	n = 2	n = 3	n = 5	n = 7	n = 10
$\theta/\pi = 1/4$	h_1	4.109	3.720	2.671	1.821	1.019
	h_2	5.319	4.706	3.283	2.189	1.194
	h_4	1.298	1.543	1.426	1.082	0.641
$\theta/\pi = 1/2$	h_1	1.981	1.408	0.684	0.418	0.154
	h_2	3.478	2.271	1.019	0.598	0.215
	h_4	2.927	2.034	0.936	0.543	0.196

Table 4.10 h-functions for through-wall cracks in bending for $R_m/t = 10$ (ABAQUS - 3D solid solution)

	Function	n = 2	n = 3	n = 5	n = 7	n = 10
$\theta/\pi = 1/4$	h_1	5.952	5.169	3.475	2.895	1.689
	h_2	6.629	5.757	3.853	3.209	1.844
	h_4	1.676	1.896	1.712	1.593	1.006
$\theta/\pi = 1/2$	h_1	2.887	2.008	1.060	0.579	0.267
	h_2	4.693	3.015	1.452	0.777	0.349
	h_4	4.038	2.756	1.364	0.592	0.116

Table 4.11 h-functions for through-wall cracks in bending for $R_m/t = 20$ 4(ABAQUS - 3D solid solution)

	Function	n = 2	n = 3	n = 5	n = 7	n = 10
$\theta/\pi = 1/4$	h_1	9.469	8.147	7.474	7.983	3.165
	h_2	8.916	7.704	5.173	2.970	1.055
	h_4	2.375	2.555	2.044	1.361	0.548
$\theta/\pi = 1/2$	h_1	5.009	3.893	2.300	2.096	1.051
	h_2	7.913	5.773	3.052	1.517	0.623
	h_4	6.611	5.023	2.727	1.379	0.572

4.2.2.6 Short-Through-Wall-Cracked Pipe Under Combined Pressure and Bending ($\theta/\pi = 1/8$, $\theta/\pi = 1/16$)

The GE/EPRI estimation method to calculate fracture parameters such as J, COD, displacements, and rotations for through-wall-cracked pipes under bending only was described in Reference 4.2 and above.

This estimation scheme can be extended for combined bending (M) and pressure (p) loads using two approaches:

1. A nondimensional parameter λ is used to define a proportionality relationship between pressure (or tension) and moment, M. The GE/EPRI elastic and plastic functions F, V and h are now also a function of λ. This relational approach is not convenient for pipes that are subjected to a fixed internal pressure and varying bending moment, the latter being the case in nuclear piping for BWR and PWR systems. Some solutions using λ were compiled in Reference 4.20.

2. The second approach is to determine the plastic h functions for a fixed internal pressure and increasing bending moment using procedures similar to those used for tension and bending alone. This approach is described next before providing solutions. The calculated h values are for an internal pressure of 15.51 MPa (2,250 psi). Hence, using these functions for a pressure of 7.24 MPa (1,050 psi) should overestimate predictions of the applied J.

Deformation and Flow Theories

In developing constitutive equations for work-hardening materials, there are two basic approaches that can be used to calculate the GE/EPRI functions. The first type of formulation is the deformation theory in the form of a total stress-strain relationship. This approach assumes that the state of stress determines the state of strain uniquely as long as the plastic deformation continues. This is identical with the nonlinear elastic stress-strain relationship with no unloading and is valid for loading paths that are only proportional. The second type of formulation is the incremental or flow theory in the form of an incremental stress-strain relationship. This theory relates the increment of plastic strain components to the state of stress and the stress increment. It is more general than the deformation theory and can be applied for a wide variety of loading conditions including nonproportional and cyclic loads. For a typical monotonic pipe test under combined bending and tension, the tensile force is usually held constant due to constant internal pressure, but the bending moment is gradually increased until the maximum load-carrying capacity of the pipe is reached. During the progression of load increments, the load factor, which is defined as the ratio of bending moment and tension, also increases, thus violating load proportionality, the essential condition to the validity of deformation theory of plasticity. However, this nonproportionality caused by applying tension first, followed by bending, or vice-versa, has little effect on both the path independence of J and on the final value of J at the end of the complete loading. In other words, for practical purposes, it is not important whether we apply tension first, followed by bending, bending followed by tension, or apply both tension and bending simultaneously. Kaiser and Sonnerlind (Refs. 4.24 and 4.25) have shown this by investigating the single-notch specimen subjected to combined tension and bending. We will also

show this here for the through-wall-cracked pipe problem that subjects the pipe to combined tension and bending.

In addition, the typical values of service pressure in a pipe are 15.51 MPa (2,250 psi) for PWRs and 7.24 MPa (1,050 psi) for BWRs. The pipe material behavior under these pressure loadings is mostly elastic with a small plastic-zone size for the crack sizes considered here. Hence, both Deformation and Flow Theories should be equally applicable for finite element analysis to determine the GE/EPRI functions. We will take advantage of this in developing the h-functions for cracked pipe subjected to combined tension and bending. The resulting estimation method is much more convenient to use compared with the original GE/EPRI method (Ref. 4.20) for combined tension/bending.

Finite Element Model and Analysis Matrix

Six finite element meshes were developed, one for each case listed in Table 4.12. A typical finite element mesh and geometric definition are illustrated in Figure 4.2. A quarter model is used to take advantage of symmetry. Twenty-noded isoparametric brick elements are used with focused elements at the crack tip. Only one element through the pipe wall is used, and, as such, the tabulated results should be considered as average values through the pipe wall.

Table 4.12 Matrix of finite element calculations for short through-wall cracks under combined bending and tension (total of 30 analyses)

Model No.	Model Name	R_m/t	n	θ/π	Remarks	Loading
1	CASE1A3DTM	5	2,3,5,7,10	0.0625	5 Runs	Tension & bending
2	CASE2A3DTM	10	2,3,5,7,10	0.0625	5 Runs	Tension & bending
3	CASE3A3DTM	20	2,3,5,7,10	0.0625	5 Runs	Tension & bending
4	CASE1B3DTM	5	2,3,5,7,10	0.1250	5 Runs	Tension & bending
5	CASE2B3DTM	10	2,3,5,7,10	0.1250	5 Runs	Tension & bending
6	CASE3B3DTM	20	2,3,5,7,10	0.1250	5 Runs	Tension & bending

Validation of Deformation Theory

In order to substantiate that deformation theory produces adequate results for nonproportional loading, a verification study was conducted to determine the adequacy of results from the deformation theory of plasticity. As an example, consider a TWC pipe with $R_m/t = 10$, $n = 5$, and $\theta/\pi = 1/8$, which is subjected to axial tension corresponding to an internal pressure of 15.51 MPa (2,250 psi) and a bending moment. It is assumed that the material stress-strain relationship can be represented by the Ramberg-Osgood equation. Two finite element analyses were conducted for this pipe using deformation and incremental stress-strain formulations. The computer code used was ABAQUS with 20-noded, 3-D solid elements. In both analyses, the axial tension due to the pressure is applied first, followed by the application of the moment. During the application of the moment, the tension is held constant. Figure 4.9 shows the results of both analyses presented in terms of J-integral plots as a function of applied bending moment. They clearly indicate that the finite element results by deformation theory provide accurate estimates of crack driving force when compared with those

obtained from flow or incremental theory. Figure 4.10 shows the percentage error for various applied loads, where the error is defined as the ratio of the difference between J from flow theory and deformation theory divided by J from flow theory times 100. From this figure, it appears that the prediction based on deformation theory is slightly higher than that based on flow theory. The maximum absolute error was less than 1 percent. Hence, the deformation theory was adequate for use in the rest of the finite element analyses. This allowed significant savings of computational effort in determining the GE/EPRI functions and results in a simpler estimation scheme. In the original GE/EPRI method for combined pressure (or tension) and bending (Ref. 4.20), a λ factor, defined as the ratio of tension force to bending moment, was defined. The h-functions were compiled for constantly increasing λ. Since the axial tension in nuclear pipe is constant and the bending moment is constantly increased, λ changes throughout the analysis. This makes the engineering analysis inconvenient since as λ changes during the moment application phase, the h-functions change, and one must reinterpolate throughout the tables. With the solutions from this report, the h-functions are constant once the pipe geometry, material properties, and constant axial tension from the pressure are defined. This will become clear shortly.

The ABAQUS analysis for each case is performed in two load steps. In the first step (Step 1), an axial tension force (corresponding to internal pressure) is applied to the end of the pipe. The second step (Step 2) consists of an increasing bending load until fully plastic conditions are obtained. The deformation theory of plasticity algorithm is used in both load steps. A reduced (2 x 2) Gaussian quadrature integration rule was used.

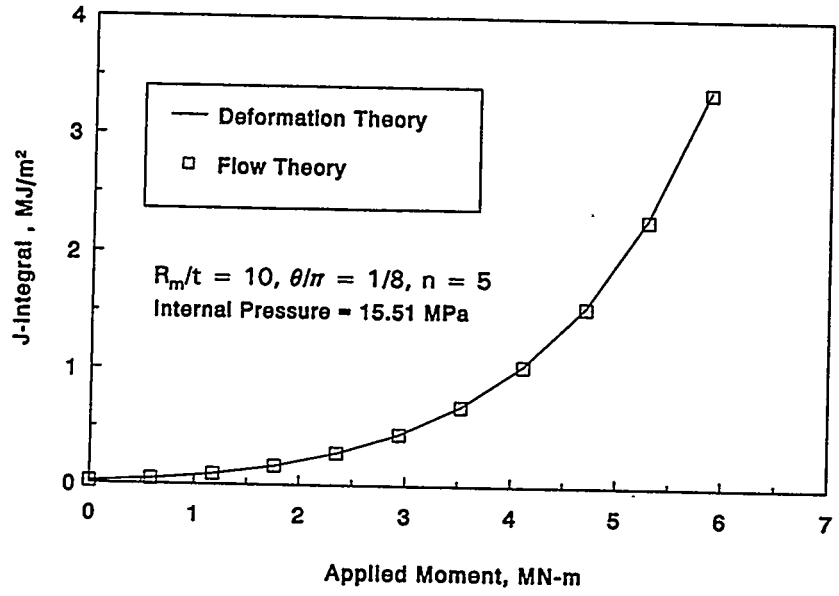

Figure 4.9 J-integral by deformation and flow theories as a function of applied bending moment for combined tension and bending non-proportional loading

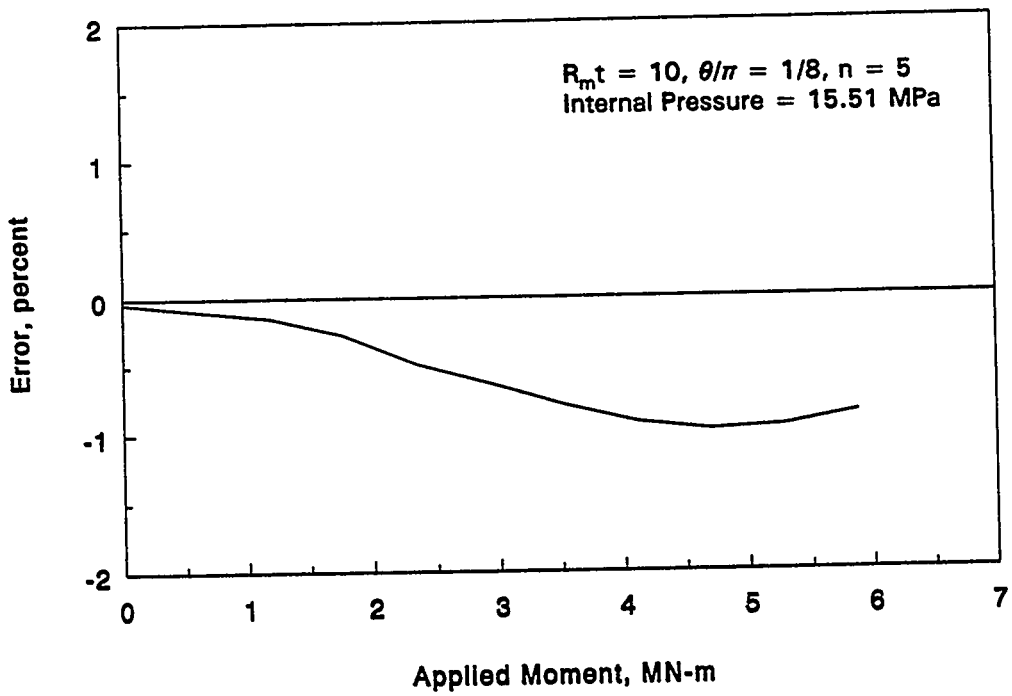

Figure 4.10 Percentage of error in J-integral estimates by deformation theory of plasticity for combined tension and bending non-proportional loading

4.2.2.7 Fracture Parameters

Following the convention of Reference 4.2, the fracture parameters J, COD (crack-mouth-opening displacement), load-line displacement, and total relative rotation due to the crack (ϕ_c) are described below. A list of additional previously undefined variables to be used in equations that follow are first described below:

R_0 = outside radius of pipe

R_i = inside radius of pipe

p = internal pressure

σ_T = applied axial stress = $pR_i^2/(R_0^2-R_i^2)$

P = $2\pi\sigma_T R_m t$ = total axial load

K_{IB} = Mode I stress intensity factor for pure bending

K_{IT} = Mode I stress intensity factor for pure tension

P_0 = $2\sigma_0 R_m t\,[\pi - \theta - 2\sin^{-1}(0.5\sin\theta)]$ = limit load (for axial tension loads when $\sigma_f = \sigma_0$)

M_0 = $4\sigma_0 R_m^2 t\,[\cos(\theta/2) - 0.5\sin(\theta)]$ = limit moment (for bending loads when $\sigma_f = \sigma_0$)

Δ^c = Axial displacement due to the crack

The various fracture parameters can now be expressed as follows, consistent with the assumptions discussed above:

$$J_{(ABAQUS)} = J_T + J_B \tag{4-35a}$$

where J_{ABAQUS} is the J value from ABAQUS under fully plastic condition at the end of Step 2. J_T is the component due to the constant applied pressure (tension) and J_B is the component due to bending with constant tension.

$$J_T = J_T^e + J_T^p \tag{4-35b}$$

where

$$J_T^e = \left[\sigma_T \frac{\sqrt{\pi a F_T}}{E}\right]^2 = \frac{K_{IT}^2}{E} \tag{4-36}$$

and

$$J_T^p = \alpha\sigma_o\epsilon_o a(1-\theta/\pi)h_1^T(P/P_o)^{n+1} \tag{4-37}$$

Similarly

$$J_B = J_B^e + J_B^p \tag{4-38}$$

$$J_B = \frac{K_{IB}^2}{E} + \alpha\sigma_o\epsilon_o a(1-\theta/\pi)\,h_1^B(M/M_o)^{n+1} \tag{4-39}$$

Hence

$$J_B = J_{ABAQUS} - J_T^e - J_B^e - J_T^P \tag{4-40}$$

Using Equations 4-39 and 4-40, h_1^B can be tabulated using:

$$h_1^B = \frac{(J_{ABAQUS} - \frac{K_{IT}^2 + K_{IB}^2}{E} - J_T^P)}{\alpha\sigma_0\epsilon_0 a(1-\theta/\pi)\ (M/M_0)^{n+1}} \tag{4-41}$$

4.2.2.8 Crack-Mouth-Opening Displacement (δ)

$$\delta_{ABAQUS} = \delta_T + \delta_B \tag{4-42}$$

where δ_{ABAQUS} is the crack-mouth-opening displacement value from ABAQUS under fully plastic conditions at the end of Step 2. δ_T is the component due to tension and δ_B is the component due to bending.

The tension component from the elastic-plastic solution is:

$$\delta_T = f_2(\theta/\pi, R_m/t)\frac{P}{E} + \alpha\epsilon_0 a h_2^T (P/P_0)^n \tag{4-43}$$

where

$$f_2(\theta/\pi, R_m/t) = \frac{2a\sigma_T}{\pi R_m t} V_1^T(\theta/\pi, R_m/t) \tag{4-44}$$

The functions h_2^T and V_1^T are obtained from the tabulated values for pipes under tension in Reference 4.2.

The bending component, using an elastic-plastic solution, is:

$$\delta_B = f_2(\theta/\pi, R_m/t)\ M/E + \alpha\epsilon_0 a h_2^B (M/M_0)^n \tag{4-45}$$

4.2.2.9 Displacement Along Pipe Lines (Δ)

$$\Delta^{c}_{ABAQUS} - \Delta^{nc} = \Delta^{c}_{T} + \Delta^{c}_{B} \tag{4-46}$$

where Δ^{c}_{ABAQUS} is the value of the displacement along the pipe axis, (i.e., the axial "stretch" due to crack) from ABAQUS under fully plastic conditions at the end of Step 2.* Δ^{c}_{T} is the component due to tension and Δ^{c}_{B} is the component due to bending.

The tension component from elastic-plastic solution is

$$\Delta^{c}_{T} = 4\frac{\sigma_T a}{E} V_2^{T}(\theta/\pi, R_m/t) + \alpha\epsilon_0 a h_3^{T}(\theta/\pi, n, R_m/t)[P/P_0]^n \tag{4-47}$$

The functions V_2^T and h_3^T are known from tables for pipes under tension in Reference 4.2.

The bending component from the elastic-plastic solution is:

$$\Delta^{c}_{B} = 4\frac{MR_m}{IE} a V_2^{B}(\theta/\pi, R_m/t) + \alpha\epsilon_0 a h_3^{B}(M/M_0)^n \tag{4-48}$$

The elastic function V_2^B is known from calculated tables for pipes under tension and bending in Reference 4.2. h_3^B is tabulated from Equations 4-44 and 4-45.

4.2.2.10 Rotation of Pipe Due to Crack (ϕ^c)

$$\phi^{c}_{ABAQUS} = \phi^{c}_{T} + \phi^{c}_{B} \tag{4-49}$$

where ϕ^{c}_{ABAQUS} is the total rotation of both ends of the pipe due to the crack as obtained from ABAQUS. ϕ^{c}_{B} is the component due to the tension and ϕ^{c}_{B} is the component due to bending.

The tension component from the elastic-plastic solution is

$$\phi^{c}_{T} = f_4(\theta/\pi, R_m/t)\frac{P}{E} + \alpha\epsilon_0 h_4^{T}\left[\frac{P}{P_0}\right]^n \tag{4-50}$$

---

* The displacement due to no cracks, Δ^{nc}, is evaluated using equations in Reference 4.2. Note that Δ^{nc} is only due to the tension load.

where

$$f_4(\theta/\pi, R_m/t) = \frac{2}{\pi R_m t} V_3^T(\theta/\pi, R_m/t) \tag{4-51}$$

The functions h_4^T and V_3^T are known from calculated tables for pipes under tension (see Ref. 4.2).

The bending component from the elastic-plastic solution is

$$\phi_B^c = \left[f_4(\theta/\pi, R_m/t)M/E + \alpha\epsilon_0 h_4^B\right][M/M_0]^n \tag{4-52}$$

where

$$f_4(\theta/\pi, R_m/t) = \left[4R_m V_3^B(\theta/\pi, R_m/t)\right]/I \tag{4-53}$$

The elastic function V_3^B is known from calculated tables for pipes under bending (see Table 4.3). Hence, using Equations 4-50 and 4-51, h_4^B is calculated as follows:

$$h_4^B = \frac{\left[\phi_{ABAQUS}^c - \frac{2P}{\pi R_m t E} V_3^T - \alpha\epsilon_0 h_4^T \left[\frac{P}{P_0}\right]^n - \frac{4R_m M}{IE} V_3^B - \phi^{nc}\right]}{\alpha\epsilon_0 a \left[\frac{M}{M_0}\right]^n} \tag{4-54}$$

ϕ^{nc} is the rotation due to the bending component only.

4.2.2.11 Equation Summary

To evaluate J, δ, Δ and ϕ for combined bending and tension, use the following equations.

$$J = J_T + J_B^e + \alpha\sigma_0\epsilon_0 a (1-\theta/\pi)\, h_1^B (M/M_0)^{n+1} \tag{4-55}$$

$$\delta = \delta_T + \delta_B^e + \alpha\epsilon_0 a h_3^B (M/M_0)^n \tag{4-56}$$

$$\Delta^c = \Delta_T^c + \alpha\epsilon_0 a h_3^B (M/M_0)^n \tag{4-57}$$

$$\phi^c = \phi_T^c + \phi_B^c|_{elastic} + \alpha\epsilon_0 h_4^B (M/M_0)^n \quad (4\text{-}58)$$

In Equations 4-55 through 4-58, J_T, δ_T, Δ_T^c, and ϕ_T^c are evaluated using the tension solutions from Reference 4.2, including both elastic and plastic components, and using the constant applied pressure of 15.51 MPa (2,250 psi). J_B^e, δ_B^e, and $\phi_B^c|_{elastic}$ are evaluated from Table 4.3.

h_1^B, h_2^B, h_3^B, and h_4^B are tabulated in Tables 4.13 through 4.15, which provide the solutions compiled for all the cases listed in Table 4.12.

Table 4.13 h-functions for circumferential through-wall-cracked pipe under combined pressure and bending for R_m/t = 5 and pressure = 15.51 MPa (2,250 psi)

	Function	n = 2	n = 3	n = 5	n = 7	n = 10
θ/π = 1/16	h_1	5.408	5.725	6.060	5.967	5.341
	h_2	6.851	7.115	7.232	6.979	6.153
	h_3	1.245	1.299	1.772	1.868	1.446
	h_4	2.746	1.591	2.045	2.917	3.472
θ/π = 1/8	h_1	4.837	4.682	4.338	3.996	3.064
	h_2	6.182	5.918	5.312	4.766	3.580
	h_3	2.013	1.662	1.423	1.232	0.813
	h_4	3.279	2.020	2.285	2.608	2.133

Table 4.14 h-functions for circumferential through-wall-cracked pipe under combined pressure and bending for R_m/t = 10 and pressure = 15.51 MPa (2,250 psi)

	Function	n = 2	n = 3	n = 5	n = 7	n = 10
θ/π = 1/16	h_1	5.929	6.409	7.157	8.052	8.312
	h_2	6.973	7.460	8.108	8.923	9.009
	h_3	1.524	1.643	2.264	2.647	2.702
	h_4	2.507	1.893	3.199	6.191	9.048
θ/π = 1/8	h_1	6.051	6.066	6.206	5.618	6.294
	h_2	6.888	6.868	6.844	6.181	6.578
	h_3	1.652	1.533	1.459	1.187	1.585
	h_4	2.624	2.089	3.055	3.036	4.495

Table 4.15 h-functions for circumferential through-wall-cracked pipe under combined pressure and bending for $R_m/t = 20$ and pressure = 15.51 MPa (2,250 psi)

	Function	n = 2	n = 3	n = 5	n = 7	n = 10
$\theta/\pi = 1/16$	h_1	6.734	7.484	10.251	13.544	15.243
	h_2	7.561	8.292	10.924	14.078	15.813
	h_3	1.210	1.369	2.479	3.696	3.870
	h_4	2.144	2.264	6.069	11.739	17.100
$\theta/\pi = 1/8$	h_1	8.621	8.917	10.846	13.282	13.836
	h_2	8.375	8.705	10.383	12.479	13.051
	h_3	1.289	1.367	1.577	2.223	2.317
	h_4	2.689	2.778	5.160	7.720	9.046

4.2.2.12 Hoop Stress Loading Considerations

As described in Section 4.2.2.6, the GE/EPRI h functions for combined bending and tension were calculated using two load steps. An axial tension (corresponding to internal pressure) was applied to the end of the pipe and then the bending moment was increased.

In order to evaluate the effect of applying hoop stress to the pipe in addition to the tension, an additional analysis was performed. The load in the first step consisted of axial tension and internal pressure applied to all inside pipe elements. The second step was identical to that in the previous analysis, i.e., an increasing bending load was applied until fully plastic conditions were obtained.

The analysis was performed using Model 2 (Table 4.12) with n = 5 and $\theta/\pi = 0.0625$ and $R_m/t = 10$.

Table 4.16 shows the h-functions for this analysis and the corresponding run where no internal pressure (only axial tension) was applied. It is seen that the pressure increases h_1, and hence, J, compared with applying tension only. The mid-thickness crack-opening displacement, δ, is also increased slightly. This may be due to local crack bulging. The load-point displacement, h_3, and pipe rotation, h_4, functions are significantly affected. Note that while the hoop stress effects may be important as seen above, they were not included in the compilations to be consistent with the original GE/EPRI solutions.

Table 4.16 h-functions for through-wall cracks for combined tension and bending with and without hoop stress from internal pressure; $R_m/t = 10$, $n = 5$, and $\theta/\pi = 0.0625$

Function	Load	
	Axial Tension and Bending	Hoop Stress, Axial Tension, and Bending
h_1 (J)	7.157	7.605
h_2 (COD)	8.108	8.247
h_3 (load-point axial displacement)	2.264	0.549
h_4 (rotation)	3.199	1.952

4.2.3 LBB.ENG2 Method

In this program, an equivalence method originally proposed by Brust and Gilles (Refs. 4.6 and 4.7) was examined to compute energy release rates for through-wall-cracked pipes (see Figure 4.11). The method, which has the acronym LBB.ENG2, involves deformation theory of plasticity, Ramberg-Osgood constitutive law, and an equivalence criterion incorporating a reduced thickness analogy for simulating system compliance due to the presence of a crack in a pipe. The method is general in the sense that it may be applied in the complete range between elastic and fully plastic conditions. Since it is based on J-tearing theory, it is subject to the usual limitations imposed upon this theory, e.g., proportional loading, etc. This has the implication that the crack growth must be small, although in practice, J-tearing methodology is used far beyond the limits of its theoretical validity with acceptable results (Ref. 4.26). Detailed derivations of both elastic and plastic components of the J-integral in this method are available in the References 4.6 and 4.7. They will not be repeated in this report. Only the final expressions are presented here. These solutions are simplified and improved compared with the original results (Ref. 4.6). This method will be extended to account for a crack in a weld in Section 4.2.4.

4.2.3.1 Elastic Solution

The elastic solutions as given in Section 4.1.2.2 are used in this analysis.

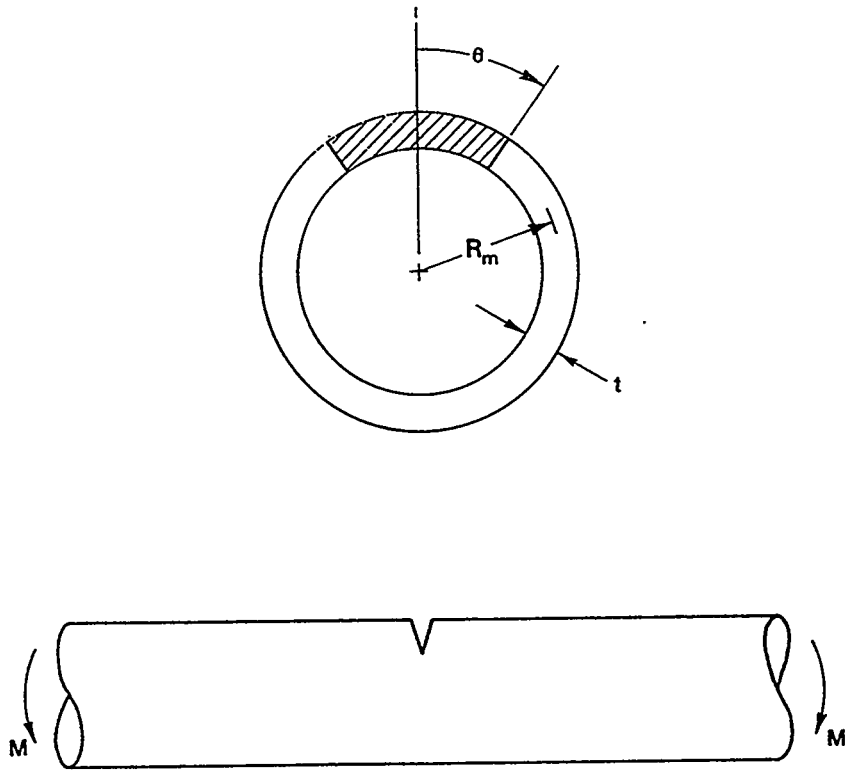

Figure 4.11 Circumferential through-wall-cracked pipe under pure bending

4.2.3.2 Plastic Solution

The plastic component, J_p, is given by (Refs. 4.6 and 4.7)

$$J_p = \frac{\alpha}{E\sigma_0^{n-1}} \frac{\pi R_m}{2(n+1)} H_B(n,\theta) L_B(n,\theta) I_B(\theta) \left[\frac{M}{\pi R_m^2 t}\right]^{n+1} \quad (4\text{-}59)$$

where σ_0 is the reference stress, α and n are Ramberg-Osgood parameters characterizing the stress-strain curve of the material, and $H_B(n,\theta)$, $L_B(n,\theta)$, and I_B are elementary functions given by

$$H_B(n,\theta) = \frac{4\theta F_B(\theta)^2}{I_B(\theta)} + \frac{1}{L_B(n,\theta)} \frac{\partial L_B(n,\theta)}{\partial \theta} \tag{4-60}$$

$$L_B(n,\theta) = \left[\frac{\pi}{4\left\{ \cos\left[\frac{\theta}{2}\right] - \frac{1}{2}\sin(\theta) \right\}} \right]^{n-1} \cdot \left[\frac{\pi}{4\hat{K}} \right]^n \tag{4-61}$$

$$I_B(\theta) = 4\int_0^\theta \theta F_B(\theta)^2 d\theta \tag{4-62}$$

in which

$$\hat{K} = \frac{\sqrt{\pi}}{2} \frac{\Gamma\left[1+\frac{1}{2}n\right]}{\Gamma\left[\frac{3}{2}+\frac{1}{2}n\right]} \tag{4-63}$$

with

$$\Gamma(u) = \int_0^\infty \xi^{u-1} \exp(-\xi)\, d\xi \tag{4-64}$$

representing the gamma function. An explicit form of I_B is also provided in Appendix A and the expression for $\partial L_B/\partial\Theta$, needed in Equation 4-60, is presented in Appendix C for the weld problem, which can also be used for base metal by selecting only one material.

When the pipe is subjected to combined bending and tension, computation of the J-integral becomes more complex, as noted in Section 4.2.2. A discussion on the conditions for achieving J-dominance and the suitability of J as a fracture parameter for combined bending and tensile loadings has been presented by Shih (Ref. 4.27) and Shih and Hutchinson (Ref. 4.28) by studying the single-edge notch specimen. Additional studies based on finite element analysis of the single-edge notch specimen subjected to combined tension and bending have also appeared (Refs. 4.24 and 4.25). An important result obtained by Sonnerlind and Kaiser (Ref. 4.24) indicates that the value of J is essentially independent of whether tension is applied, then bending; bending then tension; or both tension and bending are applied proportionally. This was also discussed in Section 4.2.2. This is not intuitively obvious since such loading clearly violates the hypothesis (necessary for valid J-tearing theory) of proportional loading. Based on this premise, an estimation method is proposed by Brust and Gilles (Ref. 4.29) for evaluating the J-integral for cracked tubular members subjected to combined tensile and bending loads. The method is similar to the case of pure bending and is also based on deformation plasticity, Ramberg-Osgood constitutive model, and an equivalence criterion incorporating a reduced thickness analogy for simulating pipe compliance. Further details of this

method regarding energy release rates due to combined bending and tension can be obtained from Reference 4.29.

4.2.3.3 Numerical Comparisons

Consider two pipes, one made from TP316 stainless steel and the other made from A106 Grade B carbon steel. The geometric and material characteristics of these pipes are given in Table 4.17. Both the J-estimation method and nonlinear finite element method (FEM) were applied to determine J for these pipes subject to several values of bending moment M. The estimation of J was performed by the LBB.ENG2 method using Equations 4-56, 4-58, and 4-60. The finite element computations were conducted by the computer code CASTEM* using triangular thin shell elements with about 4,500 degrees of freedom. J was calculated using the virtual crack extension technique.

Table 4.17 Geometric and material characteristics of two through-wall-cracked pipes

Properties	A106 Grade B Carbon Steel	TP316 Stainless Steel
Outer diameter, mm (inch)	168.9 (6.65)	105.46 (4.15)
Wall thickness, mm (inch)	10.90 (0.43)	8.41 (0.33)
Total crack angle, degrees	120	120
Modulus of elasticity, GPa (psi)	190.0 (27.6 x 10^6)	151.7 (22 x 10^6)
Reference stress σ_0, MPa (ksi)	330 (47.9)	375[a] (54.4)
α	1.124	37.32
n	7.167	4.85

(a) α was calculated based on flow stress as the reference stress.

Figure 4.12 shows the plots of J-integral versus M obtained by the LBB.ENG2 method and FEM for the TP316 stainless steel pipe. Comparisons with FEM results suggest that the LBB.ENG2 method provides accurate estimates of the J-integral for various applied loads. Similar observations are also made in Figure 4.13 with results that correspond to the A106 Grade B carbon steel pipe. Figure 4.13 also shows that when the external load becomes larger, the plastic component of J can significantly dominate over the elastic component.

* CASTEM is a finite element code developed at CEA of France.

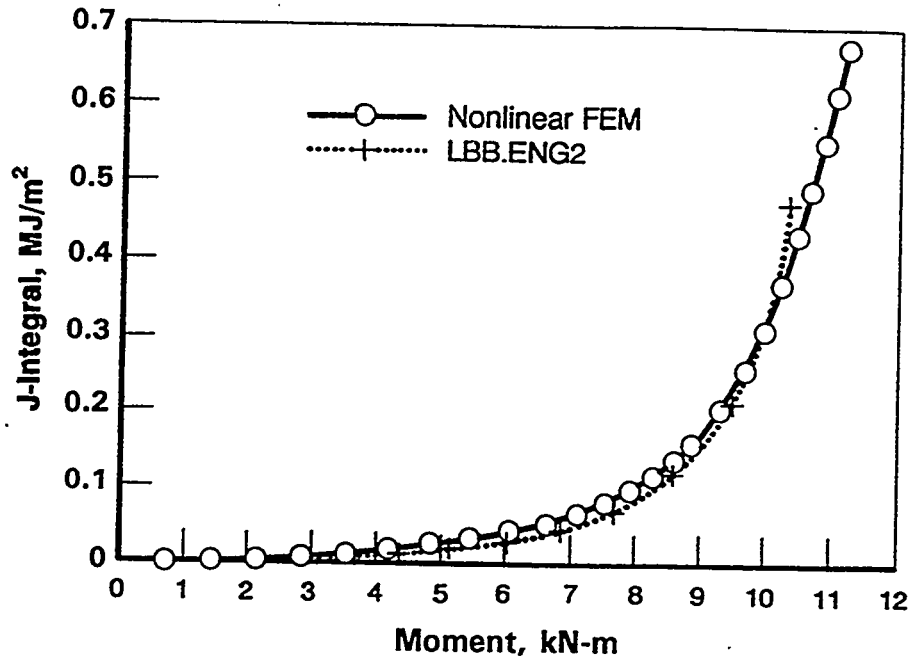

Figure 4.12 J-integral versus applied moment for the TP316 stainless steel pipe

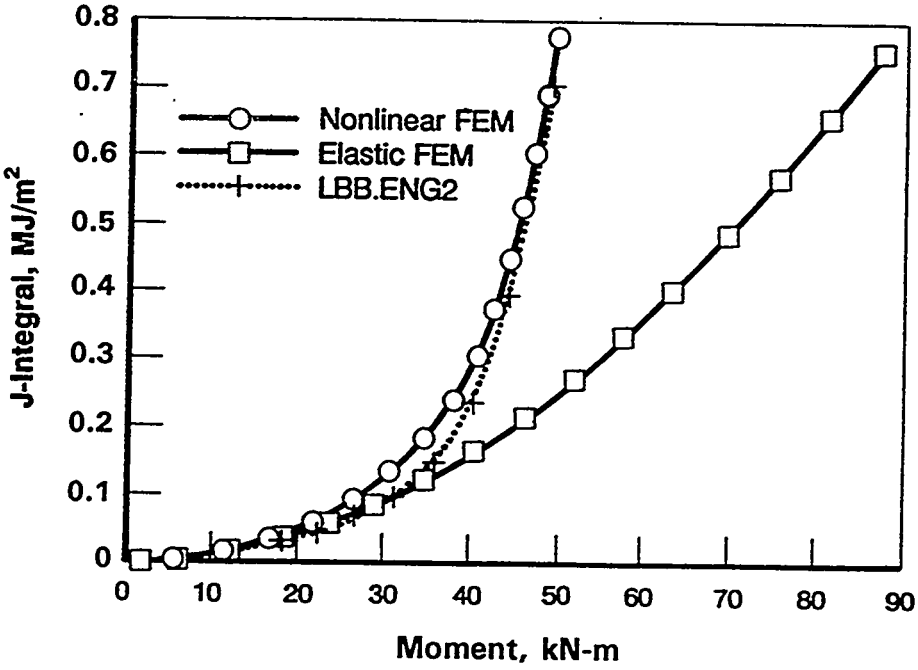

Figure 4.13 J-integral versus applied moment for the A106 Grade B carbon steel pipe

4.2.4 Weld Analysis Method - LBB.ENG3 Method

Most estimation methods that are currently available today are based on homogeneous materials and can account for strength properties of either base or weld metals. Currently, predictions are usually made using a base metal stress-strain curve and a weld metal J-resistance curve. This can lead to significant errors depending on the strength ratio of the base versus weld material.

In this program, a new methodology was developed to predict the energy release rates of TWC pipe weldments subjected to remote bending loads. The method of analysis was based on (1) the deformation theory of plasticity, (2) a constitutive law characterized by Ramberg-Osgood model, and (3) an equivalence criterion incorporating a reduced thickness analogy for simulating system compliance due to the presence of a crack in the weld metal (i.e., analogous to the LBB.ENG2 method discussed in Section 4.2.3). The equations for the J-integral in a nonlinear-elastic cracked pipe weld are derived in closed form in terms of elementary functions. This makes the proposed scheme computationally efficient for conducting routine fracture evaluations. The method uses the material properties of both the base and weld metals, which are not considered in other, current estimation methods. It is general in the sense that it may be applied in the complete range between elastic and fully plastic conditions. This method is given the acronym LBB.ENG3 and is described below.

4.2.4.1 The Pipe Girth Weld Crack Problem

Figure 4.14 illustrates a typical girth-welded pipe with a circumferential through-wall crack of total angle 2θ. The pipe mean radius, R_m, and thickness, t, are shown. Figure 4.15 illustrates the geometry for a girth weld in a pipe. Typically, the weld layers are deposited in sequence. The example of Figure 4.15 is an actual sequence from a 102-mm (4-inch) nominal diameter Schedule 80 pipe that required seven passes. The welding gives rise to a heat-affected zone (HAZ) that results in material properties which are different from those in the weld metal or base metal alone. Often cracks develop in the HAZ and may grow in a skewed fashion along or near the fusion zone (see Section 3.0) to become a through-wall crack, as illustrated in Figure 4.15. Figure 4.15 also shows a crack that grows through the weld metal, which is the type of crack assumed in the development of the method presented here. Figure 4.16 shows the pipe weld geometric assumption made here. Note that the angular and irregular nature of the actual weldment is assumed to be a straight radial bimaterial interface line for development of this model. Residual stresses and HAZ properties are not included, although they could be considered with rather minor modifications.

The total width of the weld (Figures 4.15 and 4.16) is assumed to be an average width, L_w, which is often best approximated (as a rule of thumb) to be the pipe wall thickness (i.e., $L_w \approx t$).

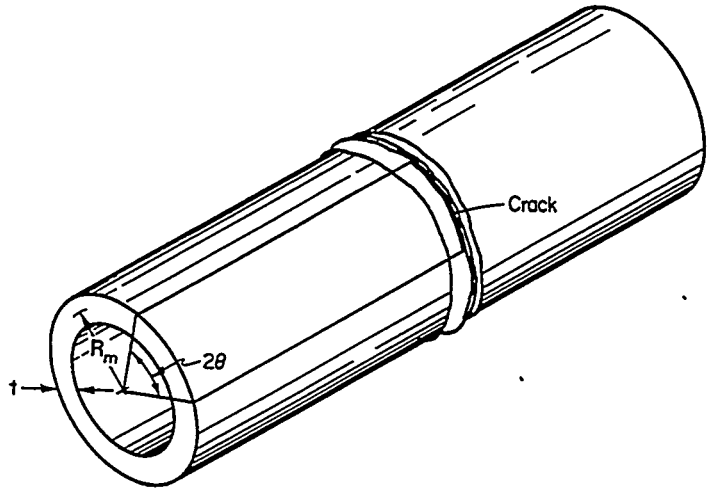

Figure 4.14 Circumferential crack in a pipe butt weld

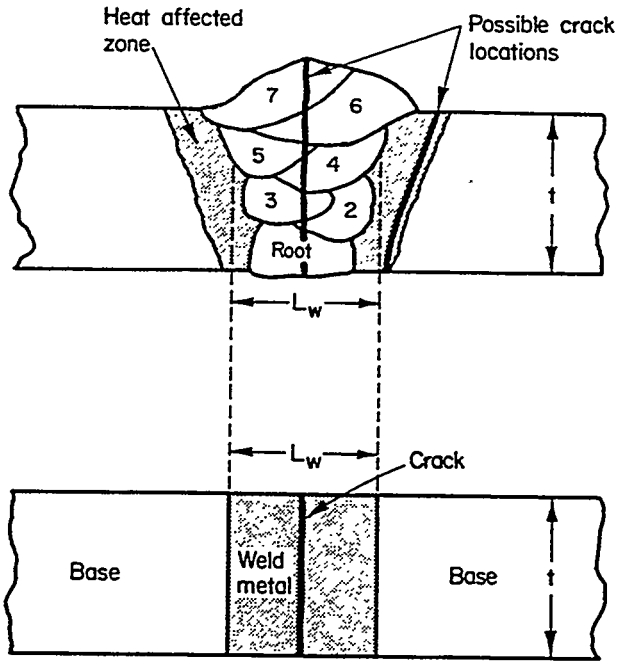

Figure 4.15 Typical girth weld sequence for a pipe and possible cracks [this is an actual sequence for a 102-mm (4-inch) nominal diameter Schedule 80 pipe and idealized pipe weld with a crack]

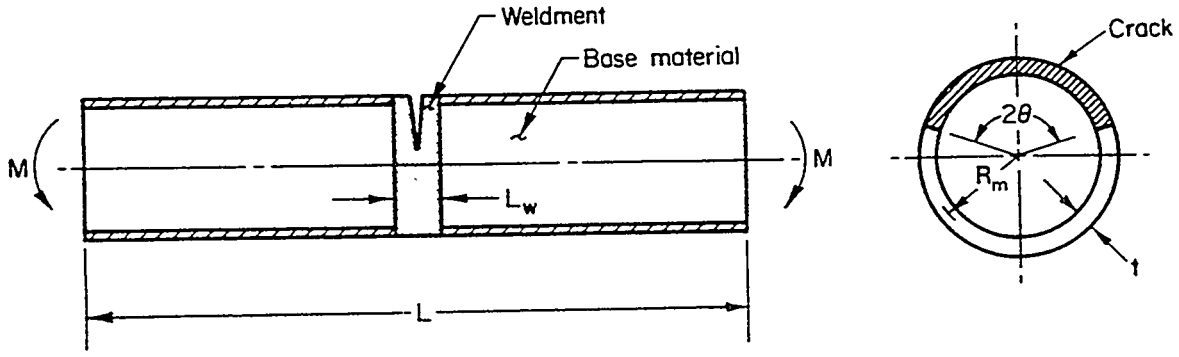

Figure 4.16 Schematics of pipe weldments with a circumferential flaw

4.2.4.2 LBB.ENG3 Method

Consider a TWC pipe under a remote bending moment M (Figure 4.17). The pipe has length, L, mean radius, R_m, thickness, t, and crack angle, 2θ, with the crack circumferentially located in the weld material of length L_w. In the development of a J-estimation scheme, it is assumed as before that the load-point rotation due to the presence of the crack, ϕ^c, and the crack-driving force, J, can be split into the elastic and the plastic components as

$$\phi^c = \phi_e^c + \phi_p^c \tag{4-65}$$

$$J = J_e + J_p \tag{4-66}$$

where the subscripts "e" and "p" refer to elastic and plastic contributions, respectively. In the elastic range, ϕ_e^c and M are uniquely related. In addition, if the deformation theory of plasticity holds, a unique relationship also exists between ϕ_p^c and M. Once these relationships are determined, the elastic component J_e and the plastic component J_p of the total energy release rate J can be obtained readily.

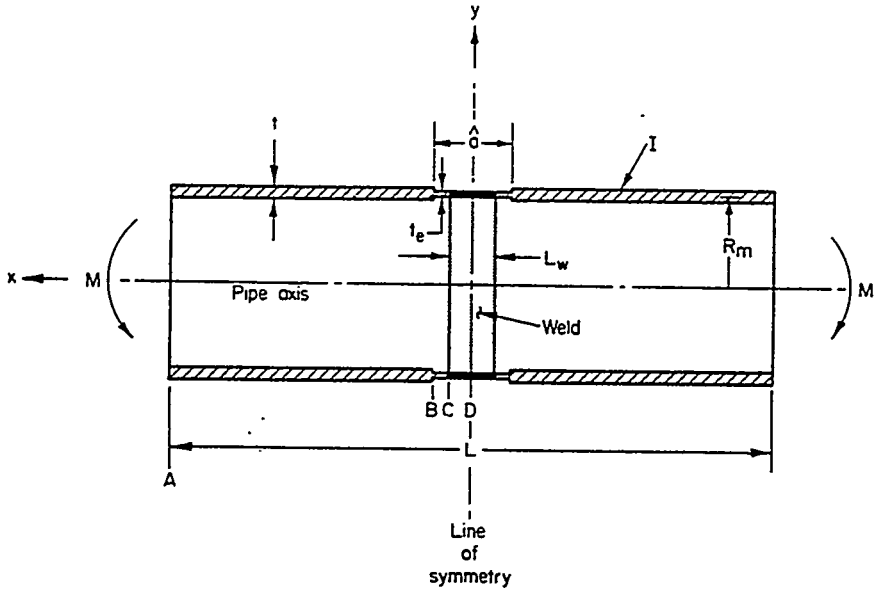

Figure 4.17 Reduced section analogy

4.2.4.3 Elastic Solution

The elastic energy release rate J_e can be defined as

$$J_e = \frac{\partial U^T}{\partial A} = \frac{\partial}{\partial A}(U^c + U^{nc}) = \frac{\partial U^c}{\partial A} \tag{4-67}$$

where U^T is the total internal strain energy, U^{nc} is the strain energy that would exist if there were no crack present, $U^c = U^T - U^{nc}$ is the additional strain energy in the pipe due to the presence of the crack, and $A = 2R_m\theta t$ is the crack area. For thin-walled pipe with Mode-I crack growth, J_e can be obtained as

$$J_e = \frac{K_I^2}{E_2} \tag{4-68}$$

where E_2 is the elastic modulus of weld material, and K_I is the mode-I stress intensity factor. From theory of linear elastic fracture mechanics, K_I for bending (K_{IB}) is given by

$$K_{IB} = \sigma \sqrt{\pi R_m \theta}\ F_B(\theta) \tag{4-69}$$

in which $\sigma = M/\pi R_m^2 t$ is the far-field applied stress and F_B is a geometry function relating K_I of a cracked shell to that for the same sized crack in an infinite plate. From Equations 4-67 to 4-69, U^c can be integrated to yield

$$U^c = \frac{M^2}{2\pi R_m^2 t E_2} I_B(\theta) \tag{4-70}$$

where,

$$I_B(\theta) = 4 \int_0^{\theta} \xi F_B(\xi)^2 \, d\xi \tag{4-71}$$

Using Castigliano's theorem,

$$\phi_e^c = \frac{\partial U^c}{\partial M} \tag{4-72}$$

which when combined with Equation (4-70) gives

$$M = \frac{E_2 \pi R_m^2 t}{I_B(\theta)} \phi_e^c \tag{4-73}$$

representing the relationship between moment and elastic rotation. Equations 4-70 and 4-71 completely specify the elastic energy release rate, J_e, and hence, the elastic solution is complete in a closed form. Equation 4-73 will be required for the calculation of J_p, explained in the next section. These developments are based on elastic solutions of Sanders (Refs. 4.18 and 4.30). Explicit functional forms of F_B and I_B are provided in Appendix A.

4.2.4.4 Plastic Solution

The plastic energy release rate J_p can be defined as

$$J_p = - \int_0^{\phi_p^c} \frac{\partial M}{\partial A} \Big|_{\phi_p^c} \, d\phi_p^c \tag{4-74}$$

The evaluation of J_p in Equation 4-74 requires the determination of the $M-\phi_p^c$ relationship as a function of crack size. When this relationship is obtained, Equation 4-74 can be used to find J_p and then can be added to J_e to determine the total J.

A widely used univariate constitutive law describing a material's stress-strain (σ-ϵ) relationship is the normalized Ramberg-Osgood model given by

$$\frac{\epsilon}{\epsilon_{0i}} = \frac{\sigma}{\sigma_{0i}} + \alpha_i \left[\frac{\sigma}{\sigma_{0i}}\right]^{n_i} \tag{4-75}$$

where σ_{0i} is a reference stress, $\epsilon_{0i} = \sigma_{0i}/E_i$ is the associated strain with elastic modulus E_i, α_i and n_i are the parameters of the model usually chosen to fit experimental data, and i=1 or 2 to represent the base and weld metal, respectively. In applying the Ramberg-Osgood relationship to the cracked pipe problem, it is necessary to relate the stresses with rotations. Ilyushin (Ref. 4.31) showed that the field solutions to the boundary value problem involving a monotonically increasing load or displacement type parameter is "proportional". Consequently, Equation 4-75 applies (minus the elastic term) and the deformation theory plasticity is assumed to be valid. Thus,

$$\phi_p^c \propto \sigma^{n_i} \tag{4-76}$$

giving

$$\phi_p^c = \hat{D}\, \sigma^{n_i} \tag{4-77}$$

where the proportionality constant $\hat{D}$ can be expressed in a convenient form,

$$\hat{D} = L_B \alpha_i \frac{I_B(\theta)}{\sigma_0^{n_i-1} E_2} \tag{4-78}$$

to allow for Equation 4-76 to be reformulated as

$$\phi_p^c = L_B \alpha_i \left[\frac{\sigma}{\sigma_{0i}}\right]^{n_i-1} \phi_e^c \tag{4-79}$$

in which the moment-elastic rotation relationship in Equation 4-73 is used. In Equation 4-79, L_B is an unknown function that needs to be determined. For the crack problem, L_B may be determined numerically. However, no analytical method exists to obtain L_B in closed form. Thus, the main task in this methodology is to determine L_B in Equation 4-79.

4.2.4.5 Evaluation of L_B

Suppose that the actual pipe can be replaced by a pipe with reduced thickness, t_e, that extends for a distance $\hat{a} \geq L_w$ at the center (Figure 4.17). Far from the crack plane, the rotation of the pipe is not greatly influenced by whether a crack exists, or some other discontinuity is present, as long as the discontinuity can approximate the effects of a crack. The reduced thickness section, which actually results in a material discontinuity, is an attempt to simulate the reduced system compliance due to the presence of a crack. This equivalence approach was originally suggested by Brust (Ref. 4.6) and was

successfully implemented to evaluate the performance of TWC pipes consisting of one single material under various loading conditions (Refs. 4.6, 4.7, and 4.8). It is assumed here that the deformation theory of plasticity controls stress-strain response and that beam theory assumptions hold.

Consider the equivalent pipe with the material discontinuity in Figure 4.17 that is subjected to a bending moment, M. Using classical beam theory, the ordinary differential equations governing displacement of beams with a Ramberg-Osgood constitutive law can be easily derived. These equations, when supplemented by the appropriate boundary and compatibility conditions, can be solved following elementary operations of calculus. Details of the algebra associated with these solutions are provided in Appendix B. The rotations (dy/dx in Equations B.2, B.5, and B.8, see Appendix B) provide an explicit relationship between the far-field plastic rotation ϕ_p^d due to material discontinuity and the corresponding elastic rotations ϕ_e^d where the new superscript "d" refers to material discontinuity. Each of these relationships can be expressed in a form analogous to Equation 4-79 as

$$\phi_p^d = L_B^d \alpha_i \left[\frac{\sigma}{\sigma_{0i}}\right]^{n_i-1} \phi_e^d \tag{4-80}$$

in which L_B^d, in general, will depend on geometry, material properties of base and weld materials, t_e, and the spatial coordinate x. While no attempt is made here for a formal proof, it will be assumed that L_B^d determined from the material discontinuity solution (Equation 4-79) approaches the actual unknown L_B in Equation 4-79.

Since L_B^d evaluated at segment CD (see Figure 4.17) cannot account for base material properties (Equation B.8), the appropriate choice is to write L_B^d at either segment AB or BC. More specifically, when the spatial location is selected to be the Point B (i.e., x=â/2), the explicit version of Equation 4-80 becomes

$$\phi_p^d = \frac{\left[\frac{M}{M_{01}}\right]^{n_1}\left[\frac{\hat{a}}{2}-\frac{L_w}{2}\right]\left[\frac{t}{t_e}\right]^{n_1} + \left[\frac{M}{M_{02}}\right]^{n_2}\frac{L_w}{2}\left[\frac{t}{t_e}\right]^{n_2}}{\left[\frac{M}{M_1}\right]\epsilon_{01}\left[\frac{\hat{a}}{2}-\frac{L_w}{2}\right]\frac{t}{t_e} + \left[\frac{M}{M_2}\right]\epsilon_{02}\frac{L_w}{2}\frac{t}{t_e}}\phi_e^d \tag{4-81}$$

where $M_i = \sigma_{0i} I/R$ is the elastic bending load corresponding to flow stress σ_{0i}, and other parameters are defined in Appendix B. Comparing Equation 4-81 with Equation 4-82 immediately gives

$$L_B^d = \frac{\left(\frac{M}{M_{01}}\right)^{n_1}\left(\frac{\hat{a}}{2}-\frac{L_w}{2}\right)\left(\frac{t}{t_e}\right)^{n_1} + \left(\frac{M}{M_{02}}\right)^{n_2}\frac{L_w}{2}\left(\frac{t}{t_e}\right)^{n_2}}{\left(\frac{M}{M_1}\right)\epsilon_{01}\left(\frac{\hat{a}}{2}-\frac{L_w}{2}\right)\frac{t}{t_e} + \left(\frac{M}{M_2}\right)\epsilon_{02}\frac{L_w}{2}\frac{t}{t_e}} \times \frac{1}{\alpha_1\left(\frac{M}{M_1}\right)^{n_1-1}} \quad (4\text{-}82)$$

Equation 4-81 apparently indicates that L_B^d has an explicit functional dependency on the external load parameter M thus violating the previously invoked Ilyushin's theorem (Equation 4-76). However, it can be shown that for the variation of load magnitude in the practical range, the correlation between L_B^d and M is not strong. This will be proven semi-empirically when this issue is further investigated in the forthcoming numerical validation. Hence, the above equation can still be treated as an expression for the invariant proportionality factor L_B^d.

4.2.4.6 Determination of t_e

The equivalent reduced thickness t_e can be obtained by forcing the limit moment of the reduced pipe section

$$M_L^d = 4\sigma_{limit}R_m^2 t_e \quad (4\text{-}83)$$

to be equivalent to the limit moment of the cracked-pipe section under pure bending

$$M_0 = 4\sigma_{limit}R_m^2 t\left[\cos\frac{\theta}{2}-\frac{1}{2}\sin\theta\right] \quad (4\text{-}84)$$

giving (Ref. 4.6)

$$t_e = t\left[\cos\frac{\theta}{2}-\frac{1}{2}\sin\theta\right] \quad (4\text{-}85)$$

However, in Reference 4.6, it has been observed that Equation 4-85 provides a fairly good approximation only for small crack angles ($0° \le 2\theta \le 90°$). For large crack angles ($2\theta \ge 120°$), t_e is found to be better represented by

$$t_e = \frac{4t}{\pi}\left[\cos\frac{\theta}{2} - \frac{1}{2}\sin\theta\right] \quad (4\text{-}86)$$

obtained when the limit moment of the reduced pipe section is calculated from a linear stress variation with maximum stress σ_{limit} (giving $M_L^d = \pi\sigma_{limit}R_m^2 t_e$) rather than the uniform stress assumed in Equations 4-84 and 4-85. For cracks with angles in the intermediate range ($90° \leq 2\theta \leq 120°$), t_e can be found from linear interpolation between these two limits (Ref. 4.6).

4.2.4.7 Estimation of J_p

Having determined L_B^d and t_e, the $M-\phi_p^c$ relationship can be obtained from Equation 4-80 via the $M-\phi_e^c$ relationship in Equation 4-73. When it is placed in Equation 4-74, it can be integrated symbolically to evaluate J_p in a closed form. It can be shown that

$$J_p = \frac{\alpha_1}{E_1\sigma_{01}^{n_1-1}} \frac{\pi R_m}{2} \frac{1}{n_1+1} H_B L_B^d I_B \left[\frac{M}{\pi R_m^2 t}\right]^{n_1+1} \tag{4-87}$$

in which

$$H_B = \frac{1}{I_B}\frac{\partial I_B}{\partial\theta} + \frac{1}{L_B^d}\frac{\partial L_B^d}{\partial\theta} \tag{4-88}$$

where the derivatives $\partial I_B/\partial\theta$ and $\partial L_B^d/\partial\theta$ are explicitly described in Appendix C. Hence, Equations 4-68 and 4-87 provide closed form expressions for J_e and J_p. These analytical forms are very convenient for both deterministic and probabilistic elastic-plastic fracture mechanics. Further details can be obtained from References 4.9 to 4.11.

Note that Equation 4-87 has similar characteristics to Equation 4-59 required to calculate J_p for a base metal crack (LBB.ENG2 method). However, from Equation 4-87, it can be seen that the tensile strength properties of both base and weld metals are accounted for in calculating the J-integral. Equation 4-87 is strongly dependent on base metal properties, but the weld metal properties are also accounted for via L_B^d (see Equation 4-82) and H_B (see Equation 4-88) functions and their partial derivatives (see Appendix C for explicit details). When differences in the base metal and weld metal properties vanish, it can be shown that Equation 4-87 reduces to Equation 4-59 as expected.

4.2.4.8 Numerical Comparisons

Consider two circumferential TWC pipe weldments, one with R_m = 52.87 mm (2.08 inch) and t = 8.56 mm (0.337 inch) ($R_m/t \simeq 6$), and the other with R_m = 55.88 mm (2.20 inch) and t = 3.81 mm (0.15 inch) ($R_m/t \simeq 15$), each of which is subjected to constant bending moment M applied at the simply supported ends. In both pipes, it is assumed that 2θ = 139 degrees and L_w = 5.59 mm (0.22 inch). The constitutive laws for the base and weld metals are assumed to follow the

parameters α_i and n_i are shown in Table 4.18. Note, the material property values shown in Table 4.18 are hypothetical values established as an illustration.

Pipes with the parameters given in Table 4.18 were analyzed to calculate energy-release rates (J-integral) by both the J-estimation method and the nonlinear finite element method. Approximate evaluation of the crack-driving force J by the proposed estimation scheme was based on Equations 4-66, 4-68, and 4-87. The FEM solutions, on the other hand, were based on 3-dimensional brick elements available in the fracture mechanics code BCLFEM, which was developed at Battelle.

Figure 4.18 shows a typical mesh representing the finite element idealization of a quarter (due to symmetry) of the TWC pipe with a crack in the weld.

Table 4.18 Parameters of material constitutive law

Material, i	σ_{0i}, MPa (psi)	E_i, GPa (psi)	α_i	n_i
Base Metal	137.9 (20,000)	175.76 (25.5 x 10^6)	3.29	3.826
Weld Metal	210.3 (30,500)	175.76 (25.5 x 10^6)	0.138	9.370

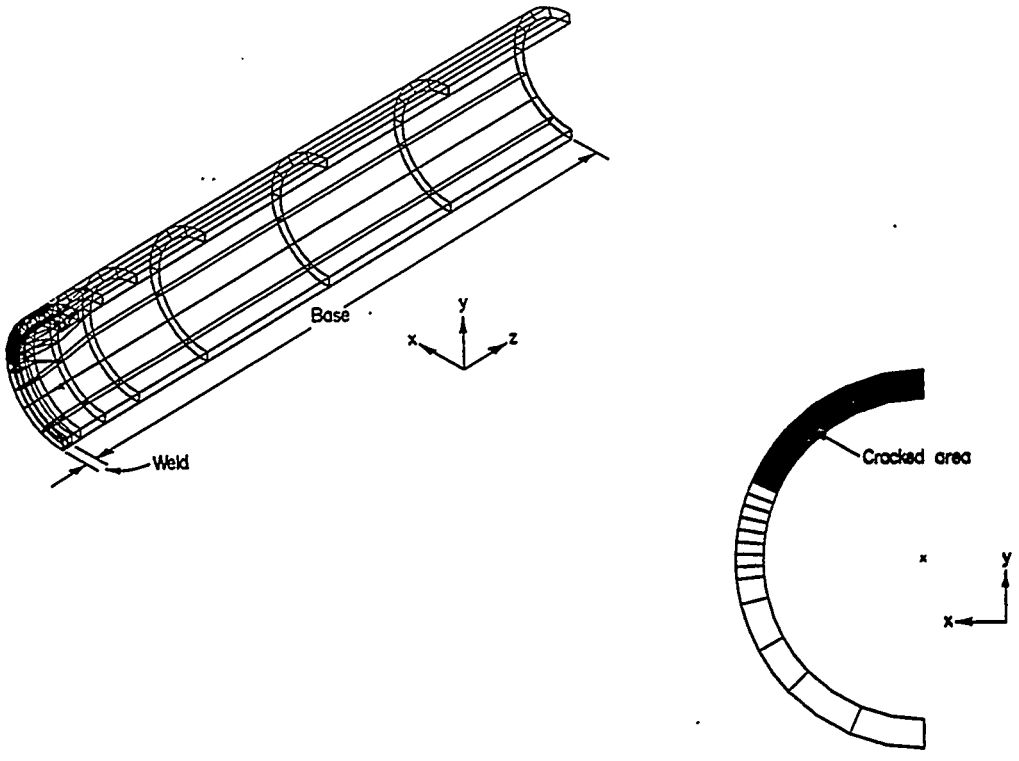

Figure 4.18 Finite element mesh of a through-wall-cracked pipe weld

Figures 4.19 and 4.20 show several plots of J versus M obtained using various levels of approximation for pipes with $R_m/t \simeq 6$ and $R_m/t \simeq 15$, respectively. Also shown in the figures are the FE results, which can be used as benchmark solutions for evaluating the accuracy of the analytical methods. Comparisons of the results of the approximate method developed in Reference 4.6 (LBB.ENG2 method) based solely on all-base- or all-weld-material properties with FE results suggest that they provide only upper and lower bounds of actual energy release rate J at any given moment, M.

Figures 4.19 and 4.20 also exhibit the results of the proposed method for several values of â representing the length of reduced thickness sections. All values of â result in reasonably good agreement with the FE solutions. Although â is treated here as a free parameter, an optimum value needs to be determined for obtaining the best estimate.

In all the example cases, the calculation of J_p was performed here based on the proportionality factor L_B^d in Equation 4-82. Although functionally dependent on an external load parameter, the weak correlation between L_B^d and M can be verified from the approximate constancy of L_B^d demonstrated in Figure 4.21. Several plots of L_B^d versus applied moment M (Equation 4-82) for both $R_m/t \simeq 6$ and $R_m/t \simeq 15$ are shown. As anticipated, they clearly indicate that for practical load ranges, L_B^d remains essentially invariant for various definitions of â.

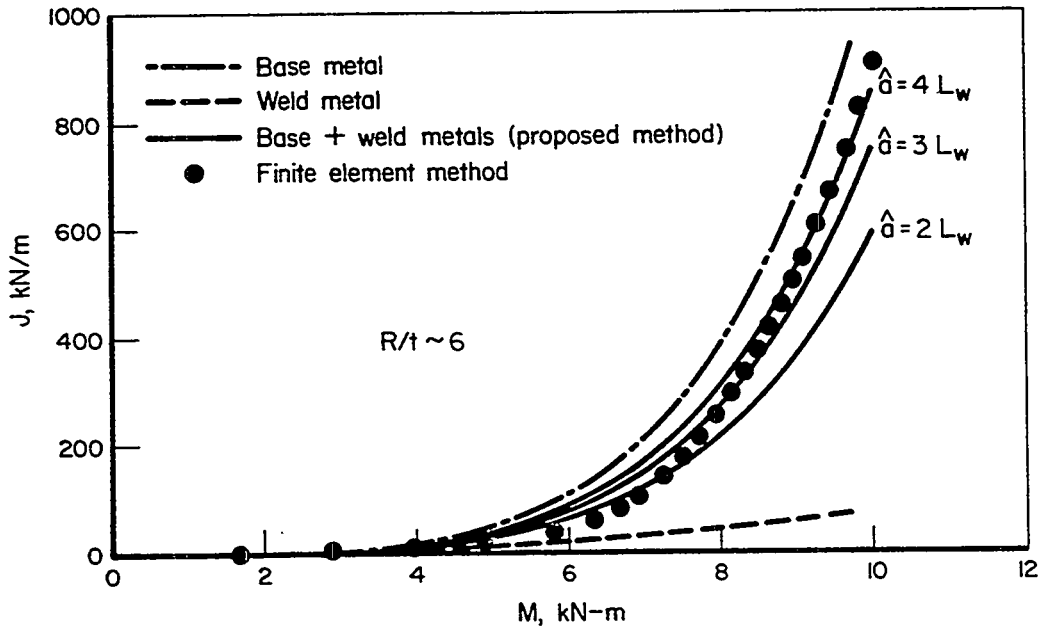

Figure 4.19 Comparisons of computed J-integral versus M ($R_m/t \simeq 6$)

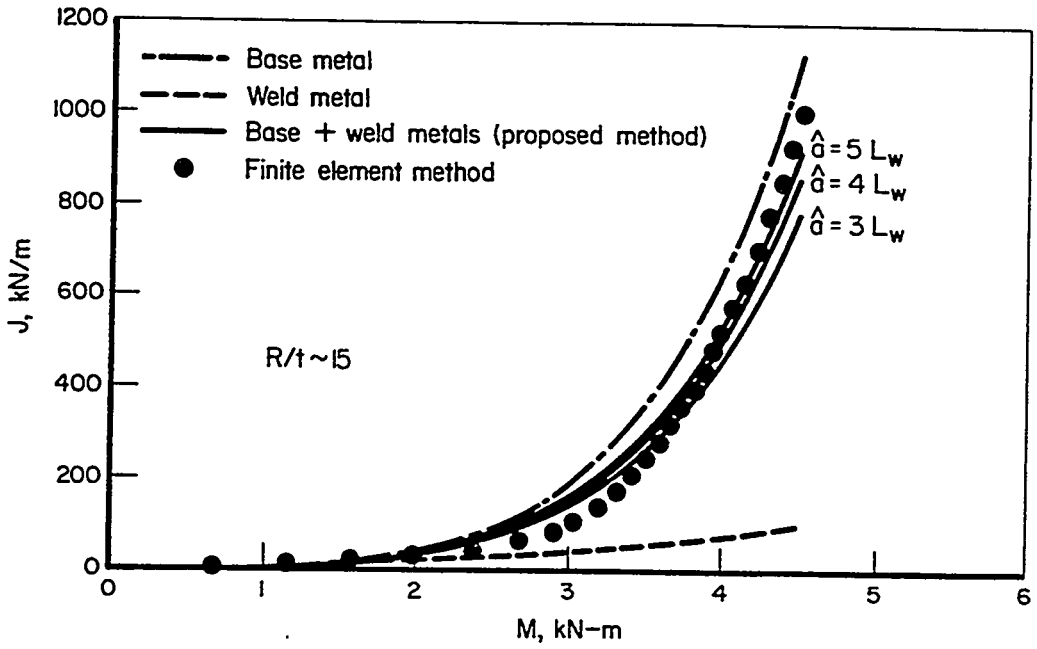

Figure 4.20 Comparisons of computed J-integral versus M ($R_m/t \simeq 15$)

4.2.4.9 Quantification of â

Several finite element analyses were carried out to determine â. Following extensive comparisons with the results of finite element analyses, â was found to be relatively insensitive to the variations in the hardening parameters n_1 and n_2 for the base and weld metals, respectively. It was also found that the optimum value of $\hat{a}/L_w$ was roughly in the neighborhood of 4 where L_w was the average width of weld metal in the pipe.

Figures 4.22 to 4.25 exhibit the plots of crack driving force J versus applied bending moment M for some of the combinations of n_1 and n_2 considered in this study. Other input parameters are kept the same as in the example problems illustrated previously. Both estimation and finite element methods are used to compute J for a given applied moment. Comparisons of the results suggest that the estimation method with the calibrated value of $\hat{a}/L_w = 4$ provides a simple yet satisfactory measure of the energy release rate J.

Note that the calibration procedure conducted here provides only a preliminary estimate of â. More refined calibration will need to be performed to investigate the dependency on pipe geometry (R_m/t), crack size (θ/π), base-to-weld metal reference stress ratio (σ_{01}/σ_{02}), and other pertinent parameters.

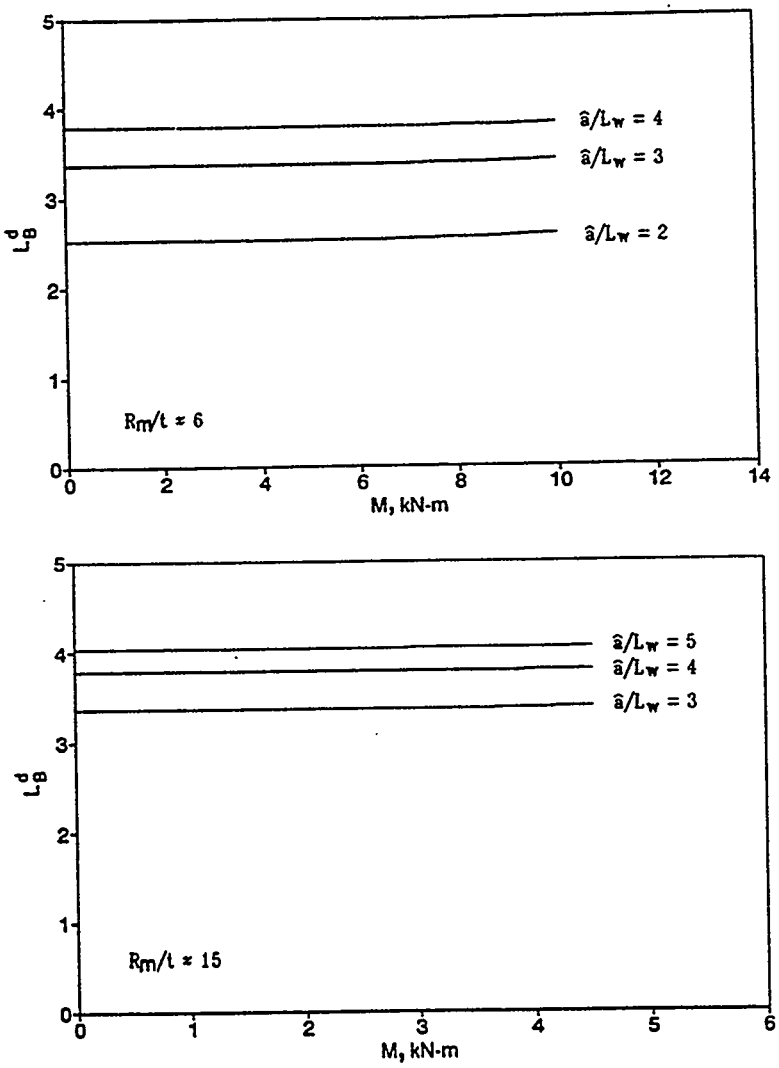

Figure 4.21 Plots of L_B^d versus M

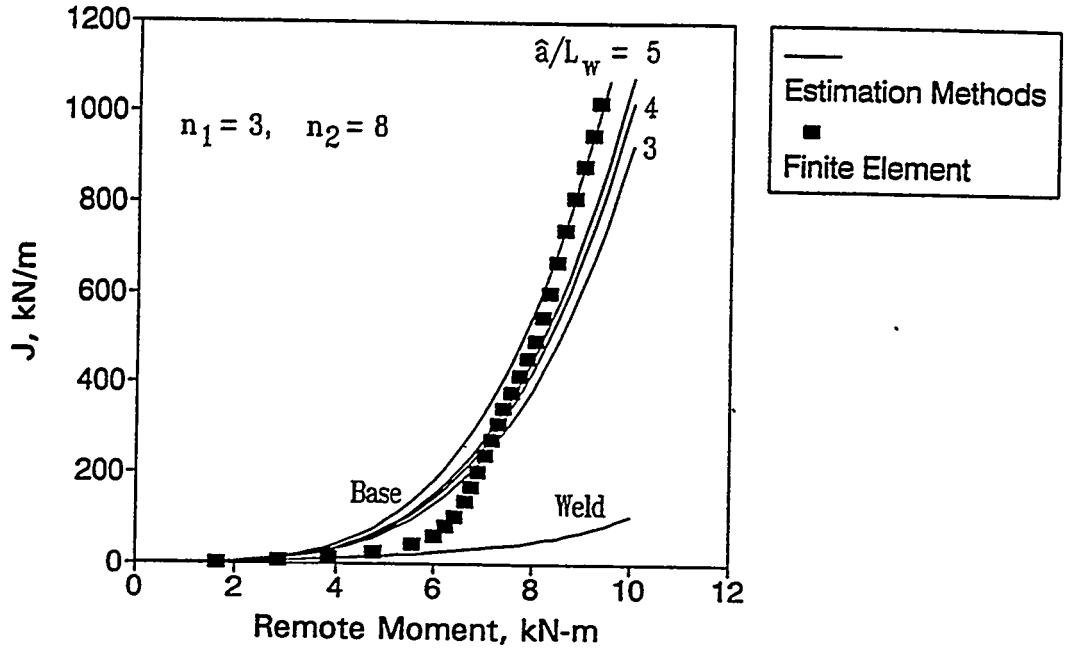

Figure 4.22 Comparisons of computed J-integral versus M (n_1=3, n_2=8)

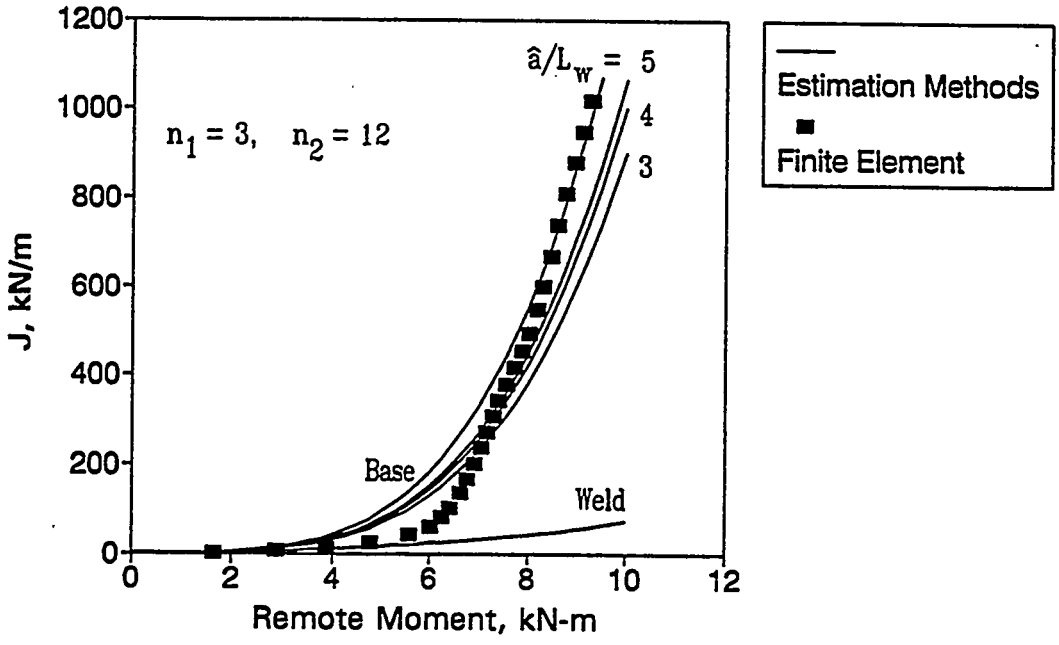

Figure 4.23 Comparisons of computed J-integral versus M (n_1=3, n_2=12)

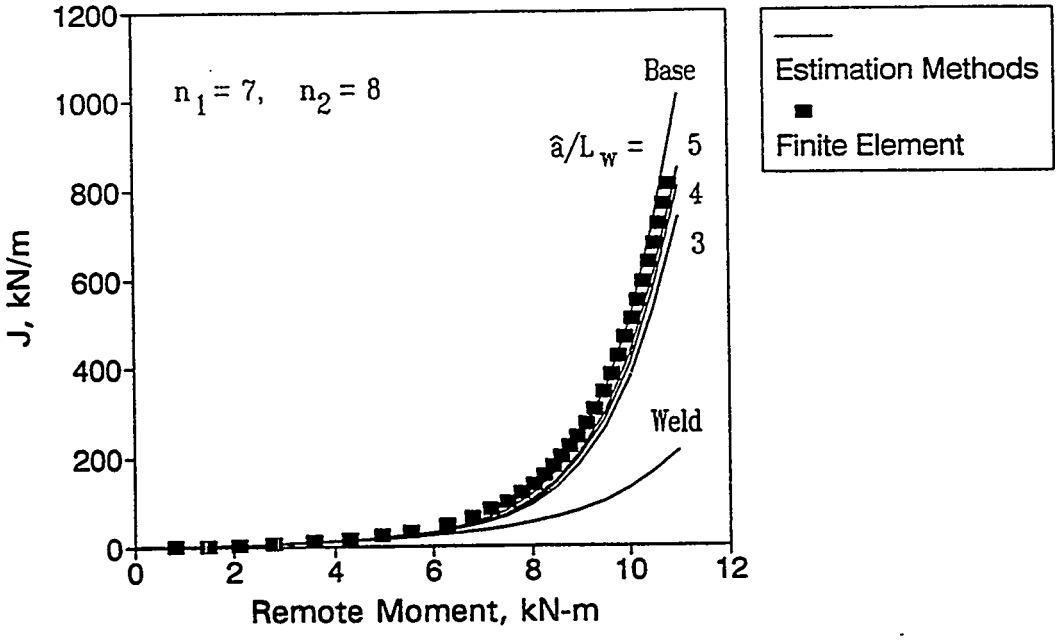

Figure 4.24 Comparisons of computed J-integral versus M (n_1=7, n_2=8)

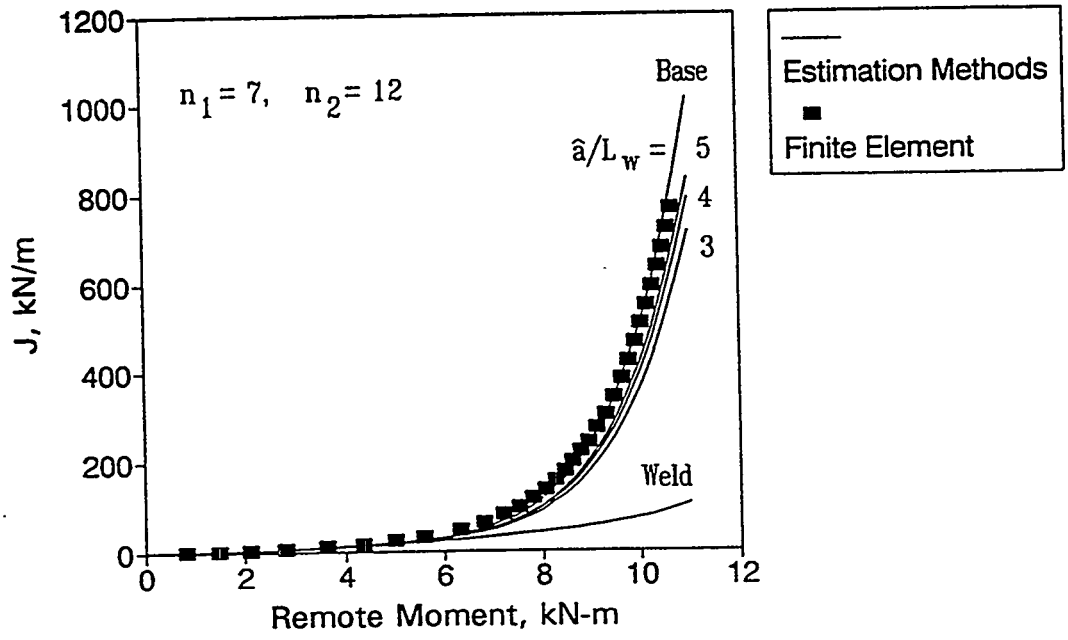

Figure 4.25 Comparisons of computed J-integral versus M (n_1=7, n_2=12)

4.2.4.10 Discussion

As noted earlier and in References 4.6, 4.10, and 4.11, the key to developing a J-estimation scheme is to determine the reduced pipe compliance due to the presence of the crack. The reduced pipe compliance has been estimated in a number of ways including using plastic-zone-correction methods in elastic solutions (Ref. 4.6) and reduced thickness sections as done here. Let us explore the consequences of this when a crack exists in a pipe weld.

Figure 4.26 shows the through-wall crack in the weld of a pipe. If the plastic zone is small in comparison to the weld width, L_w, then it is clear that an estimation scheme solution should depend only on the weld material and the corresponding Ramberg-Osgood properties. However, as the plastic zone reaches and penetrates the base metal, the far-field rotation due to the crack increases (or decreases), depending on the ratio of weld strength to base metal strength properties. In general, for welded nuclear piping, the base metal is of lower strength and can accommodate more plastic flow compared with weld metal. This additional plastic flow that occurs in the base metal would not occur if not for the presence of the crack. It is for this reason that the reduced thickness section included both weld and base material, i.e., the additional rotation due to the crack in the base metal is caused by (weld) crack-induced plasticity.

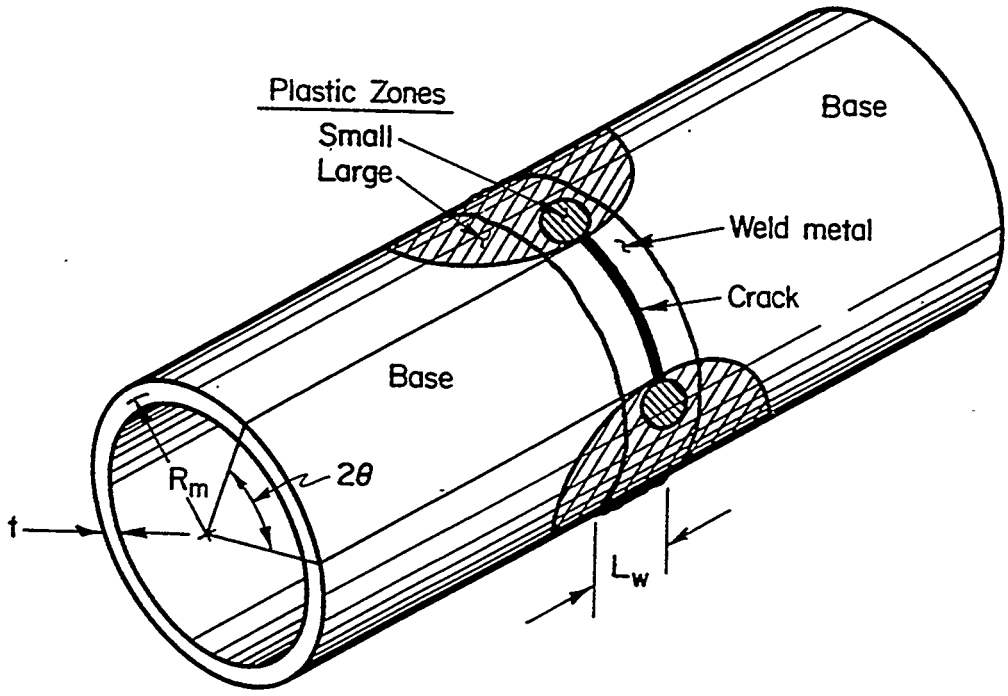

Figure 4.26 Circumferential through-wall crack in a weld showing plastic-zone sizes

Examples illustrating the performance of this method in predicting weld fracture are provided in Section 4.3. The use of this method provides improved predictions compared with assuming only base metal stress-strain properties and weld metal J-R curve data for the analysis.

4.2.5 Ovalization Effects

A cracked pipe, whether through-wall-cracked or surface-cracked, is failed by bending loads, the pipe section near the crack plane tends to ovalize. This ovalization will either increase the diameter in the plane of the bending moment, as seen in Figure 3.26, or decrease the diameter. It has been suggested that ovalization may increase or decrease the maximum load-carrying capacity of a cracked pipe depending on whether the ovalization increases or decreases the pipe diameter in the plane of the moment, respectively. As such, it may be necessary to modify the predictive methods to account for pipe ovalization. This issue is addressed in this section.

This section first provides a finite element analysis of a short TWC pipe and compares the prediction with the corresponding experimental data. Next, a summary of experimental observations to date regarding pipe ovalization is made. Finally, the implications of ovalization effects on J-estimation methods and limit-load predictions is provided.

4.2.5.1 Finite Element Prediction of Pipe Ovalization

The objective of this activity was to identify the shortcomings (if any) in existing analysis methods with respect to plastic ovalization on calculations of J. The overall objective was to make improvements in the analysis methods for better prediction of circumferential short through-wall-cracked pipes, if needed. The approach was to conduct a fully three-dimensional finite element analysis of Experiment 1.1.1.21 (see Table 3.2) including crack-initiation and crack growth. The analysis results were then compared with the experimental values, and the effect of ovalization on the J computation was evaluated.

Figures 4.27 and 4.28 show the overall schematic and dimensions of the pipe system used in Experiment 1.1.1.21. A three-dimensional finite element model was developed and is shown in Figure 4.29. The model consisted of 1/4 symmetric portion of the pipe with three different cross-sections. The model consisted of 579 elements and 3,761 nodes. The finite element analysis was performed under displacement control to a maximum load-line displacement of 160 mm (6.3 inches). Based on experimental data, the crack initiated at a load-line displacement of 62.48 mm (2.46 inches) and at a load of 1.359 kN (37,516 lbs).

Crack growth calculations were performed in ABAQUS using several load steps. The first load step was up to crack initiation. Subsequent steps consisted of releasing appropriate crack front nodes while simultaneously increasing the load-line displacement. The crack growth and applied displacement data were obtained from the experimental records. Table 4.19 shows the crack size, crack growth, and displacement data for each load step in the finite element analysis.

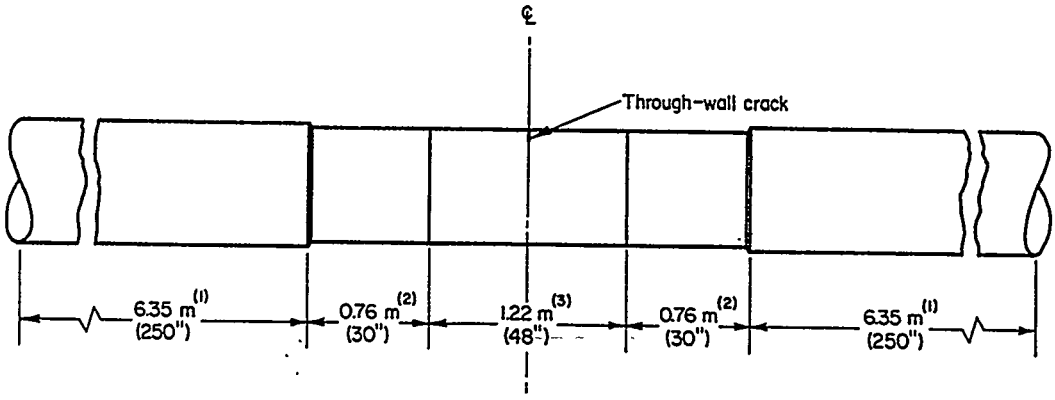

	(1)	(2)	(3)
Diameter	760 mm (30")	711 mm (28")	711 mm (28")
Wall Thickness	38.1 mm (1.5")	25.3 mm (0.995")	22.7 mm (0.893")
Ident. No.	IP-F5	DP2-F90	DP2-F26

Figure 4.27 Schematic of pipe used in Experiment 1.1.1.21

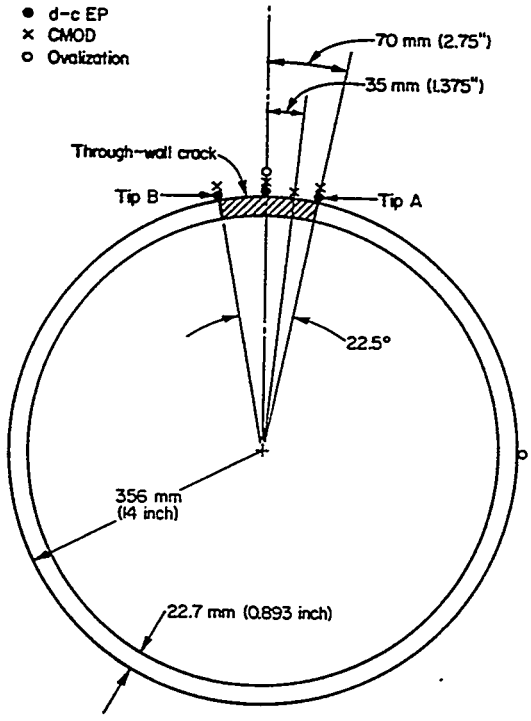

Figure 4.28 Schematic of crack geometry and instrumentation near the crack for Experiment 1.1.1.21

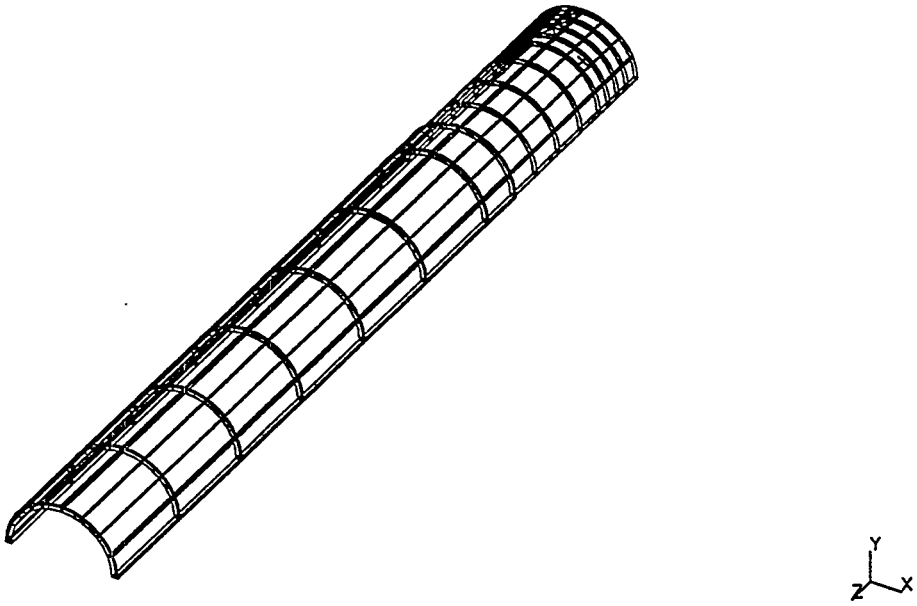

Figure 4.29 Finite element model for Experiment 1.1.1.21

Table 4.19 Crack growth data for Experiment 1.1.1.21 used in finite element analysis

Step	Pipe Displacement at the Load-Line, mm (inch)	Crack Growth from One Crack Tip, mm (inch)
1*	62.5 (2.46)	0.0 (0.0)
2	73.4 (2.89)	12.2 (0.48)
3	90.4 (3.56)	24.5 (0.96)
4	110.5 (4.35)	36.7 (1.45)
5	130.8 (5.15)	49.0 (1.93)
6	139.9 (5.51)	61.4 (2.41)
7	149.1 (5.87)	73.7 (2.89)
8	153.7 (6.05)	85.9 (3.37)
9	159.7 (6.29)	98.2 (3.86)

* Crack Initiation

Figure 4.30 shows the total load versus the pipe displacement at the load-line from the experiment and the 3D finite element calculations. The analysis results compare well with the experimental data.

The crack-mouth-opening displacement as a function of pipe displacement at the load line is shown in Figure 4.31. Data from the finite element model and the experiment compare well.

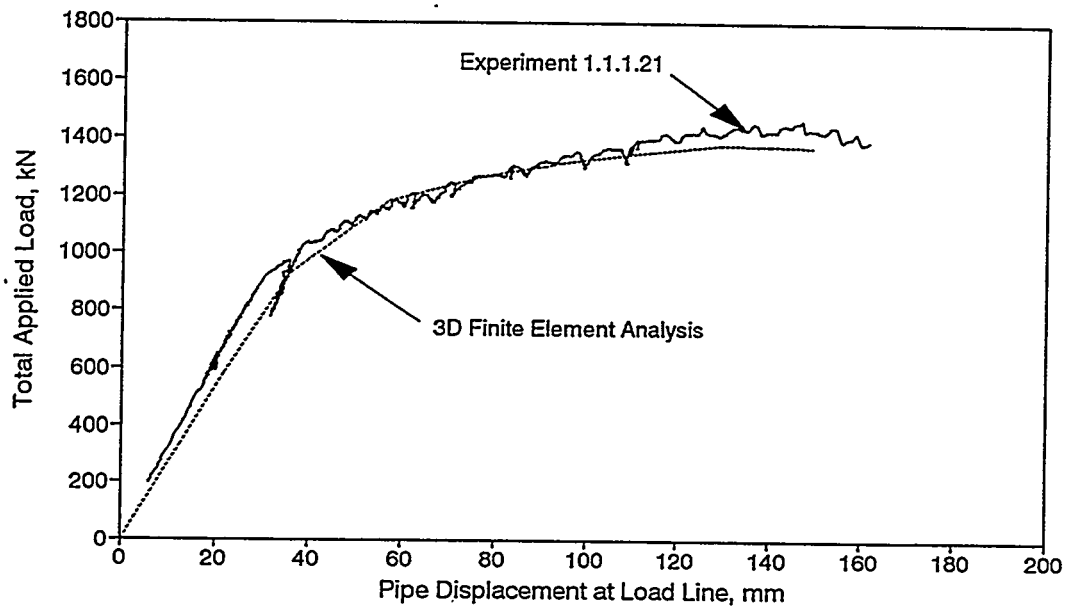

Figure 4.30 Load versus displacement comparison for Experiment 1.1.1.21

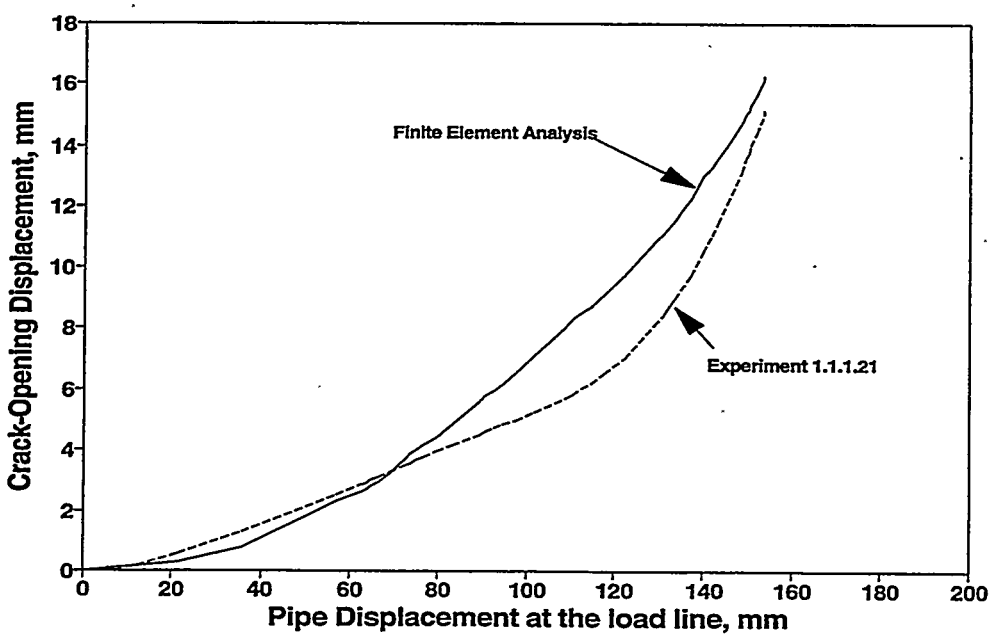

Figure 4.31 Crack-opening displacement comparison for Experiment 1.1.1.21

Figure 4.32(a) provides a plot of the computed J-integral versus pipe displacement at the load-line (machine compliance removed). Crack growth begins at a displacement of 62.48 mm (2.46 inches), with a J initiation value of about 700 kJ/m^2 (4,000 in-lb/in^2). Figure 4.32(b) shows a comparison of the J-resistance curve computed from this pipe analysis with the experimental J_D-R curve for a C(T) specimen (Figure 2.8). It is seen that the computed J at initiation is higher than the corresponding C(T) value. However, approaching 10 mm (0.39-inch) of crack growth, the curves are closer to each other. Note here that the C(T) J_D-R curve is plotted only for crack growth of about 30 percent of the uncracked ligament. Note also that the predicted pipe J-R curve does not have the typical monotonically increasing shape. This may be due to the rather course mesh used for the analysis where crack growth increments were about 12.48 mm (0.5 inch).

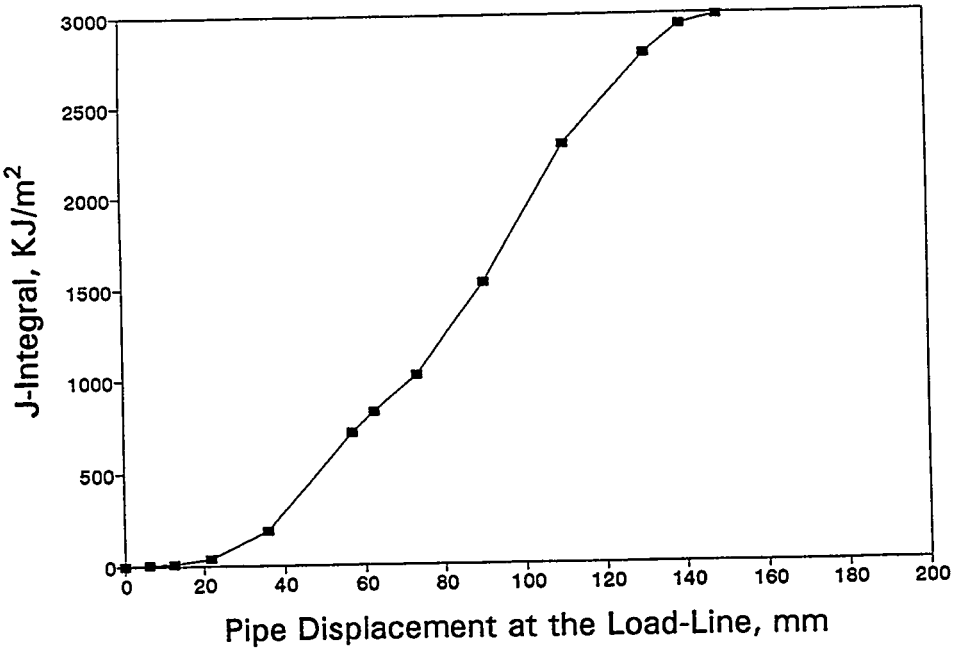

(a) J-Integral versus applied displacement

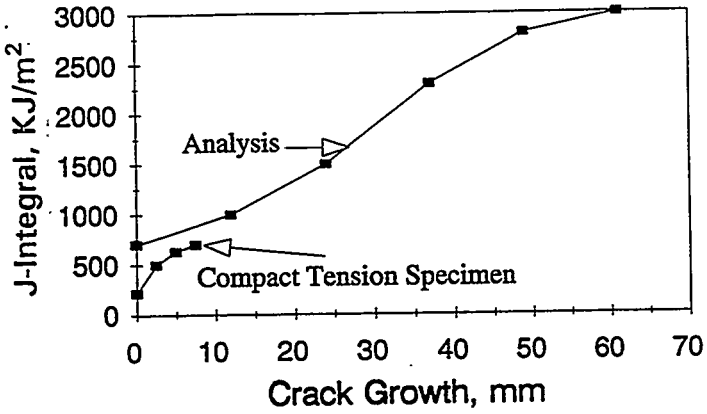

(b) Comparison of computed J-R curve and the experimental result

Figure 4.32 J versus pipe displacement and for pipe experiment and J_D-R curve for C(T) specimen for pipe material DP2-F26

Figure 4.33(a) shows predictions of crack ovalization for two different locations along the pipe as measured from the crack plane. It is seen that the pipe ovalizes in a manner to increase the pipe diameter from the top of the pipe (center of the crack) to the bottom of the pipe. Figure 4.33(b) compares the measured top to bottom ovalization with the predicted values. The top, smooth, curve is the z = 0 mm result from Figure 4.33(a), while the lower smooth curve is the z = 100 mm (3.94 inch) result from Figure 4.33(a). The experimental result represents the ovalization at the crack plane, i.e., at z = 0 mm (see the experimental procedure for measuring ovalization in Section 3.0). It is seen that the experimental ovalization results are overpredicted by the analysis. However, the trends of increasing top-to-bottom diameter are correct. Moreover, the experimental results rise and then stay constant for quite some amount of applied displacement before increasing at a displacement value of about 120 mm (4.72 inch). This result appears suspect, since ovalization tends to increase s slowly from the initial application of the load for all other cases (see Section 3.6.2).

4.2.5.2 Discussion of Ovalization Effects

From the results presented in Section 3.0 of this report, and from previous work in References 4.26 and 4.12, the following points summarize experimental observations regarding ovalization of circumferential TWC pipe subjected to bending. We assume that the crack is on the top of the pipe and is centered on the plane of the bending moment.

- For pipes with a large TWC, ovalization tends to increase the pipe diameter from top to bottom.
- For all surface-cracked pipes, ovalization tends to decrease the top to bottom pipe diameter.
- Uncracked pipes ovalize like a surface-cracked pipe, i.e., the pipe diameter decreases in the bending plane.

For all pipes with a short TWC tested in this program (see Section 3.0, Figures 3.9 to 3.14), the pipes also ovalized by increasing the pipe diameter in the bending plane. In fact, the only TWC pipe test we are aware of that did not ovalize by increasing the pipe diameter top to bottom was in Experiment 4T from Reference 4.12 (see Tables 4.20 and 4.21). This was a small-diameter pipe, 114 mm (4.48 inch), made of a very tough TP304 stainless steel (J_{Ic} = 1,769 kJ/m^2 [10,100 in-lb/in^2]) tested at room temperature. (The toughness of stainless steel is much higher at room temperature than at 288 C (550 F).

Based on these observations, we provide the following explanation of this phenomenon, which is certainly speculative since, as will be seen shortly, more information is needed to provide definitive conclusions. The very tough, small diameter pipes tested in Reference 4.12 clearly failed under Net-Section-Collapse conditions. On the other hand, all pipe tests with short cracks conducted in this program (Section 3.0) were large diameter, low toughness pipe (compared with Pipes 1T to 4T of Reference 4.12), which failed due to fracture rather than Net-Section-Collapse loads at 288 C (550 F). Since the pipe in Experiment 4T ovalized with decreasing diameter top to bottom, while all other short-cracked pipe ovalized with increasing top-to-bottom diameter, it may be concluded that this pipe deformed in a similar manner to a surface-cracked or uncracked pipe. How is this possible? Apparently, because of the high toughness, the crack did not grow until a very large moment was

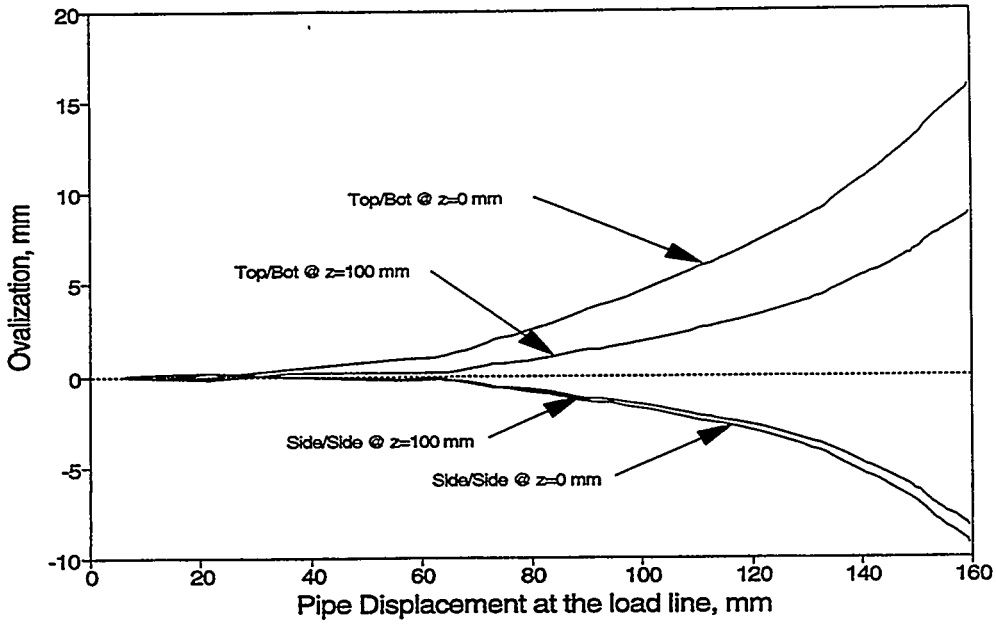

(a) Top-to-bottom and side-to-side predictions

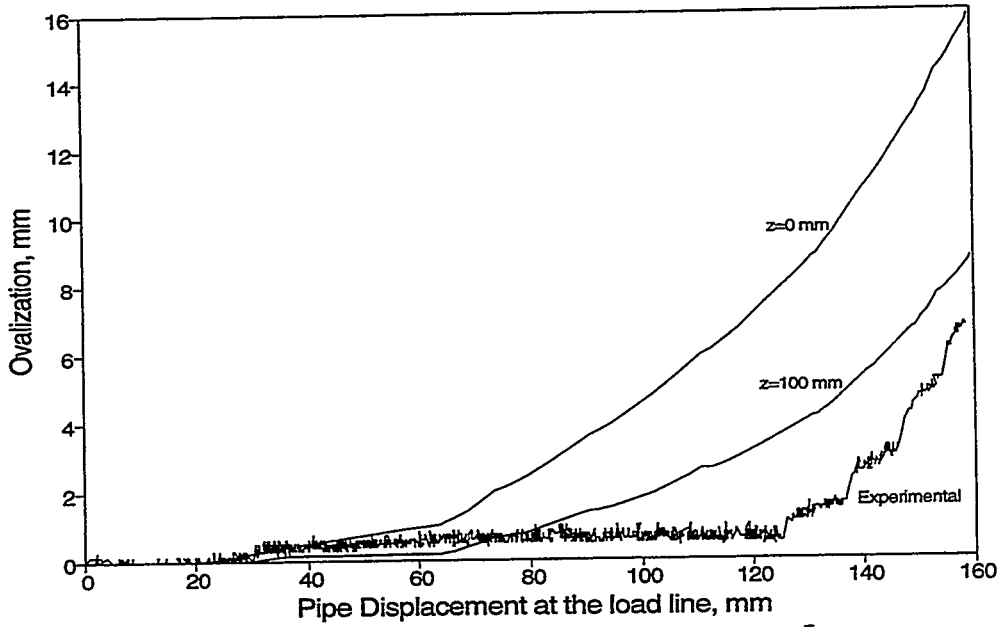

(b) Comparison of top-to-bottom predictions with experimental data taken at z=0

Figure 4.33 Ovalization predictions at and near a crack plane (z=axial distance from crack plane)

applied. Because of this, the pipe deformed as if there were no crack before and during crack growth. The other short-cracked pipes tested experienced crack growth at much lower bending moments (compared with the limit moment); and by the time large loads were applied, the crack had grown rather large in size, and hence ovalized as expected in a pipe with a large crack. ("Large" here is not precisely defined.)

Based on this discussion, if a pipe were to fail via reaching Net-Section-Collapse loads, one would expect a reduced limit load, since ovalization reduces the effective pipe diameter. In Reference 4.12, a reduction based on the four pipe tests was proposed based on the following equation:

$$M = 4R_m^2 t\sigma_f \left[(\cos(\theta/2) - \frac{1}{2}\sin(\theta)\right] V(\theta) \qquad (4\text{-}89)$$

where

$$V(\theta) = \pi/4(1.15 + 0.154\theta + 0.00175\theta^2 + 0.0805\theta^3) \qquad (4\text{-}90)$$

The term θ in Equation 4-90 is the half crack angle in radians. The first term in Equation 4-89 (i.e., everything except $V(\theta)$) is the standard Net-Section-Collapse equation (see Equation 4-84), while the second term is an empirical ovalization correction factor. ($V(\theta)$ in Equation 4-90 is slightly different from that presented in Reference 4.12, because the flow stress and θ are defined differently here). The $V(\theta)$ function becomes equal to 1 at a crack size equal to 23 percent of the pipe circumference, it equals 1.34 for $\theta/\pi = 0.5$, and it equals 0.92 for $\theta/\pi = 0.053$ (the crack size for Experiment 4T). Based on our experience in the Degraded Piping Program (Ref. 4.26), this function predicts high values for the large crack sizes. Whether it is appropriate for smaller crack sizes is not certain.

If we use Equation 4-84, (i.e., $M = 4\sigma_f R_m^2 t$) to predict failure in uncracked pipe, conflicting results are also obtained. For instance, for Experiment 4111-0 (Ref. 4.26) the predicted limit moment divided by the experimental maximum load is about 0.91. For Experiment 1.1.1.25 (tested here, see Tables 3.2 and 3.3), the predicted limit moment divided by the experimental maximum moment is 0.95. The Net-Section-Collapse analysis predictions for these two tests underpredict the maximum load, and no correction factor such as $V(\theta)$ is required.

In summary, we cannot recommend a correction factor such as $V(\theta)$ for the Net-Section-Collapse analysis of short cracks because not enough data are available on very tough materials. Indeed, failure load predictions based on methods that depend on the Net-Section-Collapse formula (Paris, LBB.NRC, and LBB.ENG) are quite good for short cracks, as shown in Section 4.3. More work is necessary before the effect of crack length on the analysis correction factors can be assessed. It should be noted that the new GE/EPRI h, V, and F functions are derived from finite element analyses, so that pipe ovalization is included in that method. Furthermore, under combined pressure and bending, the internal pressure will prevent the pipe from ovalizing, so ovalization effects would be less significant. This is discussed further in Section 4.2.2.11.

4.3 Comparison with Experimental Data

In this section, predicted loads using various engineering analysis procedures are compared with experimental data on circumferential through-wall-cracked pipes subjected to bending. The main focus is on evaluating the ability of J-estimation schemes and other analysis procedures, which are discussed in Sections 4.1 and 4.2, to predict loads, displacements, and crack growth in pipes.

In general, estimation schemes may be classified as either predictive or generative. Predictive schemes require knowledge of the crack-growth resistance (e.g., J-resistance curve) and plastic-flow (e.g., stress-strain curve) behavior of the material. This information is used to predict the load-displacement behavior of the structure including loads and displacements at crack initiation and at crack-growth instability. Results of analyses presented in this report are based on predictive J-estimation methods. Generative schemes, on the other hand, require *apriori* knowledge of the experimentally derived load-displacement record and are frequently used to calculate a J-resistance curve as a function of crack extension. This type of analysis is referred to as an η-factor analysis. An η-factor analysis can be valuable for evaluating fracture toughness data from small specimen geometry such as compact tension specimens, but it cannot be used to predict loads or displacements of a cracked pipe by itself; hence for licensing applications it may be relatively useless by itself. However, η-factor solutions are embedded into the LBB.ENG2, LBB.ENG3, LBB.NRC, LBB.GE, and Paris/Tada methods.

4.3.1 Predictive Methods for Fracture Analysis

The predictive analyses involved several engineering methods. They were:

(1) The LBB.ENG2 method (Refs. 4.6-4.8, and Section 4.2.3),
(2) The LBB.ENG3 method (Refs. 4.9-4.11, and Section 4.2.4),
(3) The LBB.NRC method (Refs. 4.5 and Section 4.1),
(4) The LBB.GE method (Ref. 4.6 and Section 4.1),
(5) The GE/EPRI method (Refs. 4.1-4.3 and Section 4.2.2),
(6) The Paris/Tada method (Ref. 4.4 and Section 4.1),
(7) The ASME Section XI IWB-3640 or 3650 pipe flaw evaluation criteria (Refs. 4.13 and 4.32 and Section 4), with a safety factor of 1.0, and
(8) The EPRI NP-192 Net-Section-Collapse (NSC) analysis (Ref. 4.12 and Section 4.1).

Methods (1) to (6) are based on elastic-plastic J-estimation schemes. Equations for calculating the J-integral by each of these methods were discussed in earlier sections. In using the GE/EPRI method, the influence functions (V-, h-functions, etc.) developed by Kumar, et al., (Ref. 4.2) and later reevaluated for smaller cracks (Ref. 4.3 and Section 4.2.2) were used. In both cases, we also investigated whether the inclusion of a plastic-zone size correction in the elastic portion of the solution would make any notable difference in the predictions. In this report, the GE/EPRI methods with the influence functions by Kumar, et al., will be identified as GE/EPRI-1A and GE/EPRI-1B when the plastic-zone size correction is applied and when the plastic-zone size correction is not applied, respectively. Similarly, the GE/EPRI methods with the new influence functions discussed earlier and in Reference 4.3 will be identified as GE/EPRI-2A and GE/EPRI-2B when the plastic-zone size

correction is applied and when the plastic-zone size correction is not applied, respectively. The R6, Revision 3, Option 1 method is discussed and compared experimental data later in this section.

Methods (7) and (8) do not consider explicit fracture-mechanics principles. They are based on simplified failure criteria representing Net-Section Collapse and some EPFM correction factors developed from the original and a different modification* to the GE/EPRI solution together with lower bound properties.

4.3.2 Idealizations of Material Properties

In performing analyses of the experiments, the constitutive law characterizing the material's stress-strain response was represented by the Ramberg-Osgood model given by

$$\frac{\epsilon}{\epsilon_0} = \frac{\sigma}{\sigma_0} + \alpha \left[\frac{\sigma}{\sigma_0}\right]^n \tag{4-91}$$

Also, the J-R curve of the pipe material was represented by a power-law equation of the form

$$J_R(\Delta a) = J_{Ic} + C_1 \left[\frac{\Delta a}{r}\right]^m \tag{4-92}$$

Note that Equations 4-91 and 4-92 are identical to Equations 4-1 and 4-2. They are repeated in this subsection for proximity of subsequent estimation analyses. All of the variables in Equation 4-91 and 4-92 were defined in Section 4.1.1.2.

4.3.2.1 Adequacy of Power-Law Models

In most J-estimation schemes, such as the GE/EPRI, LBB.GE, LBB.NRC, LBB.ENG2, and LBB.ENG3 methods, the material model in Equation 4-91 is necessary since the formulation of J-integral and other relevant fracture parameters are based on the power-law idealization. Unfortunately, there are actual material data for which it is difficult to represent the complete range of stress-strain relationships by a Ramberg-Osgood model. Reference 4.6 has some discussions on the limitation of this model. It was indicated in this reference that care must be taken in selecting the appropriate range of stress-strain data for a least-square fit by this power-law model. As shown in Figure 4.34, several possibilities exist in fitting the Ramberg-Osgood model to the test data and can correspondingly provide widely different values of model parameters, α and n. From this study (see the solid line in Figure 4.34), we found that the range of raw stress-strain data between yield strain and 80 to 90 percent of ultimate strain would provide the best representation by the Ramberg-Osgood model which confirms our past experience. All values of α and n presented in this study were computed by this approach.

---

* The J_p term was modified to have α to the [1/(n+1)] power, a questionable modification as noted in Reference 4.6.

In characterizing the fracture toughness of materials, the ASTM Deformation J-resistance curve, J_D-R curve, was used with the curve extrapolated by a power-law hardening for crack-growth beyond 30 percent of the uncracked ligament in the C(T) specimens. Because the C(T) specimens were small, large extrapolation of the data was necessary in order to predict crack growth in a large diameter pipe. Figure 4.35 shows that the power-law model of Equation 4-92 can represent fairly well the actual J_D-R data from C(T) specimens.

From our routine material characterization tests, we usually have more than one set of experimental data for both stress-strain and J_D-R curves. Hence, when there is more than one specimen, the values of material constants presented and used in our analyses represent their average properties.

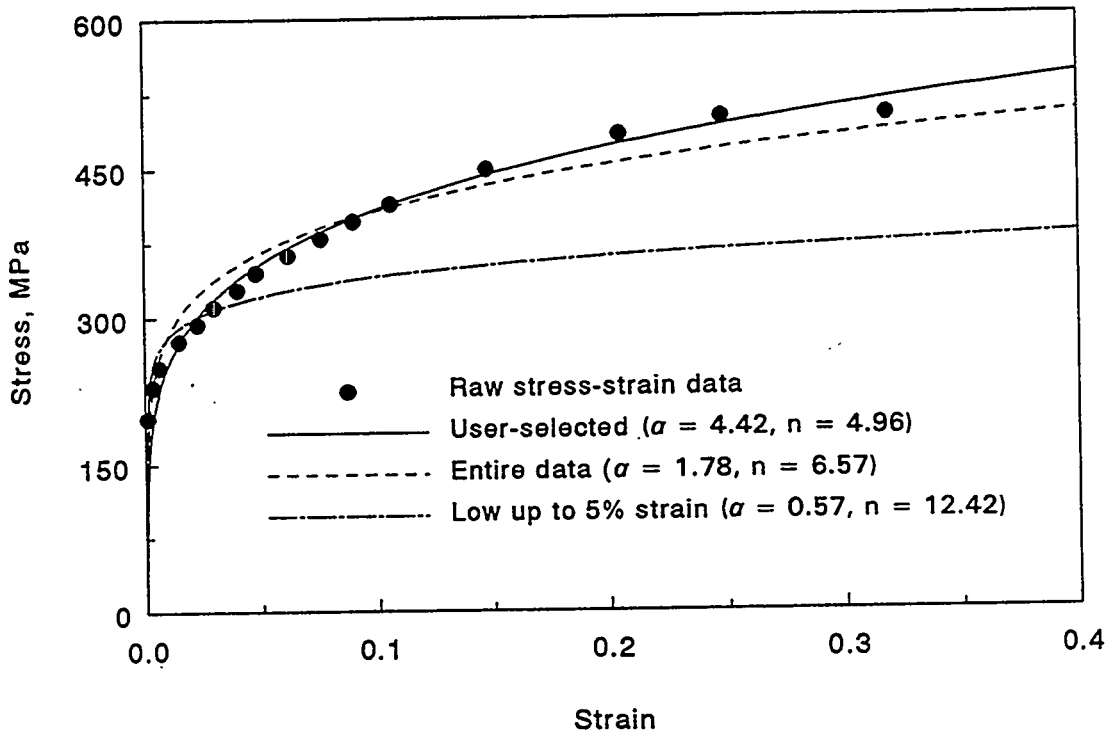

Figure 4.34 Ramberg-Osgood model for stress-strain curves

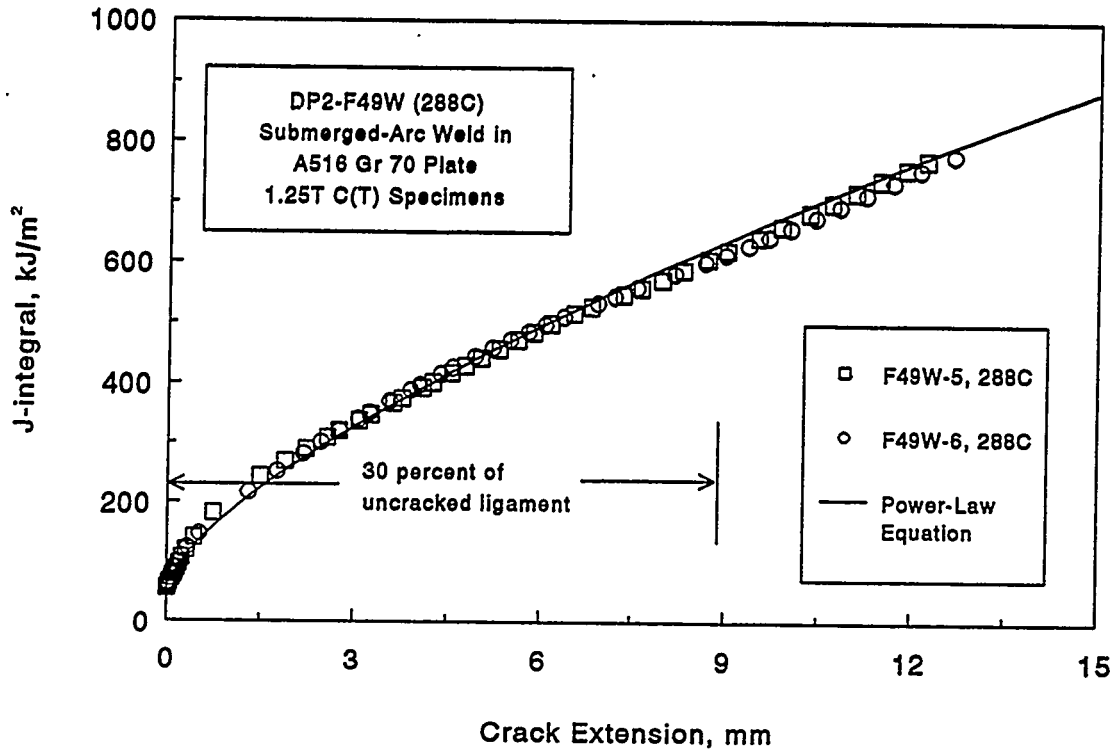

Figure 4.35 Power-law model for extrapolated J_D-R curves from compact tension specimens

4.3.3 Pipe Fracture Evaluation

In order to evaluate structural integrity, the load-carrying capacity of a piping system needs to be established. In a typical J-estimation scheme, there are several means by which it can be estimated. They are based on various definitions of failure criteria such as initiation of crack growth and unstable crack growth in elastic-plastic fracture mechanics. Failure loads based on these criteria are defined below.

4.3.3.1 Initiation Load

The initiation load, P_i, is defined as the load that corresponds to initiation of crack growth in a pipe. If J is a relevant crack driving force, P_i can be estimated by solving the following nonlinear equation

$$f(P_i) = J(P_i, a_o) - J_{Ic} = 0 \qquad (4\text{-}93)$$

in which $J(P_i,a_o)$ is the energy release rate for the initial crack size, a_o, and load, P_i, and J_{Ic} is the fracture toughness at crack initiation. Standard numerical techniques such as the bisection method (Ref. 4.17), Newton-Raphson method, or others can be applied to solve Equation 4-93.

4.3.3.2 Maximum Load

In applications of nonlinear fracture mechanics, particularly for nuclear power plants, the J-tearing theory is a very prominent concept for calculating the maximum load-carrying capacity of a pipe. It is based on the fact that fracture instability can occur after some amount of stable crack growth in tough and ductile materials with an attendant higher applied load level at fracture. Let J and J_R denote the crack-driving force and toughness of a ductile piping material as a function of load and crack size. The limit state characterizing fracture instability based on J-tearing theory is given by

$$J(P_{max}, a^*) = J_R(a^* - a) \tag{4-94}$$

$$\frac{\partial J}{\partial a}(P_{max}, a^*) = \frac{dJ_R}{da}(a^* - a) \tag{4-95}$$

where P_{max} and a^* represent load and crack size when crack growth becomes unstable. Note that Equations 4-93, 4-94, and 4-95 are identical to Equations 4-20, 4-21, and 4-22. They are also repeated here for proximity of subsequent estimation analyses. Letting $g_1(P_{max},a^*) = J - J_R$ and $g_2(P_{max},a^*) = \partial J/\partial a - dJ_R/da$ as two nonlinear functions, Equation 4-94 can be rewritten as

$$g_1(P_{max}, a^*) = 0 \tag{4-96}$$

$$g_2(P_{max}, a^*) = 0 \tag{4-97}$$

which are two nonlinear simultaneous equations with the independent variables P_{max} and a^*.

Other analyses methods discussed in this study are the ASME Section XI IWB-3640 or 3650 pipe flaw evaluation criteria and the EPRI NP-192 Net-Section-Collapse analysis. The maximum loads predicted by these methods can be obtained directly from the equations described in Section 4.1 of this report.

4.3.3.3 Load-Displacement Relationship

Another desirable feature of any J-estimation scheme is its ability to predict load-displacement or moment-rotation behavior up to and beyond maximum load. This ability is important for several reasons. First, some estimation methods, such as the Paris/Tada, LBB.NRC, LBB.ENG2, and LBB.ENG3 methods, calculate the applied crack driving force (i.e., J-integral) by estimating the moment-rotation relationship and integrating that relationship to determine the applied J. Consequently, the J values depend on how well the experimental load-displacement record is predicted.

The second reason for evaluating the load-displacement predictions involves the evaluation of LBB if significant thermal expansion (displacement-controlled) stresses exist. The instability predictions for such a compliant loading, especially if snubbers are removed for more flexible designs, depend on the accuracy of the predicted load-displacement or moment-rotation behavior.

Third, dynamic finite element analyses that require prediction of the response of a cracked piping system to dynamic (earthquake) conditions require the use of a cracked "nonlinear spring" element to model the response cost effectively. This special element requires the prediction of the cracked-pipe compliance, which again requires an adequate prediction of load-displacement or moment-rotation response (Ref. 4.17).

For many of the cases considered here, the term "load-displacement" refers to the "pipe displacement at the load-line", which is the displacement under the 4-point load saddles used in the experiments (see Figure 4.36). Since all of the estimation methods predict the moment versus rotation relationship, one must be able to estimate the pipe displacement at the load line in order to compare predictions with experimental data. The pipe displacement at the load line is estimated from predictions using the following steps:

(i) Obtain the elastic and plastic displacement Δ_{PLL}^{NC} at the load line using standard beam theory solutions for pipes without cracks,

(ii) Obtain the displacement due to cracks by multiplying the sum of the elastic and plastic rotation due to a crack by the outer span length, L, minus the inner span length, S, divided by 4, i.e.,

$$\Delta_{PLL}^{c} = \left(\phi_e^c + \phi_P^c\right)\left[\frac{L-S}{4}\right] \tag{4-98}$$

(iii) the total pipe displacement at the load line, Δ_{PLL}, is the sum of the displacements obtained in steps (i) and (ii).

4.3.3.4 NRCPIPE Computer Program

The NRCPIPE code was developed to perform elastic-plastic fracture-mechanics analysis by which the fracture-failure conditions of an engineering structure can be established in terms of sustainable load (or stress) or displacement (Ref. 4.26). For nuclear applications, engineering elastic-plastic fracture-mechanics techniques are based on the J-integral fracture parameter. Hence, various J-estimation methods for analyzing cracked pipes and piping welds were incorporated into this program. To perform a fracture analysis, the user provides the input data on the pipe and crack geometry, material stress-strain characteristics, and fracture resistance of the material (i.e., a J-R curve) as obtained from a laboratory test specimen. A wide variety of results characterizing fracture characteristics of a cracked pipe can be obtained. Further details on this program can be found in Reference 4.26.

The engineering treatment of elastic-plastic fracture mechanics is still in a dynamic state of development. Although a number of procedures have been proposed, many have not been verified by comparison with experimental data. For this reason, the NRCPIPE code was written to include numerous analysis procedures. At the user's option, NRCPIPE can perform analyses using any of these procedures. In addition, the modular structure of NRCPIPE permits inclusion of new procedures as they are developed. Incomplete blocks of code have been reserved for just this purpose.

The NRCPIPE code was originally developed under the past Degraded Piping Program (Ref. 4.26). A significant numbers of developments and enhancements were made in the Short Cracks in Piping and Piping Welds program (Ref. 4.33) and are incorporated into Version 2.0.

4.3.4 Analysis of Pure-Bending Pipe-Fracture Experiments

A total of twelve full-scale pipe-fracture experiments under pure bending were analyzed to determine the predictive capability of J-estimation schemes and other analysis methods. In all experiments, the pipes had circumferential through-wall cracks and were subjected to pure bending loads without internal pressure. The experiments involved both austenitic and ferritic steel piping with cracks located in either the base or weld metal. The initial crack lengths were both short and long and ranged between 5.3 and 38.3 percent of the pipe circumference. There were five experiments conducted at room temperature while the rest were performed at 288 C (550 F). Figure 4.36 shows a schematic of the experimental setup for one of the full-scale pipe fracture tests. More details of the tests are described in Section 3 of this report.

The pipe fracture experiments were analyzed using various predictive analysis methods described earlier. All of the J-estimation methods are available in the current versions of the NRCPIPE code (Version 1.4G and Version 2.0). Using this program, both initiation and maximum loads were computed and were compared with the test data. In some cases, load-displacement relationships were also determined and were compared with the experimental record. The pure bending pipe experiments, which were analyzed in this study, are classified into: (1) through-wall-cracked small-diameter pipes, (2) through-wall-cracked large diameter pipes, and (3) through-wall-cracked welded pipes. Results of the analyses for pure bending are given below. Comparison with the R6, Revision 3, Option 1 predictions and the pressure plus bending experiments are given later.

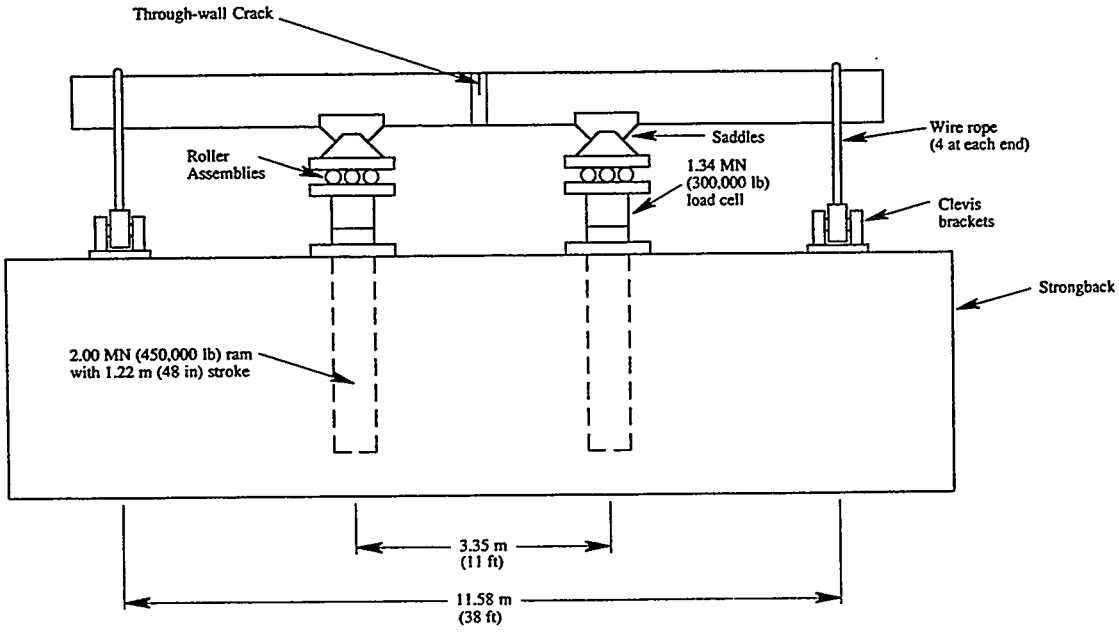

Figure 4.36 Schematic of experimental setup for Experiment 1.1.1.21

4.3.4.1 Through-Wall-Cracked Small-Diameter Pipe Bending Experiments

This section involves fracture analyses of five small-diameter, circumferential through-wall-cracked pipes typically at room temperature and under pure bending. Examples of such TWC pipe experiments are Experiments 1T, 2T, 3T, and 4T from a past EPRI sponsored program (Ref. 4.34) and Experiment 1.1.1.26 from the current Short Cracks in Piping and Piping Welds program (Ref. 4.33), both of which were conducted at Battelle. The fracture data from these tests were used to assess various J-estimation methods to predict the load-carrying capacity of TWC pipes. Comparisons were also made between the experimental data and Net-Section-Collapse and ASME Section XI flaw evaluation criteria.

The test specimens for Experiments 1T, 2T, 3T, and 4T were 101.6-mm (4-inch) nominal diameter, TP304 stainless steel pipes with circumferential through-wall cracks in the base metal with crack sizes ranging from 5.3 percent to 37.1 percent of the mean pipe circumference. The test specimen for Experiment 1.1.1.26 was a 101.6-mm (4-inch) nominal diameter Schedule 160 TP316LN stainless steel pipe with a through-wall-crack in the base metal. The crack size was 24.4 percent of the mean pipe circumference. The specific objective of Experiment 1.1.1.26 was to duplicate a similar experiment performed at Electricité de France (Ref. 4.35) using a TP316L (French designation of Z3 CND 18-12) pipe sample from the same pipe. In all experiments, the pipes were loaded in four-point bending without any internal pressure and at room temperature. The loading rates were quasi-static. Table 4.20 provides the summary of pipe geometry, test temperature, and results for these five experiments. Material properties including the power-law fit parameters (see Equations 4-92 and 4-.93 for their definitions) for the stress-strain and the C(T) specimen J_D-R curve in these experiments are given in Table 4.21.

Table 4.20 Summary of pipe geometry and results for small-diameter through-wall-cracked pipe experiments

	Experiment Number				
	1T	2T	3T	4T	1.1.1.26
Pipe Material Crack Location	SA-312 TP304 Base Metal	SA-312 TP304 Base Metal	SA-312 TP304 Base Metal	SA-312 TP304 Base Metal	TP316L Base Metal
Test Temperature, C (F)	20 (68)	20 (68)	20 (68)	20 (68)	21 (70)
Outside Pipe Diameter (D_0), mm (inch)	114.3 (4.50)	114.3 (4.50)	114.3 (4.50)	114.3 (4.50)	106.2 (4.18)
Actual Wall Thickness (t), mm (inch)	9.00 (0.354)	8.94 (0.352)	8.89 (0.350)	8.89 (0.350)	8.31 (0.327)
Crack Length (θ/π), percent	37.1	22.9	29.0	5.3	24.4
Four-point Bending Inner Span, m (inch)	0.406 (16)	0.406 (16)	0.406 (16)	0.483 (19)	0.610 (24)
Four-point Bending Outer Span, m (inch)	1.524 (60)	1.524 (60)	1.346 (53)	1.524 (60)	1.524 (60)
Initiation Load (P_i), kN (lb)	63.70 (14,300)	95.21 (21,400)	95.85 (21,500)	139.30 (31,300)	72.52 (16,300)
Maximum Load (P_{max}), kN (lb)	64.81 (14,600)	97.86 (22,000)	98.39 (22,100)	139.52 (31,400)	74.84 (16,800)

Table 4.21 Tensile strength and fracture toughness for small-diameter through-wall-cracked pipe experiments

	Experiment Number				
	1T	**2T**	**3T**	**4T**	**1.1.1.26**
Modulus of Elasticity (E), GPa (ksi)	179.25 (26,000)	179.25 (26,000)	179.25 (26,000)	179.25 (26,000)	157.46 (22,800)
Yield Stress (σ_y), MPa (psi)	247 (35,800)	247 (35,800)	247 (35,800)	247 (35,800)	254 (36,800)
Ultimate Stress (σ_u), MPa (psi)	630 (91,400)	630 (91,400)	630 (91,400)	630 (91,400)	532 (77,200)
Design Stress (S_m), MPa (psi)	138 (20,000)	138 (20,000)	138 (20,000)	138 (20,000)	115 (16,700)
Ramberg-Osgood Coefficients[a]					
α	2.56	2.56	2.56	2.56	5.50
n	5.50	5.50	5.50	5.50	4.76
Extrapolated J-R Curve Parameters[b]					
J_{Ic}, kJ/m^2 (lb-in/in^2)	1,770 (10,100)	1,770 (10,100)	1,770 (10,100)	1,770 (10,100)	879 (5,020)
C_1, kJ/m^2 (lb-in/in^2)	343.3 (1,960)	343.3 (1,960)	343.3 (1,960)	343.3 (1,960)	778.9 (4,448)
m	0.642	0.642	0.642	0.642	0.974

(a) Base-metal stress-strain curve is represented by: $\epsilon/\epsilon_0 = \sigma/\sigma_0 + \alpha(\sigma/\sigma_0)^n$, $\sigma_o = \sigma_y$, $\epsilon_o = \sigma_o/E$

(b) Base-metal J-R curve is from C(T) specimens and is represented by: $J = J_{Ic} + C_1(\Delta a/r)^m$, where r = 1 mm

4.3.4.2 Results of Analyses

Figure 4.37 shows the initiation load ratio, defined as the ratio of experimental initiation load and predicted initiation load, for Experiments 1T, 2T, 3T, 4T, and 1.1.1.26 obtained from the five different J-estimation schemes mentioned above. From the results of the four EPRI-sponsored pipe tests, it appears that most estimation methods provide reasonably accurate predictions of initiation load except for Experiment 4T. Predictions by the GE/EPRI-1A method underpredicted the loads the most. For Experiment 4T, which is a short-cracked experiment ($\theta/\pi = 0.053$), all estimation methods overpredicted the initiation loads significantly. Among the methods considered here, LBB.ENG2 overpredicted the initiation load for this experiment more than any other method.

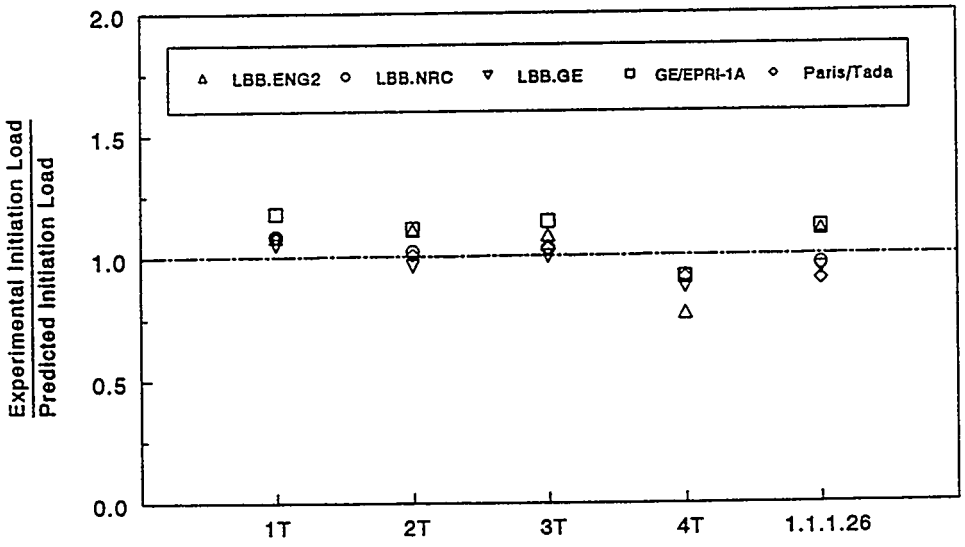

Figure 4.37 Comparisons of initiation loads from Experiments 1T, 2T, 3T, 4T, and 1.1.1.26 on the 101.6-mm (4-inch) nominal diameter TP304 and TP316L stainless steel through-wall-cracked pipes with predictions by various analyses

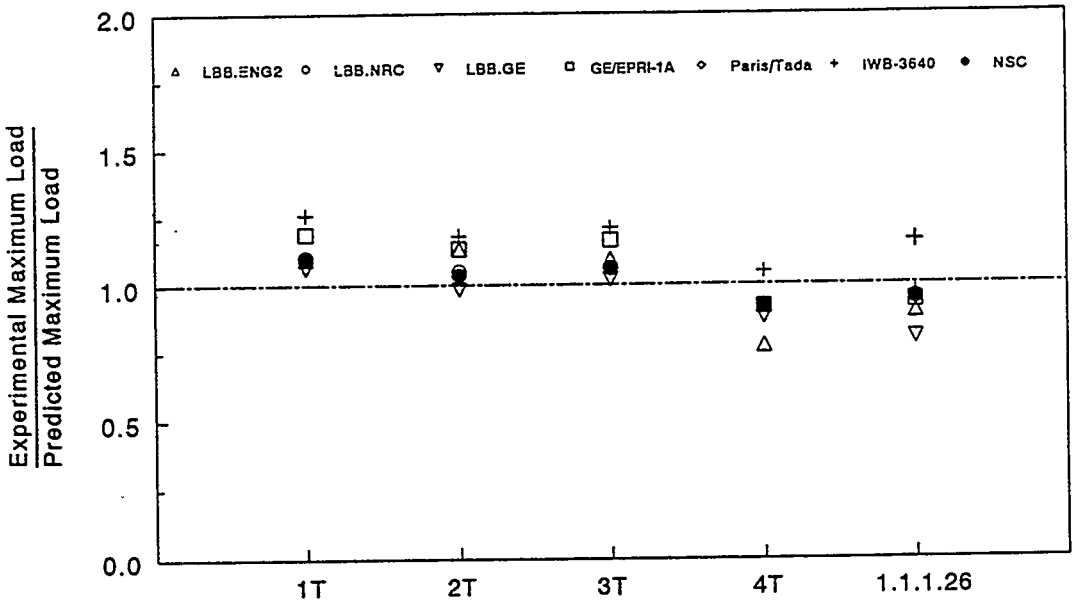

Figure 4.38 Comparisons of maximum loads from Experiments 1T, 2T, 3T, 4T, and 1.1.1.26 on the 101.6-mm (4-inch) nominal diameter stainless steel through-wall-cracked pipes with predictions by various analyses

For Experiment 1.1.1.26, all estimation methods, except the LBB.ENG2 and GE/EPRI-1A methods, overpredicted the initiation load. This is somewhat surprising since the predicted crack initiation in pipes with similar diameter and crack size from the past EPRI-sponsored experiments occurred at lower loads than the experimental values.

Similar results are also plotted in Figure 4.38 for the same pipes in terms of maximum load ratio, defined as the ratio of the experimental maximum load to the predicted maximum load for the various estimation methods. As before, results indicate that most estimation methods are reasonably accurate except for Experiments 4T and 1.1.1.26. Once again, the GE/EPRI-1A or -2A analysis significantly underpredicted the load for Experiments 1T, 2T, and 3T. Similar trends between Figures 4.37 and 4.38 are expected since for the small-diameter pipes considered in this study, both initiation and maximum load were almost coincidental.

For Experiment 1.1.1.26, all estimation methods, except for IWB-3640, overpredicted the maximum load. This was consistent with findings related to the prediction of maximum load for Experiment 4T. However, the degree of overprediction for this experiment was less than that for Experiment 4T. Predictions by LBB.ENG2 and GE/EPRI-1A or -2A methods were especially good. Figure 4.39 shows the plots of applied load versus pipe displacement at the load-line in Experiment 1.1.1.26, by several J-estimation methods and experimental data. Comparisons with fracture data suggest that the load-displacement predictions by LBB.ENG2 and GE/EPRI-1A or -2A are reasonably accurate until significant crack growth occurs in the pipe. The maximum loads by LBB.ENG2 and GE/EPRI-1A or -2A were calculated to be 85.58 kN (19,239 lb) and 80.02 kN (17,989 lb) and are slightly larger than the maximum experimental load of 74.84 kN (16,825 lb).

Figure 4.38 also presents comparisons of results with predictions based on ASME Section XI IWB-3640 flaw evaluation and Net-Section-Collapse criteria. These results show that the experimental maximum loads are close to the NSC analysis predictions for large cracks. This is expected since the pipe diameters are small. Comparisons with the ASME Section XI curve indicate that the IWB-3640 analysis underpredicts the experimental maximum loads, particularly for large TWC pipes. However, for Experiment 4T, the NSC method overpredicted the maximum experimental load - a trend also exhibited by the J-estimation schemes.

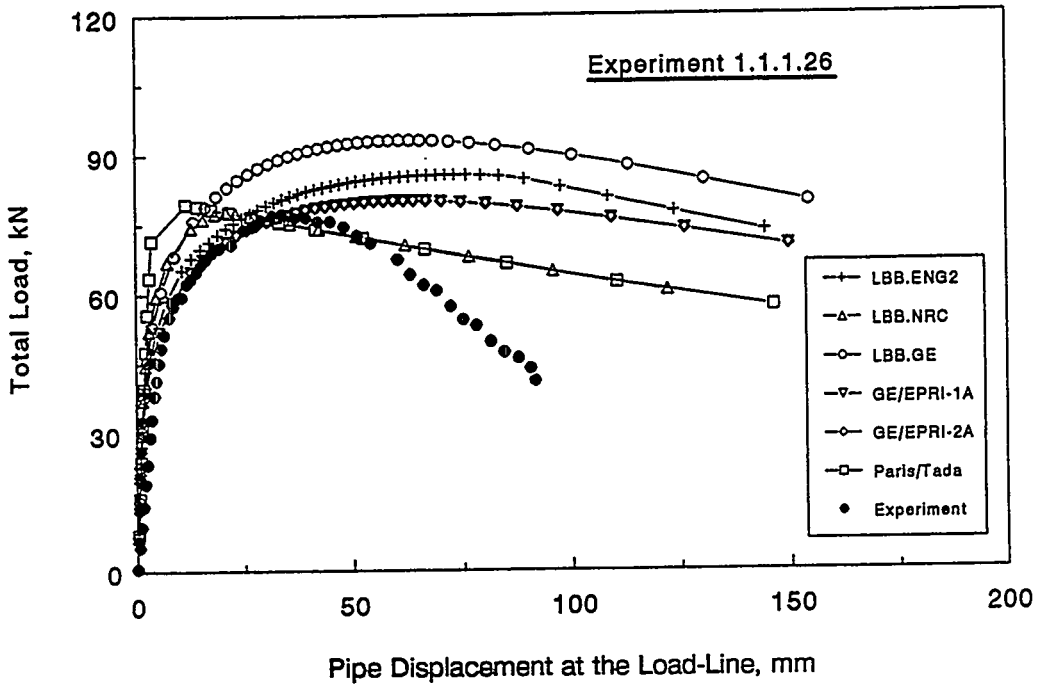

Figure 4.39 Comparison of applied load versus pipe displacement at the load-line plot from Experiment 1.1.1.26 on a 101.6-mm (4-inch) nominal diameter TP316L stainless steel through-wall-cracked pipe with predictions by various J-estimation schemes

4.3.4.3 Through-Wall-Cracked Large-Diameter Pipe Experiments

In this section, five large-diameter, through-wall-cracked pipe fracture experiments were analyzed. The pipe fracture data were previously developed to assess several J-estimation methods to predict the load-carrying capacity of TWC pipes. Experiments from the past Degraded Piping Program (Ref. 4.26) and the current Short Cracks in Piping and Piping Welds Program (Ref. 4.33) were considered. The comparisons also involved analyses based on Net-Section-Collapse and ASME Section XI flaw evaluation criteria.

The experiments from the Degraded Piping program analyzed in this study were Experiments 4111-2 and 4111-5. Experiment 4111-2 was conducted on a 711-mm (28-inch) nominal diameter A155 KC60 CL1 (A515 Grade 60) carbon steel pipe with a circumferential through-wall crack in the base metal with the crack size equal to 37 percent of the mean pipe circumference. Experiment 4111-5, on the other hand, was conducted on a 711-mm (28-inch) nominal diameter TP316 stainless steel welded pipe with a circumferential through-wall crack in the weld metal with the crack size also equal to 37 percent of the mean pipe circumference. The weld type in Experiment 4111-5 was shielded-metal arc (SMAW). Pipes with identical geometric properties were also tested in the Short Cracks in Piping and Piping Welds program (Experiments 1.1.1.21 and 1.1.1.23) in which the crack sizes were reduced to 6.25 percent of the mean pipe circumference. The objective was to evaluate the predictive capability of current analytical methods for pipes with short circumferential through-wall-crack lengths regarding the maximum load-carrying capacity. Both test specimens in Experiments 1.1.1.21 and 1.1.1.23 were 711.2-mm (28-inch) nominal diameter pipes made of A155 KC60 CL1 (A515

Grade 60) carbon steel and TP316L stainless steel, respectively. The weld type in Experiment 1.1.1.23 was submerged-arc weld (SAW). Finally, Experiment 1.1.1.24 was conducted on 609.6-mm (24-inch) nominal diameter Schedule 80 SA-333 Grade 6 carbon steel pipe with a short through-wall crack in the center of a shop-fabricated submerged-arc weld. The crack length was 7.9 percent of the mean pipe circumference. In all these experiments, the pipes were loaded in four-point bending without internal pressure at 288 C (550 F). The loading rates were quasi-static.

Table 4.22 provides the summary of pipe geometry, test temperature, and results for these five experiments. Material properties including the power-law fit parameters for the stress-strain and the C(T) specimen J_D-R curve in these experiments are given in Table 4.23. For the pipe welds (Experiments 4111-5, 1.1.1.23, and 1.1.1.24), the J_D-R curve parameters in Table 3.4 correspond to the weld metal toughness.

Table 4.22 Summary of pipe geometry and results for large-diameter through-wall-cracked pipe experiments

	Experiment Number				
	4111-2	**4111-5**	**1.1.1.21**	**1.1.1.23**	**1.1.1.24**
Pipe Material Crack Location	A515 Grade 60 Base metal	SA-240 TP316 SMAW	A515 Grade 60 Base Metal	SA-240 TP316L SAW	SA-333 Grade 6 SAW
Test Temperature, C (F)	288 (550)	288 (550)	288 (550)	288 (550)	288 (550)
Outside Pipe Diameter (D_0), mm (inch)	711 (28.0)	720 (28.3)	711 (28.0)	711 (28.0)	612 (24.1)
Actual Wall Thickness (t), mm (inch)	23.6 (0.93)	30.2 (1.19)	22.7 (0.89)	30.2 (1.19)	31.3 (1.23)
Crack Length (θ/π), percent	37.0	37.0	6.25	6.25	7.90
Four-point Bending Inner Span, m (ft)	3.35 (11.0)	3.35 (11.0)	3.35 (11.0)	3.35 (11.0)	3.35 (11.0)
Four-point Bending Outer Span, m (ft)	11.58 (38.0)	11.58 (38.0)	11.58 (38.0)	11.58 (38.0)	11.58 (38.0)
Initiation Load (P_i), kN (lb)	396 (89,000)	471 (105,900)	1,247 (280,300)	1,274 (286,400)	1,110 (249,500)
Maximum Load(P_{max}), kN (lb)	585 (131,500)	611 (137,400)	1,466 (329,600)	1,489 (334,700)	1,660 (373,200)

Table 4.23 Tensile strength and fracture toughness for large-diameter through-wall-cracked pipe experiments

	Experiment Number				
	4111-2	**4111-5**	**1.1.1.21**	**1.1.1.23**	**1.1.1.24**
Modulus of Elasticity (E), GPa (ksi)	179.2 (26,000)	182.7 (26,500)	179.2 (26,000)	182.7 (26,500)	199.9 (29,000)
Yield Stress (σ_y), MPa (psi)	231 (33,500)	229 (33,200)	231 (33,500)	143 (20,700)	229 (33,200)
Ultimate Stress (σ_u), MPa (psi)	544 (78,900)	501 (72,700)	544 (78,900)	427 (61,900)	525 (76,100)
Design Stress (S_m), MPa (psi)	114 (16,500)	121 (17,500)	114 (16,500)	96 (13,900)	125 (18,100)
Ramberg-Osgood Coefficients[a]					
α	1.1	4.42	1.15	8.71	2.14
n	5.55	4.96	5.55	3.26	4.36
Extrapolated J-R Curve Parameters[b]					
J_{Ic}, kJ/m^2 (lb-in/in^2)	207 (1,180)	109 (622)	207 (1,180)	60 (343)	59 (337)
C_1, kJ/m^2 (lb-in/in^2)	166.1 (948)	147.9 (845)	166.1 (948)	147.9 (845)	124.1 (709)
m	0.483	0.769	0.483	0.769	0.720

(a) Base-metal stress-strain curve is represented by: $\epsilon/\epsilon_0 = \sigma/\sigma_0 + \alpha(\sigma/\sigma_0)^n$, $\sigma_0 = \sigma_y$, $\epsilon_0 = \sigma_0/E$

(b) J-R curve is from C(T) specimens and is assumed to be represented by: $J = J_{Ic} + C_1 (\Delta a/r)^m$, where r = 1 mm; for welded pipe, the J-R curves correspond to the weld-metal toughness.

4.3.4.4 Results of Analyses for Experiments 4111-2 and 1.1.1.21

In Experiments 4111-2 and 1.1.1.21, the calculations were made for several crack lengths by all the analysis methods. (These two experiments were on carbon steel pipe with the crack in the base metal.) Figure 4.40 shows the predicted maximum loads by these methods and the pipe fracture data. The LBB.NRC, LBB.GE, LBB.ENG2, and Paris/Tada methods provided better prediction of the maximum load than given by the other methods. Both the LBB.ENG2 and Paris/Tada solutions were slightly underpredicted for the long crack (θ/π = 0.37) and overpredicted for the short crack (θ/π = 0.0625). However, the degree of accuracy was a little higher for the LBB.ENG2 method. The LBB.NRC and LBB.GE methods also provided close prediction of experimental results, underestimating the maximum loads slightly for both short and long cracks.

Each modification of the GE/EPRI method predicted lower maximum loads than other estimation schemes and experimental results. Differences between the GE/EPRI solutions based on influence

functions developed by Kumar, et al. (Ref. 4.2), and Brust, et al. (Ref. 4.3), were not significant when the maximum loads were compared. The difference was larger for smaller flaws and was only 2.3 percent when the crack size was 5 percent of the circumference. This may be due to smaller values of the Ramberg-Osgood exponent, n, which was only 5.55 for this pipe material. If n were larger, much more pronounced differences would occur. The major differences between the old (GE/EPRI-1A) and new (GE/EPRI-2A) GE/EPRI methods are found in the displacement predictions. Also, the inclusion of a plastic-zone correction in the GE/EPRI methods (GE/EPRI-1B and GE/EPRI-2B) appears to have only secondary effects on the maximum loads. This is not surprising since the plastic deformation is much larger than the elastic deformation when the pipe reaches its load-carrying capacity.

Figure 4.40 also shows comparisons of experimental results with predictions based on ASME Section XI flaw evaluation and Net-Section-Collapse (NSC) criteria. Results show that the experimental maximum loads fall much below the NSC analysis prediction. This is expected since the pipe diameters are large and the J-R curve is relatively low for these materials. Comparisons with the ASME Section XI IWB-3650 curve indicate that the IWB-3650 analysis significantly underpredicts the experimental maximum loads particularly for short-TWC pipes.

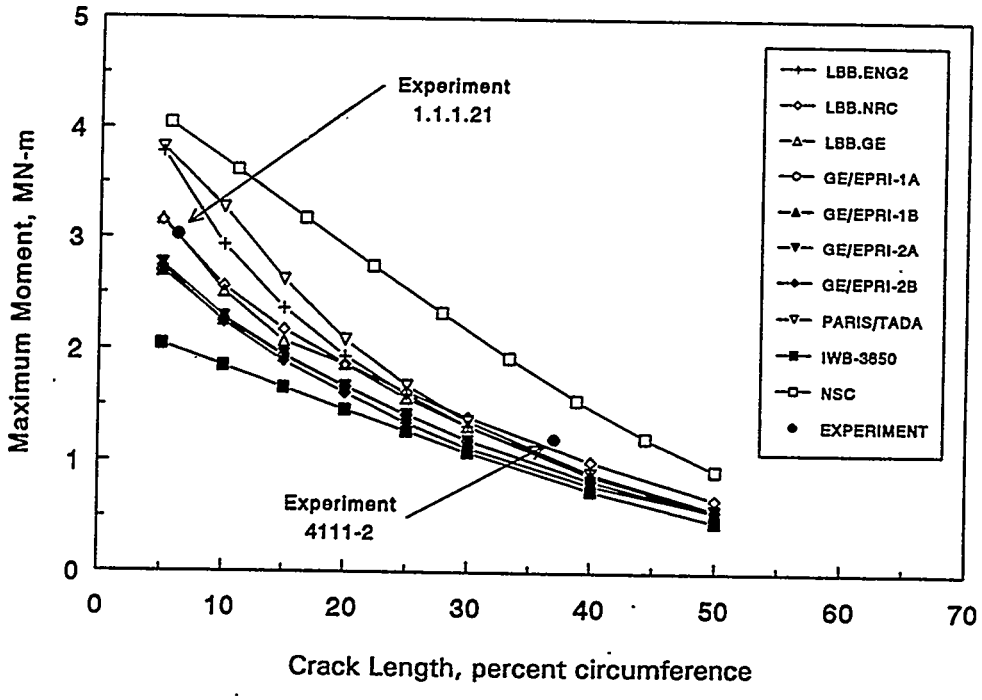

Figure 4.40 Comparisons of maximum loads as a function of crack size from Experiments 4111-2 and 1.1.1.21 on the 711.2-mm (28-inch) nominal diameter A155 KC60 CL1 (A515 Grade 60) carbon steel through-wall-cracked steam-line pipes with predictions by various analyses

4.3.4.5 Results of Analyses for Experiments 4111-5 and 1.1.1.23

In Experiments 4111-5 and 1.1.1.23, where the crack was in the weld metal, the calculations were made for several crack lengths as well. While conducting fracture analyses, we carefully investigated the pipe-specific material properties from our material characterization tests and found that they can also vary appreciably. According to Table 4.23, the tensile strength properties of the base metal (e.g., the yield strength and Ramberg-Osgood coefficients) and the toughness properties of the weld metal (e.g., the J at crack initiation) are very different for these two stainless steel welded pipes. In Reference 4.34, we computed the maximum loads for these two experiments based on the strength properties of TP316 base metal (from Experiment 4111-5) and the J-resistance properties of a submerged arc weld (from Experiment 1.1.1.23). Since there are differences in the stress-strain curves of the TP316 and TP316L base metals and the J-resistance curves of the shielded-metal arc and submerged arc welds (see Table 4.23), it is more appropriate to re-analyze these two pipe tests based on case-specific material properties. Hence, two sets of fracture analyses were conducted. They were based on pipe-specific material properties in Experiments 4111-5 and 1.1.1.23. Comparisons of subsequent results from these analyses and experimental pipe fracture data are shown in Figures 4.41 and 4.42. From Figure 4.41, when the crack is long ($\theta/\pi = 0.37$), LBB.ENG2, LBB.GE, and all the modifications to the GE/EPRI methods provided very accurate predictions of maximum load. Paris/Tada and LBB.NRC overpredicted the maximum loads. From Figure 4.42, when the crack is short ($\theta/\pi = 0.0625$), the LBB.NRC and LBB.GE methods provided reasonably accurate results of maximum load. The Paris/Tada and GE/EPRI methods significantly overpredicted and underpredicted the maximum load, respectively. The LBB.ENG2 method slightly underpredicted the load. The ASME Section XI IWB-3640 analysis also significantly underpredicted the maximum load for the short crack experiment. This was expected, since the Z-factors were based on long through-wall cracks.

Once again, differences between the GE/EPRI solutions based on influence functions developed by Kumar, et al., and those in this report were not significantly different when the maximum loads were compared. The difference was larger for smaller flaws and was only 2.2 percent when the crack size was 5 percent of the circumference. This again was due to the smaller values of the Ramberg-Osgood exponent, n, which were only 4.96 for TP316 (Experiment 4111-5) and 3.26 for TP316L (Experiment 1.1.1.23) for the pipe materials under study. As observed earlier, the inclusion of the plastic-zone correction in the GE/EPRI methods (i.e., for GE/EPRI-1B or GE/EPRI-2B) did not have any significant effects on the maximum loads.

Figures 4.41 and 4.42 also provide comparisons of results with predictions based on ASME Section XI flaw evaluation and Net-Section-Collapse criteria. As observed earlier, results show that the experimental maximum loads were much lower than the NSC analysis predictions for both long and short cracks. This was mainly because the pipe diameters were large and the J-R curve was relatively low for these materials. Comparisons with the ASME Section XI curve indicate that the IWB-3650 analysis significantly underpredicts the maximum load for short TWCs in pipes and was reasonably accurate for long TWCs in pipes. This was expected, since the Z-factors in the ASME analyses are based on long through-wall cracks.

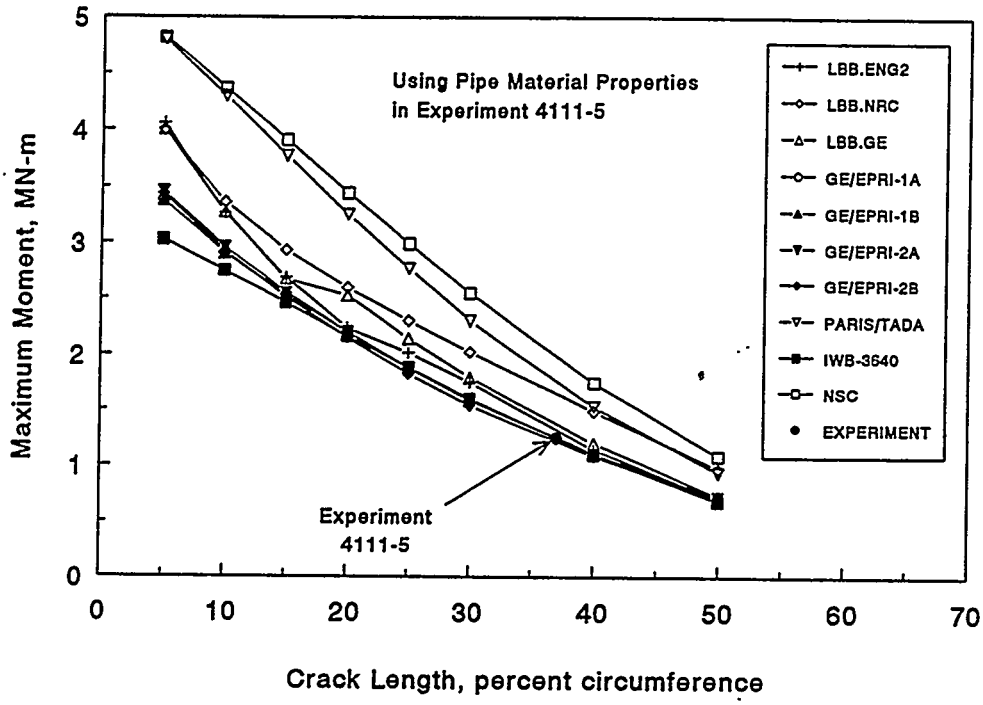

Figure 4.41 Comparisons of maximum loads from Experiment 4111-5 on the 711.2-mm (28-inch) nominal diameter through-wall-cracked BWR main recirculation line pipe with predictions by various analyses

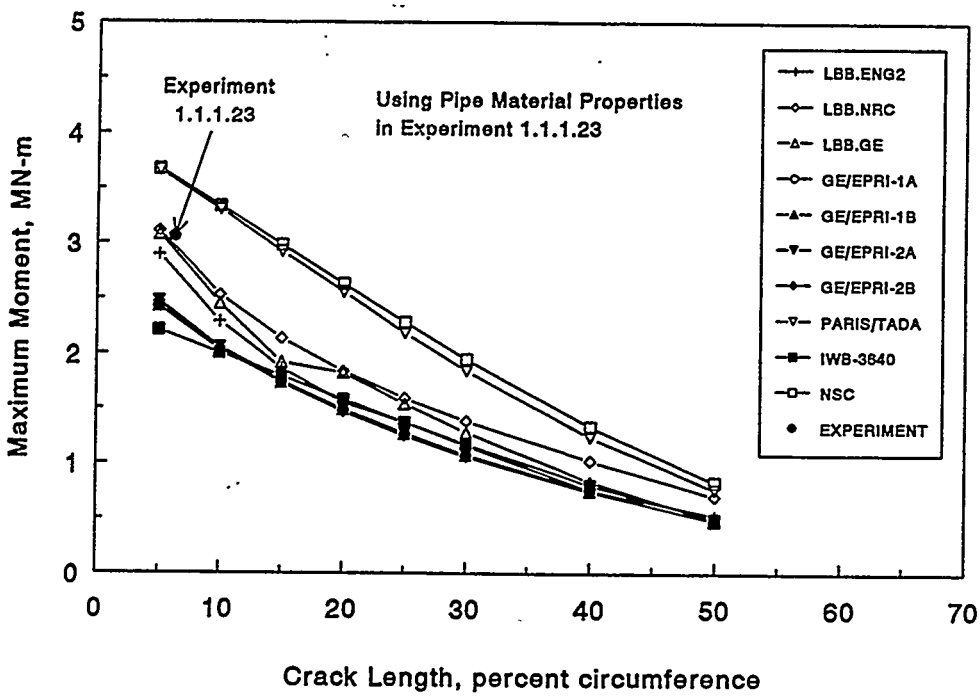

Figure 4.42 Comparisons of maximum loads from Experiment 1.1.1.23 on the 711.2-mm (28-inch) nominal diameter through-wall-cracked BWR main recirculation line pipe with predictions by various analyses

4.3.4.6 Results of Analyses for Experiment 1.1.1.24

Some of the predictive methods described earlier were also used to analyze the pipe fracture in Experiment 1.1.1.24. Figure 4.43 shows comparisons of both initiation and maximum load ratios obtained by several J-estimation schemes for this pipe experiment. Results of the GE/EPRI method were based on influence functions developed by Brust, et al., (Ref. 4.3) without any plastic-zone size correction. It appears that for Experiment 1.1.1.24, the estimation methods underpredicted both initiation and maximum loads of the pipe. The GE/EPRI method underpredicted loads more than any other J-estimation scheme. The Paris/Tada, LBB.NRC, and LBB.GE provided good predictions. Predictions by LBB.ENG2 method, which we frequently use at Battelle, were also reasonably accurate. The ASME Section XI IWB-3650 analyis overpredicted the maximum load most. The Net-Section-Collapse prediction was excellent.

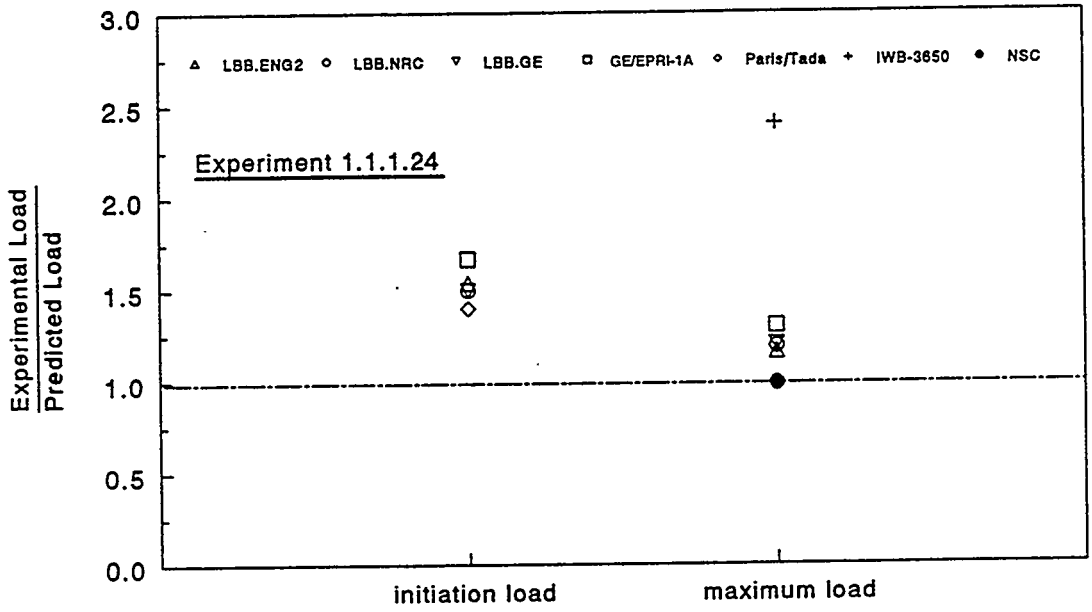

Figure 4.43 Comparisons of initiation and maximum loads from Experiment 1.1.1.24 on a 609-mm (24-inch) nominal diameter A333 Grade 6 carbon steel through-wall-cracked SAW pipe with predictions by various analyses

4.3.4.7 Through-Wall-Cracked Welded-Pipe Experiments

This section involves fracture analysis of four circumferential through-wall-cracked welded-pipe experiments that were conducted in the past Degraded Piping program (Ref. 4.33). The comparisons involved analyses based on J-estimation schemes, Net-Section-Collapse, and ASME Section XI flaw evaluation criteria.

The experiments from the Degraded Piping Program analyzed in this section were Experiments 4141-1 and 4141-5. These experiments were conducted on a 152-mm (6-inch) nominal diameter TP304 stainless steel pipe with a through-wall crack in the center of a shop-fabricated submerged-arc weld. The crack lengths in both experiments were nearly 37 percent of the pipe circumference. The only difference was that in one experiment the weld was solution annealed. The loading rates in both experiments were quasi-static. Exact dimensions of pipe geometry, test temperature, and experimental results are given in Table 4.24. Further details on these two experiments can be obtained from Reference 4.36.

Table 4.24 Summary of pipe geometry and results for welded pipe experiments

	Experiment Number	
	4141-1	4141-5
Pipe Material Crack Location	SA-376 TP304 SAW	SA-376 TP304 Solution-Annealed SAW
Test Temperature, C (F)	288 (550)	288 (550)
Outside Pipe Diameter (D_o), mm (inch)	168 (6.62)	167 (6.60)
Actual Wall Thickness (t), mm (inch)	14.3 (0.562)	14.1 (0.555)
Crack Length (θ/π), percent	37.1	38.3
Four-point Bending Inner Span, m (ft)	1.20 (3.94)	1.20 (3.94)
Four-point Bending Outer Span, m (ft)	3.250 (10.66)	3.250 (10.66)
Initiation Load (P_i), kN (lb)	58.3 (13,100)	46.3 (10,400)
Maximum Load (P_{max}), kN (lb)	73.8 (16,600)	60.5 (13,600)

4.3.4.8 Results of Analysis for Experiments 4141-1 and 4141-5

Several predictive J-estimation schemes were used to evaluate the load-carrying capacity of the TWC welded pipes in Experiments 4141-1 and 4141-5. All estimation methods, except LBB.ENG3 method, were based on stress-strain properties of base metal and toughness properties of the weld metal. The LBB.ENG3 method can account for strength properties of both base and weld metals in calculating the J-integral. See Section 4.2.4 for further details of this method.

Four samples of base metal stress-strain data and two samples of weld metal stress-strain data at test temperature were available for pipe materials in each of these two experiments. Standard curve-fit methods were used to idealize both the stress-strain and J_D-R curves by the power-law models in Equations 4-92 and 4-93, respectively. Table 4.25 shows the material properties including the Ramberg-Osgood and power-law J_D-R curve parameters. In Table 4.25, the Ramberg-Osgood coefficients and the J_D-R curve parameters were obtained for base-metal stress-strain curves and weld-metal toughness curves from 1T C(T) specimens. These properties were used to predict crack initiation loads and maximum loads by the LBB.ENG2, LBB.NRC, LBB.GE, GE/EPRI, and Paris/Tada methods. Since LBB.ENG3 method accounts for tensile strength properties of both the

base and weld metal, the corresponding Ramberg-Osgood coefficients were also calculated for the weld metal and are shown in Table 4.26. Figures 4.44 and 4.45 show the effects of solution annealing on the tensile strength and fracture toughness of the weld metal (SAW) of the pipe. There was no effect of solution-annealing on the base metal stress-strain curve, since the as-received pipe was already in the solution annealed condition. It appears that the solution annealing can lower the yield strength of weld metal by 40 percent and slightly raise the fracture toughness in the weld metal C(T) specimen tests. Since the decrease of strength is detrimental and the increase of toughness is beneficial to the pipe, it is interesting to determine which effect is the governing one and whether solution-annealing can lower or raise the load-carrying capacity of cracked pipes. Additionally, solution annealing would eliminate the weld residual stresses. Figure 4.46 shows the plots of load versus load-line displacement for Experiments 4141-1 and 4141-5 obtained from the actual test record. Results from this figure suggest that due to solution annealing, the maximum load decreases from 73.8 kN (16,590 lb) to 60.5 kN (13,600 lb) (see also Table 4.24)--a reduction of almost 18 percent from the value of maximum load of as-welded pipe. Hence, the lowering of weld-metal tensile properties may have a more pronounced effect than the increase of fracture toughness and can thus significantly reduce a pipe's load-carrying capacity.

Table 4.25 Base metal tensile test and weld metal fracture toughness values for through-wall-cracked welded pipe experiments

	Experiment Number	
	4141-1	**4141-5**
Modulus of Elasticity (E), GPa (ksi)	182.7 (26,500)	182.7 (26,500)
Yield Stress (σ_y), MPa (psi)	138 (20,000)	138 (20,000)
Ultimate Stress (σ_u), MPa (psi)	449 (65,100)	449 (65,100)
Design Stress (S_m), MPa (psi)	117 (16,950)	117 (16,950)
Ramberg-Osgood Coefficients[(a)]		
α	9.69	9.69
n	3.13	3.13
Extrapolated J-R Curve Parameters[(b)]		
J_{Ic}, kJ/m^2 (lb-in/in^2)	99 (565)	170 (971)
C_1, kJ/m^2 (lb-in/in^2)	164.1 (937)	165.8 (947)
m	0.703	0.778

(a) Base-metal stress-strain curve was assumed to be represented by:
$\epsilon/\epsilon_0 = \sigma/\sigma_0 + \alpha(\sigma/\sigma_0)^n$, $\sigma_0 = \sigma_y$, $\epsilon_0 = \sigma_0/E$

(b) Weld-metal J-R curve was from C(T) specimens and was assumed to be represented by:
$J = J_{Ic} + C_1(\Delta a/r)^m$, where r = 1 mm

Table 4.26 Tensile strength of weld metals for small- and large-diameter through-wall-cracked pipe experiments

	Experiment Number			
	4111-5[a]	1.1.1.23[a]	4141-1[a]	4141-5[a]
Modulus of Elasticity (E), GPa (ksi)	182.7 (26,500)	182.7 (26,500)	182.7 (26,500)	182.7 (26,500)
Yield Stress (σ_y), MPa (psi)	282 (40,900)	366 (53,100)	324 (47,000)	194 (28,100)
Ultimate Stress (σ_u), MPa (psi)	485 (70,300)	503 (73,000)	466 (67,600)	465 (67,400)
Ramberg-Osgood Coefficients[b]				
α	1.84	1.63	2.28	3.42
n	7.31	10.94	11.03	4.84

(a) Base metal properties previously given in Table 4.23 or Table 4.25.
(b) Weld-metal stress-strain curve was assumed to be represented by: $\epsilon/\epsilon_0 = \sigma/\sigma_0 + \alpha(\sigma/\sigma_0)^n$, $\sigma_0 = \sigma_y$, $\epsilon_0 = \sigma_0/E$

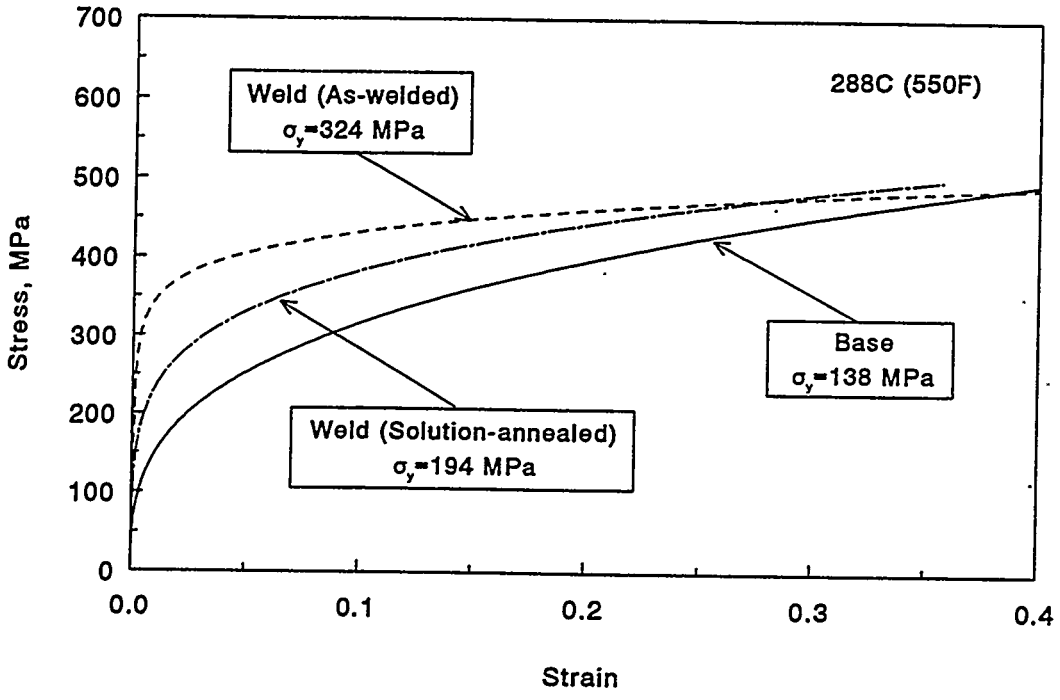

Figure 4.44 Effects of solution annealing on tensile strength properties

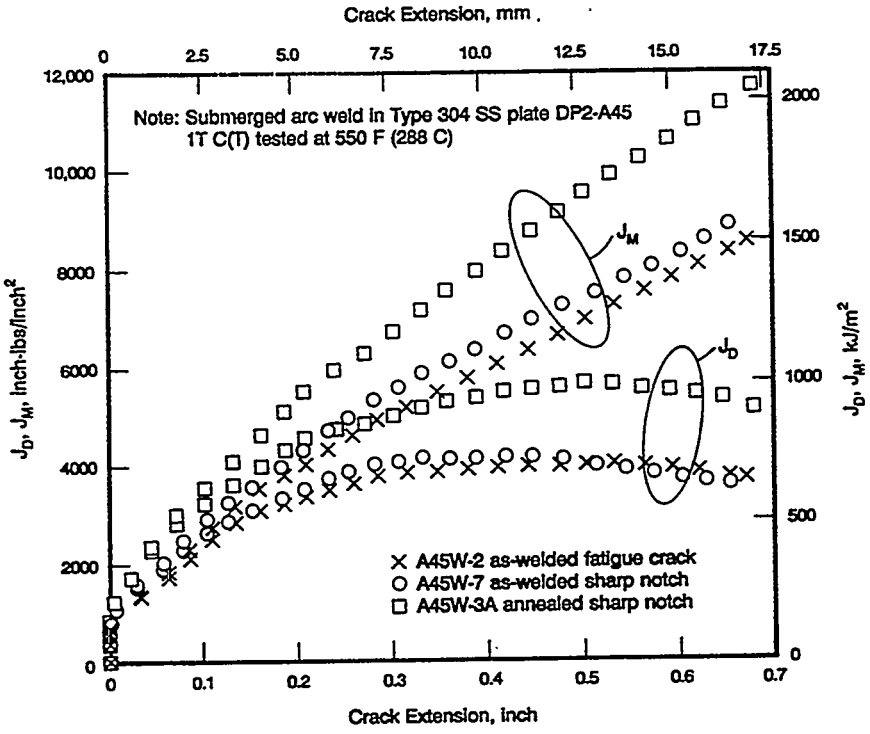

Figure 4.45 Effects of solution annealing on fracture toughness properties, from Reference 4.36

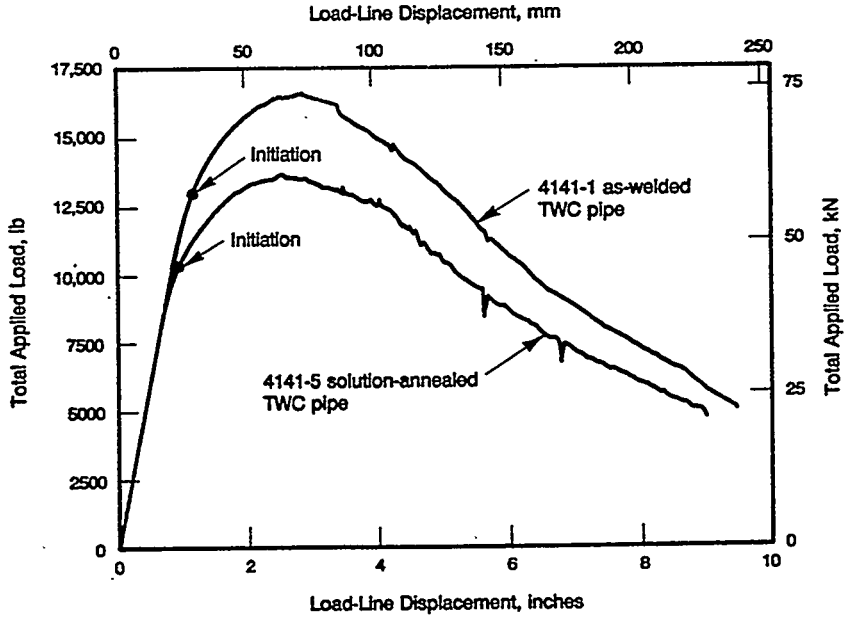

Figure 4.46 Total load versus load-line displacement record from Experiments 4141-1 and 4141-5 on 152-mm (6-inch) nominal diameter TP304 stainless steel through-wall-cracked as-welded and solution-annealed SAW pipes, from Reference 4.36

4.3.4.9 Results based on J_D-R Curves from C(T) Specimens

Figure 4.47 shows the initiation load ratio for the Experiments 4141-1 and 4141-5 obtained from five different J-estimation schemes using 1T C(T) J_D-resistance curves. From these results, all estimation methods except Paris/Tada significantly underestimated the initiation loads of both as-welded pipe (Experiment 4141-1) and solution-annealed pipes (Experiment 4141-5) when compared with test data. However, the degree of underestimation was smaller for the solution-annealed pipe, in which case the strength properties of base and weld metals were not too different. The initiation load calculated by the Paris/Tada method was closer to the experimental value although the inaccuracy was an overprediction of the initiation loads.

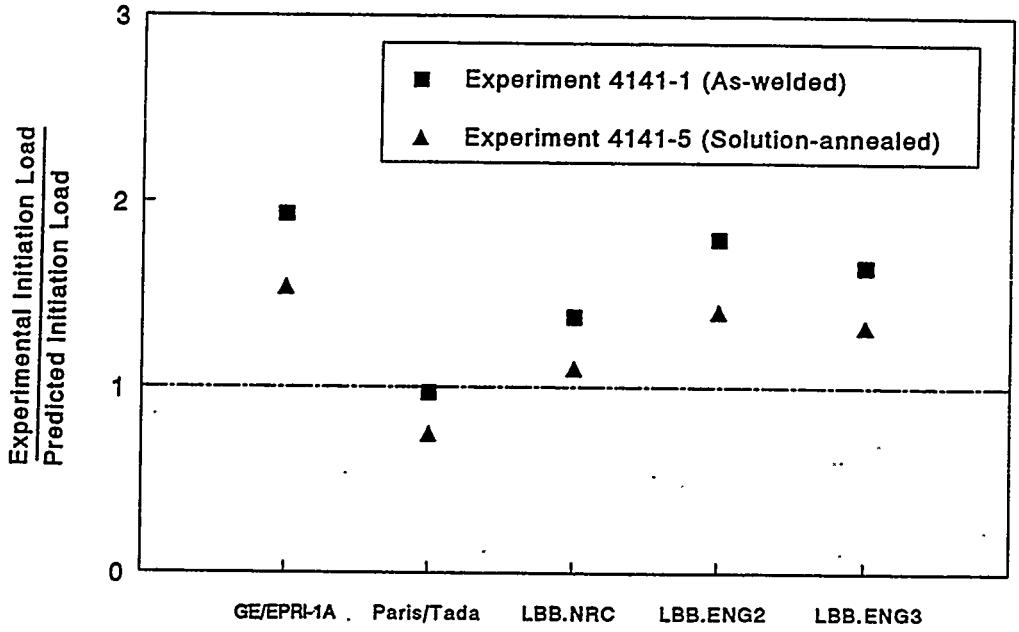

Figure 4.47 Comparisons of initiation loads from Experiments 4141-1 and 4141-5 on 152-mm (6-inch) nominal diameter TP304 stainless steel through-wall-cracked as-welded and solution-annealed SAW pipes with various analyses using C(T) specimen J_D-R curves

Similar results are also plotted for the same pipes in Figure 4.48 in terms of maximum load ratio as a function of the estimation methods. Results indicate that most estimation methods underestimated the maximum loads. As before, the degree of underestimation for the solution-annealed pipe was much less than that exhibited for the as-welded pipe. This suggests that the tensile strength properties of weld metals, if very different from that of base metals, can affect the load-carrying capacity of pipes. The Paris/Tada method, which provided better results for the as-welded pipe, was found to overestimate the load-carrying capacity for the solution-annealed pipe. The LBB.ENG3 method, which uses strength properties of both the base and weld metals, improved both initiation and maximum-load predictions by the LBB.ENG2 method. In both experiments, the degree of conservatism by LBB.ENG3 was less than other estimation methods except the Paris/Tada and LBB.NRC methods. All these results were predicted by using J_D-R curves from the 1T C(T) specimens.

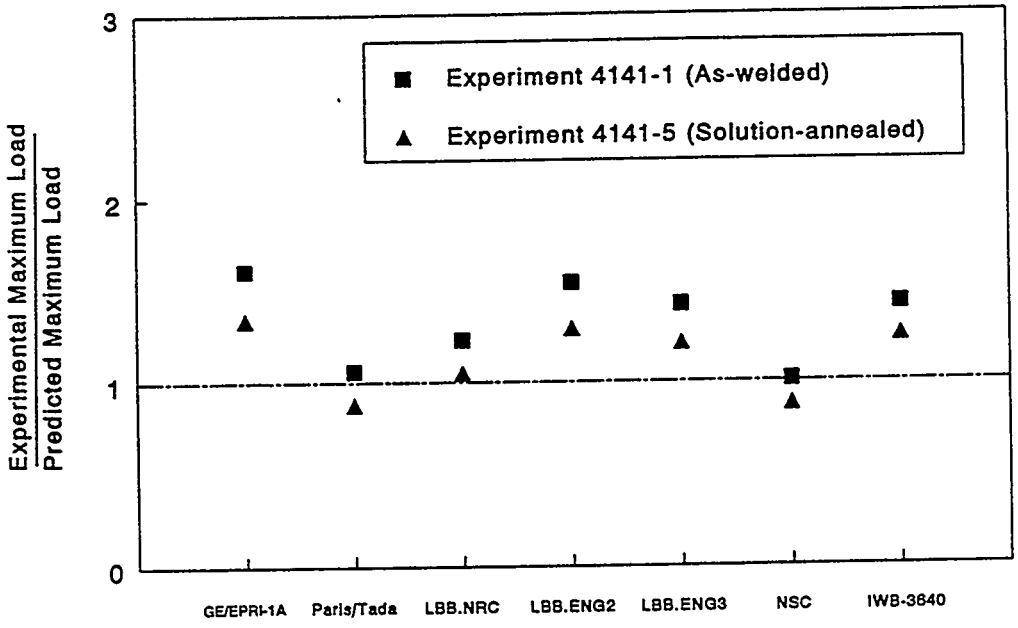

Figure 4.48 Comparisons of maximum loads from Experiments 4141-1 and 4141-5 on 152-mm (6-inch) nominal diameter TP304 stainless steel through-wall-cracked as-welded and solution-annealed SAW pipes with various analyses using C(T) specimen J_D-R curves

In Figure 4.48, results are also presented based on ASME Section XI and Net-Section-Collapse analyses. The NSC solution was very accurate for as-welded pipe, but slightly overpredicted the maximum load for the solution-annealed pipe. The ASME Section XI Appendix C method (with a safety factor of 1.0 and using the Z-factor for the exact pipe diameter) also significantly overpredicted maximum loads in both experiments.

4.3.4.10 Comparisons between J_D-R Curves from Pipes and C(T) Specimens

In order to explain the underpredictions by the J-estimation schemes, several η-factor analyses were conducted (Ref. 4.36) to generate pipe J_D-R curves using the load-displacement record from the actual pipe experiments. The objective was to determine the adequacy of the J_D-R curves from the 1T C(T) specimens. Further details on the η-factor analysis can be found in Reference 4.36.

Figure 4.49 shows the comparisons of both as-welded and solution-annealed SAW J-R curves from 1T C(T) specimens and 152-mm (6-inch) nominal diameter pipes via η-factor analyses. Both Deformation J-resistance curve, J_D-R and Modified J-resistance curve J_M-R curves are shown. Two points are worthy of discussion regarding the SAW pipe data. First, the J-R curves from both pipe experiments are greater than those from the C(T) specimens. This is believed to be mainly due to the effects of the weld thickness and weld procedures. For instance, the 1T C(T) specimens were made from 25.4-mm (1-inch) thick plate and were the full thickness of the plate. The 152-mm (6-inch) diameter pipes, however, were either 14.3-mm (0.562-inch) or 14.1-mm (0.552-inch) thick. The

weld procedures involved two layers of TIG weld, then two layers of SMAW, followed by remaining passes of SAW. Hence, with the thinner pipes the amount of SAW metal was significantly less than the 25.4-mm (1-inch) thick weldments of 1T C(T) specimens. Since the TIG weld metal was much higher in toughness (Ref. 4.37), the composite toughness of the 152-mm (6-inch) nominal diameter pipes with a 14.3-mm (0.562-inch) or 14.1-mm (0.552-inch) thickness was much higher. As confirmation, in Reference 4.36, a 406-mm (16-inch) diameter 25.4-mm (1.0-inch) thick pipe was also tested, and the pipe J-R curve agreed well with the 25.4-mm (1.0-inch) thick C(T) specimen J_M-R curves.

Another factor was also present. The 1T C(T) specimens have a weld width to specimen height that is very large compared with the pipe specimen. Hence, the plastic zones in the C(T) specimens are more confined to the weld. In the pipe, the plastic zone reaches far outside the weld to base metal boundary. Reference 4.37 discusses size effects in welded C(T) specimens and further discusses the above-described effect. This perhaps explains why the J-estimation schemes presented in Figures 4.47 and 4.48 significantly underpredicted the loads.

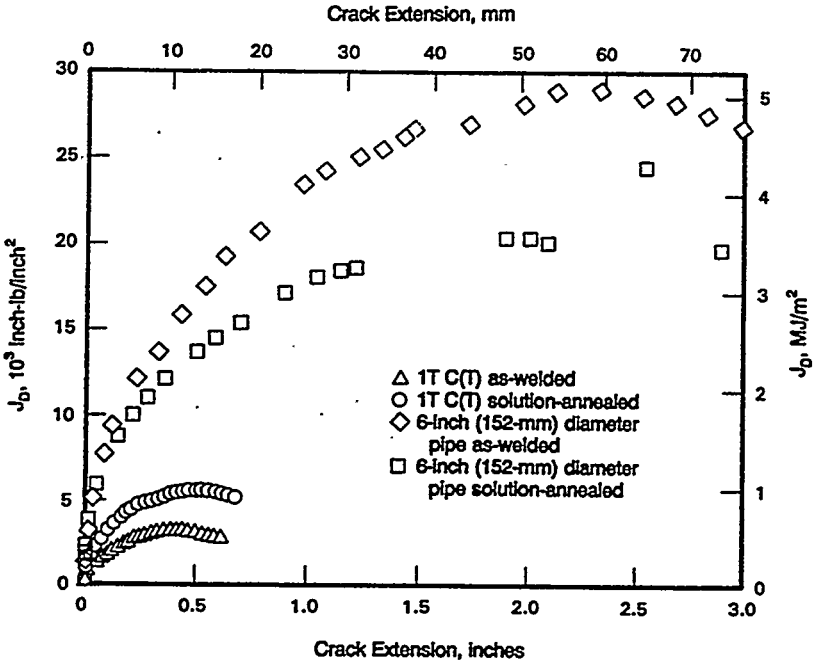

Figure 4.49 Comparisons between J-R curves from 1T C(T) specimens and 152-mm (6-inch) nominal diameter pipes via η-factor analysis, from Reference 4.36

Another point is that the pipe solution-annealed SAW J-R curve is lower than the as-welded SAW pipe J-R curve. This trend is the opposite of the C(T) specimen results (see Figure 4.49 and/or Table 4.25). For a typical η-factor analysis, the plastic component of J-integral is proportional to the area under the load-displacement record. From Figure 4.46, the area under load-displacement record for as-welded pipe (Experiment 4141-1) is larger than that for solution-annealed pipe (Experiment 4141-5). Hence, the value of J-integral, exhibited in pipe J_D-R curves, was higher for the as-welded

pipe. Nevertheless, additional C(T) specimen data for various size and thickness would be helpful in clarifying this apparent anomaly. Part of this different trend regarding the effect of solution annealing on the toughness is probably due to the η-factor solutions; both the pipe and C(T) specimens were theoretically based on a homogeneous specimen of pipe. The presence of the weld violated the initial assumptions in these analyses.

4.3.4.11 Results based on J_D-R Curves from Pipes

Following the comparisons between C(T) and pipe J-R curves, various J-estimation analyses were conducted again using the pipe J_D-R curves to determine the initiation- and maximum-load ratios in Experiments 4141-1 and 4141-5. The results are shown in Figures 4.50 and 4.51. The predictions using pipe J_D-R curves when compared with the experimental results appear to be much better than those using the 1T C(T) specimen J_D-R curves. Results show that (1) most estimation methods provide reasonably accurate load predictions, and (2) among the five estimation methods considered here, LBB.ENG3 was the most accurate method to compute both initiation and maximum loads of as-welded and solution-annealed pipes when the fracture toughness properties were generated from large-scale pipe tests. It appears that when the strength characteristics of weld-metal are considered (e.g., in the LBB.ENG3 method), the predictive capability of LBB.ENG2 method can be improved.

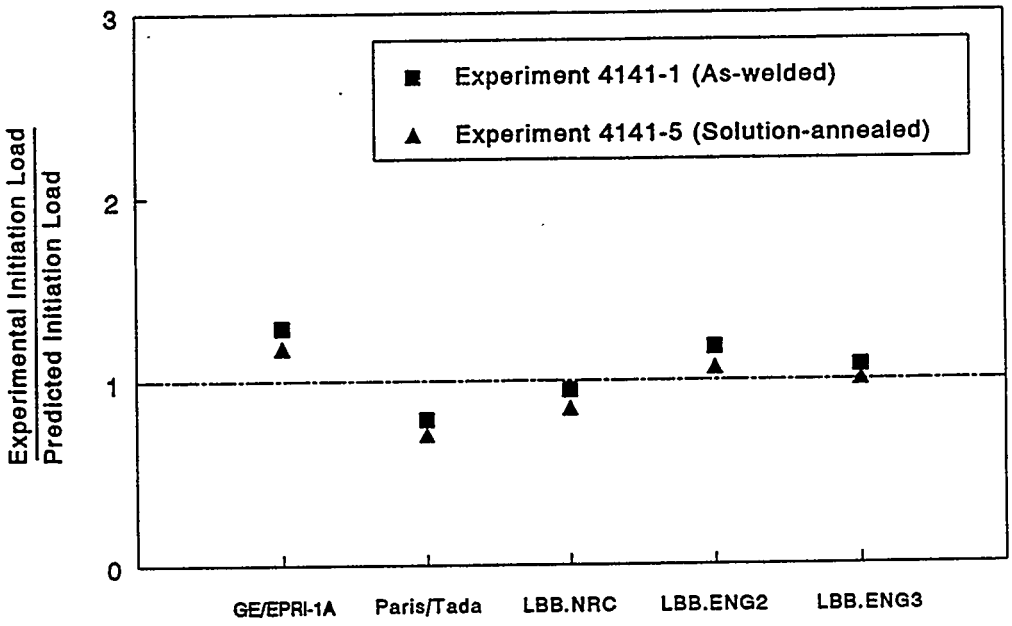

Figure 4.50 Comparisons of initiation loads from Experiments 4141-1 and 4141-5 on the 152-mm (6-inch) nominal diameter TP304 stainless steel through-wall-cracked as-welded and solution-annealed SAW pipes with various analyses using pipe J_D-R curves

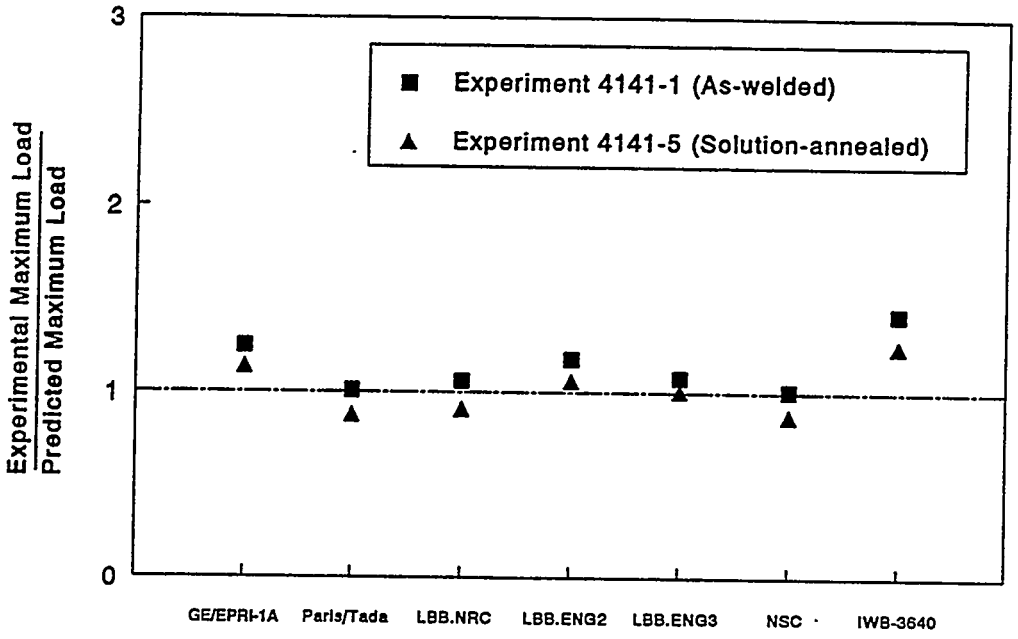

Figure 4.51 Comparisons of maximum loads from Experiments 4141-1 and 4141-5 on the 152-mm (6-inch) nominal diameter TP304 stainless steel through-wall-cracked as-welded and solution-annealed SAW pipes with various analyses using pipe J_D-R curves

Finally, Figures 4.52 and 4.53 show the plots of applied load versus load-line displacement in Experiments 4141-1 and 4141-5 by several J-estimation methods using the pipe J_D-R curves and the experimental data. Comparisons with experimental data suggest that the load-displacement predictions by LBB.ENG3 method were very good and overall were more accurate than the other J-estimation methods considered here.

4.3.4.12 Results of Analysis for Experiments 4111-5 and 1.1.1.23

Several predictive J-estimation schemes were used to evaluate the initiation and maximum loads for the pipes in Experiments 4111-5 and 1.1.1.23. Experimental details of these pipe experiments and some analysis results were already discussed in Section 4.3.4.2. In this section, these two experiments are revisited to determine if the LBB.ENG3 method can improve predictions of the load-carrying capacity of these two welded pipes. Since LBB.ENG3 method requires tensile strength properties of weld metal, the Ramberg-Osgood coefficients were calculated from the available test data. They are shown in Table 4.26.

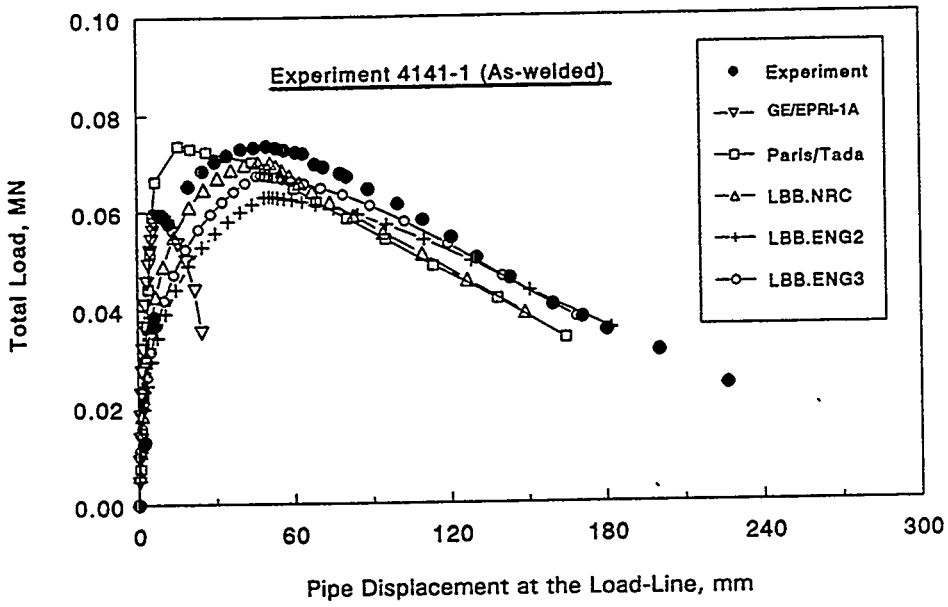

Figure 4.52 Comparison of applied load versus pipe displacement from Experiment 4141-1 TP304 through-wall-cracked as-welded SAW pipe with predictions by various J-estimation schemes using pipe J_D-R curves

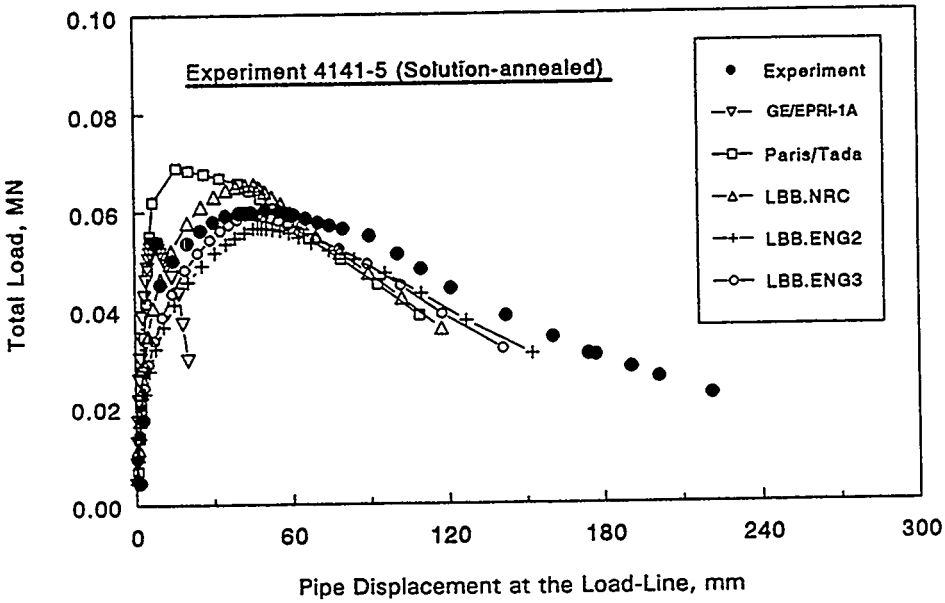

Figure 4.53 Comparison of applied load versus pipe displacement from Experiment 4141-5 TP304 stainless steel through-wall-cracked solution-annealed SAW pipe with predictions by various J-estimation schemes using pipe J_D-R curves

Figure 4.54(a) shows the initiation load ratio for Experiments 4111-5 and 1.1.1.23 obtained from five different J-estimation schemes described earlier. The results suggest that all estimation methods significantly overestimated the initiation loads for both pipes. However, the magnitude of the overprediction was much smaller for Experiment 4111-5. Similar results are plotted for the same pipes (Experiments 4111-5 and 1.1.1.23) in Figure 4.54(b) in terms of maximum load ratio as a function of the estimation methods. The results indicate that most estimation methods underestimated the maximum loads except Paris/Tada and LBB.NRC. The predictions by LBB.ENG2 and LBB.ENG3 were better than the other methods. The LBB.ENG3 method, which uses strength properties of both the base and weld metals, provided the best results. The NSC method overpredicted maximum loads significantly. The ASME Section XI IWB-3640 solution was accurate for Experiment 4111-5, but significantly underpredicted the maximum load for Experiment 1.1.1.23.

All of the above results by J-estimation analyses were predicted by using J_D-R curves from C(T) specimens. Since the wall thicknesses of these pipes were 30.2 mm (1.19 inch) and were close to the thickness of 1T C(T) specimens, the J_D-R curves from C(T) specimens should represent fairly well the actual fracture toughness of these welded pipes.

4.3.5 R6 - Option 1 Analysis

The NRC is mainly interested in using J-estimation schemes to predict elastic-plastic fracture of piping. In Europe, however, the R6 Revision 3 approach is frequently used. This section provides a brief discussion of the R6 approach and some corresponding predictions. This section was purposely kept separate from the J-tearing prediction section, since this method is not widely used in the U.S.

4.3.5.1 Background

The R6 methodology for assessing the integrity of cracked structures was developed and validated by CEGB, UK (Refs. 4.38 and 4.39). The assessment procedure consists of interpolating between the linear elastic fracture mechanics criterion for failure and the fully plastic limit-load solution using a failure assessment diagram (FAD). As such, the R6 method (like the ASME Section XI criteria) is basically a design or failure avoidance procedure with an inherent safety margin already included in the analysis, i.e., no safety factor is explicitly applied. Crack initiation and maximum-load predictions using this scheme are therefore expected to underestimate the actual or experimentally measured loads. A few example cases are analyzed at the end of this section to illustrate this point.

A schematic of the FAD, Figure 4.55 shows a plot of K_r, the ratio of the linear elastic stress intensity factor to the fracture toughness (K_I/K_{Ic}) versus L_r, the ratio of the applied load to the limit load (σ/σ_{nsc}). If the point (L_r,K_r) for the structure under consideration falls inside the failure assessment curve (FAC), it is deemed to be safe; outside this curve the structure is unsafe, as shown in Figure 4.55.

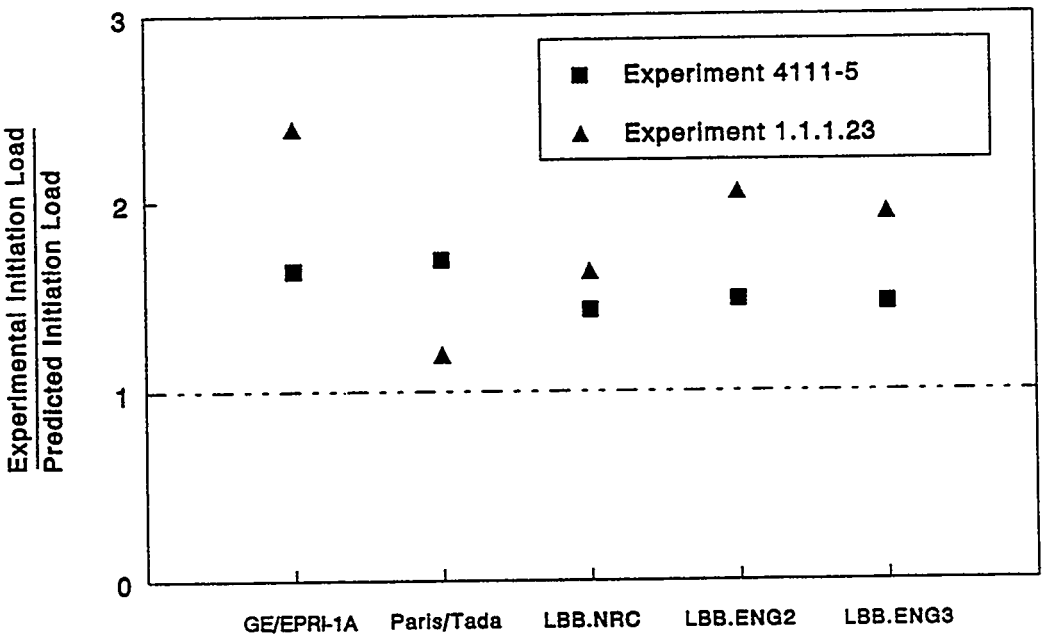

(a) Initiation load

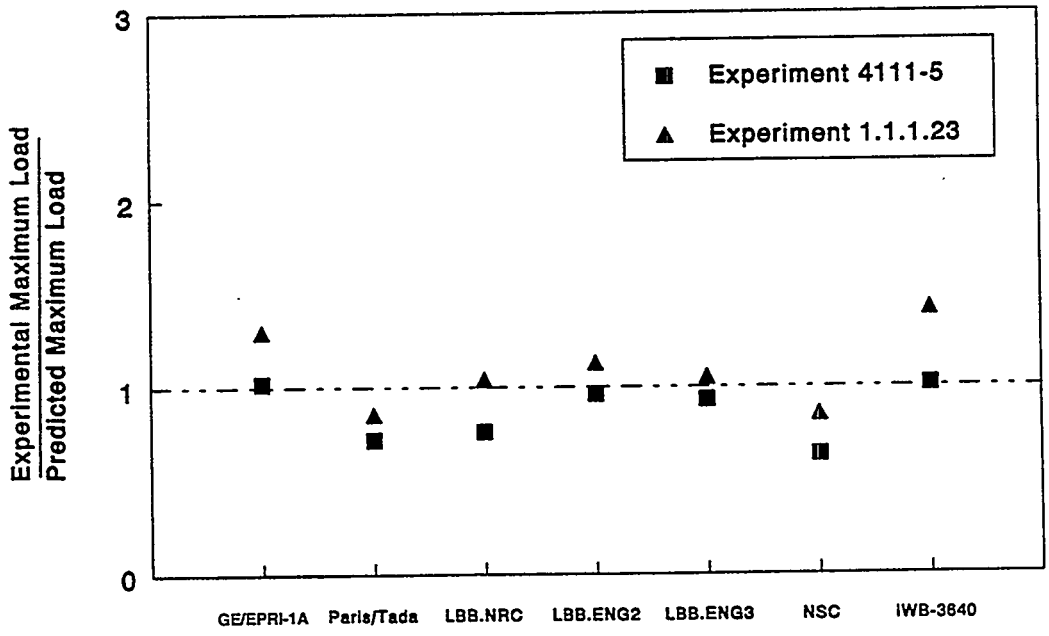

(b) Maximum load

Figure 4.54 Comparisons of loads from Experiments 4111-2 and 1.1.1.23 on the 711-mm (28-inch) nominal diameter TP316 and TP316L stainless steel through-wall-cracked SMAW and SAW pipes with predictions by various analyses using C(T) specimen J_D-R curves

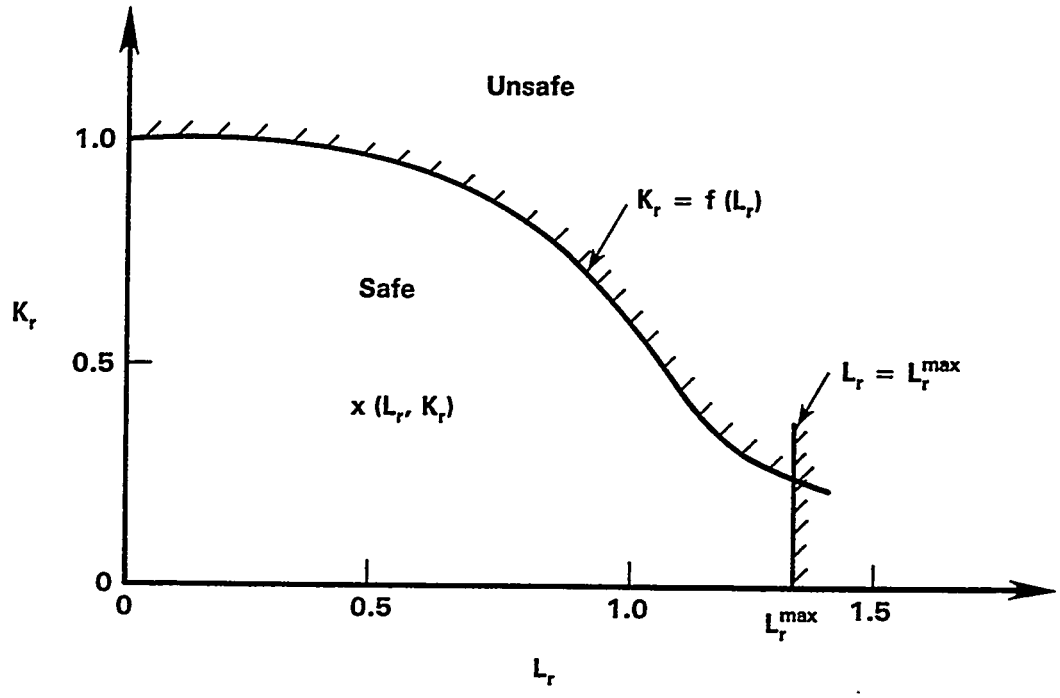

Figure 4.55 The failure assessment diagram

Three possible options for the FAC have been proposed (Ref. 4.38) depending on the type of elastic-plastic fracture analysis to be used and the type of transition required from small-scale to large-scale yielding. Details about the three options are given in References 4.38 and 4.39 and will not be discussed here. Of these, only Option 1, involving one universal FAC for all materials, has been used here and is discussed below. Unlike other J-estimation schemes, the R6 method can be used only to assess the initiation and maximum load-carrying capacity of TWC pipe and does not provide any information about the rotation, load-line displacement, or crack-opening displacement behavior of the cracked pipe.

4.3.5.2 R6 Procedure for TWC Pipe

The FAD for Option 1 is shown in Figure 4.56 along with the equation that relates K_r to L_r, given as (Ref. 4.38):

$$K_r = (1 - 0.14L_r^2)\,[0.3 + 0.7\exp(-0.65L_r^6)] \qquad (4\text{-}99)$$

For a TWC pipe under combined bending and tension (internal pressure) loads, K_r and L_r are defined as follows:

$$K_r = K_I/K_c(\Delta a) \tag{4-100}$$

and

$$K_I = K_{IT} + K_{IB} \tag{4-101}$$

where

K_{IT} = stress intensity factor due to (membrane) tension
K_{IB} = stress intensity factor due to bending

and

$K_c(\Delta a)$ = material toughness for the given amount of crack growth Δa.

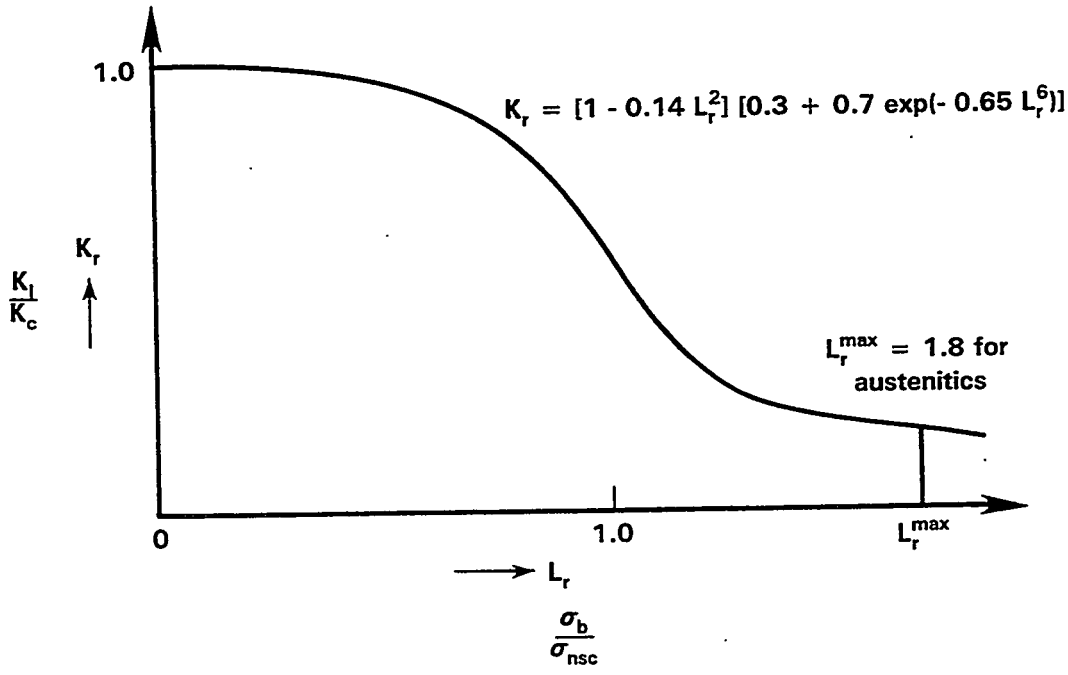

Figure 4.56 The R6 Option 1 curve

And

$$L_r = \frac{\sigma_B}{\sigma_{nsc}} \tag{4-102}$$

where

σ_B = maximum bending stress

and

σ_{nsc} = Net-Section-Collapse stress, using $\sigma_f = \sigma_y$.

The expression for K_{IT}, K_{IB}, σ_B, and σ_{nsc} are given below:

$$K_{IT} = \sigma_T\sqrt{\pi a}\, F_T \tag{4-103}$$

$$\sigma_T = \frac{pR_m}{2t}$$

$$a = R_m\theta$$

$$F_T = 1 + A_t(\theta/\pi)^{1.5} + B_t(\theta/\pi)^{2.5} + C_t(\theta/\pi)^{3.5} \tag{4-104}$$

where

t = pipe wall thickness
R_m = mean radius of pipe
p = internal pressure.

and A_t, B_t, and C_t are defined in Appendix A.

Also

$$K_{IB} = \sigma_B\sqrt{\pi a}\, F_B \tag{4-105}$$

where

$$F_B = 1 + A_b(\theta/\pi)^{1.5} + B_b(\theta/\pi)^{2.5} + C_b(\theta/\pi)^{3.5} \tag{4-106}$$

and A_b, B_b, and C_b are defined in Appendix A, and

$$\sigma_B = \frac{M}{\pi R_m^2 t} \tag{4-107}$$

M = maximum moment-carrying capacity of the pipe.

Also

$$\sigma_{nsc} = \frac{2\sigma_y}{\pi}(2\sin\beta - \sin\theta) \quad (4\text{-}108)$$

where

σ_y = yield strength for the material

$$\beta = \frac{\pi - \theta}{2} - \frac{p\pi R_m}{4t\sigma_y} \quad (4\text{-}109)$$

$$\theta = \text{crack length} = \frac{a}{R_m}$$

and

$$M_{nsc} = (\sigma_{nsc})(\pi R_m^2 t) \quad (4\text{-}110)$$

For a given pipe geometry, crack length, and material and internal pressure, all terms in the above equations are known except the moment-carrying capacity, M, of the cracked pipe.

The procedure to determine M is as follows:

i) Using the J-resistance curve, find the value of J for the given amount of crack growth Δa.

ii) Calculate

$$K_c(\Delta a) = (JE)^{1/2} \quad (4\text{-}111)$$

where E = Young's modulus of the material.

iii) Compute the two quantities A_1 and A_2 using the following equations:

$$A_1 = \frac{(\pi a)^{1/2} F_B}{K_c(\Delta a)} \quad (4\text{-}112)$$

$$A_2 = \frac{(\pi a)^{1/2} F_T \sigma_T}{K_c(\Delta a)} \quad (4\text{-}113)$$

iv) Obtain σ_{nsc} using Equation 4-108.

v) Solve for L_r numerically from the following equation, which was obtained by combining Equations 4-98 through 4-105 and eliminating σ_B.

$$K_r = A_1 \sigma_{nsc} L_r + A_2 = (1 - 0.14L_r^2)[0.3 + 0.7\exp(-0.65L_r^6)] \quad (4\text{-}114)$$

vi) The maximum moment is given by

$$M = \pi \sigma_{nsc} L_r R_m^2 t \qquad (4\text{-}115)$$

The above procedure is repeated as the crack grows using the values of J corresponding to the amount of crack growth Δa. Thus, the load-carrying capacity for each crack length is obtained from which the maximum load-carrying capacity of the cracked TWC pipe in question is determined. The above procedure has been incorporated into the PC-Code NRCPIPE (Version 2.0) used to analyze TWC pipes.

4.3.5.3 Analysis of Experiments Using R6-Option 1

Tables 4.22 and 4.23 show the pipe geometry, loading conditions, and material properties for four experiments analyzed using the R6-Option 1 procedure. The four experiments are 4111-2, 4111-5, 1.1.1.21, 1.1.1.23 in these tables. The results of this analysis are shown in Table 4.27. As seen, the ratio of the experimentally measured moments to those predicted by R6 are much greater than unity both at initiation and maximum loads. As stated above, the procedure is intended as a design or failure avoidance criteria and, hence, contains some inherent margins on the failure loads. This inherent margin was perhaps less than desired for the Experiment 4111-5 maximum load.

Table 4.27 Results of the R6 Option 1 analysis

Experiment No.	Initiation Moment, MN-m (in-lbs x 10^6)			Maximum Moment, MN-m (in-lbs x 10^6)		
	Predicted	Expt	Expt/Pred	Predicted	Expt	Expt/Pred
1.1.1.23[1]	1.62 (14.3)	2.62 (23.2)	1.62	2.39 (21.2)	3.06 (27.1)	1.28
4111-5[2]	0.66 (5.84)	0.97 (8.58)	1.47	1.22 (10.8)	1.26 (11.1)	1.03
1.1.1.21[1]	2.08 (18.4)	2.565 (22.7)	1.23	2.38 (21.1)	3.015 (26.7)	1.27
4112-2[2]	0.61 (5.35)	0.82 (7.21)	1.34	0.83 (7.31)	1.21 (10.7)	1.46

(1) From Short Cracks in Piping and Piping Welds Program
(2) From Degraded Piping Program - Phase II (Ref. 4.26)

4.3.6 Evaluation of J-R Curve for Experiment 1.1.1.21 -- η-Factor Approach

4.3.6.1. Background

As discussed in Section 3, two pipe experiments were conducted on the 710-mm (28-inch) diameter carbon steel pipe DP2-F26, one with a 6.25-percent circumferential through-wall crack and the other uncracked. The following describes the evaluation of a J-resistance curve using data from these experiments using the η-factor approach and comparison of the full-scale pipe J-R curves with those from the C(T) specimens.

The specimen geometry, material properties, and other details for the the TWC pipe experiment (1.1.1.21) and the uncracked pipe experiment (1.1.1.25) are given in Tables 2.1 and 3.2 above. A key aspect in the η-factor analysis for a short crack is that the plasticity of the uncracked pipe needs to be accounted for. This is done here using the uncracked pipe test data.

4.3.6.2 η-Factor Analysis

Correction for Dead-Weight Load. The first step in the analysis of the data involves correcting the load-load line displacement record (P-LLD) for the dead-weight load of the specimen. Using the density of the steel to be 7.63 x 10^{-5} N/mm^3 (0.281 lbs/in^3), the total dead-weight load was found to be 62.72 kN (14,100 lbs) for Experiment 1.1.1.21 (cracked pipe) and 106.76kN (24,000-lb) for Experiment 1.1.1.25 (uncracked pipe), which correspond to a moment of 257.11 kN-m (2.275 x 10^6 in-lb) and 268.7 kN-m (2.379 x 10^6 in-lb), respectively. This moment corresponds to an equivalent applied load of 62.48 kN (14,050 lb) for the cracked pipe and 65.31 kN (14,680 lb) for the uncracked pipe.

Load Displacement and Crack Growth Records. The load versus load-line displacement (LLD) records for the two tests after correcting for the dead-weight loads are shown in Figure 4.57 while the crack extension versus time curve for Experiment 1.1.1.21 is shown in Figure 4.58. Note that the crack jumps at times 8,288 seconds and 8,520 seconds in Figure 4.58. The first jump involved a crack growth of 19.70-mm (0.775-inch), 0.17 percent of the circumference, and the second involved 16.20-mm (0.638-inch), 0.16 percent of the circumference.

Load versus Plastic-Displacement Curves. At each load for the two curves the elastic displacement (load divided by the initial linear slope of the record) was subtracted from the total displacement to obtain the P–Δ^P_{PLL} curves. Here, Δ^P_{PLL} is the plastic pipe displacement at the load line and P is the total load for a 4-point bend pipe test. These curves, shown in Figure 4.59, are required for the computation of the J-R curves using the η-factor approach as shown below.

As seen in Figure 4.59, the load for the uncracked pipe is close to, but slightly lower than, that for the cracked pipe for low values of Δ^P_{PLL}. It was anticipated that the two should be the same initially, then the uncracked curve should go above the cracked curve at larger displacements. These are relatively large pipe tests, and some slight geometric variability and slight differences in properties may have caused this difference. Therefore, another correction needed to be made to these curves so that the loads for the cracked-pipe experiment are always equal to or lower than those for the

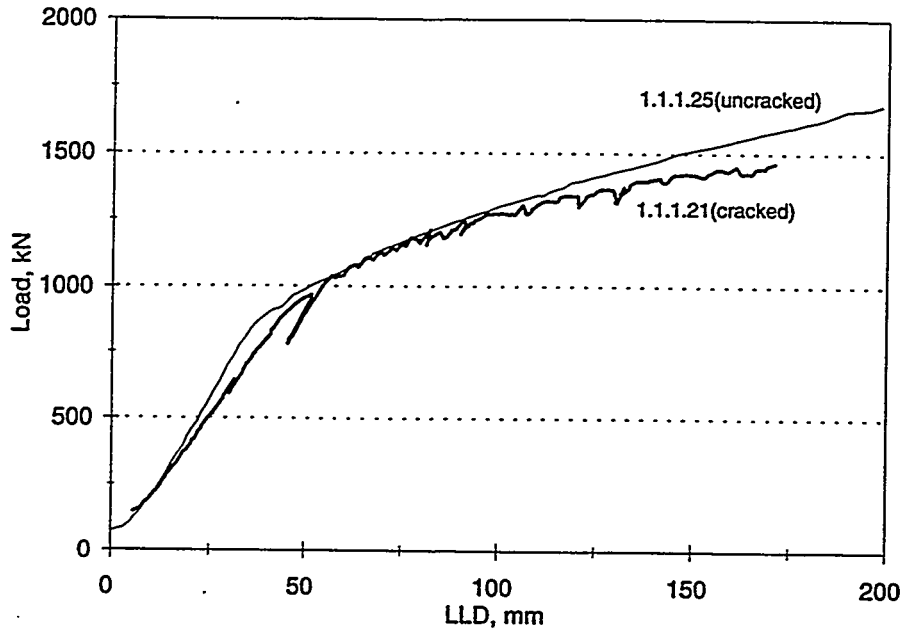

Figure 4.57 Load versus load-line displacement curves after dead-weight load correction for Experiment 1.1.1.21

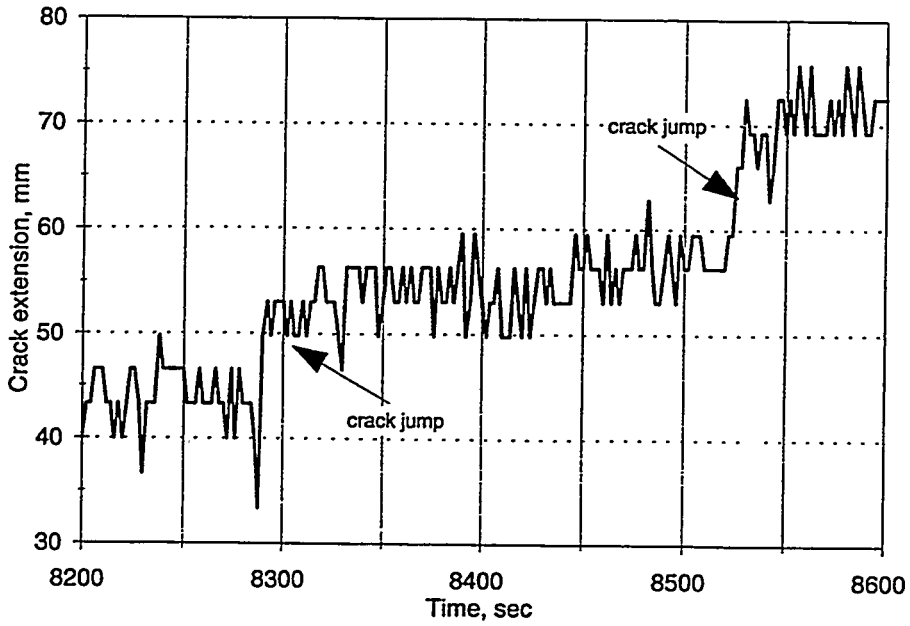

Figure 4.58 Crack length versus time for Experiment 1.1.1.21

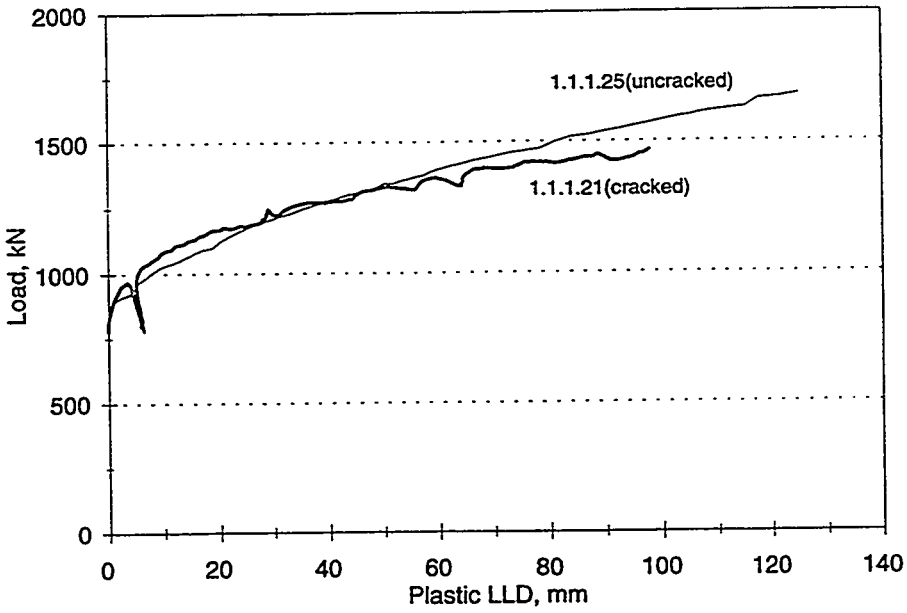

Figure 4.59 Load versus plastic displacement curve for Experiments 1.1.1.21 and 1.1.1.25

uncracked-pipe experiment. This can be done in one of two ways. The first is to shift the uncracked pipe curve vertically upwards until the two curves have a tangent point in common. The other is to shift the curve for the cracked-pipe experiment downwards until they have a common tangent point. These two possibilities present the lower and upper bound for the errors in the experiment leading to the above observations. Both these cases were used to compute the J-R curve.

Computation of the J-R Curve. After adjusting the $P-\Delta^{P}_{PLL}$ curves for the above error, the $P-\Delta^{P}_{PLL}$ curve for the uncracked pipe was fit to a third order polynomial given below:

$$\Delta^{P}_{PLL} = 72.50 - 0.2107P + 1.502 \times 10^{-4}P^2 - 3.705 \times 10^{-9}P^3 \qquad (4\text{-}116)$$

This enabled the plastic Δ^{PNC}_{PLL} (due to "no crack") to be subtracted from the Δ_{PLL} for the cracked pipe test (which includes $\Delta^{PNC}_{PLL} + \Delta^{PC}_{PLL}$ so as to obtain the $P-\Delta^{PC}_{PLL}$ curve shown in Figure 4.60). As shown, two such curves were obtained, corresponding to the lower and upper bound discussed above.

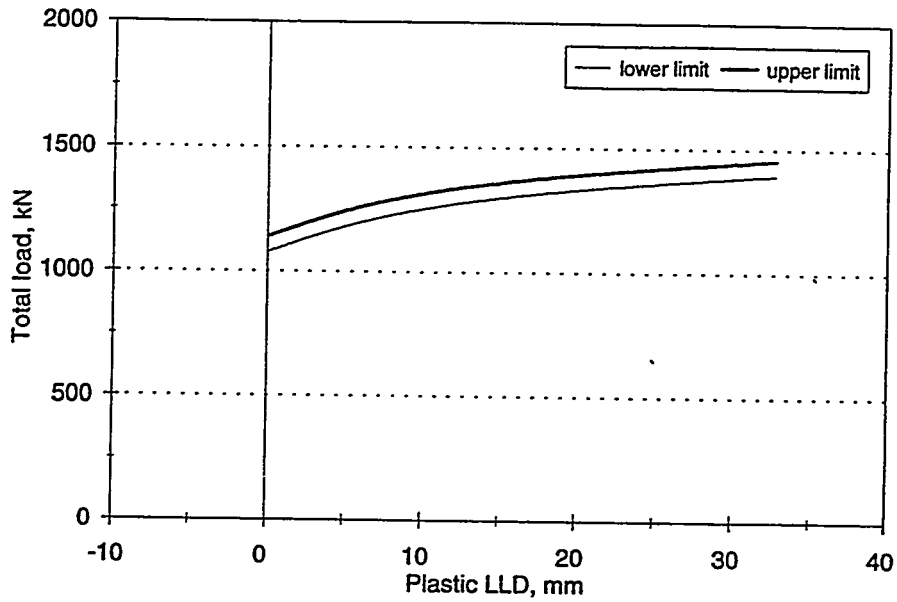

Figure 4.60 Load versus plastic deformation (due to the crack) curves for Experiment 1.1.1.21

The value of J is then computed from these $P-\Delta_{PLL}^{PC}$ curves using the following equation:

$$J = J_e + J_p \tag{4-117}$$

$$J_e = K_I^2/E \tag{4-118}$$

$$J_p = 2\int_0^{\Delta_{PLL}^{PC}} \eta P d\Delta_{PLL}^{PC} + \int_{\phi_o}^{\phi} \gamma J_{pl} d\phi \tag{4-119}$$

where,

$$\eta = - \frac{h'(\phi)}{R_m/t\ h(\phi)} \tag{4-120a}$$

$$\gamma = \frac{h''(\phi)}{h'(\phi)} \tag{4-120b}$$

$$h(\phi) = \cos(\frac{\phi}{4}) - \frac{1}{2}\sin(\frac{\phi}{2}) \tag{4-120c}$$

In the above equations, the nomenclature is as follows:

Δ_{PLL} = total pipe displacement at the load line
Δ^{P}_{PLL} = plastic pipe displacement at the load line
Δ^{PNC}_{PLL} = plastic pipe displacement at the load line with no crack
Δ^{PC}_{PLL} = plastic pipe displacement at the load line due to the cracks

The above equations have been implemented into a PC code IETAPIPE (Version 2.0). This code was used to compute J_e, J_p, and J for the pipe experiment.

The J-R curves from the pipe tests are shown in Figure 4.61, along with the J-R curve calculated from the cracked-pipe experiment alone assuming that $\Delta^{PNC}_{PLL} = 0$ (as is often done). Additionally, the J-R curves using laboratory C(T) non-side-grooved specimens at 288 C (550 F) with the same crack orientation as in the pipe are also shown in Figure 4.61. The C(T) specimen details are given in Table 2.8 above and the results are discussed in Section 2.3.

4.3.6.3 Comparison of FEM and η-Factor Values

Pipe Experiment 1.1.1.21 was also analyzed by FEM analysis as discussed in Section 4.2.5.1. The J-R curve from the FEM analysis is shown with the η-factor pipe and C(T) specimen J-R curves in Figure 4.61. Note that the FEM J-R curve is between the two pipe η-factor J-R curves. This is probably due to the following reason.

The subtraction of the uncracked pipe plasticity is a valid approach for pipe material that is remote from the crack plane. In the crack plane, and for some length of pipe in close proximity to it, the cross section is fully plastic due to the fracture process. However, subtracting uncracked pipe plasticity in this region effectively eliminates some of the energy properly associated with the η-factor analysis. It is not clear what length of pipe in close proximity to the crack plane should not be included in the uncracked-pipe plasticity correction. This length could perhaps be approximated from FEM solutions.

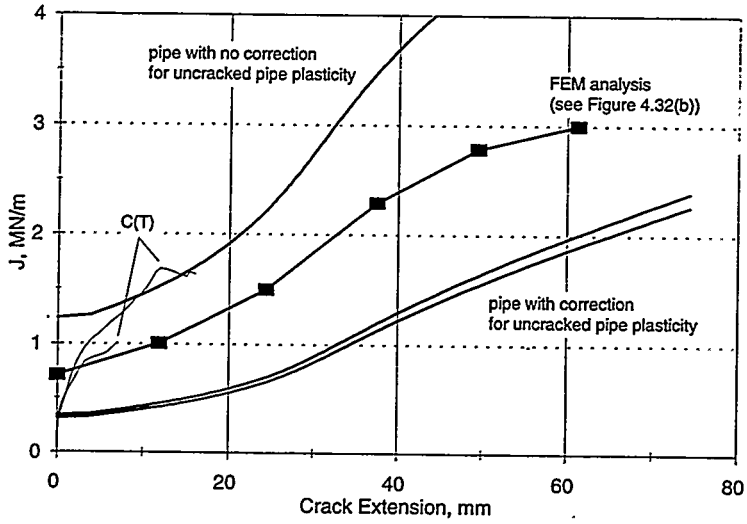

Figure 4.61 J-R curves from Pipe Experiment 1.1.1.21 and C(T) specimen F26-17 and F26-21 and FEM results (the two lower J-R curves are upper and lower limits of the load-displacement curve, see Figure 4.60)

In Experiment 1.1.1.21, the pipe diameter was 711.0 mm (28.0 inch), but the axial length of the pipe that was of this thickness was only slightly larger than one pipe diameter, i.e., 762 mm (30 inches). Most of this pipe test specimen had a larger thickness (see Section 3) and therefore did not experience plastic strains. Hence in this experimental setup, a large part of the uncracked pipe plasticity correction should not be applied, and the uncracked pipe "corrected" J-R curve in Figure 4.61 is therefore a lower bound. On the other hand, the pipe η-factor J-R curve without the uncracked pipe plasticity "correction" is an upper bound. The FEM J-R curve properly lies between the two.

For pipe η-factor analyses when the nominal stresses in the pipe are above yield, the best approach to obtain a proper pipe J-R curve may be to develop a new η-factor method based on the load versus the center-crack-opening displacement. This would eliminate the need for an uncracked-pipe plasticity correction. Such a solution could be generated through use of the new GE/EPRI functions from this report with the technique developed by Pan in Appendix A of Reference 4.40. Finally it should be noted that most of the pipe η-factor J-R curves generated in the past (Refs. 4.36, 4.37, and 4.41 to 4.45) were from pipe experiments with long enough cracks that there was no uncracked pipe plasticity. Hence the pipe J-R curves in those reports were valid.

4.3.7 η-factor Solution for Combined Bending and Tension

The J-integral is regarded as being equal to energy release rate. Assuming that J_D is independent of the loading path (see Section 4.2.2.6), and considering pressure loading of the pipe followed by 4-point bending, we may write:

$$J_D = \frac{1}{R_m t}\int_0^P \frac{\partial \Delta_{PLL}}{\partial \theta}\Big|_{s,P} dP + \frac{1}{2R_m t}\int_0^s \frac{\partial \delta}{\partial \theta}\Big|_{\phi = 0,s} ds \qquad (4\text{-}121)$$

where δ is the axial displacement, Δ_{PLL} is the pipe displacement at the load point, and ϕ is the rotation shown in Figure 4.62. Also, P is the total applied load (i.e., P/2 is applied at each load point in the 4-point bend configuration), and s is the ratio of axial stress (caused by pressure) to the flow stress, σ_f (see Figure 4.62). We assume that $\phi << 1$ and $\delta/2 <<$ moment arm. Here J_D, Δ_{PLL}, and δ are assumed to be divided into the elastic and plastic components, and the plastic component of J_D is given by

$$J_{D,PL} = \frac{1}{R_m t}\int_0^P \frac{\partial \Delta^P_{PLL}}{\partial \theta}\Big|_{s,P} dP + \frac{1}{2R_m t}\int_0^s \frac{\partial \delta^P}{\partial \theta}\Big|_{\phi = 0,s} ds \qquad (4\text{-}122)$$

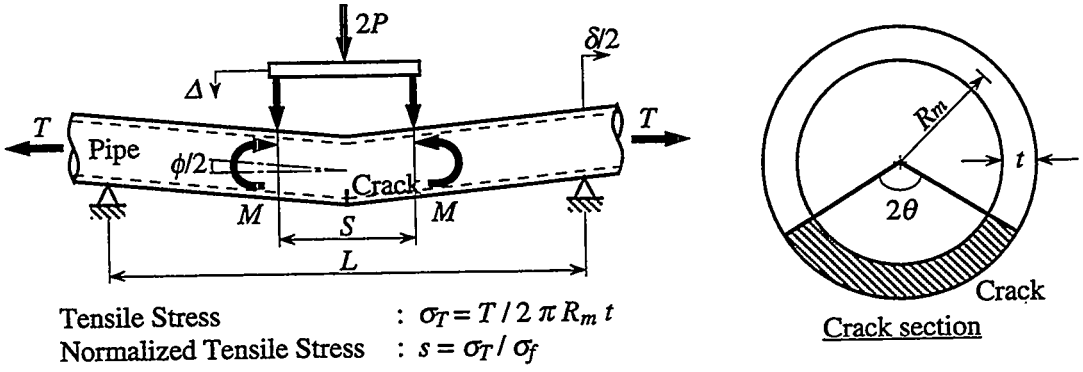

Figure 4.62 Circumferentially through-wall cracked pipe

The δ^P due to tensile load is considerd to be small, so that the second term in Equation 4-122 is negligible. Thus, Equation 4-122 can be rewritten as

$$J_{D,PL} = \frac{1}{R_m t}\int_0^P \frac{\partial \Delta^P_{PLL}}{\partial \theta}\Big|_{s,P} dP \qquad (4\text{-}123)$$

We also assume that Δ^P_{PLL} is a function only of the ratio of the applied load, P, to the Net-Section-Collapse analysis predicted load, P_L (note that P_L is the 4-point-bend limit load). P_L is expressed in terms of the Net-Section-Collapse moment, M_{nsc}, as follows;

$$P_L = \frac{2M_{nsc}}{L-S} = \frac{8\sigma_f R_m^2 t h_p(\theta,s)}{L-S} \tag{4-124}$$

$$h_p(\theta,s) = \cos\left[\frac{\theta}{2} + \frac{\pi}{2}s\right] - \frac{1}{2}\sin\theta \tag{4-125}$$

where L and S are the outer and inner span shown in Figure 4.62, respectively, and σ_f is the flow stress (defined as the mean of yield stress and ultimate strength). Therefore, Δ^P_{PLL} should be expressed as

$$\Delta^P_{PLL} = f\left[\frac{P}{h_p(\theta,s)}\right] \tag{4-126}$$

Substituting Equation 4-126 into Equation 4-123 we have

$$J_{D,PL} = 2\eta_p \int_0^{\Delta^P_{PLL}} P d\Delta^P_{PLL} \tag{4-127}$$

$$\eta_p = \eta_p(\theta,s) = -\frac{\partial h_p / \partial\theta}{2R_m t h_p(\theta,s)} \tag{4-128}$$

Thus, $J_{D,PL}$ under the condition of stable crack growth and constant tension can be evaluated from the $P-\Delta^P_{PLL}$ relation. Note that the above procedure is the η-factor approach with the function h replaced with h_p.

For the generalized case, Equation 4-126 is written in its inverse form,

$$P = h_p(\theta,s)F(\Delta^P_{PLL}) \tag{4-129}$$

In this equation, Δ^P_{PLL}, θ, and s are assumed to be independent of each other. Substituting Equation 4-129 into Equation 4-127

$$J_{D,PL} = -\frac{\partial h_p/\partial\theta}{R_m t}\int_0^{\Delta^P_{PLL}} F(\Delta^P_{PLL})\, d\Delta^P_{PLL} \tag{4-130}$$

Since $J_{D,PL}$ is a unique function of Δ^P_{PLL}, θ, and s, the exact differential of $J_{D,PL}$ gives

$$dJ_{D,PL} = \frac{\partial J_{D,PL}}{\partial \Delta^P_{PLL}} d\Delta^P_{PLL} + \frac{\partial J_{D,PL}}{\partial\theta} d\theta + \frac{\partial J_{D,PL}}{\partial s} ds \tag{4-131}$$

By substituting Equation 4-130 into Equation 4-131, we have

$$J_{D,PL} = 2\int_0^{\Delta^P_{PLL}} \eta_p P\, d\Delta^P_{PLL} + 2\int_{\theta_0}^{\theta} \gamma_p J_{D,PL} d\theta + 2\int_{s_0}^{s} \mu_p J_{D,PL} ds \tag{4-132}$$

where η_p is defined by Equation 4-128, and

$$\gamma_p = \gamma_p(\theta,s) = \frac{\partial^2 h_p/\partial\theta^2}{2\partial h_p/\partial\theta} \tag{4-133}$$

$$\mu_p = \mu_p(\theta,s) = \frac{\partial^2 h_p/\partial s\partial\theta}{2\partial h_p/\partial\theta} \tag{4-134}$$

The second term on the right side of Equation 4-132 corresponds to the contribution of the crack growth. The functions η and γ in the original η-factor approach are replaced with functions η_p and γ_p in Equations 4-128 and 4-133, respectively. The third term of the right side of Equation 4-132 corresponds to the contribution of a varying tensile load. If the axial tension is constant, this term equals 0.

4.3.8 Combined Bending and Pressure J-Resistance Curve Considerations

This section provides predicted results for the combined bending and pressure load case and compares predictions with available experimental data. All of the results presented in this report up to this point have been concerned with the pure bending load case.

Another issue covered in this section concerns the definition of the J-R curve used for the predictions. Typically the J-R curve from a compact tension specimen that has been cut from the pipe is used for predicting the failure of cracked pipe using J-Tearing theory. Small specimen J-R data are typically used because they are often the only data available, and because predicted results are generally considered to be lower bounds. This assumption is investigated here by also making predictions using η-factor J-R curves. The methods and equations for providing the η-factor J-R curves were described in the previous two sections.

4.3.8.1 Results

Six different combined bending and pressure tests were analyzed. As seen in Table 4.28, three carbon and three stainless steel pipe tests were modeled. Also listed in Table 4.28 are the pipe dimensions and other pertinent test information. Table 4.29 lists all of the material parameters necessary to perform a fracture analysis based on J-Tearing theory. All of the analysis methods used for these predictions have been described previously in this report.

Figure 4.63 shows the J-R curves used for the analysis of Experiment 1-8 from the IPIRG-2 program. Note that the extrapolated J-R curve from the compact tension C(T) specimen and the J-R curve from the combined bending and tension η-factor approach were used. Figure 4.64 shows the experimental divided by the predicted loads (or nominal stress) for both crack initiation and maximum load. The horizontal axis definitions are self evident from the captions at the bottom of the figure. Note that for both initiation and maximum load, predictions using the C(T) specimen J-R curves are lower than predictions using the η-factor J-R curve. Note also that using the ASME IWB-3650 method provides predictions that are twice the experimental values. The Net-Section-Collapse method provides the most accurate prediction of maximum load for this case despite the fact that it is a carbon steel pipe. Finally, Figure 4.65 compares the predicted load versus pipe displacement at the load line for the different methods and the experimental results. The pressure is applied first in these tests, followed by four-point bending under displacement control to failure. The drop in the displacement at about 275 mm (10.82 inches) in the experimental results just at maximum load is due to an unstable crack jump at this point.

Table 4.28 Geometry for combined bending and pressure analyses

	Experiment Number					
	IPIRG-2[a] 1-8	**IPIRG-2[a] 1-9**	**DP3-II[b] 4131-1**	**DP3-II[b] 4131-3**	**EPRI[c] RP-585-1**	**EPRI[c] RP-585-2**
Pipe Material	A106 Gr. B	A106 Gr. B	TP304	SA333 Gr. 6	TP304	TP304
Test Temperature, C (F)	288 (550)	288 (550)	288 (550)	288 (550)	3 (37)	4 (39)
Outside Pipe Diameter (D_o), mm (inch)	399 (15.7)	168 (6.61)	166 (6.55)	274 (10.8)	114 (4.50)	114 (4.50)
Actual Wall Thickness (t), mm (inch)	26.2 (1.03)	8.8 (0.35)	13.4 (0.53)	18.7 (0.74)	7.7 (0.30)	7.7 (0.30)
Crack length (θ/π), percent	12.1	25.0	37.0	37.0	37.5	21.2
Four-Point Bending Inner Span, m (ft)	3.35 (11.0)	0.91 (3.00)	1.22 (4.00)	3.35 (11.0)	1.22 (4.00)	1.22 (4.00)
Four-Point Bending Outer Span, m (ft)	11.6 (38.0)	6.10 (20.0)	3.20 (10.5)	7.92 (26.0)	2.44 (8.00)	2.44 (8.00)
Initiation Load (P_i), kN (lb)	302.0 (67,900)	29.1 (6,540)	30.9 (6,940)	70.1 (15,800)	56.3 (12,660)	ND[d]
Maximum Load (P_{max}), kN (lb)	504 (113,400)	37.6 (8,450)	39.8 (8,950)	99.5 (22,400)	56.9 (12,800)	83.2 (18,700)
Internal Pressure, MPa (psi)	15.5 (2,250)	15.5 (2,250)	17.2 (2,500)	12.5 (1,810)	7.2 (1,040)	17.2 (2,500)

(a) Data not previously published.
(b) From Reference 4.36.
(c) From Reference 4.12.
(d) ND = Not determined

Table 4.29 Material properties for combined bending and tension analyses

	Experiment Number					
	IPIRG-2[a] 1-8	IPIRG-2[a] 1-9	DP³II[b] 4131-1	DP³II[b] 4131-3	EPRI[c] RP-585-1	EPRI[c] RP-585-2
Modulus of Elasticity (E), GPA (ksi)	193.1 (28,000)	190.0 (27,500)	183.0 (26,500)	193.0 (28,000)	192.0 (27,850)	192.0 (27,850)
Yield Stress (σ_y), MPa (psi)	215 (31,300)	259 (37,500)	139 (20,200)	239 (34,700)	272 (39,500)	272 (39,500)
Ultimate Stress (σ_u), MPa (psi)	506 (73,500)	588 (85,300)	450 (65,300)	527 (76,400)	634 (92,000)	634 (92,000)
Design Stress (S_m),[d] MPa (psi)	124.8 (18,100)	124.8 (18,100)	116.9 (16,950)	124.9 (18,000)	137.9 (20,000)	137.9 (20,000)
Ramberg-Osgood[e] Coefficients						
α	1.38	2.76	5.06	3.76	1.50	1.50
n	5.05	3.56	3.84	3.84	6.63	6.63
Extrapolated[f] J-R Curve Parameters						
J_{Ic}, MJ/m² (lb-in/in²)	0.072 (411)	0.044 (251)	1.090 (6,220)	0.298 (1,700)	1.769 (10,100)	1.769 (10,100)
C_1, MJ/m² (lb-in/in²)	0.139 (794)	0.056 (320)	0.213 (1,220)	0.154 (879)	0.343 (1,960)	0.343 (1,960)
m	0.710	0.632	0.614	0.717	0.642	0.642

(a) Data not previously published.
(b) From Reference 4.36.
(c) From Reference 4.12.
(d) S_m value used for IWB 3640 or IWB 3650 analyses taken from Section II, Materials (Part D) of the ASME Code.
(e) $\epsilon/\epsilon_0 = \sigma/\sigma_0 + \alpha\,(\sigma/\sigma_0)^n$, $\epsilon_0 = \sigma_0/E$, $\sigma_o = \sigma_y$.
(f) $J = J_{Ic} + C_1\,(\Delta a/r)^m$, where r = 1 mm.

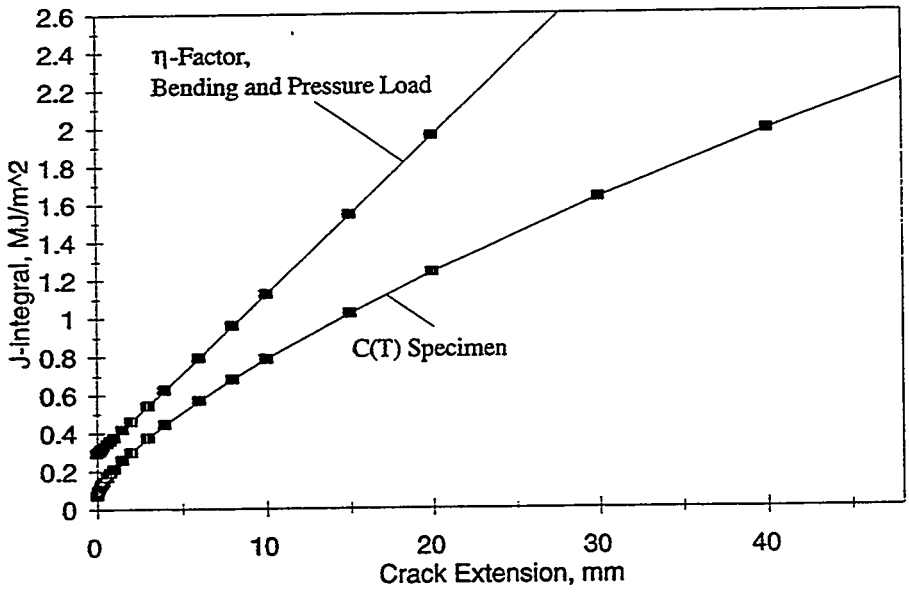

Figure 4.63 J-resistance curves for IPIRG-2 Experiment 1-8

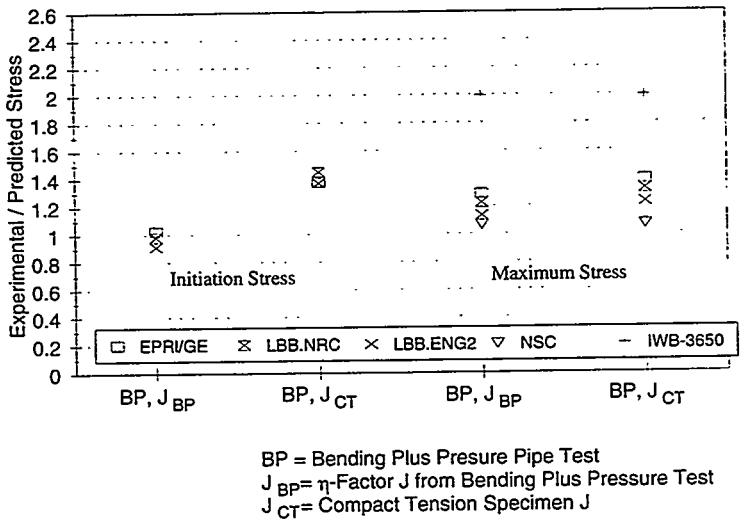

Figure 4.64 Ratios of experimental versus predicted initiation and maximum stresses from IPIRG-2 Experiment 1-8 (stress is the total maximum nominal stress, tension plus bending)

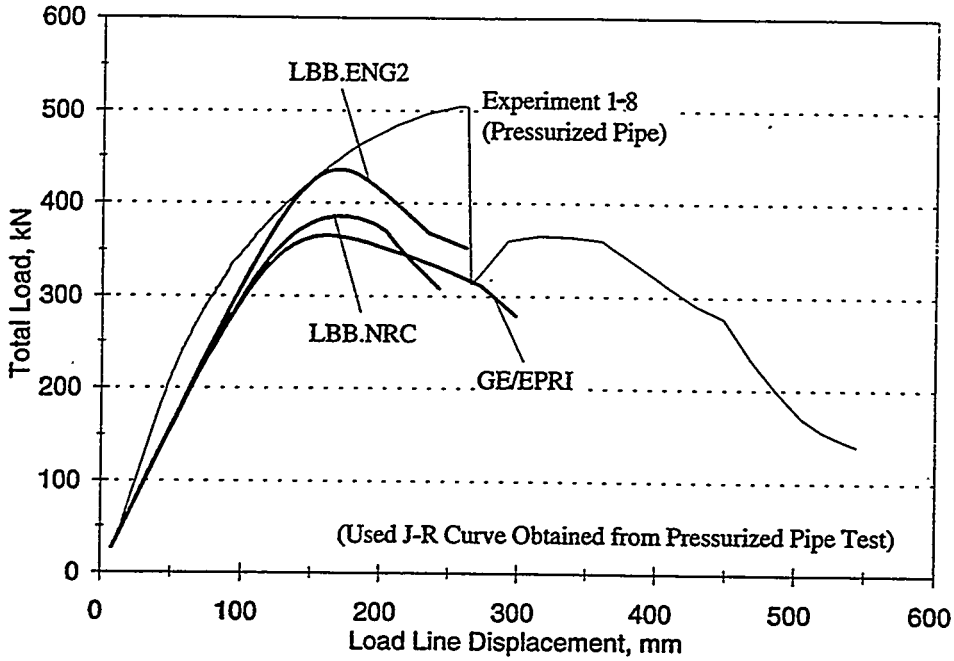

Figure 4.65 Predicted load versus pipe displacement at the load line for IPIRG-2 Experiment 1-8 (the pipe η-factor J-R curve was used here)

Figure 4.66 shows the J-R curves used for the predictions of crack initiation and maximum load for IPIRG-2 Experiment 1-9. As is typical, the η-factor J-R curve was higher than the C(T) specimen curve. Figure 4.67 shows the predicted initiation and maximum loads normalized by the experimental loads using both J-R curves. Again, the predictions using the C(T) specimen J-R curve were lower than the predictions using the η-factor J-R curve. As with IPIRG-2 Experiment 1-8, the Net-Section-Collapse method provided the best prediction of maximum load here. Figure 4.68 compares the load-displacement predictions.

Figure 4.69 shows the J-R curves used for the analyses of DP^{3}II Experiment 4131-1. Three curves are shown in this figure; one is from a C(T) specimen cut from the test pipe, one represents the pipe η-factor J-R curve from the Experiment 4131-1, and one represents an η-factor J-R curve from a bending-only pipe test. This bending test (Experiment 4131-5 from the Degraded Piping Program) was nearly identical to Experiment 4131-1 in all respects (pipe size, crack size, material, etc.) except no pressure was applied during the test. The initiation value of J was larger here in the C(T) specimen. Figure 4.70 shows the initiation load predictions compared with the experimental results for this test. Note that there are six cases; three predictions for pure bending (Experiment 4131-5) using the three different J-R curves, and three for combined bending and pressure, again using the three J-R curves from Figure 4.69. Figure 4.71 compares predicted maximum loads with experimental results for these experiments. It is also shown in Figure 4.71 that the ASME Section XI IWB-3640 method underpredicts the loads compared with the experiment. This is because $3S_m$ is greater than the flow stress (average of yield and ultimate) for this particular TP304 stainless steel pipe (see Table 4.29). Finally, the load-displacement predictions are provided in Figure 4.72.

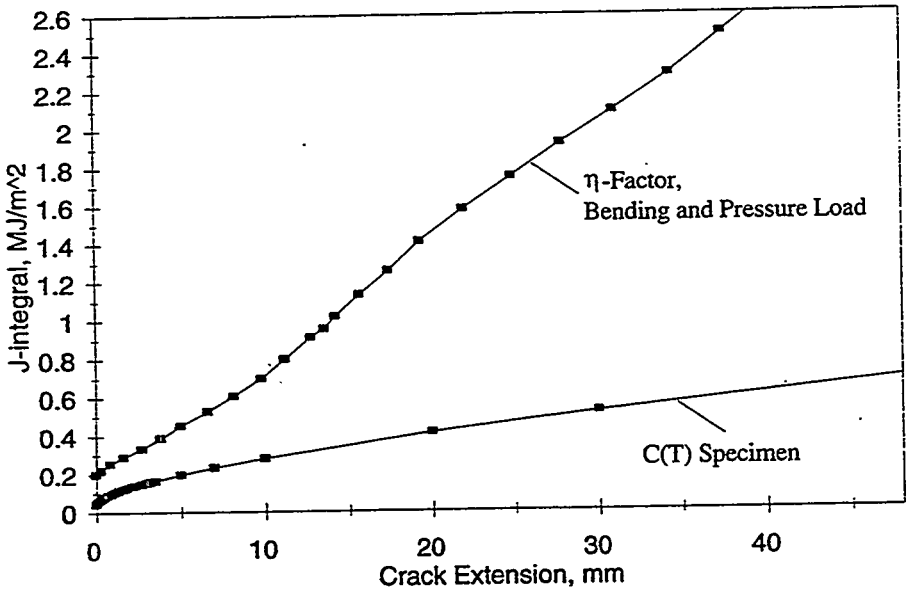

Figure 4.66 J-resistance curves for Experiment 1-8 from IPIRG-2

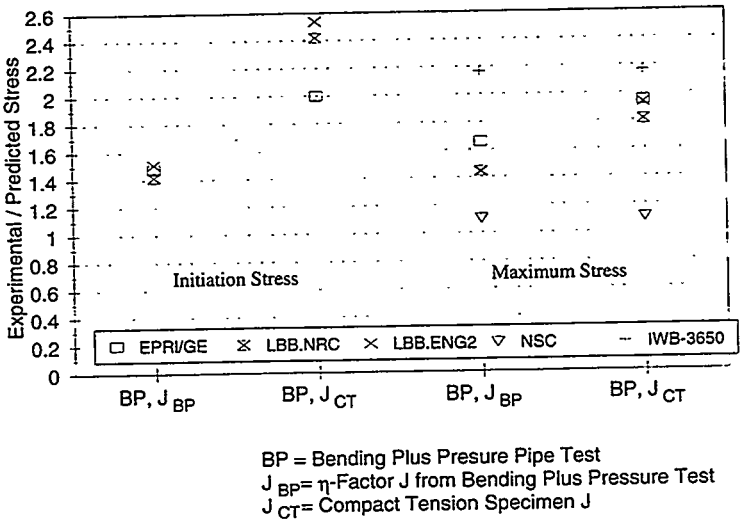

Figure 4.67 Predicted initiation and maximum stress from Experiment 1-9 of the IPIRG-2 program (stress is the total nominal stress, tension plus bending)

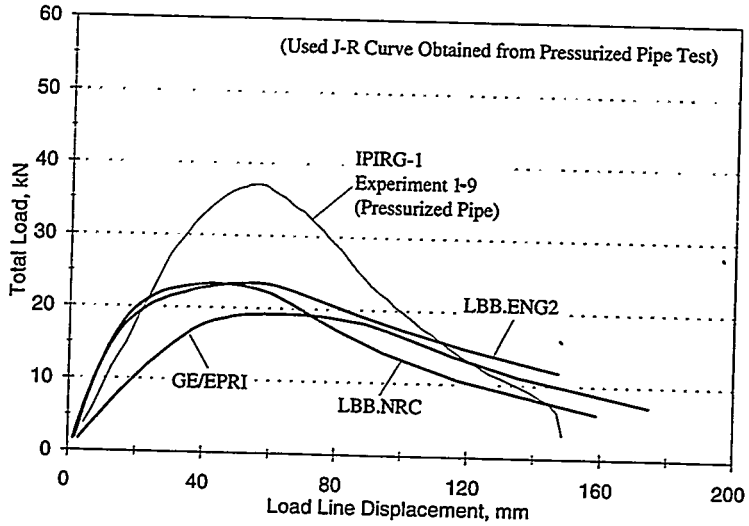

Figure 4.68 Predicted loads versus pipe displacement at the load-line for IPIRG-2 Experiment 1-9

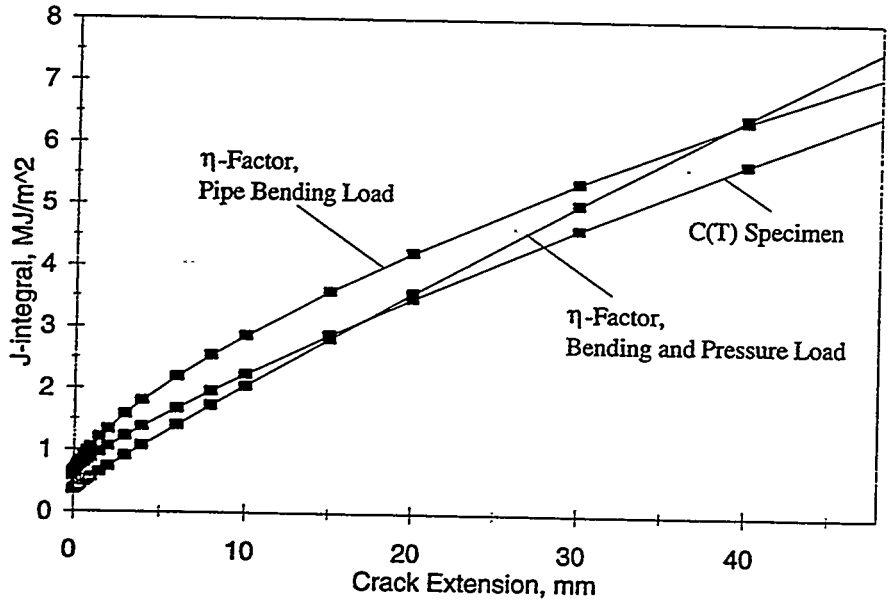

Figure 4.69 J-resistance curves for DP^{3}II Experiment 4131-1 and the η-factor solution for the pipe bending-only test from DP^{3}II Experiment 4131-5

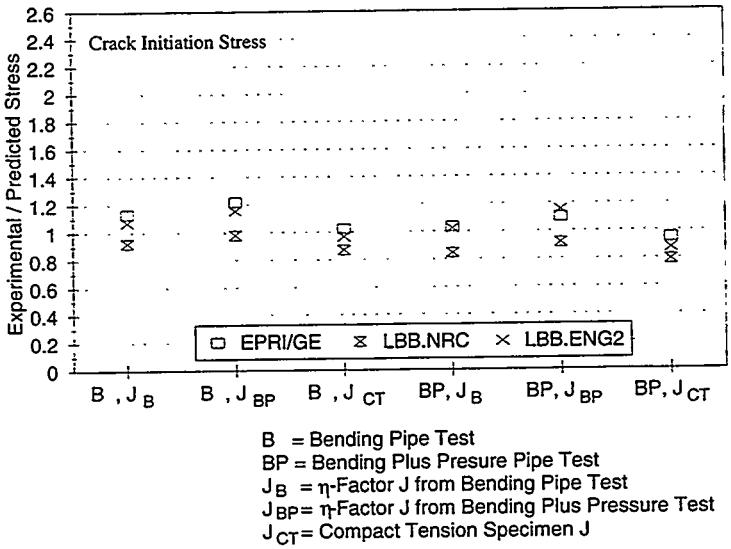

Figure 4.70 Predicted initiation stresses from Experiments 4131-1 and 4131-5 of the Degraded Piping program using the different J-R curves of Figure 4.69 (stress is the total nominal stress, tension plus bending)

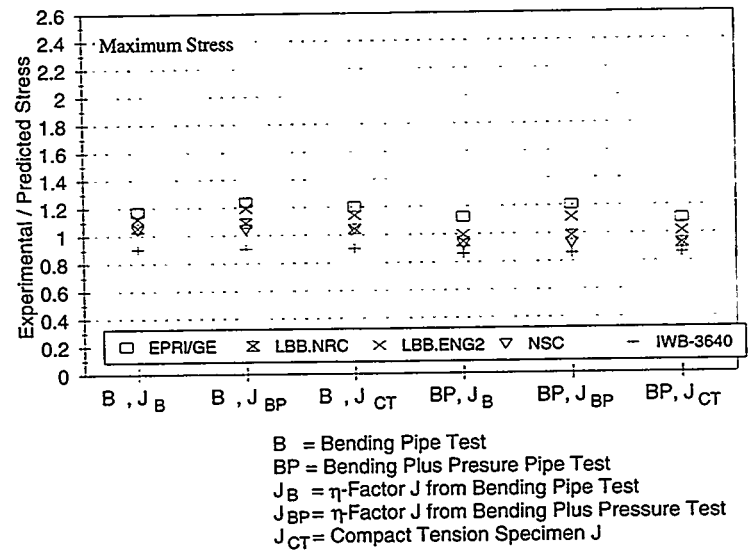

Figure 4.71 Predicted maximum stress for Experiments 4131-1 and 4131-5 of the Degraded Piping program using the three J-R curves of Figure 4.69 (stress is the total nominal stress, tension plus bending)

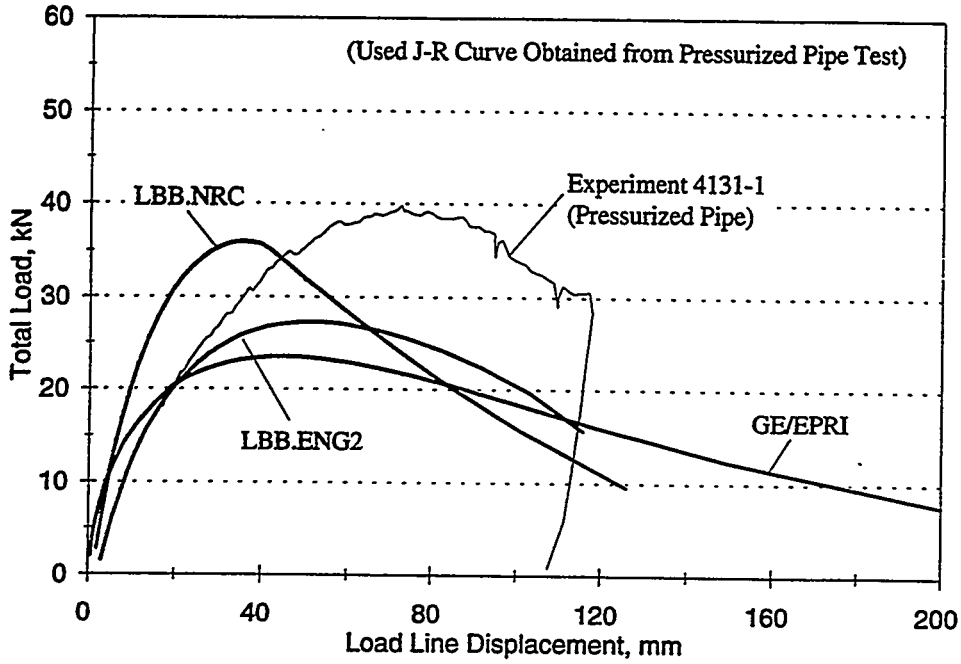

Figure 4.72 Predicted load versus pipe displacement at the load line for DP^{3}II Experiment 4131-1

Figure 4.73 shows the J-R curves used for the analyses of DP^{3}II Experiment 4131-3. Three curves are shown in this figure; one is from a C(T) specimen cut from the test pipe, one represents the η-factor J-R curve from Experiment 4131-3, and one represents an η-factor J-R curve from a bending only pipe test. This bending test (Experiment 4131-7 from the Degraded Piping Program) was nearly identical to Experiment 4131-3 in all respects (pipe size, crack size, material, etc.) except no pressure was applied during the test. The three initiation values for J were quite similar for this case. Figure 4.74 shows the initiation load predictions compared with experiment for this test. Note that there are six cases; three predictions for pure bending (Experiment 4131-7) using the three different J-R curves, and three for combined bending and pressure, again using the three J-R curves from Figure 4.73. Figure 4.75 compares predicted maximum loads with experimental results for these experiments. Here, Net-Section-Collapse solutions underpredict the loads, while IWB-3650 greatly overpredicts the experimental results. The LBB.NRC method provides the most accurate predictions. Finally, the load-displacement predictions are provided in Figure 4.76.

The results for several older EPRI tests, RP-585-1 and RP-585-2, (Ref. 4.34) are also provided. Figure 4.77 illustrates the J-R curve used for the predictions. Note that the load versus pipe displacement at the load line is not available from these tests, and hence, no η-factor pipe J-R curves could be obtained. These tests again represent combined pressure and bend tests of stainless steel pipe. Table 4.28 shows that the tests were almost identical except for different crack sizes and applied pressures. Figure 4.78 compares predictions of initiation and maximum loads with experimental results for EPRI Test RP-585-1. Here, the LBB.ENG2 method provides slightly better predictions compared with the other methods. Figure 4.79 compares the maximum-load prediction for EPRI Test RP-585-2 (the experimental initiation load was not determined).

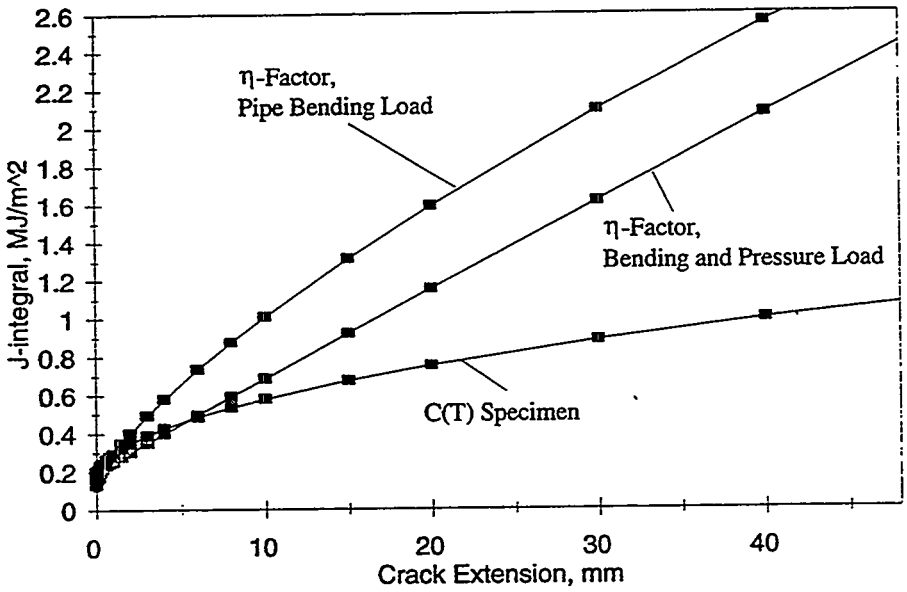

Figure 4.73 J-resistance curve for DP³II Experiment 4131-3 and the η-factor solution for the pipe bending-only test from DP³II Experiment 4131-7

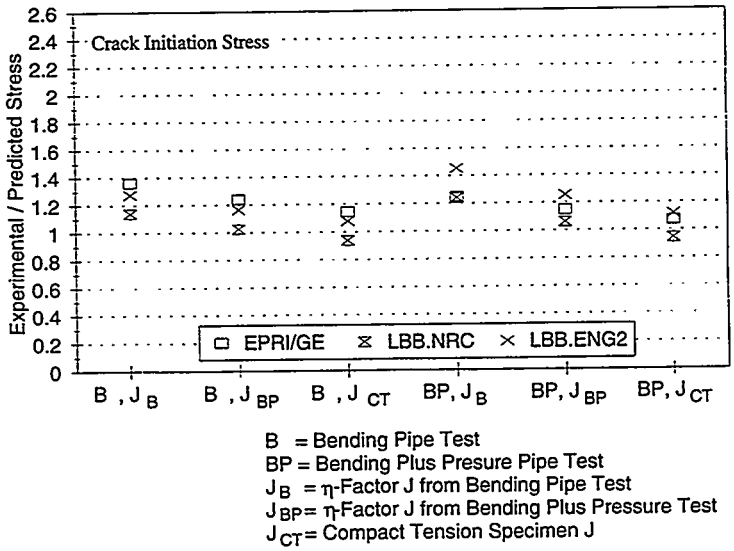

Figure 4.74 Predicted initiation stresses from DP³II Experiments 4131-3 and 4131-7 using the different J-R curves of Figure 4.73 (stress is the total nominal stress, tension plus bending)

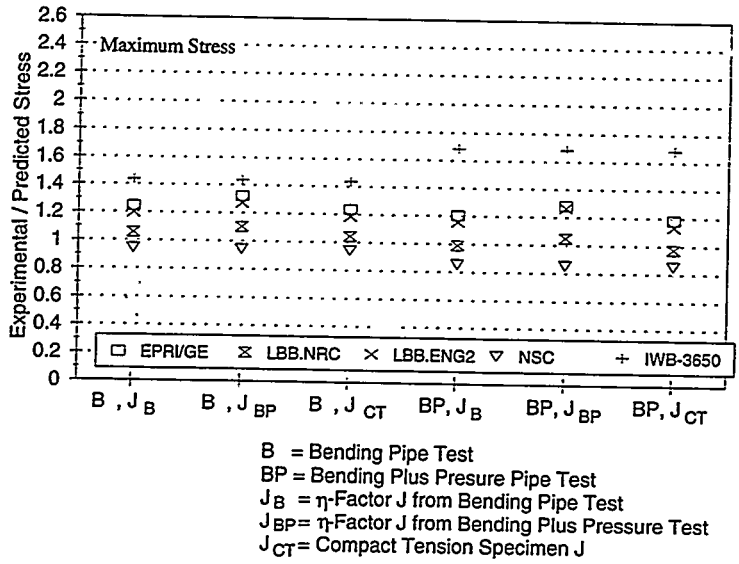

Figure 4.75 Predicted maximum stresses DP³II from Experiments 4131-3 and 4131-7 using the J-R curves from Figure 4.73 (stress is the total nominal stress, tension plus bending)

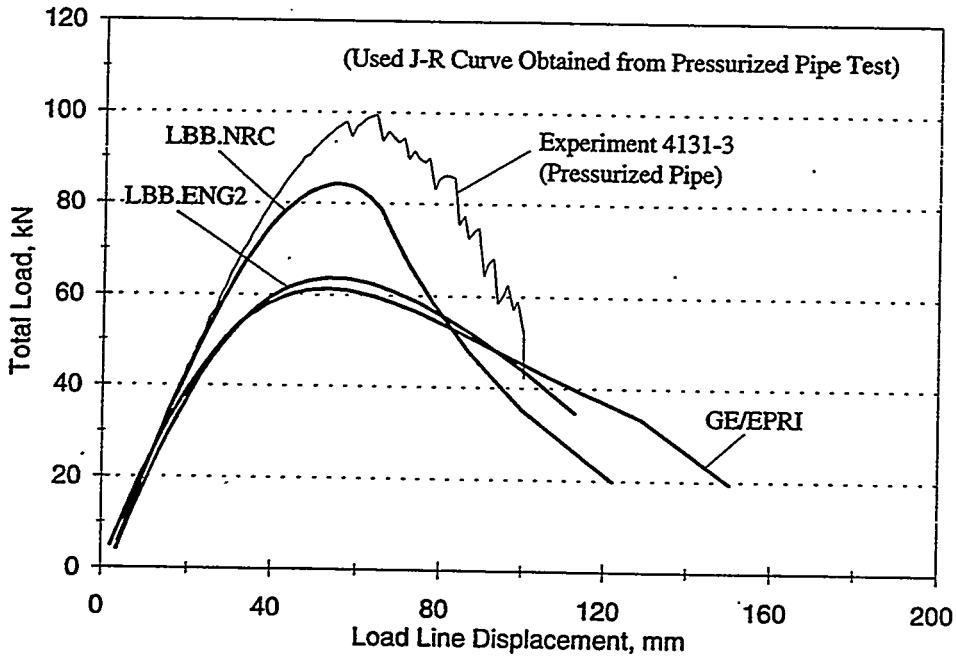

Figure 4.76 Predicted load versus pipe displacement at the load-line for DP³II Experiment 4131-3

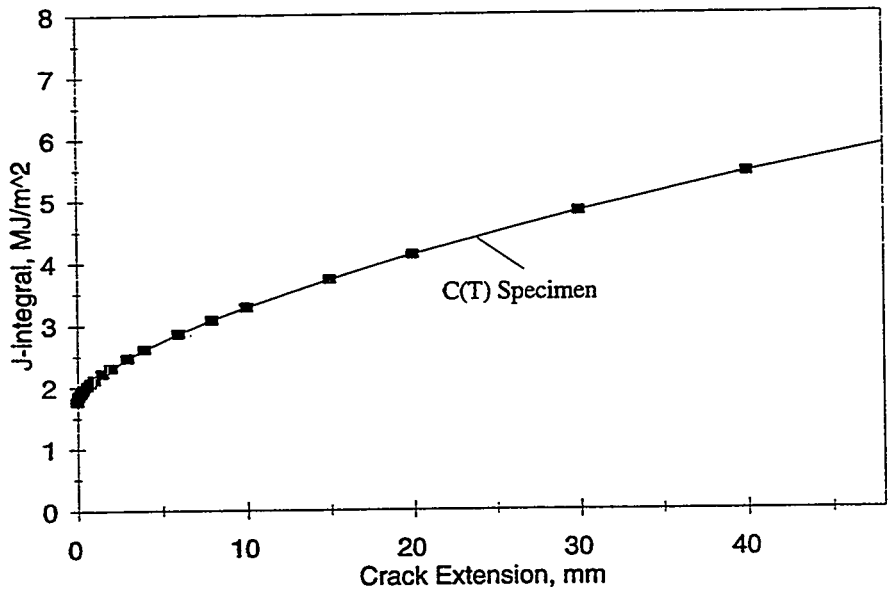

Figure 4.77 J-R curve from a compact tension specimen for EPRI Experiments RP-585-1 and RP-585-2

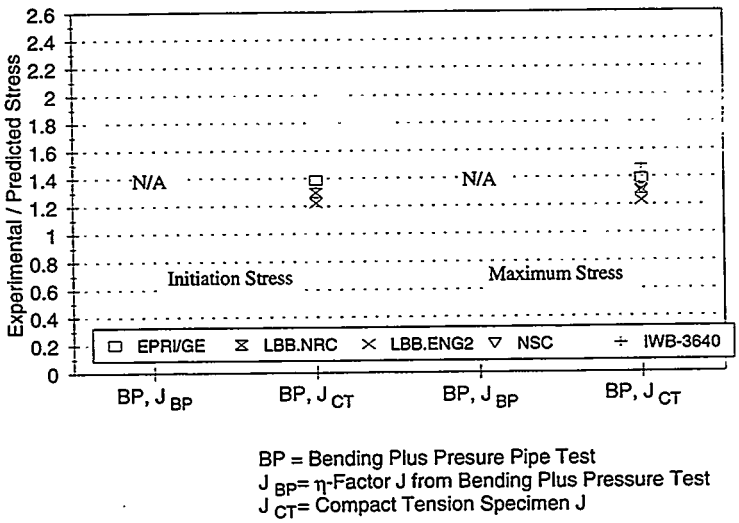

Figure 4.78 Predicted stresses compared with stresses from experiment for EPRI Test RP-585-1 (stress is the total nominal stress, tension plus bending)

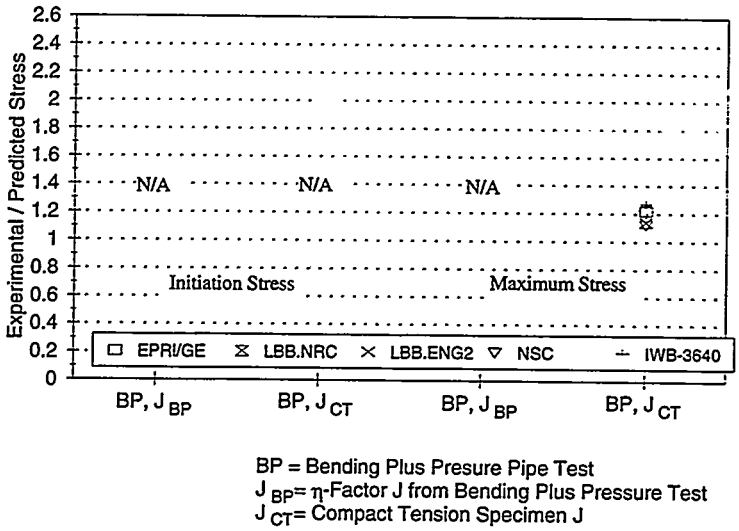

Figure 4.79 Predicted maximum stresses compared with stresses from experiment for EPRI Test RP-585-2 (stress is the total nominal stress, tension plus bending)

4.3.8.2 Discussion

The combined pressure- and bending- test predictions in general were adequate compared with the experimental data. In general, the LBB.NRC and LBB.ENG2 method provided the best predictions compared with the experimental results, while the GE/EPRI method provided the largest under-predictions of the loads. The ASME Section XI IWB-3650 method for carbon steel pipe failure prediction generally provided large underpredictions of the experimental results. However, the ASME Section XI IWB-3640 method overpredicted the load for one case (see Figure 4.71). All of the J-estimation methods provided underpredictions of the maximum loads for all J-R curves used, with the greatest underprediction occurring when the C(T) J-R curve is used.

4.3.9 Performance Evaluation of Predictive Analyses

Standard statistical analyses were performed to assess the accuracy of predictive fracture-analysis methods in estimating the initiation and the maximum loads for pipes. The statistics involved calculation of mean and coefficient of variation (COV) [COV is equal to the ratio of standard deviation to the mean] of the load ratio (initiation or maximum), where the load ratio is defined as the ratio of the experimental load to the predicted load.

4.3.9.1 Initiation Load

For the initiation load evaluations, the statistics were based on eight experiments for pure bending and five experiments for combined bending and tension. Table 4.30 shows the mean and coefficient of variation of the initiation load ratio tabulated for both of these loading conditions. From the results of this table, it appears that all J-estimation methods except the Paris/Tada method underpredicted the experimental initiation load regardless of loading conditions. Among these methods, the LBB.ENG3 (mean load ratio = 1.03) and LBB.NRC methods (mean load ratio = 1.04) provided the most accurate predictions of experimental data on the average for pure bending.

For combined bending and tension, LBB.ENG2, LBB.ENG3, and LBB.NRC methods underpredicted loads and the Paris/Tada method overpredicted loads. However, the magnitudes of underprediction and overprediction for the mean values under combined loading were slightly larger than for pure bending. The coefficients of variation for combined bending and tension were slightly larger than those for pure bending.

4.3.9.2 Maximum Load

For the maximum load evaluations, the statistics were based on twelve experiments for pure bending and six experiments for combined bending and tension. Table 4.31 shows the mean and coefficient of variation of the maximum load ratio for both of these loading conditions.

These statistical measures are presented by analyzing all pipe tests, pipes with short through-wall cracks, and pipes with cracks in weldments.

Table 4.30 Mean and coefficient of variation of initiation load ratio predicted by various deterministic fracture-mechanics analyses

	Initiation Load Ratio[a]			
	TWC Pipes Under Bending (8 tests)		TWC Pipes Under Bending Plus Tension (5 tests)	
Fracture Analysis Methods	Mean	Coefficient of Variation,[b] percent	Mean	Coefficient of Variation,[b] percent
LBB.ENG2	1.12	17.64	1.13	20.45
LBB.NRC	1.04	17.71	1.09	21.46
LBB.GE	1.05	19.28	--[c]	--[c]
GE/EPRI-1A	1.20	16.91	1.18	17.71
Paris/Tada	0.98	19.99	0.91	20.76
LBB.ENG3	1.03	10.65	1.13	20.45

(a) Initiation load ratio = experimental initiation load/predicted initiation load.
(b) Coefficient of variation = (standard deviation/mean) x 100.
(c) Not calculated.

Table 4.31 Mean and coefficient of variation of maximum load ratio predicted by various deterministic fracture-mechanics analyses

	Maximum Load Ratio[a]							
	All TWC Pipes Under Bending (12 Tests)		Short TWC Pipes Under Bending (5 Tests)		TWC Welded Pipes Under Bending (4 Tests)		All TWC Pipes Under Bending and Tension (6 Tests)	
Fracture Analysis Methods	Mean	Coefficient of Variation[b], percent	Mean	Coefficient of Variation[b], percent	Mean	Coefficient of Variation[b], percent	Mean	Coefficient of Variation[b], percent
LBB.ENG2	1.04	12.93	0.96	16.27	1.08	7.61	1.18	11.06
LBB.NRC	1.01	10.50	1.02	9.02	0.94	12.74	1.17	15.45
LBB.GE	1.01	11.62	0.98	13.91	0.98	6.38	---[c]	---[c]
GE/EPRI-1A	1.15	11.14	1.12	14.97	1.18	9.50	1.31	13.75
Paris/Tada	0.96	12.72	0.91	6.95	0.87	11.87	1.03	13.62
LBB.ENG3	1.00	12.48	0.90	11.58	1.02	5.83	1.18	11.06
ASME Section XI	1.34	26.87	1.47	34.71	1.28	13.16	1.58	27.82
- Austenitic	1.2[d]	12.96[d]	--	--	--	--	1.20[e]	21.64[e]
- Ferritic	1.78[e]	24.69[e]	--	--	--	--	1.95[e]	10.17[e]
NSC	0.91	15.36	0.89	9.11	0.84	15.92	1.06	13.64

(a) Maximum load ratio = experimental maximum load/predicted maximum load
(b) Coefficient of variation = (standard deviation/mean) × 100
(c) Not conducted
(d) From 9 tests
(e) From 3 tests

According to Table 4.31, the LBB.ENG2, LBB.ENG3, and LBB.NRC methods were more accurate than the other estimation methods when all pipe tests are considered. The mean values of maximum load ratio for these methods were very close to unity with reasonable values of COV. For pure bending, the Net-Section- Collapse method had a mean value lower than one, but the coefficient of variation was far greater than that by the above three methods. This implies that the probability of either underpredicting or overpredicting experimental results by the NSC analysis is greater than that by the LBB.ENG2, LBB.ENG3, and LBB.NRC methods. The ASME Section XI IWB-3640 or 3650 method source equations underpredicted the maximum loads the most (largest mean value = 1.47). The COV of maximum load ratio by this method was also the largest among all analysis methods considered here. Further breakdown of statistics for the austenitic and the ferritic pipes indicates that the AMSE Section XI IWB-3640 analyses are more accurate than ASME Section XI IWB-3650 analyses regardless of pipes under pure bending or combined bending and tension. From the

analyses regardless of pipes under pure bending or combined bending and tension. From the respective mean values, the LBB.GE and Paris/Tada methods slightly overpredict the maximum loads, while the GE/EPRI-1A method with a mean value of 1.15 underpredicts the maximum loads the most for the J-estimation schemes.

Similar trends of results for these statistical measures of maximum load ratio also apply for pipes with short through-wall cracks. Once again, the ASME Section XI IWB-3640 or 3650 method has the largest values of both mean and COV. For welded pipes, it appears that LBB.ENG3 is the most accurate method available. The mean and COV of maximum load ratio by LBB.ENG3 are 1.02 and 5.83 percent. The LBB.ENG2, LBB.ENG3, GE/EPRI-1A, and the ASME Section XI IWB-3640 or 3650 methods underpredict the measured loads, while the LBB.NRC, LBB.GE, Paris/Tada, and Net-Section-Collapse analysis methods are overpredict the measured loads.

Not shown in Table 4.31 is the statistical analysis of the R-6 results from Section 4.3.5 since only four experiments were analyzed. The mean and COV for those experiments were 1.26 and 12.1 percent, respectively. As discussed in Section 4.3.5, the R-6 method greatly underpredicts the maximum loads. This is appropriate since as a failure avoidance criteria with inherent conservatism, it should underpredict the failure loads more than the J-estimation schemes intended as accurate predictors.

For pipes under combined bending and tension, all analysis methods underpredicted maximum loads on the average (mean >1). It appears that the estimation methods, which made satisfactory predictions under pure bending, are less accurate for loading conditions that involve combined bending and tension. However, the COVs for combined bending and tension were comparable to those for pure bending.

4.4 References

4.1 Kumar, V., German, M., and Shih, C., "An Engineering Approach for Elastic-Plastic Fracture Analysis," EPRI Report No. NP-1931, July 1981.

4.2 Kumar, V., German, M., Wilkening, Andrews, W., deLorenzi, H., and Mowbray, D., "Advances in Elastic-Plastic Analysis," EPRI Final Report NP-3607, August 1984.

4.3 Brust, F., Rahman, S., and Ghadiali, N., "Elastic-Plastic Analysis of Small Cracks in Tubes," Proceedings of the 11th International Conference on Offshore Mechanics and Arctic Engineering, Calgary, Alberta, Canada, June 1992.

4.4 Paris, P. C. and Tada, H., "The Application of Fracture Proof Design Methods Using Tearing Instability Theory to Nuclear Piping Postulating Circumferential Through-Wall Cracks," NUREG/CR-3464, September 1983.

4.5 Klecker, R., Brust, F., and Wilkowski, G., "NRC Leak-Before-Break (LBB.NRC) Analysis Method for Circumferentially Through-Wall-Cracked Pipes Under Axial Plus Bending Loads," NUREG/CR-4572, May 1986.

4.6 Brust, F. W., "Approximate Methods for Fracture Analyses of Through-Wall Cracked Pipes," NUREG/CR-4853, February 1987.

4.7 Gilles, P. and Brust, F., "Approximate Fracture Methods for Pipes - Part I: Theory," *Nuclear Engineering and Design*, Vol. 127, pp. 1-27, 1991.

4.8 Gilles, P., Chao, K. S., and Brust, F., "Approximate Fracture Methods for Pipes - Part II: Applications," *Nuclear Engineering and Design*, Vol. 127, pp. 13-31, 1991.

4.9 Rahman, S., Brust, F., Nakagaki, M., and Gilles, P., "An Approximate Method for Estimating Energy Release Rates of Through-Wall Cracked Pipe Weldments," *Proceedings of the 1991 ASME Pressure Vessels and Piping Conference*, Vol. 215, San Diego, California, 1991.

4.10 Rahman, S. and Brust, F., "An Estimation Method for Evaluating Energy Release Rates of Circumferential Through-Wall Cracked Pipe Welds," *Engineering Fracture Mechanics*, Vol. 43, No. 3, pp. 417-430, 1992.

4.11 Rahman, S. and Brust, F., "Elastic-Plastic Fracture of Circumferential Through-Wall Cracked Pipe Welds Subject to Bending," *Journal of Pressure Vessel Technology*, Vol. 114, No. 4, pp. 410-416, November 1992.

4.12 Kanninen, M. F. and others, "Mechanical Fracture Predictions for Sensitized Stainless Steel Piping with Circumferential Cracks," Final Report, EPRI NP-192, September 1976.

4.13 "Evaluation of Flaws in Austenitic Steel Piping," Technical basis document for ASME IWB-3640 analysis procedure, prepared by Section XI Task Group for Piping Flaw Evaluation, EPRI Report NP-4690-SR, April 1986.

4.14 American Society of Mechanical Engineers Boiler and Pressure Vessel Code, December 31, 1993 Edition, see Section XI, Appendix H.

4.15 Bucci, R. J., Paris, P. C., Landes, J. D., and Rice, J. R., "J-Integral Estimation Procedures," ASTM STP 514, Part II, pp. 40-69, 1972.

4.16 Rice, J. R., Paris, P. C., Merkle, J. G., "Some Further Results of J-Integral Analysis and Estimates," ASTM STP 536, pp. 231-245, 1973.

4.17. Olson, et al., "The Next Generation Analysis Methodology for Cracked Pipe Systems Subjected to Dynamic Loads," ASME PVP, Vol. 275-1, Volume 1, 1994.

4.18 Sanders, J. L., Jr., "Circumferential Through-Crack in a Cylindrical shell Under Combined Bending and Tension," *Journal of Applied Mechanics*, Vol. 50, p. 221, March 1983.

4.19 Tada, H., Paris, P., and Irwin, G., *The Stress Analysis of Cracks Handbook*, Del Research Corporation, 1973.

4.20 Kumar, V. and German, M. D., "Elastic-Plastic Fracture Analysis of Through-Wall and Surface Flaws in Cylinders," EPRI Final Report NP-5596, January 1988.

4.21 Shih, C. F., "J-Integral Estimates for Strain Hardening Materials in Antiplane Shear Using Fully Plastic Solutions," ASTM STP 590, pp. 3-22, 1976.

4.22 Rice, J. R., "A Path-Independent Integral and the Approximate Analysis of Strain Concentration by Notches and Cracks," Trans. ASME, *Journal of Applied Mechanics*, 35, pp. 376-386, 1968.

4.23 Wilkowski, G. M., et al., "Short Cracks in Piping and Piping Welds," NUREG/CR-4599, BMI-2173, Vol. 1, No. 2, prepared by Battelle Memorial Institute, April 1992.

4.24 Kaiser, S., "An Extension of Tearing Instability Theory to Multiple Loading Parameters," *International Journal of Fracture*, 29, pp. 85-99, 1985.

4.25 Sonnerlind, H. and Kaiser, S., "The J-Integral for a SEN Specimen Under Nonproportionally Applied Bending and Tension," *Engineering Fracture Mechanics*, Vol. 24, No. 5, pp. 637-646, 1986.

4.26 Wilkowski, G. M. and others, "Degraded Piping Program - Phase II," NUREG/CR-4082, Vol. 8, March 1989.

4.27 Shih, C. F., "J-Dominance Under Plane Strain Fully Plastic Conditions: The Edge Crack Panel Subject to Combined Tension and Bending," *International Journal of Fracture*, Vol. 29, pp. 73-84, 1985.

4.28 Shih, C. F. and Hutchinson, J. W., "Combined Loading of a Fully Plastic Ligament Ahead of an Edge Crack," *Journal of Applied Mechanics*, Vol. 53, pp 271-280, June 1986.

4.29 Brust, F. W. and Gilles, P., "Approximate Methods for Fracture Analysis of Tubular Members Subjected to Combined Tensile and Bending Loads," ASME, *Journal of Offshore Mechanics and Arctic Engineering*, Vol. 116, pp 221-227, November 1994.

4.30 Sanders, J. L., "Circumferential Through-Cracks in Cylindrical Shells Under Tension," *Journal of Applied Mechanics*, Vol. 49, 103-107, March 1982.

4.31 Ilyushin, A. A., "The Theory of Small Elastic Plastic Deformations," *Prikadnaia Matematika i Mekhanika*, P.M.M., Vol. 10, 1946.

4.32 "Evaluation of Flaws in Ferritic Piping," EPRI Report NP-4824M, prepared by Novetech Corporation, October 1986.

4.33 Wilkowski, G. M., Brust, F., Francini, R., Ghadiali, N., Kilinski, T., Krishnaswamy, P., Landow, M., Marschall, C. W., Rahman, S., and Scott, P., "Short Cracks in Piping and Piping Welds," Semiannual Reports, Vols. 1, 2, and 3, Nos. 1 and 2, NUREG/CR-4599, 1990-1992.

4.34 Kanninen, M. F. and others, "Instability Predictions for Circumferentially Cracked Type-304 Stainless Steel Pipes Under Dynamic Loading - Volume 2: Appendices," EPRI Report NP-2347, Volume 2, April 1982.

4.35 Schmidt, R. A., Wilkowski, G. M., and Mayfield, M. E., "The International Piping Integrity Research Group (IPIRG) Program -- An Overview," SMiRT-11, Paper G23/1, August 1991.

4.36 Wilkowski, G., Ahmad, J., Brust, F., Guerrieri, D., Kramer, G., Kulhowvick, G., Landow, M., Marschall, C., Nakagaki, M., Papaspyropoulos, V., and Scott, P., "Analysis of Experiments on Stainless Steel Flux Welds," NUREG/CR-4878, April 1987.

4.37 Nakagaki, M., Marschall, C., and Brust, F., "Analysis of Cracks in Stainless Steel TIG Welds," NUREG/CR-4806, December 1986.

4.38 Milne, I., Ainsworth, R. A., Dowling, A. R., and Stewart, A. T. "Background To And Validation of CEGB Report R/H/R6 - Revision 3," January 1987.

4.39 Milne, I, Ainsworth, R. A., Dowling, A. R., and Stewart, A. T. "Assessment of the Integrity of Structures Containing Defects, CEGB Report R/H/R6 - Revision 3," 1986.

4.40 Kanninen, M. F., Wilkowski, G. M., Pan, J., Ahmad, J., Marschall, C. W., Gilbert, E. R., Popelar, C. H., and Broek, D., "The Development of a Plan for the Assessment of Degraded Nuclear Piping by Experimentation and Tearing Instability Fracture Mechanics Analysis," NUREG/CR-3142 Vol. 2, June 1983.

4.41 Kramer, G. and Papaspyropoulos, V., "An Assessment of Circumferentially Complex-Cracked Pipe Subjected to Bending," NUREG/CR-4687, October 1986.

4.42 Wilkowski, G., Kramer, G., Vieth, P., Francini, R., and Scott, P., "The Effect of Cyclic Loading During Ductile Tearing on Circumferentially Cracked Pipe -- Analytical Results," ASME PVP Vol. 280, pp 221-240, June 1994.

4.43 Vassilaros, M. G., Hays, R. A., Gudas, J. P., and Joyce, J. A., "J-Integral Tearing Instability Analyses for 8-Inch Diameter ASTM A106 Steel Pipe," NUREG/CR-3740, April 1984.

4.44 Hays, R. A., Vassilarious, M. G., and Gudas, J. P., "Fracture Analysis Welded Type 304 Stainless Steel Pipe," prepared by David Taylor Naval Ship R&D Center for the NRC, NUREG/CR-4538, Vol. 1, May 1986.

5. SUMMARY AND CONCLUSIONS

For LBB analyses, through-wall-crack (TWC) lengths of about 6-percent of the pipe circumference are typical for large diameter pipe. For small diameter pipe, the LBB crack size is much larger and sufficient data for those cases existed from past programs (Ref. 5.1).

The objective of this effort was to increase the database for pipes with short TWC, particularly for large diameter pipe, and verify the accuracy of existing and modified pipe fracture analyses. In support of this effort, the pipe material property database was increased to include several new materials. The material property data from this effort were entered into Version 3.0 of PIFRAC (Ref. 5.2). The pipe test data were input into the pipe fracture database CIRCUMCK.WK1 (Ref. 5.2).

Some key points from the various sections of this report are reviewed below.

Material Characterization Efforts

For the several different pipe materials characterized in this effort four important points are noteworthy.

(1) The high Mn-Mo carbon steel pipe submerged-arc weld evaluated in this program (DP2-F49W) was produced using a weld procedure employed in 90-percent of B&W piping welds. Data on welds made by this weld procedure were not previously available. The B&W Mn-Mo-Ni weld procedure which was used to make the welds assessed in the Degraded Piping Program (Ref. 5.1) was used in the other 10-percent of their carbon steel piping welds, as well as for some of their pressure vessel welds. For the C(T) specimen tests at 22 C (72 F) on the high Mn-Mo weld evaluated in this program, only a small amount of stable crack growth ocurred prior to the specimens undergoing an unstable, cleavage fracture. At 288 C (550 F), the two welds had virtually identical J-R curves.

(2) The French TP316L pipe material had an unusually low elastic modulus of 22,840,000 psi (157.5 GPa) at room temperature. This was verified by tests by several organizations in France.

(3) The stainless steel SAW evaluated in this program was created using the same General Electric weld procedure used in the Degraded Piping Program (Ref. 5.3) and the IPIRG-1 Program (Ref. 5.4). There were significant differences in the weld metal yield strengths between the three welds evaluated in this program, the Degraded Piping Program, and the IPIRG-1 Program, but the J-R curves of the three different welds were not significantly different. The stainless steel welds had a lower toughness than the B&W high Mn-Mo carbon steel weld.

(4) Crack instabilities occurred in the side-grooved C(T) specimens for the material evaluated in the 28-inch nominal diameter A515 Grade 60 carbon steel pipe experiment, but not in the non-side-grooved specimens. These crack instabilities also occurred in the pipe experiment and were attributed to dynamic strain aging effects. However, materials that are susceptible to

dynamic strain aging also typically exhibit serrations on their stress-strain curves. The stress-strain curves for this material exhibited no such serrations, which may be the result of differences in the effective strain rate between the tensile and the C(T) or cracked-pipe specimens.

Pipe Fracture Experiments

Prior to this program, there was very little experimental data from tests on pipes with short through-wall cracks. To help fill this deficiency, five experiments were performed as follows:

- two A515 Grade 60 carbon steel base metal experiments both at 288 C (550 F), one with a 6.25-percent circumferential crack and one with no crack,
- one TP316 stainless steel pipe experiment at 288 C (550 F) with the crack in the submerged-arc weld and a crack length to pipe circumference ratio of 6.25-percent,
- one A106 Grade B carbon steel pipe experiment at 288 C (550 F) with the crack in a submerged-arc weld and a crack length to pipe circumference ratio of 7.9 percent, and
- one experiment performed at room temperature on a French TP316L stainless steel pipe with a crack 24.4-percent of the circumference in the base metal.

Data from these tests were entered into the CIRCUMCK.WK1 database.

For each experiment, the applied loads, displacements, crack-growth history, crack-mouth-opening displacement, pipe rotation, ovalization, and temperature were recorded. These data were then used for comparison with the results predicted using the J-estimation methods in order to document the accuracy of the predictive methods.

The highlights of these experiments are summarized in the following paragraphs.

(1) The French TP316L pipe experiment was a repeat of an Electricité de France (EDF) pipe experiment. This experiment was conducted to assess the reproducibility of pipe test data between laboratories. The Battelle and EDF maximum loads agreed within 3 percent of each other. This is within the 5 percent repeatability of pipe experiments observed in other identical pipe tests conducted at Battelle. The confirmation of this test was important for the following reason.

For several of the Battelle U.S. TP304 stainless steel pipe experiments tested in the past, finite element analyses (FEA) by several organizations underpredicted the loads at crack initiation by 20 to 30 percent (Ref. 5.5). However, for the French pipe experiment, the results from several different FEA agreed well with the experimental results (Ref. 5.5). The FEAs agreed well with each other for each experiment, so those analyses were validated. One concern was the possibility of experimental error between the French and Battelle results. The test result from this program shows that there was no significant experimental error. After an exhaustive review of the experimental data and analyses, it is believed that the only explanation of the

FEM underprediction of the U.S. TP304 stainless is due to differences in the constitutive behavior.

Interestingly, the French TP316L stainless steel showed significant anisotropy as is indicated by the elliptical fracture surface in the longitudinal tensile test specimen (Ref. 5.6). The U.S. TP304 steel showed no signs of anisotropy. The French steel also had an unusually low elastic modulus, as noted earlier in this section. Therefore, precise fracture analyses of stainless steel base metals may require more attention to the constitutive behavior of the material. The FEM underprediction for the U.S. stainless steel may be the reason the GE/EPRI (FEM based) method is consistently underpredicting the experimental failure loads.

(2) Three pipe experiments were conducted on the same 28-inch nominal diameter A515 Grade 60 pipe. These were: an uncracked-pipe experiment (from this program), a pipe experiment with a TWC of 6.25 percent of the pipe circumference crack (from this program), and a pipe experiment with a 37-percent circumferential TWC (from Reference 5.1). Surprisingly, the 6.25-percent-cracked-pipe maximum load was only 65 percent of the uncracked pipe maximum load. From the Net-Section-Collapse analysis it was expected that the loads would be within 5 percent of each other for the uncracked-pipe and short-cracked-pipe experiments. Hence, the failure was an elastic-plastic fracture even though it had such a short crack length.

(3) Ovalization measurements from all of the pipe experiments showed that all of the TWC-pipe experiments ovalized in the opposite plane as the uncracked pipe, but the magnitude of the ovalization was small.

(4) During the stainless steel welded pipe experiment, the crack grew two-thirds longer on one side than the other side. The side with the longer crack growth had the crack follow the fusion line of the weld, even though the initial TWC was in the center of the weld. On the short crack growth side, the crack grew from the center of the weld to the fusion line and then into the base metal. In another report from the Short Cracks in Piping and Piping Welds Program ("Stainless Steel Submerged Arc Weld Fusion-Line Toughness," NUREG/CR-6251), it was found that the J-R curve from a stainless steel SAW fusion line was much lower than the base metal and the weld metal J-R curves after small amounts of crack growth. This explains why the crack grew from the center of the weld to the fusion line. It is not known why on one side the crack grew from the fusion line into the base metal, since the base metal toughness is so much higher. However, the fact that it did grow into the base metal on this side explains why the crack on this side would be shorter than the crack on the other side, the one which followed the fusion line.

Pipe Fracture Analyses

The analysis results reported here focussed on simple predictive methods based on J-Tearing theory. The J-estimation methods evaluated were the GE/EPRI, Paris/Tada, LBB.NRC, LBB.ENG2, LBB.ENG3, and the R-6 Option 1 analyses. In addition, new GE/EPRI solutions were developed for short cracks, along with a new methodology to predict the fracture behavior of cracks in pipe welds (LBB.ENG3). Improvements were also made to the methods to increase the accuracy of fracture predictions for pipe with short through-wall cracks. In summary, all predictive methods attempted to

estimate the crack-driving force as measured with the J-integral either by using a matrix of numerical solutions (GE/EPRI) or by estimating the load-displacement record and predicting J using mathematical principles. Often numerical solutions were also used to verify the accuracy of the J-estimation schemes.

Predictions of all pipe fracture experiments were made and compared with the corresponding experimental results. Crack initiation loads, maximum loads, crack growth response, and load-point displacements were compared between experiment and analysis. (Crack opening displacement analyses and comparisons with experimental data are covered in a separate report, NUREG/CR-6300 - "Refinement and Evaluation of Crack-Opening Analyses for Short Circumferential Through-Wall Cracks in Pipes"). The key findings from the current report are given below.

(1) An η-factor analysis procedure for calculating the J-R curve from short-TWC-pipe experiments was developed and compared with FEM results. The results showed that accounting for the uncracked pipe or remote plasticity that occurs with short cracks can be done only in a bounding manner. For determining the J-R curve from a pipe with a short-TWC, it would be better to develop an η-factor analysis that uses the load versus center-crack-opening displacement data to eliminate the concern of the plasticity from the uncracked pipe. This new η-factor function could be developed using the new GE/EPRI functions from this program.

For pipes under combined pressure plus bending loads, an η-factor analysis method was developed and used to analyze several past pipe experiments with long through-wall cracks. For two different pipes there were both pure bending and pressure plus bending experiments. The J-R curve from the pure bending pipe experiment was slightly higher than the J-R curve from the pressure plus bending experiment for each pipe; however, the differences were not significant.

(2) The newly developed GE/EPRI functions had significant improvement in the displacement predictions, but not for the load predictions.

(3) Combined tension and bending GE/EPRI functions for pipes at PWR pressures were developed. If used for BWR pipe analyses, these functions will underpredict the actual cracked-pipe loads but overpredict the displacements.

In one set of calculations, it was also found that the hoop stress significantly affected the GE/EPRI crack-opening and pipe displacement functions under combined loading. However, the new GE/EPRI functions developed and implemented into the NRCPIPE code (Ref. 5.2) were for combined tension and bending without hoop stress considerations.

(4) Ovalization effects were found to be small, and hence were not specifically included in the J-estimation schemes (other than the GE/EPRI method that is FEM based and hence inherently incorporates ovalization effects). Under pressure loading, it is anticipated that the ovalization effects on loads would become even smaller.

(5) A modification to the LBB.ENG2 analysis (called LBB.ENG3) was developed to include the strength of the weld and base metals in the J-estimation scheme. This was the first and at this

writing remains the only J-estimation scheme that accounts for cracks in weld metal. Better predictions were made in some cases and little difference occurred in others.

(6) Various pipe fracture analyses were compared with the pure bending data from this program, the Degraded Piping Program, and pressure plus bend data from other programs. The comparisons showed the following.

- There was better agreement between analyses for long cracks than for short cracks.
- The analyses that gave the most accurate predictions were the LBB.NRC, LBB.ENG2, and LBB.GE methods.
- Of all the J-estimation schemes, the GE/EPRI analyses consistently underpredicted the experimental loads the most. It did not matter if the plastic zone was included in the elastic term or not, nor if the old or new h_1 functions were used. There were differences in the old and new GE/EPRI h_i function, but since M is proportional to $(J/h_1)^{\frac{1}{n+1}}$, the effect on the moment predictions was small.
- The Paris/Tada and Net-Section-Collapse analyses were erratic, sometimes underpredicting and sometimes overpredicting the loads significantly.
- The ASME Section XI IWB-3640 and IWB-3650 pipe fracture analyses (without safety factors) generally underpredicted the experimental loads the most of all analyses; however, in one stainless steel pipe base-metal-crack experiment, the IWB-3640 analysis overpredicted the experimental maximum load. In this experiment, the strength of the pipe was very close to the Code values at temperature, perhaps indicating that the choice of $3S_m$ for flow stress is slightly too high for a material that just meets the Code strength values.
- There was less accuracy in the prediction of the pipe experiments under combined pressure plus bending than for pure bending, but the relative accuracy was the same for the estimation schemes under either combined bending plus pressure or pure bending.
- The R6, Revision 3, Option 1 method comparison with the experimental results showed that the method always underpredicts the maximum load. For the experiments analyzed, the average value of the ratio of the experimental maximum load to the R-6, Option 1 prediction was 1.26. This method underpredicted loads the most of all the methods.

(7) The fracture-mechanics-based analyses throughout this report were conducted using a Ramberg-Osgood fit of the stress-strain curve over a strain range of 0.1 percent strain to the strain corresponding to 80-percent of the ultimate strength for the engineering stress-strain curve. C(T) specimen J-R curves were extrapolated using the C(T) specimen data for crack growth up to 30 percent of the initial specimen ligament and a power-law equation for extrapolating the J-R curve for larger amounts of crack growth (Ref. 5.7). In general, it was found that the standard C(T) specimen J-R curve was lower than the quasi-static pipe test J-R

curve from an η-factor analysis. Therefore, predictions using C(T) specimens for quasi-static loaded pipes (as in this program) should underestimate the actual loads during crack growth. However, work in other programs showed that when the pipe is loaded dynamically or under cyclic tearing (as in a seismic event), then the J-R curve from the pipe test can be lower than J-R curves developed using the ASTM Standard, quasi-static, monotonically loaded, C(T) specimen testing procedure (Ref. 5.8).

5.1 References

5.1 Wilkowski, G. M., and others, "Degraded Piping Program-Phase II," Summary of Technical Results and Their Significance to Leak-Before-Break and In-Service Flaw Acceptance Criteria, March 1984 - January 1989, Battelle, NUREG/CR-4082, Vol. 8, March 1989.

5.2 Wilkowski, G. M. and others, "Short Cracks in Piping and Piping Welds," Sixth Semiannual Report, NUREG/CR-4599, Vol. 3, No. 2, March 1994.

5.3 Wilkowski, G. M., and others, "Analysis of Experiments on Stainless Steel Flux Welds," NUREG/CR-4878, April 1987.

5.4 Marschall, C. W., Landow, M., and Wilkowski, G. M., "Loading Rate Effects on Strength and Fracture Toughness of Pipe Steels Used in Task 1 of the IPIRG Program," NUREG/CR-6098, October 1993.

5.5 Brust, et al., "Comparison Between Finite Element Analysis Predictions and Pipe Fracture Experiments", *Nuclear Engineering and Design*, 143, pp 201-215 (1993).

5.6 Wilkowski, G. M. and others, "Short Cracks in Piping and Piping Welds," Battelle, NUREG/CR-4599, Vol. 2, No. 1, June 1992.

5.7 Wilkowski, G. M., Marschall, C. W., and Landow, M., "Extrapolations of C(T) Specimens J-R Curves for Use in Pipe Flaw Evaluations," ASTM STP 1074, pp 56-84, 1990.

5.8 Wilkowski, G., Kramer, G., Vieth, P., Francini, R., and Scott, P., "The Effect of Cyclic Loading During Ductile Tearing on Circumferentially Cracked Pipe -- Analytical Results," ASME PVP Vol. 280, pp 221-240, June 1994.

APPENDIX A

F_B and I_B Functions

Appendix A F_B and I_B Functions

A.1 F_B AND I_B Functions

Using Sanders' solutions (Refs. A.1 and A.2) by shell theory and energy integral technique, Paris and Tada (Ref. A.3) have developed the following approximations of F_B and I_B.

$$F_B(\theta) \simeq 1 + A_b\left[\frac{\theta}{\pi}\right]^{1.5} + B_b\left[\frac{\theta}{\pi}\right]^{2.5} + C_b\left[\frac{\theta}{\pi}\right]^{3.5} \tag{A-1}$$

where

$$\begin{aligned} A_b &= -3.2654 + 1.5278\left[\frac{R_m}{t}\right] - 0.0727\left[\frac{R_m}{t}\right]^2 + 0.0016\left[\frac{R_m}{t}\right]^3 \\ B_b &= 11.3632 - 3.9141\left[\frac{R_m}{t}\right] + 0.1862\left[\frac{R_m}{t}\right]^2 - 0.0041\left[\frac{R_m}{t}\right]^3 \\ C_b &= -3.1861 + 3.8476\left[\frac{R_m}{t}\right] - 0.1830\left[\frac{R_m}{t}\right]^2 + 0.0040\left[\frac{R_m}{t}\right]^3 \end{aligned} \tag{A-2}$$

and

$$\begin{aligned} I_B(\theta) &= 4\int_0^{\theta} \xi F_B(\xi)^2 d\xi \\ &\simeq 2\theta^2\left[1 + 8\left[\frac{\theta}{\pi}\right]^{1.5} I_{b_1} + \left[\frac{\theta}{\pi}\right]^3 \left(I_{b_2} + I_{b_3}\right)\right] \end{aligned} \tag{A-3}$$

where

$$\begin{aligned} I_{b_1} &= \frac{A_b}{7} + \frac{B_b}{9}\left[\frac{\theta}{\pi}\right] + \frac{C_b}{11}\left[\frac{\theta}{\pi}\right]^2 \\ I_{b_2} &= \frac{A_b^2}{2.5} + \frac{A_b B_b}{1.5}\left[\frac{\theta}{\pi}\right] + \frac{2A_bC_b + B_b^2}{3.5}\left[\frac{\theta}{\pi}\right]^2 \\ I_{b_3} &= \frac{B_bC_b}{2}\left[\frac{\theta}{\pi}\right]^3 + \frac{C_b^2}{4.5}\left[\frac{\theta}{\pi}\right]^4 \end{aligned} \tag{A-4}$$

Also, for tension:

$$
\begin{aligned}
A_t &= -2.02917 + 1.6773(R_m/t) - 0.07987(R_m/t)^2 + 0.00176(R_m/t)^3 \\
B_t &= 7.09987 - 4.42394(R_m/t) + 0.21036(R_m/t) - 0.00463(R_m/t)^3 \\
C_t &= 7.79661 + 5.16676(R_m/t) - 0.24577(R_m/t)^2 + 0.00541(R_m/t)^3
\end{aligned}
\qquad \text{(A-5)}
$$

A.2 References

A.1 Sanders, J. L., "Circumferential Through-Cracks in Cylindrical Shells Under Tension," Journal of Applied Mechanics, Vol. 49, 103-107, March 1982.

A.2 Sanders, J. L., "Circumferential Through-Crack in a Cylindrical Shell Under Combined Bending and Tension," Journal of Applied Mechanics, Vol. 50 p. 221, March 1983.

A.3 Paris, P. C. and Tada, H., "The Application of Fracture Proof Design Methods Using Tearing Instability Theory to Nuclear Piping Postulating Circumferential Through-Wall Cracks," NUREG/CR-3464, 1983.

APPENDIX B

Plastic Solution of Equivalent Pipe

Appendix B Plastic Solution of Equivalent Pipe

B.1 Governing Differential Equations

Using classical beam theory for small deformation, the governing differential equations for the pipe shown in Figure 4.17 are:

1. Segment AB ($\hat{a}/2 \le x \le L/2$)

$$\frac{d^2y}{dx^2} = \frac{1}{R_m}\left[\frac{M}{M_{01}}\right]^{n_1} \tag{B-1}$$

$$\frac{dy}{dx} = \frac{1}{R_m}\left[\frac{M}{M_{01}}\right]^{n_1} x + C_1 \tag{B-2}$$

$$y = \frac{1}{R_m}\left[\frac{M}{M_{01}}\right]^{n_1} \frac{x^2}{2} + C_1 x + C_2 \tag{B-3}$$

2. Segment BC ($L_w/2 \le x \le \hat{a}/2$)

$$\frac{d^2y}{dx^2} = \frac{1}{R_m}\left[\frac{M}{M_{01}}\right]^{n_1}\left[\frac{t}{t_e}\right]^{n_1} \tag{B-4}$$

$$\frac{dy}{dx} = \frac{1}{R_m}\left[\frac{M}{M_{01}}\right]^{n_1}\left[\frac{t}{t_e}\right]^{n_1} x + C_3 \tag{B-5}$$

$$y = \frac{1}{R_m}\left[\frac{M}{M_{01}}\right]^{n_1}\left[\frac{t}{t_e}\right]^{n_1} \frac{x^2}{2} + C_3 x + C_4 \tag{B-6}$$

3. Segment CD ($0 \le x \le L_w/2$)

$$\frac{d^2y}{dx^2} = \frac{1}{R_m}\left[\frac{M}{M_{02}}\right]^{n_2}\left[\frac{t}{t_e}\right]^{n_2} \tag{B-7}$$

$$\frac{dy}{dx} = \frac{1}{R_m}\left[\frac{M}{M_{02}}\right]^{n_2}\left[\frac{t}{t_e}\right]^{n_2} x + C_5 \tag{B-8}$$

$$y = \frac{1}{R_m}\left[\frac{M}{M_{02}}\right]^{n_2}\left[\frac{t}{t_e}\right]^{n_2} \frac{x^2}{2} + C_5 x + C_6 \tag{B-9}$$

where

$$M_{0i} = \frac{4K_i I\hat{K}_i}{\pi R_m},\ K_i = \frac{\sigma_{0i}}{(\alpha_i \epsilon_{0i})^{1/n_i}},\ \hat{K}_i = \frac{\sqrt{\pi}}{2}\frac{\Gamma\left[1+\frac{1}{2n_i}\right]}{\Gamma\left[\frac{3}{2}+\frac{1}{2n_i}\right]} \tag{B-10}$$

with the gamma function

$$\Gamma(u) = \int_0^\infty \xi^{u-1}\exp(-\xi)\,d\xi \tag{B-11}$$

and $I \simeq \pi R_m^3 t$ is the moment of inertia of uncracked pipe cross-section. Enforcing appropriate boundary and compatibility conditions, the constants C_1 to C_6 can be determined as:

$$C_1 = -\frac{1}{R_m}\left[\frac{M}{M_{01}}\right]^{n_1}\left[\frac{\alpha}{2}\left\{1-\left[\frac{t}{t_e}\right]^{n_1}\right\}+\frac{L_w}{2}\left[\frac{t}{t_e}\right]^{n_1}\right]+\frac{1}{R_m}\left[\frac{M}{M_{02}}\right]^{n_2}\left[\frac{L_w}{2}\left[\frac{t}{t_e}\right]^{n_2}\right] \tag{B-12}$$

$$C_2 = \frac{1}{R_m}\left[\frac{M}{M_{01}}\right]^{n_1}\left[-\frac{L^2}{8}+\frac{L}{2}\frac{\hat{a}}{2}\left\{1-\left[\frac{t}{t_e}\right]^{n_1}\right\}+\frac{L}{2}\frac{L_w}{2}\left[\frac{t}{t_e}\right]^{n_1}\right]- \frac{1}{R_m}\left[\frac{M}{M_{02}}\right]^{n_2}\left[\frac{L}{2}\frac{L_w}{2}\left[\frac{t}{t_e}\right]^{n_2}\right] \tag{B-13}$$

$$C_3 = -\frac{1}{R_m}\left[\frac{M}{M_{01}}\right]^{n_1}\left[\frac{L_w}{2}\left[\frac{t}{t_e}\right]^{n_1}\right]+\frac{1}{R_m}\left[\frac{M}{M_{02}}\right]^{n_2}\left[\frac{L_w}{2}\left[\frac{t}{t_e}\right]^{n_2}\right] \tag{B-14}$$

$$C_4 = \frac{1}{R_m}\left[\frac{M}{M_{01}}\right]^{n_1}\left[-\frac{L^2}{8}+\frac{L}{2}\frac{\hat{a}}{2}\left\{1-\left[\frac{t}{t_e}\right]^{n_1}\right\}+\frac{L}{2}\frac{L_w}{2}\left[\frac{t}{t_e}\right]^{n_1}-\frac{\hat{a}^2}{8}\right] - \frac{1}{R_m}\left[\frac{M}{M_{02}}\right]^{n_2}\left[\frac{L}{2}\frac{L_w}{2}\left[\frac{t}{t_e}\right]^{n_2}\right] \quad \text{(B-15)}$$

$$C_5 = 0 \quad \text{(B-16)}$$

$$C_6 = \frac{1}{R_m}\left[\frac{M}{M_{01}}\right]^{n_1}\times \left[-\frac{L^2}{8}+\frac{L}{2}\frac{\hat{a}}{2}\left\{1-\left[\frac{t}{t_e}\right]^{n_1}\right\}+\frac{L}{2}\frac{L_w}{2}\left[\frac{t}{t_e}\right]^{n_1}-\frac{\hat{a}^2}{8}-\frac{L_w^2}{8}\left[\frac{t}{t_e}\right]^{n_1}\right] - \frac{1}{R_m}\left[\frac{M}{M_{02}}\right]^{n_2}\left[\frac{L_w^2}{8}\left[\frac{t}{t_e}\right]^{n_2}-\frac{L}{2}\frac{L_w}{2}\left[\frac{t}{t_e}\right]^{n_2}\right] \quad \text{(B-17)}$$

APPENDIX C

Partial Derivatives $\partial I_B/\partial\theta$ and $\partial L_B/\partial\theta$

Appendix C Partial Derivatives $\partial I_B/\partial\theta$ and $\partial L_B/\partial\theta$

C.1 Partial Derivatives $\partial I_B/\partial\theta$ and $\partial L^D_B/\partial\theta$

The expression for the derivatives $\partial I_B/\partial\theta$ and $\partial L_B/\partial\theta$ are given below:

$$\frac{\partial I_B}{\partial\theta} = 4\theta F_B(\theta)^2 \tag{C-1}$$

$$\frac{\partial L_B}{\partial\theta} = \frac{1}{[\overline{A}_3 G_1(\theta)]^2} \left\{ \begin{array}{l} \overline{A}_3 G_1(\theta)[\overline{A}_1 G'_{n_1}(\theta) + \overline{A}_2 G'_{n_2}(\theta)] - \\ \overline{A}_3 G'_1(\theta)[\overline{A}_1 G_{n_1}(\theta) + \overline{A}_2 G_{n_2}(\theta)] \end{array} \right\} \tag{C-2}$$

in which

$$\begin{aligned} G_k(\theta) &= \left[\cos\frac{\theta}{2} - \frac{1}{2}\sin\theta\right]^{-k} \\ G'_k(\theta) &= \frac{k}{2}\left[\sin\frac{\theta}{2} + \cos\theta\right] G_{k+1}(\theta) \end{aligned} \tag{C-3}$$

$$\begin{aligned} \overline{A}_1 &= \left[\frac{M}{M_{01}}\right]^{n_1}\left[\frac{\hat{a}}{2} - \frac{L_w}{2}\right] C^{-n_1} \frac{1}{\alpha_1\left[\frac{M}{M_1}\right]^{n_1-1}} \\ \overline{A}_2 &= \left[\frac{M}{M_{02}}\right]^{n_2}\left[\frac{L_w}{2}\right] C^{-n_2} \frac{1}{\alpha_1\left[\frac{M}{M_1}\right]^{n_1-1}} \\ \overline{A}_3 &= \left[\frac{M}{M_1}\right]\epsilon_{01}\left[\frac{\hat{a}}{2} - \frac{L_w}{2}\right] C^{-1} + \left[\frac{M}{M_2}\right]\epsilon_{02}\left[\frac{L_w}{2}\right] C^{-1} \end{aligned} \tag{C-4}$$

where $\overline{C} = 1$ or $\overline{C} = 4/\pi$ according to whether $0° \le 2\theta \le 90°$ or $2\theta \ge 120°$, respectively. When $90° \le 2\theta \le 120°$, $\overline{C}$ can be interpolated from the above two limits (Ref. C.1).

C.2 References

C.1 Brust, F. W., "Approximate Methods for Fracture Analyses of Through-Wall Cracked Pipe," NUREG/CR-4853, February 1987.

NRC FORM 335 (2-89) NRCM 1102, 3201, 3202

U.S. NUCLEAR REGULATORY COMMISSION

BIBLIOGRAPHIC DATA SHEET

(See instructions on the reverse)

1. REPORT NUMBER (Assigned by NRC. Add Vol., Supp., Rev., and Addendum Numbers, if any.)

NUREG/CR-6235
BMI-2179

2. TITLE AND SUBTITLE

Assessment of Short Through-Wall Circumferential Cracks in Pipes

Experiments and Analysis

March 1990 - December 1994

3. DATE REPORT PUBLISHED

MONTH	YEAR
April	1995

4. FIN OR GRANT NUMBER

B5702

5. AUTHOR(S)

F. W. Brust, P. Scott, S. Rahman, N. Ghadiali, T. Kilinski, B. Francini, C. W. Marschall, N. Miura*, P. Krishnaswamy, G. M. Wilkowski

6. TYPE OF REPORT

Technical

7. PERIOD COVERED *(Inclusive Dates)*

3/90 - 12/94

8. PERFORMING ORGANIZATION – NAME AND ADDRESS *(If NRC, provide Division, Office or Region, U.S. Nuclear Regulatory Commission, and mailing address; if contractor, provide name and mailing address.)*

Battelle
505 King Avenue
Columbus, OH 43201-2693

*Central Research Institute of Electric Power Industry
Komae Research Laboratory
Tokyo 201 Japan

9. SPONSORING ORGANIZATION – NAME AND ADDRESS *(If NRC, type "Same as above"; if contractor, provide NRC Division, Office or Region, U.S. Nuclear Regulatory Commission, and mailing address.)*

Division of Engineering Technology
Office of Nuclear Regulatory Research
U.S. Nuclear Regulatory Commission
Washington, D.C. 20555-0001

10. SUPPLEMENTARY NOTES

11. ABSTRACT *(200 words or less)*

This topical report summarizes the work performed for the Nuclear Regulatory Commission's (NRC) research program entitled "Short Cracks in Piping and Piping Welds" that specifically focuses on pipes with short through-wall cracks. Previous NRC efforts, conducted under the Degraded Piping Program, focused on understanding the fracture behavior of larger cracks in piping and fundamental fracture mechanics developments necessary for this technology. This report gives details on: (i) material property determinations, (ii) pipe fracture experiments, and (iii) development, modification, and validation of fracture analysis methods. The material property data required to analyze the experimental results are included. These data were also implemented into the NRC's PIFRAC database. Three pipe experiments with short through-wall cracks were conducted on large diameter pipe. Also, experiments were conducted on a large-diameter uncracked pipe and a pipe with a moderate-size through-wall crack. The analysis results reported here focus on simple predictive methods based on the J-Tearing theory as well as limit-load and ASME Section XI analyses. Some of these methods were improved for short-crack-length predictions. The accuracy of the various methods was determined by comparisons with experimental results from this and other programs.

12. KEY WORDS/DESCRIPTORS *(List words or phrases that will assist researchers in locating the report.)*

Fracture, pipe, J-integral, circumferential crack, through-wall crack, ferritic steel, austenitic steel, welds, leak before break

13. AVAILABILITY STATEMENT

Unlimited

14. SECURITY CLASSIFICATION

(This Page) Unclassified

(This Report) Unclassified

15. NUMBER OF PAGES

16. PRICE

NRC FORM 335 (2-89)